

Structural, magnetic and electrical transport properties of GaN-based magnetic semiconductors and hybrid structures

Dissertation
zur Erlangung des Doktorgrades
der Mathematisch-Naturwissenschaftlichen Fakultäten
der Georg-August-Universität zu Göttingen

vorgelegt von
Amilcar Bedoya Pinto
aus Lima, Peru

Göttingen, 2010

D7

Referentin: Prof. Dr. Angela Rizzi

Koreferent: Prof. Dr. Thomas Schäpers

Tag der mündlichen Prüfung: 9. November 2010

Table of Contents

Table of Contents	i
Introduction	1
1 Theoretical Background	5
1.1 Gallium Nitride: Defects and doping	6
1.1.1 Native defects	7
1.1.2 Residual impurities	11
1.1.3 Magnetic doping	14
1.2 Electronic transport in doped semiconductors	16
1.2.1 Single-activated electronic transport	17
1.2.2 Coexistence of single-activated and hopping transport	22
1.2.3 Theory of Hopping Conduction	24
1.2.4 Mott's law and Variable-Range-Hopping conduction	36
1.2.5 Correlation effects in Hopping conduction: The Coulomb Gap	40
1.2.6 Band and Hopping conduction under magnetic fields: The Hall- Effect	49
2 Experimental methods	53
2.1 Substrate choice	54
2.2 Preparation of Ohmic contacts	55
2.3 Four-point resistance measurements	57
2.3.1 The van der Pauw method	57
2.3.2 Hall-bar geometry	59
2.3.3 Measurement Set-Up	60
3 Experimental Results and Discussion	63
3.1 Undoped GaN	64
3.2 Mn-doped GaN	70
3.2.1 Growth conditions and structural properties	71
3.2.2 Magnetic properties	76
3.2.3 Optical properties: Photo-Luminescence	89
3.2.4 Electrical transport properties	90

3.3	Gd-doped GaN	101
3.3.1	Growth conditions and structural properties	101
3.3.2	Magnetic properties	106
3.3.3	Electrical transport properties	110
3.3.4	Defect identification: Spectroscopy studies	121
3.4	MnGa/GaN hybrid structures	134
3.4.1	Experimental details	134
3.4.2	Growth and structural properties	135
3.4.3	Magnetic properties	137
3.4.4	Electrical transport	138
4	Summary and Outlook	145
A	Diamagnetic background correction	151
B	Positron Annihilation Spectroscopy	155
	Bibliography	157

Introduction

Semiconductors, materials in which the charge transport can be well controlled, are at present invaluable ingredients in the emerging field of information technology. The elemental modules for information processing are field-effect transistors (FETs), which are semiconductor switching devices where the charge is manipulated by an external electric field. On the other hand, information storage requires the use of the electron spin. While the concept of magnetic recording has been known for a long time, the discovery of the GMR-Effect [1, 2] was a milestone which showed that the electron transport can be indeed controlled through the spin state of the conducting electrons. That was the beginning of a new research field in solid-state physics, which combines both charge and spin of the electrons, called Spintronics. Considering the spin as an additional degree of freedom in the already known electronic processes, attracted many theoretical and experimental efforts in the last two decades. In particular, if the integration of the spin functionality in semiconductor structures is performed in a reliable and efficient way, the advantages from the „magnetic world“ such as programmability or non-volatility, could be added to the well established semiconductor device technology.

Two approaches have been mainly investigated to induce spin-polarized currents in a semiconductor. One approach is the doping of a semiconducting host material with magnetic atoms, aiming for an intrinsic ferromagnetic coupling, while the second approach consists in the preparation of heterostructures to inject spin-polarized currents from a ferromagnetic layer into the semiconductor. For the latter, metal-semiconductor hybrid structures have been investigated, putting special emphasis on minimizing the detrimental influence of the interface on the injection efficiency. However, given the possibility to achieve ferromagnetism in a semiconductor by doping, it would be of advantage to use a magnetic semiconductor as a spin injector. First, the all-semiconductor epitaxial growth results in a smooth interface which favors the spin injection efficiency, and second, the problem of the metal-semiconductor resistivity mismatch is avoided. Moreover, the achievement of magnetic semiconductors with robust magnetic properties, combined with semiconductor channels with long spin coherence times, seems to be the perfect solution to design high-performance, all-semiconducting spintronic devices.

However, the story is too good to be true. While there has been indeed success in measuring exceptionally long coherence times in non-magnetic semiconductors (three orders of magnitude longer than in non-magnetic metals) [3], the existence of a magnetic semiconductor with robust magnetic properties is still a controversial issue. For

the latter, it should be mentioned that the typical concentration of the magnetic substituents is low (1-10 at%) since the semiconducting properties of the host should not be affected by the alloying process. (This material class is hence called dilute magnetic semiconductors (DMS)). On the other hand, the concentration of magnetic species should be great enough to account for a long-ranged magnetic coupling, so that both conditions leave a rather small concentration window for the achievement of a functional dilute magnetic semiconductor. Although many research groups have observed room-temperature ferromagnetism in a wide range of host semiconductors and magnetic dopants, a major challenge is still a reproducible and well-defined preparation of DMS layers and a comprehensive understanding of the magnetic coupling mechanisms. Mn-doped GaAs, perhaps the most studied DMS, is the exception. Both theoretical and experimental studies on this material unambiguously agree about the existence of intrinsic ferromagnetic properties [4]. The underlying magnetic coupling mechanism has its origin in the hybridization of the p-states of Ga (valence band) and the d-states of Mn, the so called p-d exchange interaction. Though well understood, the main drawback of the GaMnAs system is its Curie-Temperature of about 190 K, which disqualify the material system for potential applications. Following a theoretical prediction by Dietl *et al.* [5] based on the p-d exchange coupling, which suggested ZnO and GaN as the most promising host semiconductors for the realization of room-temperature DMS, the quest for the room-temperature magnetic semiconductor gained momentum. In the first half of this decade, hundreds of articles have been published claiming the existence of room-temperature ferromagnetism in DMS systems, featuring combinations of wide-gap/narrow-gap host semiconductors with magnetic, and even non-magnetic dopants. Most of the studies just relied on integral magnetometry and did not deliver a consistent picture of the underlying coupling mechanism. Fortunately, the DMS community became critical, especially in the second half of this decade, and it turned out that many ferromagnetic signals measured by magnetometry were stemming either from substrate impurities or nano-sized magnetic clusters -not detectable by standard characterization methods-, thus not being an intrinsic property of a magnetic semiconductor. In this sense, the key improvement was the use of all possible characterization methods which indeed helped to judge the authenticity of intrinsic ferromagnetism in dilute magnetic semiconductors. In particular, the electrical transport properties have indeed important implications on the coupling mechanisms in DMS. For instance, a p-d exchange interaction in III-V semiconductors (e.g. in GaMnAs) gives rise to the polarization of the valence band and the existence of free holes, and has to be consistent with p-type conductivity. A carrier mediated ferromagnetism (e.g. RKKY) can be ruled out by the observation of an insulating behavior. In this respect, the magnetic coupling in a ferromagnetic insulator can be only explained by a *double-exchange* or *super-exchange* mechanism, which do not require the presence of free carriers. It is evident that the magnetic and electrical transport properties of dilute magnetic semiconductors are closely related to each other. The underlying physics behind is that the electronic states of

the dopants which carry the unpaired spins accounting for the magnetic properties (e.g. d-states of transition metals) will also dominate the electronic properties of the host semiconductor, since the magnetic doping level is usually in the percent range, much higher than the typical native defect concentration in the host semiconductor (10^{16}cm^{-3} - 10^{19}cm^{-3}). Consequently, the Fermi-level will be determined by the energetic location of the last filled states of the magnetic dopants, provided that the states lie within the bandgap of the host semiconductor, rendering it n-type, p-type, insulating or even metallic. In this respect, the incorporation site (e.g. substitutional, interstitial or antisite) and charge state of the magnetic dopants do influence the energetic position of the last filled states, so that complementary structural and optical characterization of the DMS is highly desirable.

In this work, the doping of Mn and Gd atoms on the wide-gap semiconductor GaN has been investigated in epitaxial layers grown by molecular-beam epitaxy (MBE). Both DMS systems have been already reported to exhibit room-temperature ferromagnetic properties and have therefore been suggested as potential candidates for their integration in spintronic devices. While for GaMnN the numerous experimental reports about the magnetic properties are widely scattered and in many cases even contradictory [6, 7, 8, 9, 10, 11, 12] the experimental findings of GaGdN seem to find an agreement about a ferromagnetic ordering at room-temperature [13, 14, 15, 16, 17, 18], but its origin is still unclear. For the latter case, colossal magnetic moments per magnetic impurity have been observed at very low Gd-concentrations [19], making the scenario even more controversial. The present work will concentrate on the investigation of the electrical transport properties of both GaMnN and GaGdN DMS systems, which might help to clarify which coupling mechanism is behind the observed ferromagnetic behavior. As an alternative to dilute magnetic semiconductors, the properties of MnGa metallic layers epitaxially grown on GaN will be shortly discussed, in view of the realization of spin-injection from a metallic electrode. Chapter 1 starts with the formation of native defects of un(intentionally)doped GaN, and how the scenario is expected to change by introducing Mn- and Gd as extrinsic dopants; and gives an insight into the theory of electronic transport in lightly doped semiconductors, which will serve as a guide to interpret the experimental results. The sample preparation, as well as the basic considerations to choose a suitable substrate for electrical transport measurements is shortly described in Chapter 2. In Chapter 3, the experimental results concerning the structural, magnetic and electrical transport properties of GaMnN and GaGdN diluted magnetic semiconductors and MnGa/GaN metal-semiconductor hybrid structures are presented and discussed, before closing with the last section devoted to summarize and comment on the prospects of the studied material systems.

1. Theoretical Background

Before studying the influence of extrinsic magnetic doping in the wide-gap semiconductor GaN, it is imperative to understand the properties of the undoped material. In this chapter, some general aspects concerning formation and incorporation of defects during the GaN growth process will be presented, taking into account comprehensive studies found in literature. Both native defects and extrinsic residual impurities will be treated, since they will determine the electronic structure of as-grown GaN, which is taken as the starting point to investigate the effect of the magnetic impurities on the electronic properties of GaN-based DMS. In addition, in order to interpret the experimental results, the most important electrical transport processes in lightly doped semiconductors will be presented and discussed, putting special emphasis on electronic transport within an impurity band of localized states. The type of electronic transport and the derivation of the respective characteristic quantities will give important information about the nature and properties of the impurities which have been used for doping.

1.1 Gallium Nitride: Defects and doping

The semiconductor Gallium Nitride (GaN), well known for its application in blue-light emitting diodes (LEDs), has a direct bandgap with an energy of 3.4 eV. It crystallizes either in the wurtzite or cubic structure, being the former the stable phase for bulk GaN, with the lattice parameters $a=3.189 \text{ \AA}$ and $c=5.186 \text{ \AA}$ [20]. GaN epitaxial layers are usually grown on Al_2O_3 , SiC or AlN substrates, with the $[0001]$ direction perpendicular to the growth surface. Fig. 1.1 depicts the structure of wurtzite GaN in top- and cross-sectional view.

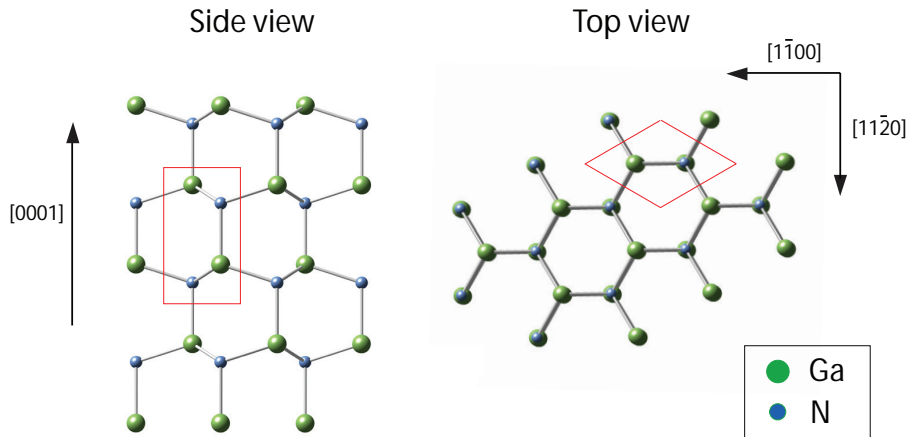


Figure 1.1: GaN wurtzite structure in cross-sectional and top view. The stacking of the Ga-N planes correspond to the Ga-polarity, which is the common stacking sequence in GaN epitaxial layers. The elementary cell is marked in red.

The most common techniques to grow high-quality GaN epitaxial layers are molecular beam epitaxy (MBE), metal-organic chemical vapor deposition (MOCVD) and hydride vapor phase epitaxy (HVPE). The recent development of alternative techniques at extreme pressure and temperature conditions [21, 22] opened up the possibility to produce bulk GaN crystals of a few hundred microns thickness. Depending on the growth conditions (in particular, pressure and temperature) given by each growth technique, the concentration of defects and impurities which will dominate the electronic properties of GaN, can differ by a few orders of magnitude. Although the vast majority of as-grown samples is found to be n-type, the source of n-type doping does not have to be the same. While ultra-high vacuum conditions are expected to suppress the concentration of extrinsic impurities such that the role of native defects comes into play, a high concentration of extrinsic impurities like oxygen and hydrogen is unavoidable under high-pressure growth conditions. In this sense, based on theoretical calculations, the formation energies of native and extrinsic impurities will be presented in the next subsections.

1.1.1 Native defects

Native point defects in GaN can be easily classified by taking into account all Ga- and N configurations other than substitutional, which are the vacancy, the interstitial and the antisite, yielding three defect types for each atom. The n-type conductivity of GaN has been first associated to the presence of nitrogen vacancies (V_N), according to empirical [23, 24, 25] and theoretical [26, 27] findings. However, the fast development of density functional theory enabled not only the calculation of the electronic structure of the native defects, but also the defect formation energy, which is an important parameter for the determination of the dominant defect at given conditions. Neugebauer and Van de Walle [28] performed a comprehensive theoretical study of all native defects in the relevant charge states, describing their electronic structure, defect geometry and formation energies. The study was extended taking into account both Ga- and N-rich growth regimes [29], in order to cover most of the experimental growth window. It should be mentioned that the formation energies were calculated under the condition of thermodynamic equilibrium, where the defect concentration can be inferred from the expression

$$c = N_{sites} N_{cf} \exp(E^f / k_B T) \quad (1.1)$$

where E^f denotes the formation energy, N_{sites} the number of lattice sites per unit volume where the defect can be incorporated, k_B the Boltzmann constant, T the temperature and N_{cf} the number of equivalent configurations in which a the defect can be incorporated. For vacancies, antisites and substitutional defects N_{cf} is equal to 1, provided that there is no symmetry breaking [29]; otherwise, N_{cf} has to be taken as the number of inequivalent configurations in which the defect can be incorporated in the same site. The condition of thermodynamic equilibrium, which holds the validity of (1.1), is not strictly satisfied in the experiment. The synthesis of GaN is done at temperatures of 1000 °C - 1100 °C (MOCVD) and around 800 °C (MBE), so that the mobility of the native defects should be sufficiently high to attain an equilibrium state [30], at least for the MOCVD-grown GaN samples. The lower temperature in the MBE growth leads to the formation of kinetic barriers which may impede that the defects reach their equilibrium concentration, precluding a quantitative determination of their concentration. Still, the magnitude of the formation energy will dictate which defects will be preferably formed during growth.

Fig. 1.2 shows the calculated formation energies E^f for the various native defects in GaN as a function of the Fermi-energy, taken from [29]. A positive slope of E^f is characteristic for defects which act as donors, while the negative slope resembles an acceptor behavior. An increment of the slope of E^f corresponds to a change of the charge state of the defect, whereas the neutral state is described by a horizontal line. The Fermi-energy is considered from the valence band edge (zero-energy) to the conduction band edge (3.4 eV) of GaN.

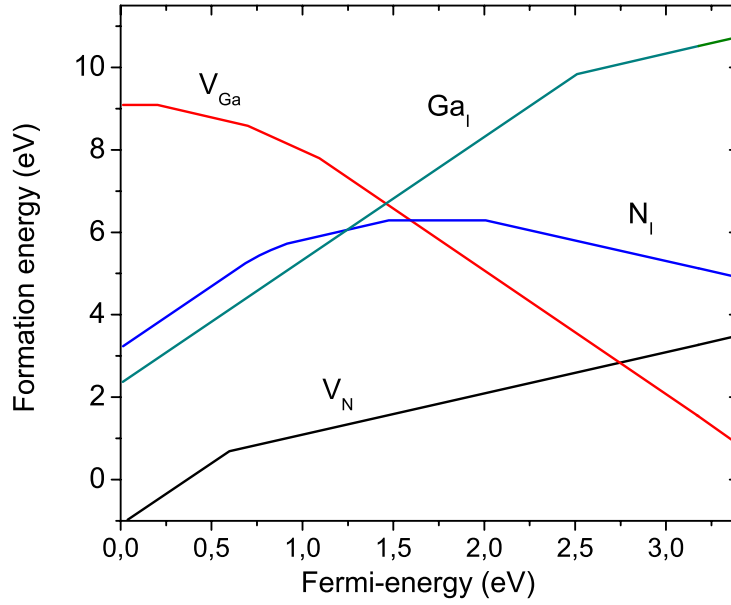


Figure 1.2: Formation energies of the most relevant native point defects in GaN under Ga-rich conditions and at thermodynamic equilibrium, according to [29]. The antisites have a higher formation energy (not shown).

From Fig. 1.2 it is evident that the lowest formation energies correspond to the vacancies (V_{Ga} , V_N). The formation of the nitrogen vacancy V_N is promoted at p-type conditions (when the Fermi-energy is close to the valence band) up to a Fermi energy of around 2.75 eV, where the formation energy of the gallium vacancy V_{Ga} becomes lower. When the Fermi-energy is close to the conduction band, the difference in formation ΔE^f between V_{Ga} and V_N reaches nearly 3 eV, so that a high concentration of V_N at n-type conditions seems very unlikely. These findings put into debate the source of the n-type conductivity in as-grown GaN. However, there are a few considerations which should be taken into account when interpreting the calculated formation energies within the experimental scenario:

- The first factor, as already mentioned, is the deviation from „thermodynamic equilibrium“ during the growth process. The calculations assume that the atoms are highly mobile, thus not taking into account the presence of kinetic barriers. It may occur that certain point defects with high formation energies, once formed, cannot be released when the system tries to recover equilibrium conditions, precluding a quantitative determination of the real defect concentration.
- Second, the defect formation energy of Ga- and N-related point defects strongly depends on the atom fluxes which are supplied during growth, i.e., the Ga/N flux ratio. In this respect, Fig. 1.2 shows the scenario for Ga-rich conditions, which resembles the experimental conditions for high-quality GaN epitaxy.

- Third, given the dependence of E^f on the Fermi-energy, it is important to know the location of the Fermi energy at time $t=0$, that is, when the first Ga and N atoms arrive at the surface of the substrate. This is the starting point for all the physical thoughts to describe the defect formation during the growth process: (i) which defects will be preferably formed in the early stage of growth, (ii) how they affect the Fermi-energy of the system, (iii) and how the renormalization of the Fermi-energy leads to a new scenario in the formation energy landscape. An iteration of the steps (i)-(iii) is necessary until the system attains equilibrium, delivering the final (bulk) defect concentrations and the corresponding Fermi-energy.

While the first and second points do not represent a problem to marry theory and experiment, the last issue is indeed difficult to clarify. One possibility is that the Fermi-energy at $t=0$ is determined by the electronic structure of the substrate surface. In this case, not only the substrate choice for GaN epitaxy will have an influence on the Fermi-energy, but also the fact if there are existing surface states which might contribute to Fermi-level pinning.

For the sake of concreteness, the defect formation process will be discussed considering following experimental scenario: GaN is homoepitaxially grown on MOCVD-GaN template by molecular beam epitaxy (MBE) under Ga-rich conditions, and at a substrate temperature of $T_s=800^\circ\text{C}$. Although the defect concentrations cannot be accurately inferred due to possible kinetic barriers at such growth temperature, the formation energies of the native defects -summarized in Fig. 1.2- should apply to the scenario. In order to determine which defects will be formed at the early stage of growth, the position of the Fermi-energy in the substrate surface should be taken into account. In-situ x-ray-photoemission spectroscopy measurements on the MOCVD-GaN surface [31] showed the presence of surface states, which give rise to a Fermi-level pinning at 2.89 eV above the valence band. Taking this value as the initial ($t=0$) Fermi-energy, it can be inferred from Fig. 1.2 that the gallium vacancy V_{Ga} in the 3^- charge state is the native defect with lowest formation energy. The subsequent incorporation of V_{Ga} , which acts as an acceptor, will shift the Fermi-energy towards the valence band, where the formation of the nitrogen vacancy V_N becomes energetically favorable. In turn, nitrogen vacancies V_N (single donors) are incorporated in the growth process, having a compensating effect on the gallium vacancies. This process will occur until charge neutrality is reached, condition which defines the equilibrium defect concentrations of V_{Ga} and V_N and the position of the Fermi-level throughout the bulk (provided that the growth temperature remains constant until the end of the growth process). The final Fermi-energy is expected to lie near the point where the formation energies of V_{Ga} and V_N become comparable. For the above interpretation, it is assumed that the Fermi-level pinning at the surface of the growing GaN-layer is similar in magnitude as at the GaN substrate surface, and does not change during the growth process. However, it is well known that high-quality epitaxy of GaN

by MBE, yielding a good surface morphology and crystal quality, is achieved under Ga-rich conditions with the stabilization of a Ga-bilayer on the surface, where the N-atoms are able to interdiffuse giving rise to the bulk growth of the material underneath. The scenario of Ga excess on the surface has been confirmed as the most favorable for GaN growth from calculations of surface energy barriers [32], sketched in Fig. 1.3. Under these conditions, the Fermi-level at the surface of the growing GaN layer is modified. Kocan *et al.* [31] measured the Fermi-energy of GaN with a Ga-rich surface by in-situ x-ray photoemission spectroscopy (XPS) and found that E_F was lowered compared to the substrate surface, yielding a value of 1.65 eV above the valence band. Coming back to the formation energy dependence, the shift of the Fermi-energy towards the midgap region at the growing surface makes the formation of V_N much more favorable, since the formation energies of all other native defects are very high. The sequence to determine the bulk electronic properties is the same: a high concentration of V_N shifts the Fermi-energy towards the conduction band, leading to the formation of V_{Ga} which have a compensating effect, until charge neutrality defines again the equilibrium defect concentration and the Fermi-level in the bulk. The existence of a lower Fermi-energy at the growth surface implies a higher energy window where V_N is preferably formed, leading to a higher V_N concentration which influences the resulting bulk electronic properties.

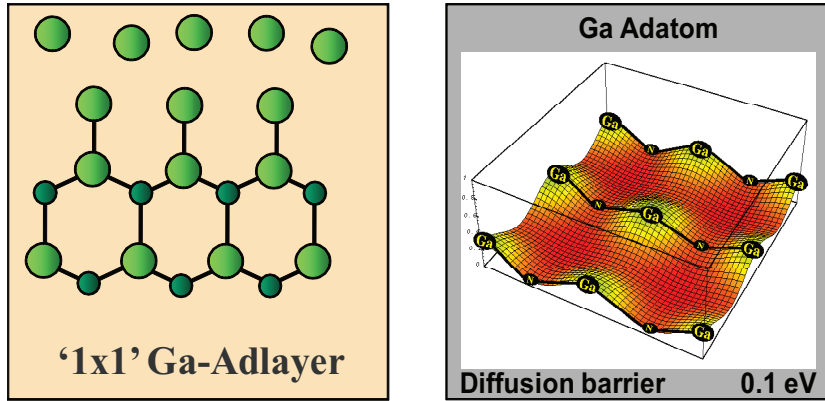


Figure 1.3: Formation of a Ga-bilayer as the energetically most favorable scenario for GaN-growth, taken from [33]. The diffusion barrier for Ga-atoms is nearly five times lower compared to the N-atoms (not shown), according to [32]. The Ga-atoms at the surface are very mobile and thus able to incorporate N-atoms to form GaN underneath, leading to a controlled two-dimensional growth. The Fermi-energy at the surface is therefore determined by the Ga atoms. Note that this scenario is only feasible at Ga-rich growth conditions.

Considering these arguments, it is not a straightforward issue to interpret from theory if the nitrogen vacancies V_N are the defects which determine the n-type conductivity. Assuming equilibrium concentrations of $c(V_N^+) = 3 \times 10^{17} \text{ cm}^{-3}$ and $c(V_{Ga}^{3-}) = 1 \times 10^{17} \text{ cm}^{-3}$ (the simplest case for charge neutrality) and ionization energies of $E_d = 0.1 \text{ eV}$ and

$E_a=1.2$ eV, we obtain $E_c-E_F=0.3$ eV at growth temperature ($T=1100$ K) and $E_c-E_F=0.11$ eV at room-temperature, where E_c is the energy of the conduction band edge. This would imply that the totality of V_N donors are ionized at room-temperature, fact which is not in agreement with electrical transport studies of as-grown GaN by different growth methods [34]. It should be noted that the equilibrium defect concentrations might vary depending on the growth surface potential and existing kinetic barriers, nevertheless, the formation energy of the nitrogen vacancy V_N appears too high to account for the observed n-type conductivity with free carrier concentrations of the order of 10^{17} - 10^{19} cm³ which are experimentally observed.

So far, we have considered the formation of native defects under ideal growth conditions, where only the two atom species (Ga and N) are present in appreciable concentrations. Even under ultra-high vacuum conditions, the presence of residual impurities, coming either from the effusion cells or already present in the chamber atmosphere, is unavoidable. Based on the same arguments, the formation energies of the most typical residual impurities in GaN will be introduced in the next section.

1.1.2 Residual impurities

The pioneering work of Neugebauer *et al.* [28] in terms of defect formation energies based on density-functional-theory (DFT) put into debate the long accepted notion of the nitrogen vacancy V_N as the responsible defect for the observed unintentional n-type conductivity in as-grown GaN. The determination and control of the dominant defects in GaN is an important requirement for material engineering and design of GaN-based heterostructures, which stimulated further theoretical and experimental research.

Fig. 1.4 summarizes the formation energies for several species which might be present during the growth process. Four impurities have been considered: Oxygen (O), hydrogen (H), silicon (Si) and carbon (C) in the energetically most favorable occupation configuration, respectively. Starting with the donor impurities, the silicon incorporation on Ga-sites (Si_{Ga}) has the lowest formation energy, followed by the oxygen substitution of nitrogen (O_N). All these simply charged donors (+) have lower formation energies than the native vacancy V_N almost over the whole bandgap range, so that at first sight, any of these impurities could be the source for the experimentally observed n-type conductivity. Regarding the acceptors, C_N has a very low formation energy at n-type conditions, which might strongly compensate any of the impurity donors, shifting the Fermi energy towards the middle of the bandgap. Thus, the experimental observation of n-type conductivity in as-grown GaN rules out the presence of carbon in appreciable concentrations. The hydrogen interstitial (H_i) is a special case, since it behaves as an amphoteric impurity, acting as a donor at p-type and as an acceptor at n-type conditions.

The scenario of n-type conductivity is easy to interpret assuming Si_{Ga} as the dominant

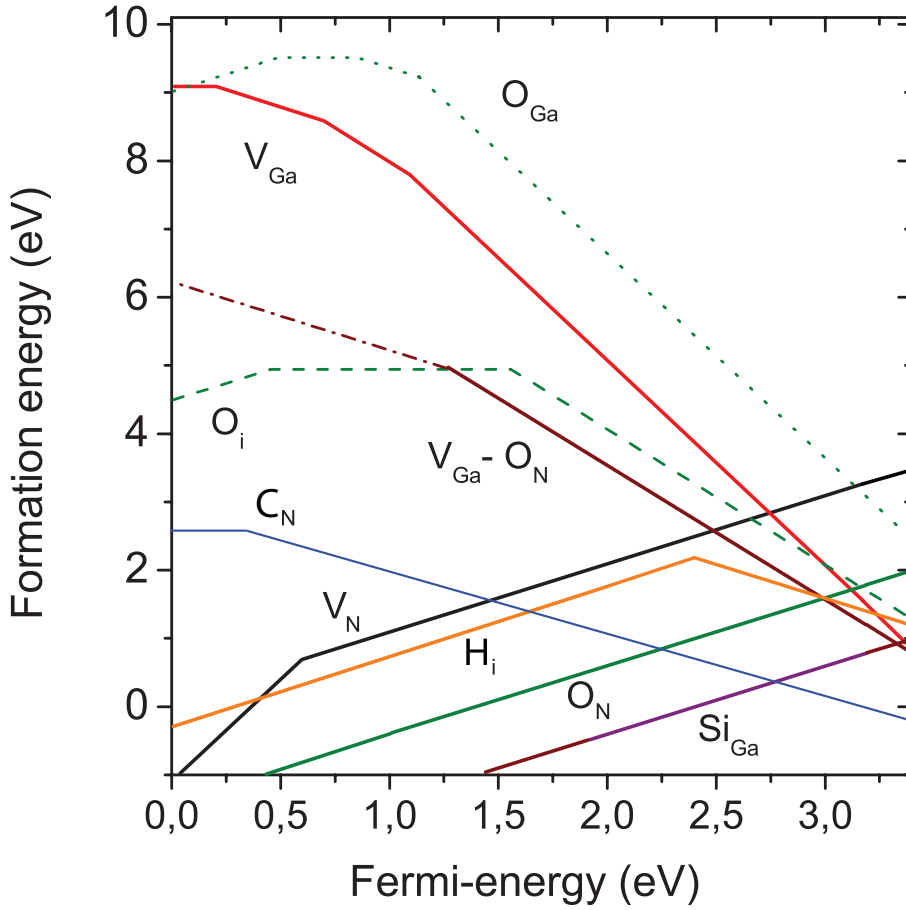


Figure 1.4: Formation energies of the residual impurities which are likely to be present in a typical GaN growth process. For comparison, the two dominating native defects (V_N , V_{Ga}) are also shown. The data is taken from the same authors which calculate the native defect formation energies [28, 35, 29, 36] for consistency reasons. Only the formation energies of oxygen interstitials and antisites (dashed lines) are taken from [37]. In all the cases, the calculations are performed assuming Ga-rich conditions.

residual impurity. The low formation energy of Si_{Ga} throughout the bandgap will render the material n-type, although it might be partly compensated either by hydrogen interstitials or by the formation of V_{Ga} or $V_{Ga}-O_N$ complexes (provided that oxygen is also present) when the Fermi-energy lies close to the conduction band. The competition between Si_{Ga} and $V_{Ga}-O_N$ was studied by Neugebauer *et al.* [35], who calculated the equilibrium defect concentrations as a function of temperature according to (1.1), finding that between 1100 K and 1400 K (typical MBE/MOCVD growth temperatures) the concentration of $V_{Ga}-O_N$ was at least one order of magnitude smaller than Si_{Ga} . For instance, this was the thermodynamically derived consistency proof of the old empirical recipe of taking silicon to achieve n-type doping in GaN. However, if silicon is present in negligible concentrations, oxygen takes over as the dominant donor. The formation energy of O_N is somewhat higher than Si_{Ga} , enabling stronger

compensation effects due to the Ga-vacancies and interstitial hydrogen.

So far, general trends have been discussed. It should be noted that the availability of residual impurities which can be incorporated during the growth process depends strongly on the growth technique. For example, because of the carrier gas, HVPE, MOCVD or ammonia-assisted MBE expose the growing material to large concentrations of hydrogen. The oxygen content, on the other hand, is very high ($\approx 10^{19}$ - 10^{21}cm^{-3}) for μm -thick GaN bulk layers prepared by high-pressure techniques [38, 39], appreciable by MOCVD and HVPE ($\approx 10^{18}$ - 10^{19}cm^{-3}) due to the atmospheric pressure used during growth, and is expected to be low in MBE processes owing to the ultra-high vacuum environment. The lowest free carrier concentrations are indeed found at MBE-grown GaN samples, in concordance with their low oxygen content. This is an indication that the oxygen incorporation at nitrogen sites (O_N) might be the main source for the unintentional n-type conductivity in MBE-grown samples. However, recalling the formation energies depicted in Fig. 1.4 at n-type conditions, the possibility of an interstitial occupation of the oxygen impurities (O_i) should not be neglected. The low formation energy of oxygen interstitials at n-type conditions should be kept in mind, since this defect might play an important role by forming complexes when additional magnetic impurities (e.g. Gd) are used for doping.

Concerning the acceptors which are expected to be incorporated under n-type conditions, the hydrogen interstitial is the most difficult to detect. On the other hand, the role of the gallium vacancy V_{Ga} has been intensively investigated via positron annihilation spectroscopy (PAS) by *Saarinen* and co-workers [40]. The concentration of V_{Ga} has been found to increase with increasing donor concentration (V_N , O_N or Si_{Ga}), supporting the formation energy trends depicted in Fig. 1.4. Furthermore, the accuracy of the PAS-method has been tested by correlating the III/V molar ratio supplied during growth to the resulting V_{Ga} concentration, which varied from 10^{16}cm^{-3} to 10^{19}cm^{-3} by progressively changing the growth conditions from Ga-rich to N-rich [41]. Another important finding from positron annihilation experiments was the evidence of the impurity decoration of a single V_{Ga} during growth, inferring concentration trends of V_{Ga} - O_N complexes as a function of oxygen doping in HVPE-samples, and indications of V_{Ga} -H complexes in samples grown by MOCVD [42]. Again, the preferable formation of V_{Ga} - O_N acceptor complexes is in well agreement with formation energy arguments.

In summary, the agreement between the theoretical and experimental studies deliver a round picture concerning defect formation trends during GaN growth. In the absence of residual impurities, the interplay between the native V_{Ga} and V_N defects will determine the electronic structure of GaN, whereas the location of the Fermi-energy during the growth process is of great importance. Considering residual impurities, both oxygen and silicon donors represent the most likely source for n-type conductivity, while high concentrations of carbon (incorporated as C_N) might seriously compensate the material (eventually rendering it semi-insulating). The formation energies of V_{Ga} - O_N , V_{Ga} , H_i and O_i are only relevant at Fermi-energies near the conduction band, so

that these defects might just induce a partial compensation. Since the growth conditions dictate the availability of residual impurities, each growth method represents a new case-study, which can be well predicted by the thermodynamical compendium summarized in Figs. 1.2 and 1.4.

1.1.3 Magnetic doping

As mentioned in the introduction, the feasibility of GaN-based dilute magnetic semiconductors with intrinsic room-temperature ferromagnetic properties is a controversial topic. The interplay between electronic transport and magnetic properties has been found to be crucial to identify the coupling mechanisms in DMS systems [43, 44, 45]. Therefore, it is imperative to study not only the *magnetic*, but also the *electronic* effect of the magnetic dopants in the host semiconductor. In the previous section, the relevant native defects and residual impurities which can be formed during growth have been presented. However, the additional doping with magnetic impurities changes the scenario, especially if the magnetic dopant concentration is of the same order of magnitude as the unintentional doping. In particular, the affinity between the magnetic impurities and native defects or residual impurities has to be taken into account, since the formation of certain complexes might be energetically favorable during growth.¹ In some cases, the growth conditions are even changed in order to enable the preferential incorporation of the magnetic dopants, which leads to a different scenario in terms of native defect formation and residual impurity incorporation. However, if the magnetic dopant concentration is sufficiently high, the electronic properties will be entirely determined by the electronic states of the magnetic impurities.

Assuming that Mn and Gd are incorporated on Ga-sites, the resulting charge state of the magnetic impurities will be 3^+ , yielding following electronic configurations: $\text{Mn}^{3+}:[\text{Ar}]3d^4$ and $\text{Gd}^{3+}:[\text{Xe}]4f^75d^0$. Thus, the last filled states of the magnetic impurities are $3d^4$ and $4f^7$, which contribute with $4\mu_B$ and $7\mu_B$ per impurity to the total magnetic moment. The electronic effect of the magnetic impurities is determined by the energetic location of the last filled states relative to the bandgap of the host GaN. Fig. 1.5 shows schematically the 3d- and 4f-spin-split states of Mn and Gd, respectively. The remarkable difference between Mn and Gd is that while Mn induces energy states within the bandgap of GaN (spin-up channel), the 4f-states (spin up/down) of Gd are expected to be resonant with the valence and the conduction band, respectively (the exchange splitting of 4f-states of Gd in compounds is found to be around 12 eV according to photoemission studies [46]). For Mn-doping in GaN, the exchange splitting shifts the unoccupied 3d-spin-down(\downarrow) states over the conduction band, while the 3d-(\uparrow)states are expected to be energetically deep within

¹in view of the complex scenario, it is more instructive to discuss these cases specifically in connection with the experimental results, presented in Chapter 3.

the GaN bandgap. The partially occupied 3d-states have, in addition, a considerable energy splitting due to the action of the crystal field, as depicted in Fig. 1.5. As a consequence, while both dopants might give rise to magnetic interactions due to their unpaired spins, it is clear that the *electronic* effect induced by these magnetic impurities turns out to be very different. Although the quantitative analysis is complicated and will proceed later on in connection with the experimental results, some trends can be still anticipated: the substitutional Mn-incorporation in GaN should compensate the residual impurities (assuming $c_{Mn} \geq c_{imp}$), leading to electronic localization, whereas the substitutional incorporation of Gd should, at first sight, not strongly affect the electronic properties of unintentionally doped GaN, since the 4f-states are expected to lie outside the GaN bandgap.

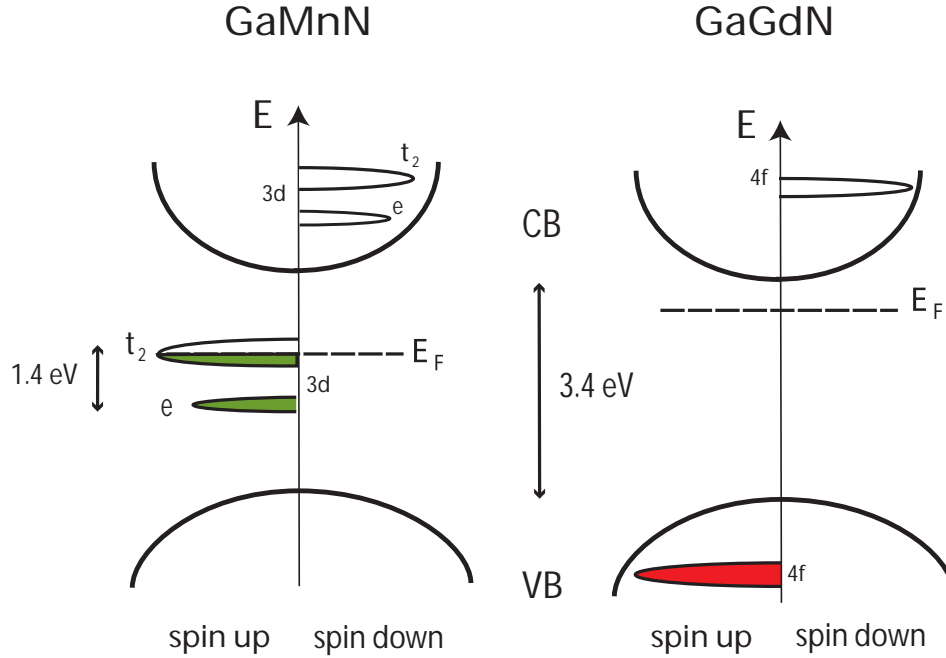


Figure 1.5: Schematic illustration of the density of states of Mn-3d (left) and Gd-4f (right) relative to the band edges of GaN. The Fermi-energy E_F is shifted towards midgap due to the Mn-doping, while it should remain near the conduction band for Gd-doping. A substitutional incorporation (charge state 3^+) is assumed for either case.

So far, the effect of defect formation and impurity doping on the electronic structure of the host semiconductor has been discussed. Apart from the concentration, the nature and electronic properties of the impurities will have important implications on the carrier transport in the doped semiconductor. In the next section, a general survey about the relevant carrier transport mechanisms in lightly doped semiconductors will be given, since it will provide a lot of important connections which should help to interpret the experimental results obtained in this work. In particular, it serves as a basis to understand the interplay between carrier localization and magnetic interactions in dilute magnetic semiconductors.

1.2 Electronic transport in lightly doped semiconductors

A semiconductor is considered lightly doped, if its impurity concentration N satisfies the inequality $Na^3 \ll 1$, where a is the Bohr radius of the impurity state. Localization of electrons at the Fermi-level provides a physical criterion for distinguishing between the ranges of light and heavy doping: in lightly doped semiconductors, electronic states at the Fermi-level are localized and the low-temperature conduction is *activated*, whereas in heavily doped semiconductors, states are delocalized and conduction is of metallic nature. The transition between metallic and activated conduction is known as the Mott-transition, and occurs typically when the criterion $n_c^{1/3}a \approx 0.25$ is fulfilled, being n_c the critical carrier concentration, or equivalently, the net concentration of the majority impurities. In the following, only the conduction mechanisms of semiconductors in the lightly doped regime (i.e. with localized electronic states) will be considered, since it resembles the case of our experimental conditions.

In a simple picture of a semiconductor with only one type of impurity doping, the temperature is the parameter which is determinant in distinguishing conduction regimes. Fig. 1.6 represents schematically on a semi-logarithmic plot the inverse temperature dependence of the resistivity, where a linear dependence is characteristic of *activated* transport. Four different regimes can be distinguished; the temperature range A corresponds to *intrinsic* conduction, while ranges B-D correspond to *extrinsic* conduction, that is, when the conduction is entirely determined by the nature and concentration of impurities. The intrinsic electrical conductivity arises due to thermal activation of carriers across the energetic gap separating the valence and conduction bands, therefore it is observed at very high temperatures and its intrinsic carrier concentration decreases rapidly with decreasing temperature due to the large activation energy. In the regime B, all the impurities are still ionized (have given their electrons to the conduction band) and hence the carrier concentration is independent of temperature. Thus, the temperature dependence of the resistivity is entirely determined by that of the mobility, eventually leading to a decrease of the resistivity with decreasing temperature, e.g. through weaker phonon scattering. In the temperature range C, as the temperature is further decreased, the impurity electrons which are in the conduction band are gradually recaptured by the impurity centers, phenomenon which is often called „freeze-out“. Last but not least, the regime D corresponds to electrical conduction by *hopping*, which occurs at very low temperatures where the electrons are just able to surpass very low energy barriers. Unlike single-activated transport (regime C), the existence of a sizable energetic dispersion of the impurity levels is one of the fundamental concepts of hopping transport, since the electrons will reach the states which are next in energy within the impurity band. For the sake of completeness, the widely studied semiconductor germanium (Ge) with a donor concentration of $N_D \approx 10^{15}$ is exemplified in order to get a feeling for the temperature ranges where each conduction mechanism prevails, as depicted in Fig. 1.6.

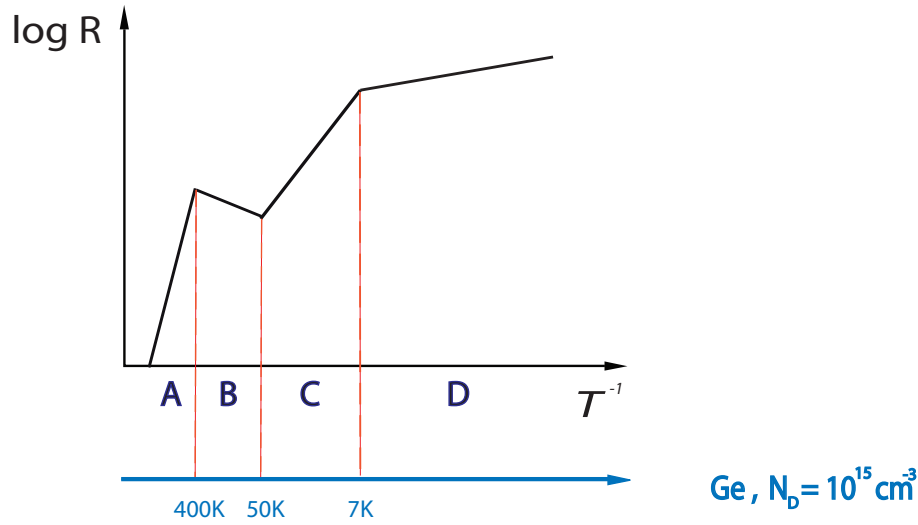


Figure 1.6: Schematic representation of the conduction regimes in lightly doped semiconductors. The semiconductor Ge, with a donor concentration of $N_D=10^{15}\text{cm}^{-3}$ is taken as an example to link the universal behavior of the resistivity with real values of crossover temperatures.

In the following sections, a quantitative explanation of the conduction mechanisms and the derivation of parameters related to the electronic transport will be provided. In particular, the temperature dependence of the carrier concentration and mobility in the freeze-out regime for shallow impurities will be derived, as well as the different conduction mechanisms and their temperature dependences in the hopping regime. These concepts will be of key importance for the understanding of the experimental results obtained in this work.

1.2.1 Single-activated electronic transport

The *extrinsic* electrical conductivity of a semiconductor can be easily derived if one neglects the energy dispersion of the impurity levels (the impurity band width) and assumes that all impurity centers have equal ionization energy E_0 , or equivalently, that the electrons bound to the impurities possess a single activation energy ΔE . This scenario is mostly applicable to shallow impurities. Knowing the band structure of the semiconductor, as well as the localized states caused by the presence of shallow impurities, the calculation of the electrical conductivity of the semiconductor requires to find the number of mobile charges, at thermal equilibrium. For this purpose, the calculation of the occupation probabilities of the accessible energy levels are needed. The electrons have spin-1/2 and are fermions, therefore the system only contains one electron per single-particle quantum state. For a given wave vector, there are two quantum states with different spins which can be occupied simultaneously (up- and down spin). Thus, the most appropriate statistical distribution to describe the

occupation probability of electrons for a given energy state E will be

$$f_e = \frac{1}{1 + \exp(\frac{E-E_F}{k_B T})} \quad (1.2)$$

known as the Fermi-Dirac distribution, where E_F denotes the Fermi-energy and k_B the Boltzmann constant. Analogously, the probability of occupation by a hole is

$$f_h = 1 - f_e = \frac{1}{1 + \exp(\frac{E_F-E}{k_B T})}. \quad (1.3)$$

The carrier density of states n gives the population of carriers at a particular energy. For example, n_{CB} will be the density of states of electrons in the conduction band, which are able to contribute to electrical transport. According to the band structure model, if the constant energy surfaces are spheres, and if there is only one energy minimum at the vicinity of the band-gap, the value of $n_{CB}(E)$ for the two spin orientations and unit volume is given by

$$n_{CB}(E) = 4\pi(2m_e^*)^{3/2}(1/h^3)(E - E_c)^{1/2} \quad (1.4)$$

being E_c the energy at the conduction band minimum, m_e^* the effective electron mass and h the Planck-constant. Combining population number and occupation probability of carriers, it is possible to calculate the electron number at a given energy E . The number of electrons n in the conduction band is therefore

$$n = \int_{CB} n_{CB}(E) f(E) dE \quad (1.5)$$

As a solution of the integral, the expression obtained depends mainly on the temperature of the system [47]

$$n(T) = n_0 T^{3/2} \exp \left[\frac{-(E_c - E_F)}{k_B T} \right] \quad (1.6)$$

where E_c is the energy of the conduction band minimum and E_F the Fermi-energy. It is worth to mention, however, that the constant n_0 in equation (1.6) contains the electron effective mass m_e^* , which considers the influence of the crystal potential on the electron, thus having different values for each semiconductor.

The calculation of the hole carrier concentration in the *p-doped* case is analogous, taking into consideration the energy at the valence band minimum E_v , the acceptor level E_a , and the hole effective mass m_h^* instead.

Another consequence of temperature, when considering *n-* or *p-*doped semiconductors, is that the ionization of impurities will come to a saturation. Assuming the simple case of uncompensated *n-type* semiconductors, which means there are no acceptors which could be potentially ionized ($n_a^- = 0$), electrical neutrality will lead to

$$n + n_a^- = p + n_d^+ \xrightarrow{n_a^- = 0} n = p + n_d^+ \quad (1.7)$$

where n_d^+ and n_a^- represent the number of ionized donors/acceptors. After separating ionized donors n_d^+ into total donors N_d minus neutral donors n_d^0 , and using the electron occupation probability (1.2) for each case, following relation will remain:

$$(n - p)n = \frac{N_c}{2}(N_d - n + p) \exp\left(\frac{-E_d - E_c}{k_B T}\right) \quad (1.8)$$

where N_c is equal to the expression

$$n_0 \cdot T^{3/2} = 2\left(\frac{2\pi m_e^* k_B T}{h^2}\right)^{3/2} \quad (1.9)$$

in equation (1.6), sometimes called the effective or equivalent density of states of the conduction band.

For a good interpretation of equation (1.8) in n-type semiconductors, it is suitable to consider three different temperature ranges:

- (a) At very low temperatures the ionization of the donors is weak and the hole concentration is negligible (the Fermi energy is very high in the bandgap), which yields the relation $N_d \gg n \gg p$. Neglecting n and p compared to the total donor concentration N_d (equation (1.8)) becomes

$$n(T) = \left(\frac{N_c N_d}{2}\right)^{1/2} \cdot \exp\left(\frac{E_d - E_c}{2k_B T}\right) \quad (1.10)$$

The electron number increases, with an activation energy equal to half the binding energy of the donor. The Fermi level still lies between the donor level and the conduction band.

- (b) At intermediate temperatures, the exponential of Eq.(1.8) is of order 1 and the hole number is still negligible. The relation (1.8) can be written as

$$(N_d - n) = \frac{2n^2}{N_c \cdot \exp\left(\frac{E_d - E_c}{k_B T}\right)} \quad (1.11)$$

The density of states of the conduction band $N_c(T) \propto T^{3/2}$ will be much larger than N_d , due to its temperature dependence, so the solution $n \rightarrow N_d$ will be a good approximation. The free carrier concentration equals the total donor concentration, which means that all the donors have been ionized; the saturation regime has been reached. However, the thermal energy is still too low for activating electrons from the valence band. During the process of saturation, the Fermi-energy will decrease and shift deeper within the band, lying lower than the donor energy level.

- (c) At high temperatures, the intrinsic regime will be recovered, since all the donors have already been ionized, and the thermal energy of the electrons allows to excite carriers through the bandgap. The electron concentration n will vary

then as $\exp(-E_g/2k_B T)$, the equation will be analogous as in case (a) but with $\Delta E = E_g$.

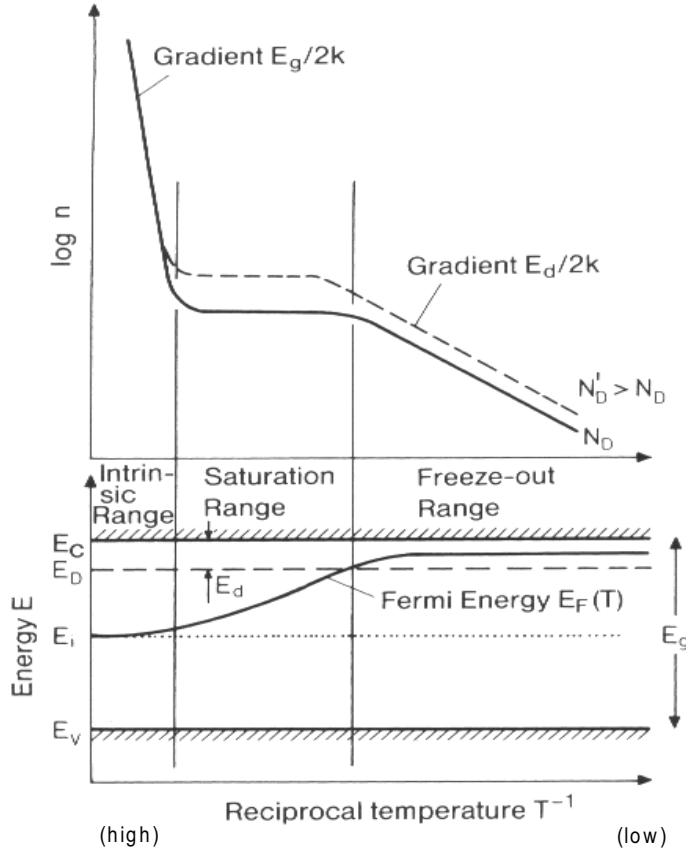


Figure 1.7: Variation of the logarithm of the carrier concentration and the Fermi-energy as a function of the inverse temperature for an n-type semiconductor, taken from [47].

The effect of temperature on the carrier concentration n_E has a substantial influence on the electrical conductivity of a semiconductor, which is defined as

$$\sigma = \sigma_e + \sigma_h = n\mu_e e + p\mu_h e \quad (1.12)$$

In this expression, n and p are the electron and hole concentrations, respectively; and $\mu_{e(h)}$ is called the electron (hole) mobility. It is important to determine the majority carriers of the studied system, since the term in the sum which includes the majority carriers will prevail. So we will have three different cases:

- (a) for n-doping:

$$\sigma = n\mu_e e + p\mu_h e \xrightarrow{n \gg p} n\mu_e e \quad (1.13)$$

- (b) for p-doping:

$$\sigma = n\mu_e e + p\mu_h e \xrightarrow{p \gg n} p\mu_e e \quad (1.14)$$

- (c) and in the intrinsic case, the relation (1.12) will remain unchanged, due to the equal concentrations of electrons and holes ($n=p$).

For all the cases, the *mobility* is another parameter which influences the electrical conductivity. A good carrier mobility, in common words, could be explained as the capability of carriers to travel from one point to another efficiently, with less collisions or disturbances. To have a deeper look on the role of the mobility, the different scattering mechanisms of carriers should be considered.

- Scattering by lattice vibrations (subindex:L), also called *phonons*. The amplitude of the vibrations increases with temperature and it is expected that the collision probability also increases with T. As a result, the time τ between two collisions and hence the mobility will decrease as

$$\mu_L \propto \tau \propto T^{-3/2} \quad (1.15)$$

- Collisions with ionized impurities (subindex:I) and the effect of the Coulomb-field. The temperature dependence of the mobility adopts the form [48]

$$\mu_I \propto T^{\frac{3}{2}} \quad (1.16)$$

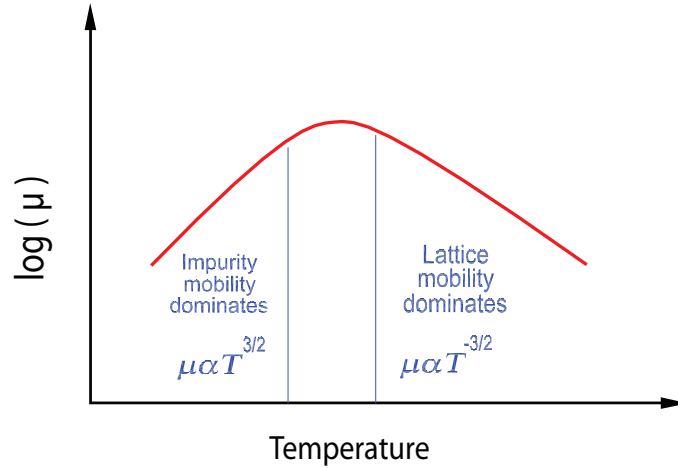


Figure 1.8: Variation of the carrier mobility with temperature.

If the temperature is increased, the motion of the atoms in the crystal becomes faster and the distance which they move from their central positions becomes greater. In

addition to this, the thermal velocity of the electron will increase. These two changes will have opposite effects on τ_I and τ_L . (Note that the time τ between collisions is proportional to the mobility.) The frequency of lattice collisions will clearly increase since the atoms are oscillating more rapidly and sweeping out a greater volume. Due to this fact, τ_L decreases with temperature. On the other hand, the value of τ_I increases with temperature since the greater the thermal energy of the carrier the less it is affected by the coulombic force of the impurity atom. At low temperatures, μ_{total} is dominated by the impurity component and increases with increasing temperature, until, as temperature rises, lattice collisions become dominant and the mobility begins to fall again.

As we have summarized the temperature dependences of the mobility and carrier concentration in the freeze-out regime, it is clear that the mobility does not have a strong variation with temperature. Hence the variation of the conductivity σ will be influenced dominantly by the $n(T)$ behavior, which follows an exponential relation with $\exp(\frac{-\Delta E}{2k_B T})$. This explains the very strong increase in conductivity with temperature and provides a method of measuring the energy gaps in lightly doped semiconductors. In contrast to metals, where the number of carriers is constant, the conductivity of semiconductors increases with temperature mainly through the increased number of carriers.

1.2.2 Coexistence of single-activated and hopping transport

The gradual freezing-out of conduction electrons with decreasing temperature eventually leads to a situation in which the main contribution to the electrical conductivity comes from electrons hopping directly between impurities without any excursion to the conduction band. Electrons jump from occupied impurity states to empty ones, and therefore the presence of empty states is a necessary condition. The hopping mechanism of conduction corresponds to a very low mobility, since the electron jumps are associated with a weak overlap of wave-function tails from neighboring impurities. Nevertheless, it wins in the competition with band conduction at low temperatures, because the number of free carriers which can participate in the latter process is exponentially small. The total resistivity can be expressed as

$$\rho_T = \rho_1 \exp\left(\frac{\epsilon_1}{k_B T}\right) + \rho_3 \exp\left(\frac{\epsilon_3}{k_B T}\right) \quad (1.17)$$

where the indexes 1 and 3 correspond to band- and hopping conduction, respectively. The activation energy ϵ_3 of hopping conduction is small compared to ϵ_1 , because the dispersion of the energy levels in the (donor) impurity band is usually smaller than the energy gap between the impurity states and the conduction band. As we are dealing with lightly doped semiconductors, the impurity band width will stay relatively narrow, thus holding the relation $\epsilon_1 \gg \epsilon_3$. The scenario is sketched in Fig.1.9.

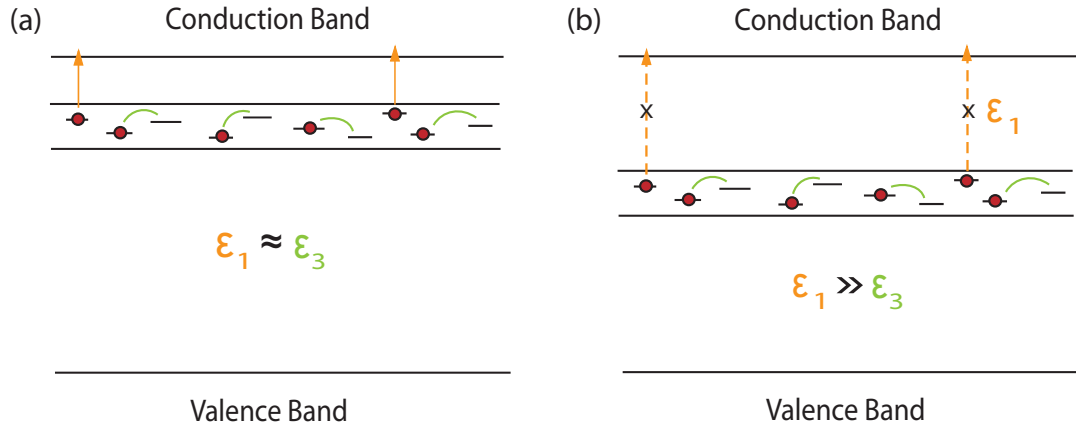


Figure 1.9: Schematic picture of a lightly doped semiconductor, where the impurities states have energetic dispersion, forming an impurity band. (a) Scenario of shallow impurities, where the activation energies of band and hopping conduction are of the same order of magnitude ($\epsilon_1 \approx \epsilon_3$) leading to the coexistence of both transport mechanisms. Deep impurities (b), where the conduction is entirely dominated by hopping events due to the very large activation energy ϵ_1 .

In the hopping regime, when the impurity concentration is increased, the activation energy is first enhanced due to the increasing random Coulomb potential of charged impurities. However, a further increase in the concentration enhances the wave-function overlap of neighboring centers and leads to a smaller ϵ_3 . There is a critical concentration where the hopping activation energy ϵ_3 vanishes, indicative of a transition from activated to metallic conductivity. The range of concentrations near the metal-insulator transition (MIT) is difficult to interpret quantitatively, therefore, we restrict in discussing the mechanism of hopping conduction with non-vanishing activation energy. Another characteristic feature of hopping conduction is an extremely strong dependence of the quantity ρ_3 in (1.17) on the impurity concentration N_{imp} . This sharp dependence can be described as

$$\rho_3 = \rho_{03} e^{f(N_{imp})} \quad (1.18)$$

where both ρ_{03} and $f(N_{imp})$ are power-law functions of the impurity concentration. In order to clarify the exponential dependence of the hopping conductivity on impurity concentration, we start at the case when separation between impurities are much larger than the Bohr radius of the impurity state. At such distances the wave functions fall exponentially, therefore, the overlap integrals also drop exponentially with increasing distance between impurities, so that the hopping probability and

hence the electrical conductivity will follow the same behavior. The exponential dependence of conductivity on impurity concentration is one important fingerprint of hopping phenomena.

In addition to the band and the hopping mechanisms of conduction, semiconductors with low compensation display another activated transport mechanism which manifests itself in a limited range of concentrations near the Mott-transition², and works at the intermediate temperature range between the band and the hopping conductivity regime. It arises when the impurity possesses a second electronic state with much larger Bohr radius, so that the wave functions overlap strongly leading to the formation of a second impurity band, whose width might be great enough to merge with the conduction or valence band edges. The so-called ϵ_2 -conduction has been experimentally observed in germanium and silicon [49, 50], but its theoretical description has not been developed yet. That is why we will just consider „ ϵ_3 conduction“ when referring to hopping conduction.

As described in Fig.1.9, the coexistence of band- and hopping conduction works only in semiconductors where the impurity states are not so far away from the conduction or valence band edges and has been observed in a couple of material systems [51, 52]. However, if the impurities induce states which are energetically *deep* in the bandgap of the semiconductor, the electronic transport will be entirely dominated by hopping events between localized states, where the interaction with phonons and the overlap of the localized wave functions play an important role. A quantitative description of the conduction mechanism in the *pure* hopping regime will be presented in the next section.

1.2.3 Theory of Hopping Conduction

In order to introduce the concepts which form the basis of the hopping conduction theory, we start with the approach suggested by Miller and Abrahams [53]. The recipe is as follows: Start with electron wave functions localized at individual impurities (e.g. donors), then calculate the probability that an electron transition will occur between two impurities i and j with the emission or absorption of a phonon. Next, calculate the number of transitions $i \rightarrow j$ per unit time. In the absence of an electric field, an equal number of electrons undergo the reverse transition. However, when an electric field is applied, the forward and the reverse transitions will not be balanced, giving rise to a current proportional to the field. Evaluating this current yields the resistance R_{ij} of a given transition, and thus the problem is reduced to calculating the electrical conductivity of an equivalent network of random resistors, as sketched in Fig.1.10.

A very detailed calculation of the random resistor problem can be found in Ref.[53]. Nevertheless, we will summarize the most important concepts and steps to understand what is the essence of hopping conductivity phenomena. The scenario starts with two

²when the metal-insulator-transition is reached due to electronic correlations

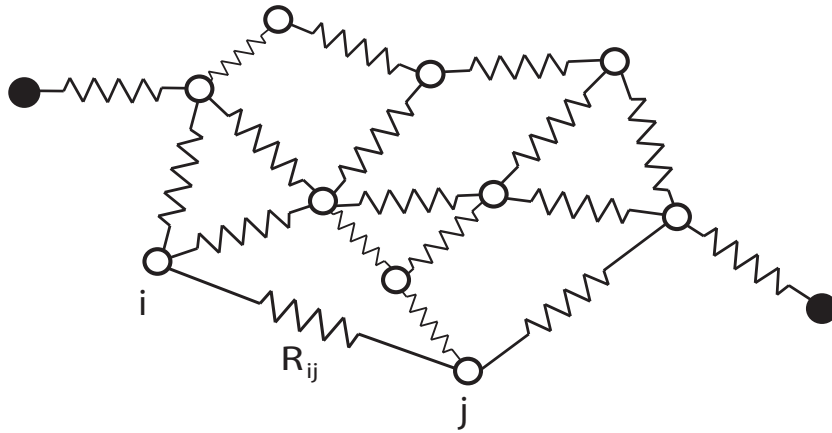


Figure 1.10: Random resistor network proposed by Miller and Abrahams [53]. The vertices correspond to impurity sites with energetic and spatial distribution, quantities which determine the hopping probability ($\propto R_{ij}$) between each pair of sites. The macroscopic conductivity is determined by the resistance path with lower sets of resistances R_{ij} .

impurities (for simplicity, donors) i and j which are placed at the coordinates r_i and r_j and are supposed to share one electron. The ground-state wave function of an isolated impurity is of Bloch-type $\psi(r-r_i) \equiv \psi(r)$, which satisfies the single-electron Hamiltonian in an ideal lattice with the Coulomb-potential

$$H = \frac{\hbar^2}{2m}\Delta + V_{lattice} + \frac{e^2}{\kappa|r - r_i|} \quad (1.19)$$

where Δ is the Laplace-operator and κ is the dielectric constant of the medium. For lightly doped semiconductors, the distance r_{ij} is much larger than the characteristic wave-function size, so that the overlap of the functions ψ_i and ψ_j will be weak. The interaction between the electron and both donors produces a splitting of the degenerate state. Within the framework of the LCAO³ method, the split-state wave functions represent a symmetric and an antisymmetric combination of the atomic functions:

$$\psi_{1,2} = \frac{\psi_i \pm \psi_j}{\sqrt{2}(1 \pm \int \psi_i^* \psi_j dr)^{1/2}} \quad (1.20)$$

yielding the eigenenergies of states 1 and 2 according to the Hamiltonian in (1.19)

$$E_{2,1} = -E_0 - \frac{e^2}{\kappa r_{ij}} \pm I_{ij} \quad (1.21)$$

where $-E_0$ is the energy level of an isolated impurity and I_{ij} is the energy overlap integral. For an hydrogenic-like function the following expression is obtained:

³Linear Combination of Atomic Orbitals

$$I_{ij} = \frac{2}{3} \left(\frac{e^2}{\kappa a} \right) \exp \left(\frac{-r_{ij}}{a} \right) \quad (1.22)$$

where a denotes the Bohr-radius of the impurity state. A more accurate calculation of the energy splitting $E_{2,1}$ which goes beyond the LCAO method by taking into account the deformed shape of the wave function inbetween two impurity centers -where their potential are comparable-, results in replacing the factor $2/3$ by $2/e$ [54]. Moreover, in a lightly doped semiconductor the above described situation is not realized in practice, because of the strong interaction $W(r)$ between the electron and the charged impurities surrounding the donors i and j . When the difference in potential energy $W(r)$ at the sites i and j is larger than the overlap energy I_{ij} between the donors, the following inequality

$$\Delta_i^j \gg I_{ij} \quad ; \quad \Delta_i^j \equiv W(r_j) - W(r_i) \quad (1.23)$$

leads to a new set of wave functions by including the potential energy $W(r)$ in the Hamiltonian and performing a variational calculation[53]. The two lowest states are of the form

$$\Psi_i = \Psi_i + \frac{I_{ij}}{\Delta_i^j} \Psi_j \quad (1.24)$$

$$\Psi_j = \Psi_j - \frac{I_{ij}}{\Delta_i^j} \Psi_i \quad (1.25)$$

An electron transition from state Ψ_i to Ψ_j implies a transfer of charge $-e$ on the distance r_{ij} . By calculating the eigenenergies, the energy difference between both states yield

$$\Delta E_{ij} = E_i - E_j = \Delta_i^j + \frac{(I_{ij})^2}{\Delta_i^j} \quad (1.26)$$

and amounts to Δ_i^j for $\Delta_i^j \gg I_{ij}$. Therefore, the energy of an absorbed phonon in the transition $i \rightarrow j$ corresponds to Δ_i^j . Although the value of Δ_i^j is usually of a few meV, the transition $i \rightarrow j$ requires the participation of a long-wave acoustic phonon. According to [53], it is assumed that electrons interact only with one acoustic branch whose spectrum is isotropic. The transition probability is given by

$$\gamma_{ij} = \frac{2\pi V_0}{\hbar(2\pi)^3} \int |M_{\mathbf{q}}|^2 \delta(\hbar v_s \mathbf{q} - \Delta_i^j) d\mathbf{q} \quad (1.27)$$

where V_0 is the volume of the crystal, v_s the speed of sound, \mathbf{q} is the phonon wave vector, and $|M_{\mathbf{q}}|$ the matrix element of electron-phonon interaction. For the case of an hydrogenic wave function and a donor separation r_{ij} much larger than the effective

Bohr radius⁴ a , the transition probability of the hopping electron can be then written in the form

$$\gamma_{ij} = \gamma_{ij}^0 \exp\left(\frac{-2r_{ij}}{a}\right) N(\Delta_i^j) \quad (1.28)$$

where γ_{ij}^0 summarizes the term which does not have any exponential dependence on r_{ij} , Δ_i^j and a . The term $N(\Delta_i^j)$, on the other hand, arises from the electron-phonon matrix element $|M_{\mathbf{q}}|$ and is equal to

$$N(\Delta_i^j) = \left[\exp\left(\frac{\Delta_i^j}{kT}\right) - 1 \right]^{-1} \quad (1.29)$$

So far, the probability of an electron transition between two localized impurity centers at the sites i and j has been derived. The second step of the approach by Miller and Abrahams is the calculation of the number of transitions $i \rightarrow j$ per unit time. For that purpose, we introduce the quantity $n_i=(0,1)$ as the i -th donor occupation number which fluctuates in time. The transition $i \rightarrow j$ is only possible when the initial state is populated and the final empty ($n_i=1, n_j=0$), so that the number of electrons making this transition per unit time is given by

$$\Gamma_{ij} = \langle \gamma_{ij} n_i (1 - n_j) \rangle \quad (1.30)$$

The quantity γ_{ij} also fluctuates in time, due to the fluctuating occupation numbers for other donors which are neighbors of i and j . The surrounding potential energy landscape $W(r)$ thus changes over time, giving rise to fluctuations in Δ_i^j and hence in γ_{ij} . For simplicity, we assume that the site occupation numbers and energies do not fluctuate in time, but remain equal to their average values, typical trick of a self-consistent field-approximation⁵. Each donor is characterized by the (i) average occupation number $\langle n_i \rangle \equiv f_i$, (ii) and the time-averaged electronic level energy in the field of all other impurities and electrons ϵ_i . The phonon energy absorbed in the transition will be thus $\Delta_i^j = \epsilon_j - \epsilon_i$. Under this approximation, the transition probability $i \rightarrow j$ per unit time is given by

$$\Gamma_{ij} = \gamma_{ij}^0 \exp\left(\frac{-2r_{ij}}{a}\right) N(\epsilon_j - \epsilon_i) f_i (1 - f_j) \quad (1.31)$$

For the reverse process, $j \rightarrow i$, which happens with the emission of a phonon, one obtains

$$\Gamma_{ji} = \gamma_{ij}^0 \exp\left(\frac{-2r_{ij}}{a}\right) [N(\epsilon_j - \epsilon_i) + 1] f_j (1 - f_i) \quad (1.32)$$

⁴also defined as „localization radius“, term which describe the characteristic size of the spatial region in which the wave function is not exponentially small.

⁵analogous to the Hartree-approximation

It should be mentioned that, while this approximation of time-averaging nicely holds to describe the exponential dependence of ρ_3 or the activation energy ϵ_3 in the limits of low and high compensation, is no longer valid for processes in which correlation effects are of tangible importance.

Coming back to the calculation of the electrical current between i and j , which is nothing else than the difference between forward and reverse electron transition probabilities

$$J_{ij} = -e(\Gamma_{ij} - \Gamma_{ji}) \quad (1.33)$$

one obtains that there is a balance between the transitions $i \rightarrow j$ and $j \rightarrow i$ in the absence of an electric field E . To elucidate that, consider the functions f_i which are given by the equilibrium expression

$$f_i = f_i^0 = \left[\frac{1}{2} \exp \frac{\epsilon_i^0 - \mu}{kT} + 1 \right]^{-1} \quad (1.34)$$

where ϵ_i^0 is the average energy on site i at $E=0$, μ is the electrochemical potential of the system and the factor $1/2$ is associated with two possible spin states for an occupied site. Variations of the electric field E will redistribute electrons over donors, creating corrections δf_i and $\delta \epsilon_i$ so that the equation 1.34 converts to

$$f_i(E) = f_i^0 + \delta f_i = \left[1 + \frac{1}{2} \exp \frac{\epsilon_i^0 - \delta \mu_i - \mu}{kT} \right]^{-1} \quad (1.35)$$

where $\epsilon_i^0 = \epsilon_i - \delta \epsilon_i$. If the electric field is so small that the corrections $\delta \mu_i$ and $\delta \epsilon_i$ are small compared to kT , then one can expand the functions f_i , f_j , and $N(\epsilon_i - \epsilon_j)$ in the expressions for Γ_{ij} and Γ_{ji} as power series in these corrections. Using algebraic manipulations with Eqs. 1.31,1.32,1.33,1.34 the current J_{ij} can be written in the form

$$J_{ij} = \frac{e\Gamma_{ij}^0}{kT} [\delta \mu_j + \delta \epsilon_j - (\delta \mu_i + \delta \epsilon_i)] \quad (1.36)$$

being Γ_{ij}^0 the frequency (probability per unit time) of transitions $i \rightarrow j$ and $j \rightarrow i$ in equilibrium. It is now visualized that just the corrections given by the electric field $E \neq 0$ to the potentials and distributions at i and j lead to a non-vanishing electrical current, which according to Ohm's law takes the shape

$$J_{ij} = R_{ij}^{-1}(U_i - U_j) \quad (1.37)$$

where

$$R_{ij} = \frac{kT}{e^2 \Gamma_{ij}^0} \quad (1.38)$$

and

$$-eU_i = \delta\mu_i + \delta\epsilon_i = \delta\mu_i + e\mathbf{E} \cdot \mathbf{r}_i + \frac{e^2}{\kappa} \sum_{k \neq i}^{\text{don}} \frac{\delta f_k}{|r_i - r_k|} \quad (1.39)$$

The first term in $\delta\epsilon_i$ describes the direct action of the external field \mathbf{E} , and the second describes the variation in the Coulomb potential due to a redistribution of electrons. Coming back to the Ohm's law description of the electrical conductivity for a given transition $i \rightarrow j$, the quantity $-eU_i$ can be regarded as a local value of the electrochemical potential on donor i , counted from the electron chemical potential μ , so that $U_i - U_j$ can be interpreted as a voltage drop and R_{ij} as the resistance of the transition. Extrapolating to the macroscopic case where many donors are present, the total current through the sample, which is the sum of all current paths crossing through the electrodes, will be obtained provided that the quantities U_i can be calculated. However, it is not necessary to know all the individual terms U_i ; the donors which are adjacent to the metallic electrodes take the value of the electrode potential. If the sample has the length L the applied voltage between terminal electrodes is equal to eEL . All other voltages are determined by the condition of equality of currents flowing in- and out of each donor.

Although the calculation of each donor potential $-eU_i$ is really time-consuming for macroscopic samples, it can be in principle performed. The hopping conductivity is hence completely determined by the resistances R_{ij} of the random network, which according to (1.38) is governed primarily by the time-averaged transition probability Γ_{ij} . It is convenient to separate two factors in the expression (1.31) which describe Γ_{ij} , one depending exponentially on the distances r_{ij} and the donor energies ϵ_{ij} , and all other containing weaker, power-law dependences on these parameters. By substituting the equilibrium functions N^0 , f_i^0 and f_j^0 into the expression for Γ_{ij} , and considering sufficient low temperatures where $kT \ll |\epsilon_i^0 - \epsilon_j^0|, |\epsilon_i^0 - \mu|, |\epsilon_j^0 - \mu|$, the quantity Γ_{ij}^0 becomes

$$\Gamma_{ij}^0 = \gamma_{ij}^0 \exp(2r_{ij}/a) \exp(\epsilon_{ij}/kT) \quad (1.40)$$

where

$$\epsilon_{ij} = 1/2 [|\epsilon_i^0 - \epsilon_j^0| + |\epsilon_i^0 - \mu| + |\epsilon_j^0 - \mu|] \quad (1.41)$$

Finally, we arrive at the expression which contains the essential dependences of hopping conductivity:

$$R_{ij} = \frac{kT}{e^2 \gamma_{ij}^0} \exp\left(\frac{2r_{ij}}{a} + \frac{\epsilon_{ij}}{kT}\right) \quad (1.42)$$

The resistance of a given transition $i \rightarrow j$ will be thus determined, on the one hand, by the relation between impurity distance and wave function extension, and between potential energy difference at the sites i and j (energy barrier) and available thermal energy, on the other hand. It is therefore plausible that, at very large impurity

separation r_{ij} or at very high energy barriers ϵ_{ij} (or an addition of both effects) the resistance R_{ij} is exponentially high, making the given transition very rare or inexistent. In order to determine the *total* resistance of the resistor network containing N_d vertices, it is important to evaluate the dispersion of the parameters involved in the exponential part of R_{ij} described in Eq.(1.42). The characteristic dimension of the wave function localized at the donor sites -in the following denoted as localization length ξ - depends on the nature of the donor impurity and therefore its dispersion can be primarily neglected. In contrast, it is clear that the separation between impurities r_{ij} has a considerable dispersion in real crystals. At sufficiently low temperatures, the energy term might also have a tangible dispersion, affecting the distribution of resistance values R_{ij} .

Miller and Abrahams [53] made the first approach to calculate the total resistance of the random network by averaging local values of resistances R_{ij} . The biggest difficulty was to deal with a wide spectrum of distances r_{ij} , which lead to the existence of regions of radius r larger than the mean impurity distance $r_{mean}=(N_d)^{-1/3}$ where chains of series resistance break. The scenario is illustrated in Fig.1.11. It is evident that the current from one electrode to the other will depend strongly on the fact, if there are other resistance chains with much lower series resistance which are able to bypass the void, which describe the regions where $r \geq r_{mean}$. It is evident that the relative number of broken and unbroken chains plays an important role for the total conductivity: the Miller-Abrahams random resistor network is a percolation problem.

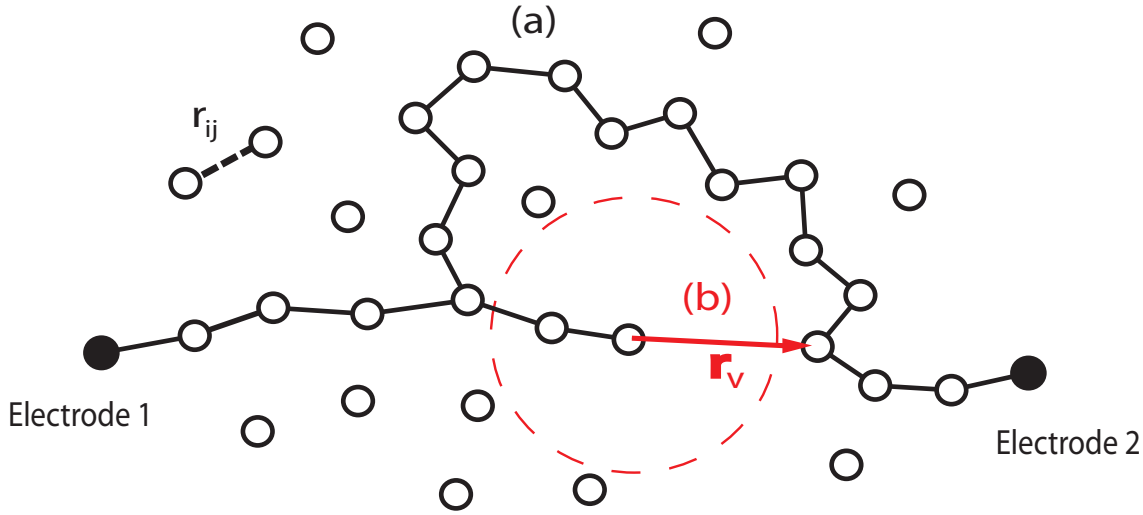


Figure 1.11: Schematic description of a parallel circuit consisting in (a) a series resistance chain where all the vertices fulfill the condition $r_{ij} \leq r_{mean}$ and (b) a single connection by crossing a void of radius $r_v \geq r_{mean}$. If the low-resistance chains exist in sufficient number, the voids will be all bypassed by conducting current from one electrode to the other.

The percolation theory was successfully applied to solve the Miller-Abrahams random resistor network problem [55, 56, 57] and hence describe the macroscopic hopping conductivity. In particular, it was shown that the percolation method worked well for a sufficiently large dispersion of resistances, which ideally corresponds the experimental cases. An important result of the percolation theory is the existence of a critical value x_c which is denoted as the percolation threshold. For instance, the parameter x can be regarded as the ratio between unbroken and broken conductivity bonds of the Miller-Abrahams random network, or equivalently, as the probability that a transition $i \rightarrow j$ happens (connected) or not (broken bond). Such probability is governed primarily by the exponential part of Eq.(1.40), so that the parameter

$$x_{ij} = \frac{2r_{ij}}{a} + \frac{\epsilon_{ij}}{kT} \quad (1.43)$$

is the right one to be included in the framework of percolation theory. Thus each resistor R_{ij} is described as

$$R_{ij} = R_{ij}^0 e^{x_{ij}} \quad (1.44)$$

In order to evaluate the exponential part of the macroscopic hopping conductivity, we start with the situation where only the resistances with $x_{ij} \leq x$ are switched on. Then, we gradually increase x until we reach the percolation condition over conducting resistances. This is obviously the case at $x=x_c$, where x_c is the percolation threshold for a random site problem[58], with the bonding criterion⁶

$$x_{ij} \leq x \quad (1.45)$$

Increasing x from x_c to $x_c + 1$ results in the formation of a critical subnetwork of resistances, which shunts all resistances whose x_{ij} 's are substantially larger than $x_c + 1$: the electrical conductivity of the critical subnetwork itself is determined by resistances with x_{ij} close to x_c . As a consequence, the macroscopic hopping conductivity can be written as

$$\rho = \rho_0 e^{x_c} \quad (1.46)$$

since the exponential dependence of the hopping conductivity on all parameters (r_{ij}, ϵ_{ij}, a) resides of the percolation threshold parameter x_{ij} (Eq. 1.43). This should be taken as the starting point for all investigations of macroscopic hopping conductivity. In order to see how physical results follow from this expression, we consider first the the case when ρ_3 , defined by Eq. (1.18) in the preceding section, only depends on the impurity concentration. The network of resistances for the ρ_3 -problem⁷ is given by

⁶the criterion to be fulfilled so that sites i and j are considered bonded

⁷where the resistivity depends only on the impurity separation

$$R_{ij} = R_{ij}^0 e^{(2r_{ij}/a)} \quad (1.47)$$

where the bonding criterion adopts the simple form

$$\frac{2r_{ij}}{a} \leq x \Rightarrow r_{ij} \leq \frac{ax}{2} \quad (1.48)$$

which means that the connectivity of a pair of impurities depends only on their separation. Consequently, x_c can be expressed in terms of the percolation radius r_c , as

$$x_c = \frac{2r_c}{a} \quad (1.49)$$

In turn, the exponent of the macroscopic electrical conductivity (Eq. 1.46) is entirely determined by jumps over the distance of the percolation radius r_c . Calculation of the percolation radius of spheres through a finite array of N random sites is an old problem and has been performed generally [59, 60] and specifically to evaluate the percolation radius of long-ranged magnetic interactions [61]. The best results found in literature for the sphere problem yield

$$\frac{4\pi}{3}Nr_c^3 = 2.7 \pm 0.1 \Rightarrow r_c = (0.865 \pm 0.015)N^{-1/3} \quad (1.50)$$

where N is correspondingly the concentration of vertices of the Miller-Abrahams network, or equivalently the concentration of majority impurities. The determination of r_c defines x_c via Eq.(1.49) and we find for the ρ_3 conductivity

$$\rho_3 = \rho_{03}e^{x_c} = \rho_{03} \exp\left(\frac{c}{N^{1/3}a}\right) \quad (1.51)$$

where $c=1.73\pm0.03$. Comparing this expression with (1.18) we successfully obtained the sought dependence $f(N_{imp})$ of the hopping conductivity on the majority impurity concentration. It should be noted that this dependence is applicable only when the wave functions localized on the majority impurities are isotropic and hydrogenic-like decaying at large distances according to the law $\Phi(r) \propto \exp(-r/a)$. For the case of anisotropic wave-functions (e.g ellipsoidal), the approach of a sphere percolation problem can be taken by considering a geometrical correction due to the change of localization volume⁸, yielding the following impurity-concentration dependence

$$x_c = f(N_{imp}) = \frac{c}{N^{1/3}(a^2b)^{1/3}} \quad (1.52)$$

where a and b correspond to the long and short ellipsoidal diameters, and c is the same numerical coefficient as in the isotropic case. For instance, this determination allows to study crystals which are under the influence of deformation potentials which alter the shape of the localized wave functions, e.g. uniaxial strain.

⁸the volume of the spatial region in which the wave function is not exponentially small

So far, the percolation theory has been applied to solve the hopping conductivity problem where the transitions R_{ij} only depend on the impurity separation. When the energy term ϵ_{ij}/kT in R_{ij} is not negligible, it has to be included in the bonding criterion which takes the form

$$\frac{2r_{ij}}{a} + \frac{\epsilon_{ij}}{kT} \leq x \quad (1.53)$$

The simplest case for evaluating the exponential temperature dependence of the hopping conduction, which resides entirely in the term ϵ_{ij}/kT , corresponds to semiconductors with low degree of compensation. The impurity band and the density of states is sketched in Fig. 1.12. Two important features can be extracted from the scenario of low compensation: First, most donor levels are very close to the unperturbed level⁹, which is taken to define the zero energy. Consequently, the vast majority of transitions $i \rightarrow j$ will take place between donor states near the density-of-states (DOS) maximum. Second, since the Fermi-energy μ lies at the upper extremum of the DOS-tail, the donor energies ϵ_i and ϵ_j are very small compared to the Fermi-energy μ . By recalling expression (1.41), one obtains $\epsilon_{ij} \approx \mu$ and thus the bonding criterion can be adapted as

$$x_c^0 + \frac{\mu}{kT} \leq x \quad (1.54)$$

where $x_c^0 = 2r_c/a$ is the known percolation threshold for the problem where the transition probability only depends on the impurity separation. It is important to keep in mind that the second term in (1.54) is independent of the selection of the sites i and j , so that it will behave as an additive constant when searching for the percolation threshold x_c of the whole problem:

$$x_c = x_c^0 + \frac{\mu}{kT} \quad (1.55)$$

so that the macroscopic hopping resistivity takes the form

$$\rho = \rho_{03} e^{x_c^0} e^{\mu/kT} \quad (1.56)$$

The existence of a constant activation energy in the low-compensation regime can be well understood: the states near the Fermi-energy are very rare, so that the long spatial distance between them, according to the Miller-Abrahams theory, represent a conduction channel of „broken chains“ which is easily bypassed by the much more conductive channel of donor states which are abundant thus having a strong overlap; nevertheless, the latter transitions have to pay the price of an activation energy μ to contribute to the conductivity. Again, we notice the important role of the shape of the impurity band DOS and the position of the Fermi-level (see Fig. 1.12) when

⁹the energy level which would result if there were no energetic dispersion of the available states, i. e. if the impurity band width would converge to zero

making useful approximations to solve hopping conductivity problems. In a similar fashion, the hopping conductivity can be derived in the limit of high compensation assuming an analogous impurity band distribution.

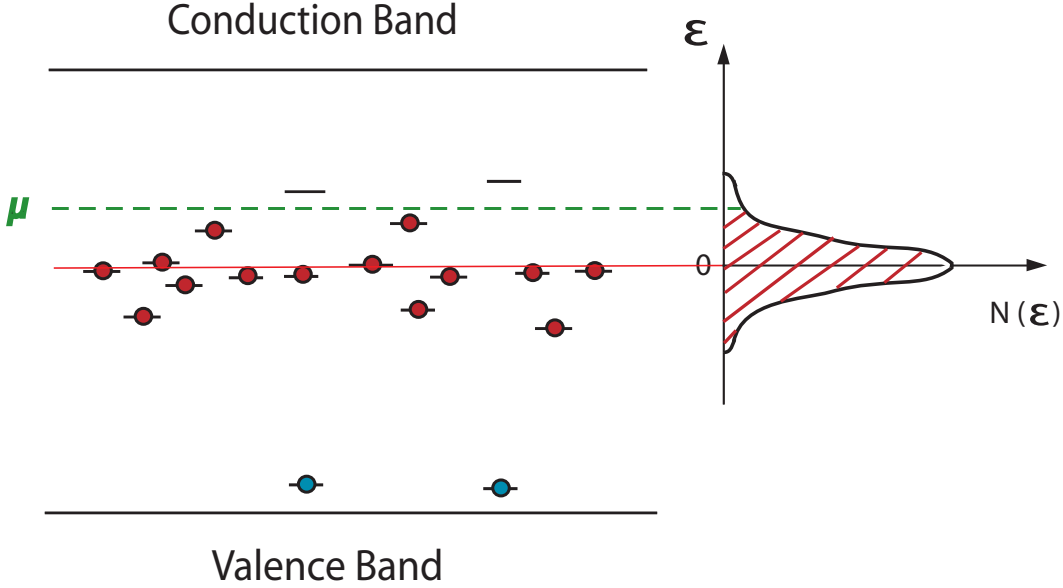


Figure 1.12: Schematic representation of the impurity band and the density of states (DOS) at low compensation. The electrons of the donors which are trapped by acceptor states are painted in blue. The zero-energy lies at the isolated impurity level, and the Fermi energy (μ) lies in the upper band tail, such that the electrons which contribute to the conductivity at the DOS-maximum have to be activated by the energy μ .

The situation is different when dealing with semiconductors either in intermediate ranges of compensation or with a very sharp density-of-states profile, where the simplified picture of a constant activation energy is not necessary valid. However, by considering the general bonding criterion (1.53) and the inequality

$$\frac{\epsilon_{ij}}{kT} \ll \frac{2r_{ij}}{a} \quad (1.57)$$

it was demonstrated that there is indeed a constant activation energy[62]. The authors in [62] included the perturbation method in the framework of percolation theory. Without going into details, the physical implications of this inequality will be discussed in order to understand the concept of a constant activation energy in hopping conduction. Starting again with the Miller-Abrahams random resistor network, the selection of resistances R_{ij} according to the bonding criterion (1.53) will be governed by the distance r_{ij} between transitions, if the inequality is fulfilled. As a consequence, the energy barriers ϵ_{ij} will have less influence on the percolation threshold, and can be treated as a first-order perturbation problem. Assuming that the energies ϵ_i and ϵ_j are uncorrelated and homogeneously distributed, the perturbation analysis [62] yields

$$\epsilon_{ij} = \langle \epsilon_{ij} \rangle \quad (1.58)$$

which means that the macroscopic activation energy is the average of all energy barriers ϵ_{ij} whose dispersion is described by a distribution function $f(\epsilon_{ij})$. Coming to a more realistic situation, we have to take into account the correlation between on-site energies ϵ_i and ϵ_j (e.g via Coulomb-interaction between impurities) which depend on the impurity separation r_{ij} . The characteristic distance r_{ij} at which the correlation is still appreciable is denoted as the energy correlation length r_{corr} . Moreover, the probability that a pair (i,j) corresponds to a given energy ϵ_{ij} is different for pairs with different r_{ij} , meaning that the distribution function $f(\epsilon_{ij})$ will depend on r_{ij} . The increase in the percolation threshold from $x_c^0 (=2r_c/a)$ to x_c when the bonding criterion is changed from $x_c^0 \leq x$ to $x_c^0 + \Delta x_{ij} \leq x$ occurs due to those pairs for which

$$x_{ij}^0 < x_c^0 \quad ; \quad x_{ij}^0 + \Delta x_{ij} > x_c^0. \quad (1.59)$$

The first condition (equivalent to $r_{ij} < r_c$) implies that, as long as the „new“ percolation problem is still governed by r_{ij} , only transitions between impurities whose distances are shorter than the percolation radius (connected resistors in the Miller-Abrahams network) can actively change the percolation threshold; while the second condition tells us that, if the percolation threshold is changed, has to be due to the energy term $\Delta x_{ij} = \epsilon_{ij}/kT$. Since we are analyzing the case when $\Delta x_{ij} \ll x_c^0$, both inequalities in (1.59) are just fulfilled for the pairs with x_c very close to x_c^0 , in other words, only the pairs with r_{ij} close to the percolation radius r_c will change the percolation threshold when including their energy term ϵ_{ij} . Due to the random distribution of impurities, the number of the relevant pairs with $r_{ij} \approx r_c$ is rather small, and their typical separation much larger than the average impurity distance. As a consequence, the ϵ_{ij} of the relevant pairs can be considered to be uncorrelated, which enables again the use of the perturbation method to determine the activation energy [62]:

$$\epsilon_3 = \langle \epsilon_{ij} \rangle |_{r_{ij}=r_c} \quad (1.60)$$

being the only constraint that the average is taken not over all the available energies but over the relevant ones, i.e., the pairs for which $r_{ij}=r_c$. There have been a few studies testing the suitability of the perturbation theory considering arbitrary energy distributions $f(\epsilon_{ij})$ [62, 63, 64], which successfully confirmed the existence of a constant activation energy.

The constant activation energy in hopping conductivity is thus a general feature of the cases when the energy term (ϵ_{ij}/kT) is negligible compared to $(2r_{ij}/a)$. This behavior is observed experimentally for impurities with localized electrons (small localization radius a) and/or at high temperatures. Under these circumstances, the energy barriers ϵ_{ij} do not play a major role in the selection of resistances to solve the percolation problem and are rather included as a small perturbation. Therefore, as soon the percolation condition (tuned by r_{ij}) is fulfilled, the transitions $i \rightarrow j$

will be governed by nearest neighbors; that is why hopping conductivity with constant activation energy is often called nearest-neighbor-hopping (NNH). However, at temperatures which are sufficiently low or at localization radii a which are near the metal-insulator transition, the activation energy is no longer constant. The individual energy barrier between sites i and j is no longer negligible and influences the selection of resistances; it may happen that an electron, looking for a convenient energy barrier, hops over distances larger than the average distance between impurities. This phenomena is called variable-range-hopping and will be discussed in the next section. So far, we have provided the essential tools to understand the collective phenomenon of hopping conductivity. The random resistor network of Miller and Abrahams was presented as an illustrative model which starts by the evaluation of an individual transition and, with the help of percolation theory, ends with a transparent description of the macroscopic hopping conductivity.

1.2.4 Mott's law and Variable-Range-Hopping conduction

The basic concept of variable-range-hopping is, as the name reveals, the electronic transport by hopping over variable distances caused by the minimization of energy when undergoing a transition between two remote sites i and j . At sufficiently low temperatures, the macroscopic conductivity is determined by the states whose energies are close to the Fermi-level. Mott [65] was the first one to notice that at low temperatures, the activation energy ϵ decreased with decreasing temperature, from where he derived the celebrated Mott's law

$$\rho(T) = \rho_0 \exp [(T_0/T)]^{1/4} \quad (1.61)$$

with

$$T_0 = \frac{\beta}{k_B N(\mu) \xi} \quad (1.62)$$

where $N(\mu)$ is the density of states at the Fermi-energy, k_B the Boltzmann constant, ξ the localization radius of the relevant states, and β a numerical coefficient. Mott's original derivation could not give an exact value of the coefficient β , since he gave only a qualitative description of the emergence of variable-range-hopping transport in an impurity band with constant density of states at the Fermi-level. Fig. 1.13 shows schematically the impurity band structure which was the starting point to describe variable-range-hopping. Recalling the dominant exponential terms in the expression (1.42) for the hopping resistance R_{ij} it is natural to suppose that, at very low temperatures, only resistances having very small values of ϵ_{ij} will contribute to conduction. This implies that the relevant states (i,j) have to lie energetically in a narrow region near the Fermi-level, described by the energy interval ϵ_0 , as shown in Fig. 1.13. At the same time, the relevant states are far away from each other, therefore, their spatial distribution can be considered uncorrelated. Furthermore,

because of the narrow width of the band ϵ_0 , the density of states in the region $[\mu \pm \epsilon_0]$ can be regarded as constant, so that the total number of relevant states is given by

$$N(\epsilon_0) = 2N(\mu)\epsilon_0 \quad (1.63)$$

In order to derive the resistance corresponding to all the sites i for which $|\epsilon_i - \mu| \leq \epsilon_0$, the average energy barrier and distance between hops in the narrow band can be estimated as $\langle \epsilon_{ij} \rangle = \epsilon_0$ and $\langle r_{ij} \rangle = [N(\epsilon_0)]^{-1/3}$, respectively. Using these average expressions, the macroscopic resistivity can be written as

$$\rho = \rho_0 \exp \left[\frac{1}{N(\epsilon_0)^{1/3} \xi} + \frac{\epsilon_0}{kT} \right] = \rho_0 \exp \left[\frac{1}{[2N(\mu)\epsilon_0]^{1/3} \xi} + \frac{\epsilon_0}{kT} \right] \quad (1.64)$$

For large values of ϵ_0 , the second term dominates in the exponential part of (1.64), which implies a decreasing $\rho(\epsilon_0)$ with decreasing ϵ_0 . As the width of the narrow band ϵ_0 becomes smaller, the states become very rare and their decreasing overlap plays the dominant role, resulting in an increase of $\rho(\epsilon_0)$. The competition between spatial overlap and energy leads to a resistance minimum when both terms in the exponent of (1.64) become equal. The temperature-dependent energy ϵ_0 which yields the minimum resistance takes then the form

$$\epsilon_0(T) = \frac{(kT)^{3/4}}{[N(\mu)\xi^3]^{1/4}} \quad (1.65)$$

This expression, which corresponds to the „optimal band width“ of the relevant states, contains the physical essence of variable-range-hopping transport. In particular, it describes the scenario of minimum resistivity, analogous to the obtention of the percolation threshold in a Miller-Abrahams random resistor network. By substituting $\epsilon_0(T)$ into the resistivity expression (1.64) one arrives at Mott's law (1.61). The $T^{-1/4}$ dependence of the hopping resistivity is characteristic of variable-range-hopping with a constant density of states at the Fermi-level, scenario which was given the name of Mott variable-range-hopping (Mott-VRH), in spirit of Mott's rather intuitive derivation.

The quantity $\epsilon_0(T)$ corresponds to the average activation energy between hops of the relevant sites, and the derivative $d(\ln \rho)/d(kT)^{-1}$ yields the activation energy at a given temperature. From (1.65) it is evident that the activation energy decreases monotonically as $T^{3/4}$ with decreasing temperature. Unlike the high-temperature scenario of constant activation energy, where the hopping length is temperature independent and of the order of the mean separation between impurities (nearest-neighbor-hopping), the average hopping length in the VRH-regime does vary with temperature. From Eq.(1.64) we infer

$$\bar{R}_{hop} \propto [N(\mu)\epsilon_0(T)]^{-1/3} \propto \xi (T_0/T)^{1/4} \quad (1.66)$$

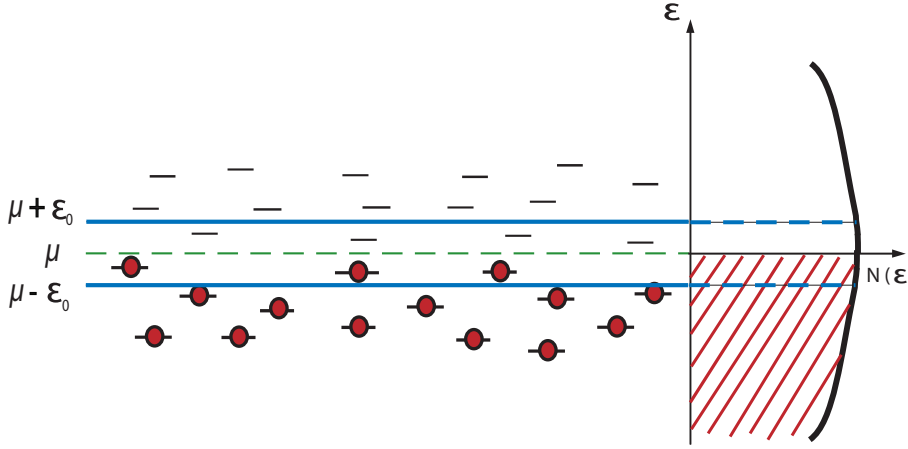


Figure 1.13: Section of an impurity band near the Fermi-level, with a constant density of states. At low temperatures, the relevant states for hopping transport are the ones within a energy interval ϵ_0 around the Fermi-level μ , which corresponds to the „optimal“ band in Mott’s derivation.

The average hopping length thus increases as $T^{-1/4}$ as the temperature is lowered, and may reach values much greater than the average distance between impurities. Despite the qualitative character of Mott’s original derivation, the description of the physics of variable-range-hopping is very consistent. Still, for a quantitative analysis (e.g. comparison with experimental data) the knowledge of the coefficient β in the numerator of the characteristic temperature T_0 is necessary. A more rigorous derivation of Mott’s law has been later done by Ambegaokar *et al.* [55] using the percolation method, where the coefficient β could be determined. For the sake of completeness, the solution of the macroscopic hopping conductivity by the percolation method at the limit of low temperatures will be summarized. As usual, the starting point for the percolation Ansatz is the bonding criterion

$$\frac{2r_{ij}}{\xi} + \frac{\epsilon_{ij}}{kT} \leq x \quad (1.67)$$

where both terms should be taken as relevant for the search of the percolation threshold x_c . The largest possible values of ϵ_{ij} and r_{ij} are defined as:

$$\epsilon_{max} = kTx; \quad r_{max} = \frac{\xi x}{2} \quad (1.68)$$

such that $\epsilon_{ij} \leq \epsilon_{max}$, which applies for both $|\epsilon_i - \mu|$ and $|\epsilon_j - \mu|$. Ambegaokar *et al.* [55] formulated the percolation problem using dimensionless variables in the form

$$d_i = r_i / r_{max} \quad (1.69)$$

$$\Delta_i = (\epsilon_i - \mu)/\epsilon_{max} \quad (1.70)$$

so that the bonding criterion adopts the form

$$d_{ij} + \Delta_{ij} \leq 1 \quad (1.71)$$

where

$$d_{ij} = |d_i - d_j| = r_{ij}/r_{max} \quad (1.72)$$

and

$$\Delta_{ij} = \frac{1}{2} (|\Delta_i| + |\Delta_j| + |\Delta_i - \Delta_j|) \quad (1.73)$$

Considering again the impurity band structure depicted in Fig. 1.13 with a constant density of states in the region $|\Delta_{i,j}| < 1$, the total number of states will be given by

$$N(x) = 2N(\mu)\epsilon_{max}r_{max}^3 = \frac{1}{4}N(\mu)k_BT\xi^3x^4 \quad (1.74)$$

so that determining the percolation threshold x_c requires to find the critical concentration N_c at which percolation first occurs, taking into account randomly located sites distributed in the energy interval $|\Delta_i| < 1$. The percolation threshold will be equal to

$$x_c = \left[\frac{4n_c}{N(\mu)k_BT\xi^3} \right]^{1/4} \quad (1.75)$$

and the macroscopic hopping resistivity can be written as

$$\rho(T) = \rho_0 e^{x_c} = \rho_0 \exp \left[\frac{4n_c}{N(\mu)k_BT\xi^3} \right]^{1/4} \quad (1.76)$$

This expression corresponds to Mott's law, with $\beta=4n_c$. It is not surprising that Mott's qualitative derivation and the solution offered by the percolation method are of the same form, since both approaches consider the scenario of sufficiently low temperatures and the same impurity band structure depicted in Fig. 1.13. For an accurate determination of the coefficient β , the above dimensionless percolation problem was numerically solved by the Monte Carlo method [66]. An extrapolation to an infinite array gives following values

$$n_c = 5.3 \pm 0.3; \quad \beta = 21.2 \pm 1.2 \quad (1.77)$$

The validity of Mott's law can be extended to lower dimensions. The quantity $N(\mu)$ can be understood as the n -dimensional density of states, and $[N(\epsilon_0)]^{1/3}$ can be replaced by $[N(\epsilon_0)]^{1/n}$. Repeating Mott's qualitative derivation described above, one obtains a law of the form $\rho=\rho_0 \exp (T_0/T)^{1/p}$ with $p=(d+1)^{-1}$.

On the other hand, Mott's law loses his validity when the density of states at the Fermi-level is no longer constant. This situation might arise when sizable correlation effects are present, leading to the formation of an energy gap at the Fermi-level. The influence of a vanishing density of states at E_F on the hopping conductivity will be discussed in the next section.

1.2.5 Correlation effects in Hopping conduction: The Coulomb Gap

In a medium where electronic correlations play an important role, it is imperative to identify the different kinds of impurities and their charge state. A lightly doped semiconductor contains mainly three kinds of sites chaotically arranged in space: (i) positively charged donors which have given up their electron to acceptors, (ii) neutral donors, and (iii) acceptors which permanently host an electron and are negatively charged. (For the sake of simplicity, we are considering an n-type semiconductor). All impurities are assumed to be fixed in space, but electrons can hop from one to another. Furthermore, the electron hops will be influenced by the Coulomb-potential of the impurities, which are likewise correlated if the average impurity separation is not too big. At zero temperature, the distribution of electrons over donors is determined by the condition of minimum electrostatic energy, which is a function of the occupation number of the participating impurities, described by the Hamiltonian

$$H_{el} = \frac{e^2}{\kappa} \left[\frac{1}{2} \sum_k^{don} \sum_{k' \neq k}^{don} \frac{(1 - n_k)(1 - n_{k'})}{r_{kk'}} - \sum_k^{don} \sum_i^{acc} \frac{(1 - n_k)}{r_{ik}} + \frac{1}{2} \sum_i^{acc} \sum_{j \neq i}^{acc} \frac{1}{r_{ij}} \right] \quad (1.78)$$

where κ is the dielectric constant of the medium. The determination of the occupation numbers and on-site energies corresponding to the ground state is a complicated many-body problem. However, it was solved for the limiting cases of low and high compensation [57, 67]. At intermediate compensation, when there is no small parameter which could lead to the simplification of the problem, the Coulomb-interaction has to be rigorously considered for all nearest neighbors of the localized electron. In this sense, Pollak and Knotek [68] showed that the density of states must have a minimum around the Fermi-level. Other authors [69, 70] confirmed the existence of an energy gap by computer experiments, being able to calculate the density of states and model the structure of the impurity band. The region where the density of states vanishes has been therefore named the 'Coulomb Gap'. The scenario is schematically depicted in Fig. 1.14.

The approach which was used to find the ground-state electrostatic energy of a given donor-acceptor configuration consists in the following. First, one minimizes the expression (1.78) with respect to one arbitrary occupation number, then with respect to a simultaneous variation of two occupation numbers, and so on. This procedure

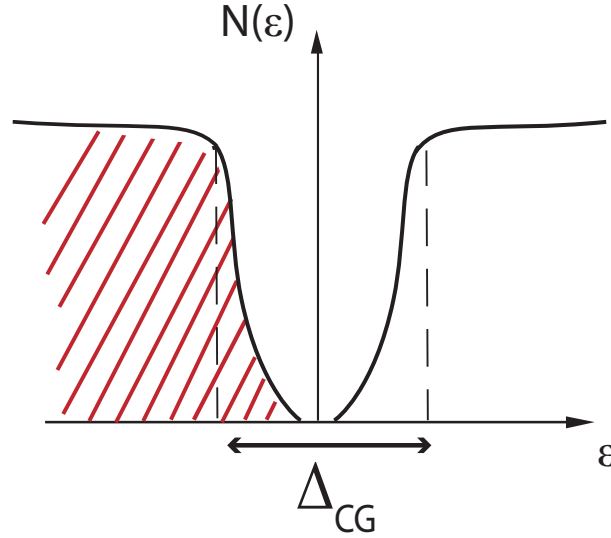


Figure 1.14: Impurity band with vanishing density of states at the Fermi energy. The energy interval where the DOS starts to decrease, is called the „Coulomb-gap“.

delivers a fast convergence, as confirmed by numerical calculations[69]. The derivation of the emergence of the Coulomb-gap follows taking into account two conditions for the transition $i \rightarrow j$ under the Coulomb potential, and starting from the ground state Hamiltonian. At a first stage, any variation of the occupation number n_i of a donor i will result in a perturbation of the ground-state Hamiltonian H_{min} . A positive increment will result provided that

$$n_i = \begin{cases} 0 & \epsilon_i > 0 \\ 1 & \epsilon_i < 0 \end{cases} \quad (1.79)$$

where ϵ_i is the energy counted from the Fermi-level μ , which is set as the zero-energy. In turn, this condition just stresses that states with energies below the Fermi-level are filled and those above are empty. The numerical experiments in [69] showed that the energy H satisfying the above condition for all donors, differs just by a few percent from the ground-state energy H_{min} . In the next stage, the energy increment Δ_i^j to the ground-state Hamiltonian H_{min} for the transition from a filled donor i to an empty donor j needs to be positive

$$\Delta_i^j = \epsilon_j - \epsilon_i - \frac{e^2}{\kappa r_{ij}} > 0 \quad (1.80)$$

It is not difficult to derive Δ_i^j from physical arguments. In order to push the electron from site i to the continuum, one requires the energy $-\epsilon_i$, and the energy to bring it back to the empty site j amounts to ϵ_j . However, in the second stage, the system is not in the ground-state any more: the electron has left a positive charged hole on

site i , whose attraction diminishes the energy by $-e^2/\kappa r_{ij}$. Equivalently, it can be regarded as the necessary energy to form an electron-hole pair, taking into account the interaction between electron and hole. The inequality (1.80) has to be valid for any pair of donors with $\epsilon_j > 0$ and $\epsilon_i < 0$, according to (1.79). Considering donors whose energies are comprised in a narrow band of width ϵ_0 as the relevant ones for the electronic transport (we are still dealing with very low temperatures), the initial and final state for any transition $i \rightarrow j$ have to lie on opposite sides of the Fermi-level, as shown in Fig. 1.15. Furthermore, taking into account the inequality (1.80) for the maximum energy difference between the states i and j , which is equal to $\epsilon_0/2 - (-\epsilon_0/2) = \epsilon_0$, one obtains

$$\Delta_i^j(max) = \epsilon_0 - \frac{e^2}{\kappa r_{ij}} > 0 \Rightarrow \epsilon_0 > \frac{e^2}{\kappa r_{ij}} \quad (1.81)$$

so that the relevant donors must be spatially separated by a distance r_{ij} not less than $e^2/\kappa\epsilon_0$. Therefore, the donor concentration $[N(\epsilon_0)]^{-1/3} \propto r_{ij}$ should not exceed the value of $\epsilon_0^3\kappa^3/e^6$. Moreover, by evaluating the density of states $N_D(\epsilon_0) = dn(\epsilon_0)/d\epsilon_0$, it can be observed that it vanishes when $\epsilon_0 \rightarrow 0$, at least as fast as ϵ_0^2 . A faster decrease of the density of states would mean that the average donor separation is greater than $e^2/\kappa\epsilon_0$, which leads to a much weaker Coulombic-interaction. Such a weak interaction could not be responsible for lowering the density states, coming to the conclusion that the density of states has to decrease quadratically towards the Fermi-level, as

$$N(\epsilon_0) = \frac{\alpha\epsilon_0^2\kappa^3}{e^6} \quad (1.82)$$

where α is a numerical coefficient equal to $3/\pi$ [69]. Within the approximation based on (1.81), the density of states near the Fermi-level takes the universal form [69, 71] described in (1.82), since neither the donor concentration nor the degree of compensation enters the ϵ^2 law. The width of the Coulomb-gap Δ_{CG} is inferred from the energy where the density of states is equal to the unperturbed density of states N_0 , as

$$N_0 = \frac{\alpha\Delta_{CG}^2\kappa^3}{e^6} \Rightarrow \Delta_{CG} = \frac{e^3N_0^{1/2}}{\kappa^{3/2}} \quad (1.83)$$

The emergence of the Coulomb-gap near the Fermi-energy μ has been qualitatively derived, in a similar fashion as Mott's variable-range-hopping using the approximation of a narrow band ϵ_0 of relevant states near the Fermi-energy. Both qualitative approaches underlie the condition of sufficiently low temperatures. However, it is worth to mention that the existence of a constant energy at the Fermi-level in Mott's derivation, which would mean the absence of a Coulomb-gap, is justified only when the coulombic correlation energies are negligible compared to the average hopping energy (which is similar to the optimal band $\epsilon_0(T)$ in order of magnitude) of the transitions $i \rightarrow j$ at a given temperature.

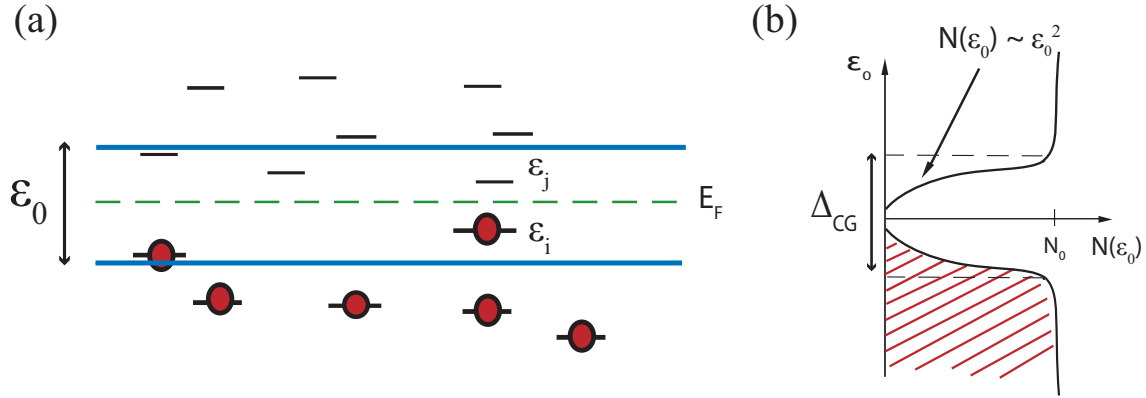


Figure 1.15: (a) Impurity states in a narrow band near the Fermi-energy. The ground-state requires that empty donors have a positive energy ϵ_j and occupied donors a negative energy ϵ_i . The maximum Δ_i^j for a relevant transition is in the order of ϵ_0 . (b) Resulting density of states after considering the relevant single-electron transitions under the effect of Coulomb interactions.

Furthermore, the quadratic dependence of the density states near the Fermi-level has important implications for the macroscopic conductivity. Considering a generalized energy dependent density of states [56]

$$N(\epsilon) = N_0 [|\epsilon - \mu|]^n \quad (1.84)$$

the resulting total number of relevant states near the Fermi-energy is given by

$$n(\epsilon_0) = N_0 \int_{\mu - \epsilon_0}^{\mu + \epsilon_0} N(\epsilon) d\epsilon = \frac{2}{n+1} N_0 \epsilon_0^{n+1} \quad (1.85)$$

where N_0 is the density of states far outside the coulomb gap. By replacing this expression in (1.64) and following Mott's original derivation based on the optimal band of minimum resistivity, one obtains

$$\rho(T) = \rho_0 \exp [(T_0/T)]^p \quad (1.86)$$

where the hopping exponent p is related to the power n of the density of states behavior as

$$p = \frac{n+1}{n+4} \quad (1.87)$$

The consistency of this general relation can be easily tested: for $n=0$, which resembles a constant density of states, one recovers $p=1/4$ (Mott-VRH); and for a quadratic dependence $n=2$ due to single-electron Coulombic interactions, the exponent $p=1/2$ (Efros-Shklovskii-VRH) is retrieved. The quantity T_0 in (1.86) is often called the characteristic hopping temperature, and in the Efros-Shklovskii regime ($p=1/2$) it amounts to

$$T_0 = \frac{\beta e^2}{\kappa \xi} \quad (1.88)$$

where β is a numerical factor, ξ denotes the localization radius and κ the static dielectric constant. Note that for the derivation of T_0 , the explicit form of the density of states (1.82) has been taken into account.

So far, we have concentrated on the effect of Coulomb-potential on single-electron transitions. The next stage is the minimization of the electrostatic energy described in (1.78) taking into account simultaneous transfer of many electrons. The many-electron problem was first considered in [72, 73], and the main result of the energy minimization was that the density of states at low energies exhibits a much sharper decay than quadratic, as

$$N(\epsilon) \propto e^{-\beta_1 \Delta / |\epsilon|} \quad (1.89)$$

where Δ is the Coulomb-gap width and β_1 a numerical coefficient. The physical explanation of this modified density of states behavior towards the Fermi-energy, underlies the fact that the system possesses another channel of low-energy elementary excitations, whose energy transfer is also defined by Δ_i^j (Eq. 1.80). Indeed, one empty and one filled donor can form a pair whose transfer energy Δ_i^j is very small, even though the single-electron energies $|\epsilon_i|$ and $|\epsilon_j|$ for each donor lie outside the optimal band ϵ_0 (Fig. 1.15). The existence of these pairs requires that the donor separation r_{ij} is sufficiently small, since according to (1.80), the term $e^2/\kappa r_{ij}$ has to compensate a large positive quantity $\epsilon_j - \epsilon_i$. Recall that initial and final state must lie on opposite sides of the Fermi level, i.e., $\epsilon_j > 0$ $\epsilon_i < 0$. The value of r_{ij} for such a pair is hence of the order of the average distance between impurities. Therefore, these low-energy pairs (also called 'soft pairs') represent compact formations, usually isolated from other pairs, and do not make any important contribution in the conductivity. However, one should be aware of their existence, since these are the pairs which, for instance, dominate in the absorption of low-frequency radiation.

While the electron transitions within 'soft pairs' do not play an important role for the macroscopic conductivity (the $T^{-1/2}$ law is still valid), the potential which is created by their excitation does. The excitation of a 'soft pair' results in an additional dipole moment compared to the ground state. The energy required to excite several pairs must therefore include dipole-dipole interaction energy, whose sign depend on the pair orientation. By definition of the ground state, the total energy of any excitation must be positive. The interaction between 'soft pairs' and the single-particle excitations of low energy ϵ can be also understood as the influence of additional surrounding dipole-fields in the vicinity of (for the conductivity) relevant single-particle transitions. Analogously, a relevant single-particle transition $i \rightarrow j$ which is not supposed to occur in normal conditions, can happen through the induction of electron transfers in surrounding soft pairs, if the induced polarization lowers the potential energy on site j . The scenario is sketched in Fig. 1.16.

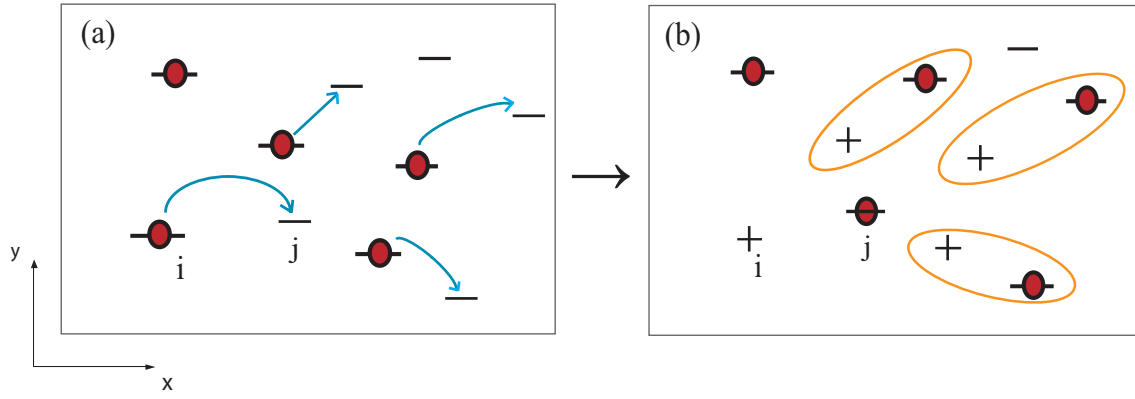


Figure 1.16: Sketch of how a single-particle transition $i \rightarrow j$ can induce soft-pair-excitations in the surroundings when the resulting polarization lowers the potential energy at site j . Initial (a) and final (b) state of the many-electron transition.

This situation is similar to the polaron effect in ionic crystals. However, in the present case the polarization does not arise due to ion displacements but because of electron transitions within soft pairs. The concept of 'electronic polaron' was introduced independently by Efros [72] and Mott [74] in the late 70s.

The excitation of 'soft pairs' has a substantial effect on the density of states $N(\epsilon)$. The expression for Δ_i^j (1.80) which describes the energy needed for a single-electron transition, needs to be corrected because of the polarization energy of surrounding soft pairs. Using the same arguments which led to the derivation of the law $N(\epsilon) \propto \epsilon^2$, but including the corrected Δ_i^j and considering a large number of soft pair excitations for each $i \rightarrow j$ transition, an exponential dependence of the form (1.89) is obtained [75, 76]. The recipe was to stabilize the ground-state against a certain amount of many-electron, „polaronic“ transitions. Using Poisson statistics, the distribution of transitions which have the smallest total excitation energy (the „best“ pairs) have been calculated [76], resulting in an exponential („hard“) gap of the order of $\Delta_{CG}/5$, where Δ_{CG} is the Coulomb gap width, as shown in Fig. 1.17. It is worth to recall that the Coulomb gap width (1.83) depends on the dielectric permittivity κ which has to be corrected due to the excitation of soft pairs, as

$$\kappa = \kappa_{host} + 4\pi\chi \quad ; \quad \chi = e^2 N_0 \xi^2 \quad (1.90)$$

where κ_{host} is the dielectric permittivity of the host lattice and χ is the contribution to the permittivity due to the excited electronic polarons [77]. The polaronic enhancement of the dielectric permittivity depends primarily on the localization length ξ , so that κ increases with increasing overlap of the wave functions, eventually diverging at the metal-insulator transition. This phenomenon is known as „polarization catastrophe“ and has been observed experimentally in uncompensated silicon [78, 79]. At low impurity concentrations, however, the polaronic contribution to the dielectric

permittivity is expected to be small. Another quantity which depends on κ is the characteristic temperature T_0 in the Efros-Shklovskii $T^{-1/2}$ resistivity law. In this sense, the polaronic contribution $4\pi\chi$ due to many-electron interactions should be also considered.

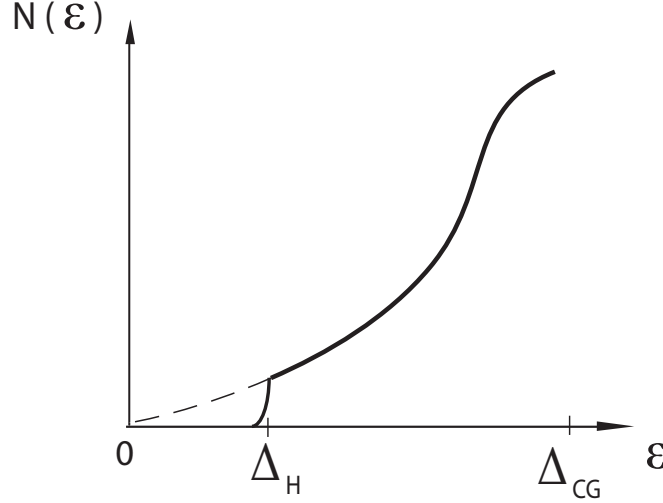


Figure 1.17: Density of states in a system where many-electron interactions play an important role. The 'hard gap' emerges at an energy of the order of $\Delta_{CG}/5$, according to [76]. The Fermi energy is set at zero.

The emergence of an exponential „hard gap“ within the Coulomb-gap due to electronic polaron excitations (Fig. 1.17) has a substantial influence on the macroscopic resistivity at very low temperatures. The relevant states near the Fermi-level 'feel' the hard gap as a finite energy difference and the temperature dependence of the resistivity recovers a single-activated behavior:

$$\rho(T) = \rho_0 \exp\left(\frac{\Delta_h}{T}\right) \quad (1.91)$$

It is generally difficult to observe the hard gap regime experimentally. Either the hard gap activation energy is so small compared to the average hopping energy at accessibly low temperatures, or the resistance becomes unmeasurably high at temperatures still corresponding to the Efros-Shklovskii ($T^{1/2}$) regime. However, there are suitable systems, where the combination of relevant parameters (bandgap of the host semiconductor, impurity concentration, degree of compensation, energetic position of the impurity band) enables the observation of the T^{-1} activated behavior at low temperatures, characteristic of the hard-gap regime [80, 81, 82].

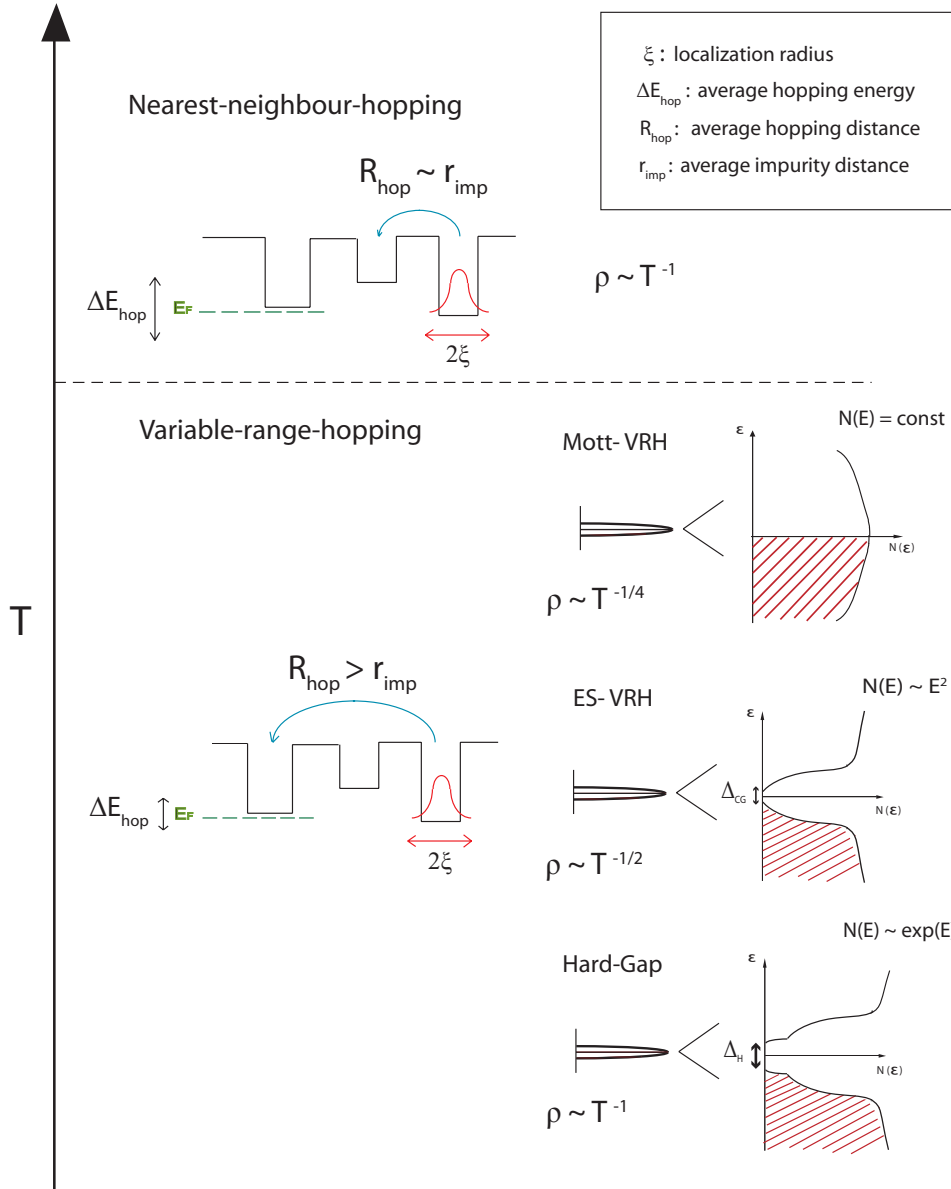


Figure 1.18: Overview of the hopping regimes as a function of temperature. The characteristic features of each scenario are highlighted.

Résumé

As suggested in the beginning of the section, analyzing the temperature dependence of the resistivity in a lightly doped semiconductor opens up the possibility to study a variety of electronic transport processes. An overview of the transport regimes as a function of temperature is presented in Fig. 1.18. The occurrence of a crossover between the different regimes substantially changes the underlying physics of the electronic transport, which are reflected in the characteristic quantities. In particular,

when the dopants induce strongly localized states, i.e., the electronic transport is dominated by hopping within an impurity band, the inferred characteristic quantities provide a way to describe and model the impurity band without making use of *ab-initio* calculations. With this knowledge, important conclusions about the nature of the impurities present in the host semiconductor can be drawn.

1.2.6 Band and Hopping conduction under magnetic fields: The Hall-Effect

In the presence of a magnetic field, the free carriers which contribute to electrical transport experience a deviation in their trajectory, due to the Lorentz-force

$$\vec{F} = q \cdot \vec{v} \times \vec{B} \quad (1.92)$$

which is maximal when the external magnetic field \vec{B} is applied perpendicular to the carrier direction of motion (given by the carrier velocity \vec{v}) and vanishes when \vec{B} is applied parallel to it. The absolute value of q is the elementary charge and its sign depends on the carrier type. If the carrier current is flowing in the x -direction, with a magnetic field applied in z -direction, the Lorentz-force will bend the trajectories of the carriers and thus produce an electrical field in y -direction, called also *Hall-field*. This phenomena is not as simple as it seems from the first impression, since the carriers will be exposed, during their trajectory, to different collision mechanisms, already described in section 1.2.1. Therefore, a complete description of the kinetics of the electrons (equation of motion) has to be considered.

Assuming that the transport mechanism in a semiconductor is governed by only one type of carriers (e.g electrons), the system can be treated in the one-band model. Considering the linearized Boltzmann equation as the most suitable equation of motion for the description of traveling electrons which are exposed to collisions, in the presence of an electric field \vec{E} and a magnetic field \vec{B} , the following relation is obtained:

$$\vec{E} = \rho_0 \vec{j} + \frac{e\tau}{m} \rho_0 (\vec{B} \times \vec{j}) \quad (1.93)$$

where \vec{j} represent the current density of the electrons, τ is the time between collisions (see section 1.2.1) and ρ_0 is the resistivity of the semiconductor in the absence of a magnetic field. From Eq. (1.93) it can be clearly concluded that the electrical field \vec{E} needed to produce the electron current has to be divided in two components. The component parallel to the current \vec{j} is given through the relation

$$E_{parallel} = \rho_0 J \quad (1.94)$$

which corresponds to Ohm's law. In the parallel configuration, the resistivity is not influenced by the magnetic field, which means that there is no magnetoresistive effect. In the transversal component E_H (*Hall-field*)

$$E_H = \frac{e\tau}{m} \rho_0 B J \quad (1.95)$$

there is indeed a change in the resistivity. Comparing Eq. (1.95) with Ohm's law, the hall resistivity can be obtained as the proportionality factor between E_H and J

$$\rho_{xy} = \frac{E_H}{J} = \frac{e\tau}{m}\rho_0 B \quad (1.96)$$

Using the definition of the conductivity in absence of a magnetic field and considering only electrons as carriers, namely $\sigma_0 = \rho_0^{-1} = \frac{ne^2\tau}{m}$ in order to eliminate the relaxation time, a very useful relation is obtained:

$$\rho_{xy}(B) = \frac{B}{ne} \quad (1.97)$$

The field dependence of the hall resistivity can be measured experimentally. As it can be seen from the equation, there will be a linear proportionality between ρ_{xy} and B . The carrier concentration is obtained through the slope of the linear function $\rho_{xy}(B)$ and the type of carrier is determined through its sign. The factor $(1/ne)$ is called *Hall-coefficient* or *Hall-constant*. With the relation $\sigma = ne\mu$, the Hall-mobility can be expressed in terms of the Hall constant:

$$R_H = \frac{1}{ne} \quad (1.98)$$

$$\mu_H = \frac{\sigma}{ne} = \sigma R_H \quad (1.99)$$

This calculations in the one-band model have indeed their limitations. As soon as there are holes which are also contributing to the electrical transport, the model has to be extended. The holes will be affected by the external magnetic field in a different way than electrons. Because of the positive charge, the holes will create a Hall-field in the opposite direction, thus compensating the field created by the electrons. It is worth to mention that this compensation is not symmetric. Even the specific case of an n-and p-doped semiconductor with equal number of donors and acceptors would not decrease the Hall-field to zero, due to the different effective masses and mobilities. In Hall-effect measurements, these compensation effects may be the first suspects, if, for example, the measured Hall-voltage has a very low value despite a higher expected carrier concentration. The experimental interpretation of the Hall-Effect in a doped semiconductor is therefore not an easy issue, and it should be submitted to a careful analysis.

In addition, considering the case where band- and hopping conduction are coexistent, the Hall-resistivity, the Hall-coefficient R_H and hence the mobility will not behave according to equations (1.98,1.99). In order to describe the process, the electrons participating in electrical conduction are divided into two groups: conduction band electrons (σ_c, R_c) and impurity-band electrons with hopping conductivity σ_h and Hall coefficient R_h . A simple phenomenological calculation [83] gives the following expression for the observable Hall coefficient:

$$R = \frac{R_c\sigma_c^2 + R_h\sigma_h^2}{(\sigma_c + \sigma_h)^2} \quad (1.100)$$

The hopping Hall-mobility $\mu_h = R_h \sigma_h$ is expected to be much smaller compared to the band mobility $\mu_c = R_c \sigma_c$. For $\sigma_c \gg \sigma_h$, the equations (1.98), (1.99) are recovered. At $\sigma_h \approx \sigma_c$, the conductivity mechanism changes from band to hopping. When the hopping conductivity is dominant ($\sigma_c \ll \sigma_h$), the total Hall-coefficient can be expressed as

$$R = \frac{R_c \sigma_c^2}{\sigma_h^2} = \frac{\mu_c e}{\sigma_h^2} n(T) \quad (1.101)$$

In turn, measuring the Hall-coefficient in the region where hopping conductivity dominates, does not allow to separate the Hall-mobility μ_h and the hopping Hall-coefficient R_h from the conductivity σ_h . Another possibility is to consider the regime of very low temperatures, where the carriers cannot be any longer transported to the conduction band, i.e., when the conductivity is entirely determined by hopping transitions between localized states. Theories of the Hall-effect in the nearest-neighbor-hopping (NNH) [84] and variable-range-hopping (VRH) regime [85, 86] have been proposed. The approach to solve the Hall-conductivity problem was the same as the longitudinal conductivity: to find the critical subnetwork of (transversal) hopping transitions in a Miller-Abrahams random resistor by means of the percolation method. The relevant hopping transitions were calculated considering the interference mechanism developed by Holstein [87], which suggests that the observation of an ordinary Hall-effect in hopping conductors requires at least *triads* of sites and a magnetic flux through the triangles (polygons) formed by the sites. It was shown that the transition probability Γ_{ij} contains an additional contribution $\delta\Gamma_{ij}^H$ which is linear in the magnetic field, arising from the interference between the amplitudes of a direct ($i \rightarrow j$) and indirect ($i \rightarrow k \rightarrow j$) transition. The scenario is depicted in Fig. 1.19.

The magnetic field induces an Aharonov-Bohm phase for the electrons that are transported around the triangle, such that the transition probabilities Γ_{ij} and Γ_{ji} are not equal, creating an imbalance of populations of sites i and j . The balance is restored by the emergence of an additional potential difference $\Delta\mu_{ij}$ which is manifested as a Hall-voltage. The Hall-current flowing between i and j is thus given by

$$J_{ij}^H = e(\delta\Gamma_{ij}^H - \delta\Gamma_{ji}^H) \quad (1.102)$$

which is the same expression as (1.33) with the index H to denote that the current is transversal to the applied electric field. Taking into account these concepts, the r_{ij} -percolation problem (where the transition probability only depends on the separation-NNH)[84] and the percolation problem with site and energy disorder (VRH)[85, 86] have been solved. The main result was that the hopping Hall-mobility was many orders of magnitude smaller than the longitudinal mobility μ_0 , and in particular, showed a decay with temperature in the variable-range-hopping regime [86], as

$$\mu_H \propto \exp(-T_0^H/T)^{1/4} \quad (1.103)$$

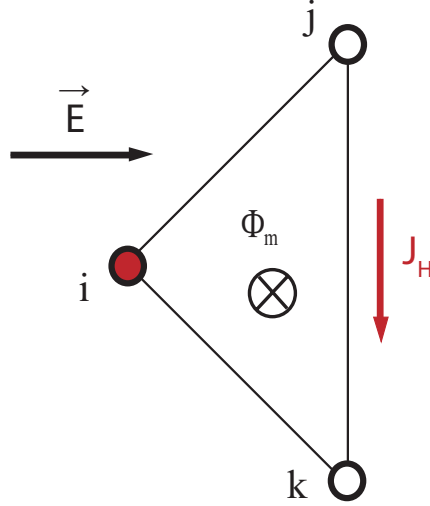


Figure 1.19: Minimal triad configuration for the emergence of a hopping current J_H transversal to the electric field. The interference of direct $i \rightarrow j$ and indirect (over the site k) transitions gives rise to a current contribution which is linear in magnetic field. The magnetic flux through the triangle causes an imbalance of hopping probabilities for a $i \rightarrow j$ and a $j \rightarrow i$ transitions.

where T_0^H is the characteristic temperature of the longitudinal resistivity appearing in Mott's law reduced by a factor of 50, according to [86].

Nevertheless, the experimental observation of the Hall-voltage as an exclusive effect of hopping electrons in the regime where band- and hopping transport are coexistent, as well as in the variable-range-hopping regime (where the Hall-resistance becomes very high due to the low mobility) has remained a challenge in lightly doped semiconductors [88, 89]. Furthermore, the sign of the Hall-coefficient is not unambiguously determined by the sign of the charge carrier, since it depends not only on the geometrical arrangement of sites but also on the nature (s,p-like) and relative orientations of the involved orbitals where the carriers are able to hop [90].

In summary, the evaluation of the Hall-effect becomes complicated as the electronic transport by hopping dominates against band conduction. The low Hall-mobility in the variable-range-hopping regime hinders the experimental analysis of the linear dependence of the transversal conductivity with magnetic field predicted by the theory, whereas the non-straightforward sign determination of the Hall-coefficient does not allow to ascribe electrons or holes as the majority carriers.

2. Experimental methods

This chapter presents a brief description of the major considerations which should be taken into account by performing reliable electrical transport measurements. In particular, the fabrication of ohmic contacts which hold for a broad range of sample resistances, as well as the sample preparation prior to the measurement, are presented. Standard characterization techniques as X-ray diffraction (XRD), energy dispersive X-ray spectroscopy (EDX), secondary ion mass spectroscopy (SIMS) or superconducting quantum interference device (SQUID) can be numerous found in literature and are therefore not the main scope of this chapter. A short presentation of the sample series which have been grown by molecular beam epitaxy (MBE) is also given, since their characterization is the main subject of this work. The classification of the samples -according to the substrate used for growth- is defined, which should serve as an orientation along the last chapter.

2.1 Substrate choice

In epitaxial growth processes, it is well known that the substrate choice for a given material is a very important issue. One distinguishes thereby between *homoepitaxial* (lattice-matched) and *heteroepitaxial* (lattice-mismatched) growth, being the former the optimal starting point to achieve excellent properties in terms of crystalline quality. The most common substrates for GaN epitaxial growth are Al_2O_3 , AlN, SiC and GaN-bulk crystals. However, depending on the techniques which might be applied to characterize the epitaxial layers, the choice of a lattice-matched substrate is not always suitable. For instance, homoepitaxial growth of GaN is not optimal for X-ray-diffraction characterization (XRD), since the reflections from substrate and epitaxial layer are at the same angular positions, so that slight changes in the crystal parameters of the epilayer are difficult to be extracted. On the other hand, the measurement of small magnetic signals (e.g. in dilute magnetic semiconductors by means of SQUID) requires that the large substrate volume contains a negligible contamination of magnetic impurities, especially if the thickness of the epitaxial layer is very short or if the magnetic doping is in the highly-diluted limit. Last but not least, for electrical transport measurements, it is desirable that the substrate possess a very high resistance in order to enable a broad conductivity range in which the epitaxial layer can be characterized without parallel conduction effects.

Since it is very difficult to find a substrate which fulfills all the aforementioned conditions, Mn- and Gd-doped GaN, as well as unintentionally doped GaN epitaxial layers have been grown on five different substrate types. The suitability of the main characterization methods performed in this work, depending on the substrate choice, is summarized in Table 2.1.

Series	Substrate type	XRD	SQUID	el.Transport
(A)	MOCVD-GaN/ Al_2O_3 (Lumilog)	-	+	- -
(B)	6H-SiC (Sterling)	++	+	+
(B)	6H-SiC (Dow Corning)	++	+	++
(C)	MOCVD-GaN:C/ Al_2O_3 (IAF)	-	+	++
(C)	MOCVD-GaN:Fe/ Al_2O_3 (IAF)	-	-	+

Table 2.1: Substrates which have been chosen for the growth and characterization of Mn- and Gd-doped GaN. The suitability is encoded as follows: (++) optimal, (+) useful, (-) doable (- -) unreliable

According to these considerations, the samples are classified in three groups. Series A, grown homoepitaxially on conductive GaN-templates, Series B, grown heteroepitaxially on highly-resistive 6H-SiC(0001), and Series C, grown homoepitaxially on highly-resistive (doped) GaN-templates. Note that the series labeling (A→C) corresponds to the chronology on the substrate acquisition, so that the majority of the available samples are from Series A and B. For series C, the samples grown on GaN:Fe/ Al_2O_3

consist of just one or two cross-check references for electrical measurements, so that they will be completely omitted for the rest of the discussion.

All samples have been grown by plasma-assisted molecular beam epitaxy (MBE). The GaMnN layers (Series A,B and C) have been grown in a commercial *Varian Mod Gen II* facility, with a base pressure of $p \leq 7 \times 10^{-11}$ mbar, and at a substrate temperature of $T_s = 770^\circ\text{C}$. In comparison, the GaGdN layers (Series A and B) have been grown in a custom-build MBE-facility (*ELSA*), with a base pressure of $p \leq 1 \times 10^{-10}$ mbar and a substrate temperature of $T_s = 763^\circ\text{C}$. For the samples grown on MOCVD-templates, the substrates were outgassed for 10h at a temperature of 650°C to achieve a clean surface prior to growth. On the other hand, the 6H-SiC substrates were subjected to a more careful treatment, due to the affinity of the material to form an oxide at the surface, which might affect the nucleation process in the early stage of growth. Before loading the substrate in the vacuum chamber, the substrate was immersed in a HF (50%) solution (2 minutes). In the vacuum chamber, prior to growth, the 6H-SiC substrates are annealed at 900°C and subjected to a Ga-cleaning procedure [91], in order to remove the last oxygen traces from the surface by the formation of volatile GaO_2 . The optimization of the growth conditions will be discussed in section (3.1).

2.2 Preparation of Ohmic contacts

Given the importance of the wide-gap semiconductor GaN in optical and electronic devices, such as light-emitting diodes (LEDs) or high-mobility electron transistors (HEMTs), the preparation of low-resistance ohmic contacts is a state-of-the-art issue. However, most of the ohmic contacts are prepared on highly conductive n-type (or p-type) GaN, which are the most common epilayers in the industrial processes. It is well known that the realization of ohmic contacts is sensitive to the position of the Fermi-level in the semiconductor, so that a universal recipe which holds for a broad range of conductivities is not automatically given. Ti/Al based multilayers, have been found to be the most suitable materials to prepare ohmic contacts in n-type GaN and are known more than a decade ago [92]. The formation of the alloy TiN upon annealing creates a degenerate n-type GaN region, owing to the large amount of nitrogen vacancies at the GaN/TiN interface, forming a low resistance ohmic contact. A third barrier layer is usually deposited in order to prevent the outdiffusion of Al to the surface, which might degrade the contact characteristics. Au deposition is used to cap the surface.

By measuring the *IV*-characteristics of a set of GaN epitaxial layers (both conductive and highly-resistive samples), good ohmic contacts were obtained with the multilayer (Ti/Al/Ti/Au) in two different thickness configurations: (30/160/40/40)nm and (22/45/30/40)nm, being the former the most reliable up to high resistances. The Ti/Al/Ti metal stack was deposited by electron beam evaporation, and the Au cap layer by thermal evaporation in a commercial evaporation (*Univex 350*) chamber with

a base pressure of with a base pressure of $p \leq 10^{-6}$ mbar. The contacts were annealed in a rapid thermal annealing (RTA) facility at 850 °C during 30 s. Fig. 2.1 shows the IV -characteristics of a conductive and a highly-resistive GaN layer, indicating that the ohmic behavior holds at such high resistances.

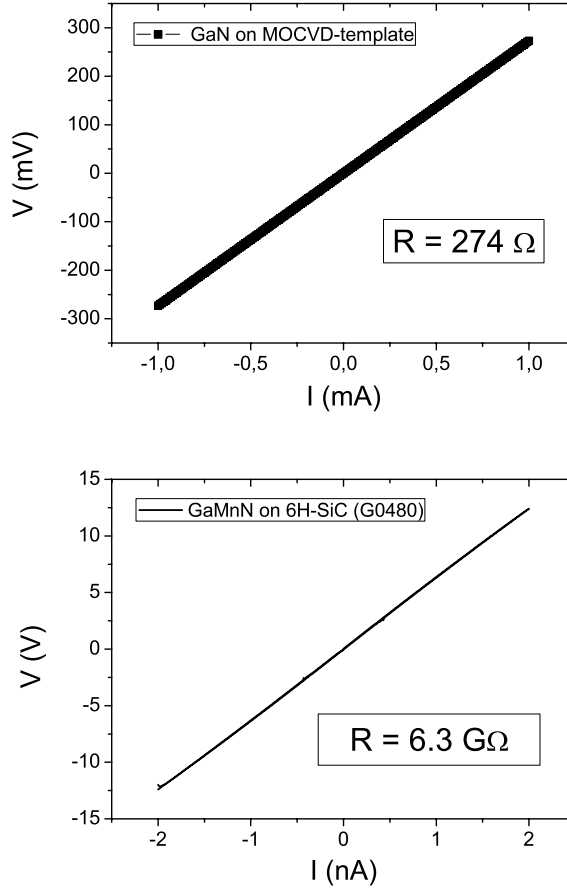


Figure 2.1: IV -characteristics of a n-type conductive GaN (top) and a highly-resistive GaMnN sample (bottom). Note that the linear behavior holds up to high resistances. The GaMnN layer (G0480) is the most insulating sample investigated in the present work.

The importance of reliable ohmic contacts for performing electrical transport measurements is evident: The measured resistance will not change by performing the measurement at different voltages, so that the dependence of the resistance on external parameters, such as the temperature or the magnetic field, can be analyzed in a systematic way.

2.3 Four-point resistance measurements

Resistance measurements are typically performed using four-point terminals to cancel the effect of contact resistance. The most common geometries to measure the resistivity and the Hall-voltage, are the *van der Pauw* and the *Hall-bar* geometry. While the former has the advantage of a fast sample preparation, the latter, due to its reduced dimensions, allows to locally probe the electrical properties of the sample. Both methods have been used in the present work and will be described in the following sections.

2.3.1 The van der Pauw method

The pioneering work of L. J. van der Pauw [93] showed that it is possible to measure the specific resistivity and the Hall effect on a sample of an arbitrary shape, which has to fulfill following conditions:

- a constant thickness in the region of interest
- an uninterrupted surface area

For the contacts, following considerations have to be taken:

- they have to be small compared to the sample dimensions
- they have to be placed on the sample edges

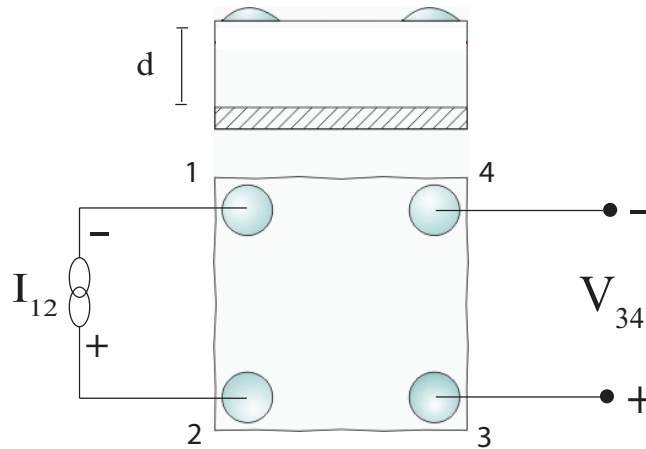


Figure 2.2: Sketch of a contacted sample in the van der Pauw geometry. While the surface dimensions are not important, the thickness d has to be constant in the region of interest. The notation of current and voltage corresponds to the resistivity measurement configuration. For the Hall-Effect, the voltage is measured perpendicular (2-4) to the applied current (1-3).

Fig. 2.2 shows a sketch of a contacted sample in the van der Pauw geometry. Using the defined contact numeration, the resistivity is equal to

$$R_{2134} = \frac{U_{34}}{I_{21}} \quad (2.1)$$

where the indexes denote the directions of current flow and the polarity of the measuring electrodes. According to [93], the conductivity is defined as

$$\sigma = \frac{\ln 2}{\pi d} \frac{2}{R_{2134} + R_{3241}} [f(Q)]^{-1} \quad (2.2)$$

where

$$Q = \frac{R_{2134}}{R_{3241}} \quad (2.3)$$

f is a correction factor for the geometrical asymmetry (not for material anisotropy or inhomogeneity), that depends on the symmetry factor Q , defined as the ratio of the resistivities for two pairs with a common contact. For an ideal square sample, the symmetry factor is $Q = 1$. Good sample preparation will routinely achieve a value less than 1.2, although values of Q up to 1.5 will still yield reasonable measurements. Values of $Q > 1.5$ are usually a result of badly defined van der Pauw patterns, non-Ohmic contacts or anisotropic samples. A rectangular sample will naturally have values of $Q > 1$ so that for these samples the symmetry factor cannot be used to monitor sample quality. The correction factor f can be obtained using following approximation

$$f \cong 1 - 0.34657 A - 0.09236 A^2 \quad (2.4)$$

where

$$A = \left[\frac{Q - 1}{Q + 1} \right]^2 \quad (2.5)$$

This approximation holds for samples which do not show a large asymmetry ($Q < 10$). In order to reduce non-symmetry effects to the calculation of the resistivity, it is useful to average the resistivity over all possible permutations of the four contacts with the respective forward and reverse current directions. So the resistivity takes the form

$$\rho = \frac{\pi d}{\ln 2} \frac{1}{8} [(R_{2134} - R_{1234} + R_{3241} - R_{2341})f_A + (R_{4312} - R_{3412} + R_{1423} - R_{4123})f_B] \quad (2.6)$$

where the correction factors f_A and f_B are given according to the definition in Eq. 2.4, and the symmetry factors Q_A and Q_B account also for the reverse current direction. An analogous treatment is applied for the Hall-Effect measurement. Thereby, the Hall-voltage is measured perpendicular to the current, and averaged over all possible

permutations taking into account both current and magnetic field polarities. The Hall-coefficient can be calculated as

$$R_H = \frac{1}{8} \frac{d}{B_z} [(R_{3142}(B+) - R_{1342}(B+) + R_{1342}(B-) - R_{3142}(B-)) + (R_{4213}(B+) - R_{2413}(B+) + R_{2413}(B-) - R_{4213}(B-))] \quad (2.7)$$

2.3.2 Hall-bar geometry

Unlike the van der Pauw method, where the average over many configurations is required, the resistivity and the Hall-Effect in a *Hall-bar* structure can be obtained by measuring a single voltage (V_{xx}, V_{xy}), respectively. While the measurement analysis is simpler than in the van der Pauw geometry, the preparation of *Hall-bar* structures requires in general four different process stages:

- Optical lithography (Contact pattern)
- Contact deposition with subsequently Lift-Off
- Second optical lithography run (MESA pattern)
- Etching process (insulation)

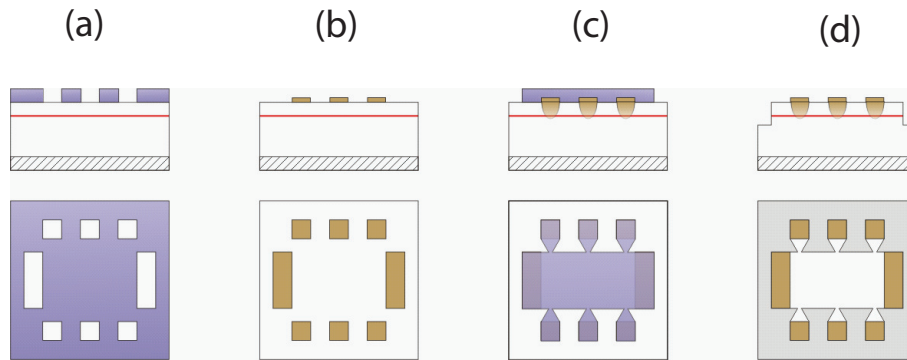


Figure 2.3: The four steps for a Hall-bar preparation: (a) Pattern for contact deposition via optical lithography (b) contact deposition and lift-off (c) MESA-structure (d) Insulation through etching process.

These four basic steps are schematically depicted in Fig. 2.3. To ensure optimal conditions, the preparation is carried out in a clean-room facility. Optical lithography is a technique which enables to pattern structures on sample surfaces, via UV-light irradiation of a resist layer. Before exposing the sample to light irradiation, a thin layer of photo-resistive material (Photolack AR-3510) was deposited on the film surface and distributed homogeneously by means of a spin coater, to be finally heated

at 110°C (hard baking). The resist layer will chemically react to the UV-light, so that the exposed areas will be exempt from the resist layer after developing (positive resist). This step is performed using a mask-aligner (SUSS MJB4).

The lithography process is used to select the area either where the contacts should be placed (Fig. 2.3(a)), or to pre-pattern the MESA-structure to account for the insulation between the contact arms (Fig. 2.3(c)). The insulation is achieved via reactive-ion etching (RIE). Optical micrographs of Hall-bar structures after the four preparation steps are shown in Fig. 2.4.

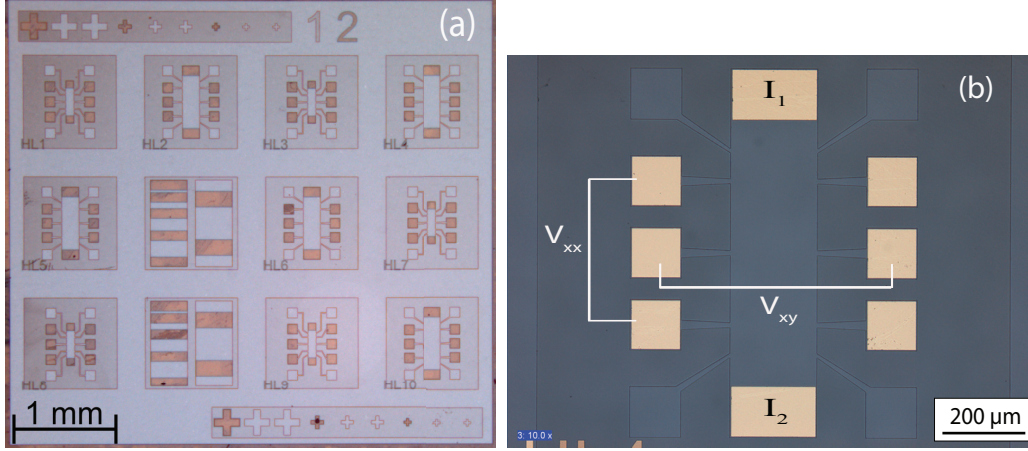


Figure 2.4: (a) Overview of Hall-bar structures used in the present work. (b) Hall-bar structure after the four preparation steps, ready to be contacted (right).

Besides the current contacts which are located at the top and the bottom of the Hall-bar, just four contacts are needed to perform both resistivity and Hall-Effect measurements: two for the voltage V_{xx} parallel to the current, and two for the voltage V_{xy} perpendicular to the current. The darker regions in the picture (Fig.2.4(b)) correspond to the etched material. For a reliable measurement, there should be no cross-talk between the contacts. Therefore, the choice of an insulating substrate should be strongly taken into consideration.

2.3.3 Measurement Set-Up

Prior to the measurements, the samples, either prepared in the van der Pauw or Hall-Bar geometry, have to be mounted in the sample holder and contacted to the measurement electronics. The samples are mounted on a chip carrier and contacted with a commercial wedge bonder, using thin aluminum wires ($d = 50\mu\text{m}$). The set-up is sketched in Fig. 2.5.

Temperature and field- dependent measurements were performed in a custom-build continuous flow cryostat (4K-320K), equipped with an electromagnet allowing field-dependent measurements up to 1 T (Fig. 2.5). DC-measurements were performed

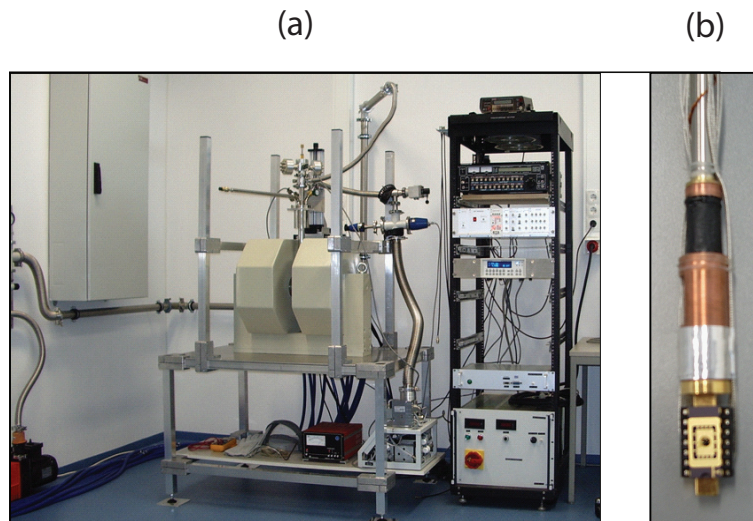


Figure 2.5: Measurement set-up (a) and sample holder with inserted chip carrier (b).

using a precision current source (Keithley 6220)¹ and a multimeter (Keithley 2000), up to high resistances ($\approx 1\text{T}\Omega$). For conductive samples ($R \leq 1\text{M}\Omega$), a physical property measurement system (PPMS) was alternatively used for high-field measurements (up to 9 T) or to perform resistivity measurements at very low temperatures (2-4 K).

¹output resistance: $\geq 10^{14} \Omega$, resolution: 0.1 pA

3. Experimental Results and Discussion

In this chapter, the effect of Mn- and Gd-incorporation on the structural, magnetic and electrical transport properties will be presented and discussed. While the structural and magnetic properties of reference undoped samples will be considered directly within the discussion of Mn- and Gd-doped GaN, a separate section is devoted to the electrical transport properties of as-grown GaN epilayers. Thereby, the identification of the dominating defects and the resulting transport mechanisms is on the foreground. The change of electronic transport behavior owing to Mn- and Gd-doping will have important implications on the nature and magnitude of the observed magnetic interactions. In addition, some preliminary characterization results of $\text{Mn}_x\text{Ga}_{1-x}$ ferromagnetic layers epitaxially grown on GaN will be presented in the last section, in view of spin-injection from the ferromagnet into the semiconducting GaN.

3.1 Undoped GaN

Recalling section (1.1), where the defect formation landscape in GaN was discussed in great detail, the n-type conductivity observed in as-grown GaN was ascribed to the incorporation of residual impurities, such as oxygen or silicon. However, it has been argued that the growth conditions (e.g. pressure, carrier gases, III/V molar ratio) determine the availability of residual impurities. In particular, the surface potential, i.e., the location of the Fermi-energy during growth, has to be considered for an accurate interpretation of the thermodynamical approaches concerning the defect formation energies. The reference GaN samples were grown by plasma-assisted molecular-beam-epitaxy (MBE) on both MOCVD-GaN/Al₂O₃ and GaN:C/Al₂O₃ templates as well as 6H-SiC(0001) substrates at a temperature of $T_s=760^\circ\text{C}$. The base pressure in the growth chamber was $p \leq 1 \times 10^{-10}\text{mbar}$. The III/V flux ratio was adjusted in the range where the best structural and morphological properties are found, which corresponds to the Ga-rich regime near the stoichiometrical point, denoted as the intermediate regime in Fig. 3.1. Furthermore, the optimal surface morphology is found when exactly two monolayers of Ga are present at the surface during growth, condition which is often described as the „bilayer point“. A further Ga-enrichment leads to a Ga-metal accumulation in form of droplets. These conditions have been already studied within our group and more details can be found in Refs. [33, 94, 95]; however, they are briefly recalled to complete the description of the growth scenario for an optimal connection to the thermodynamic predictions introduced in section (1.1).

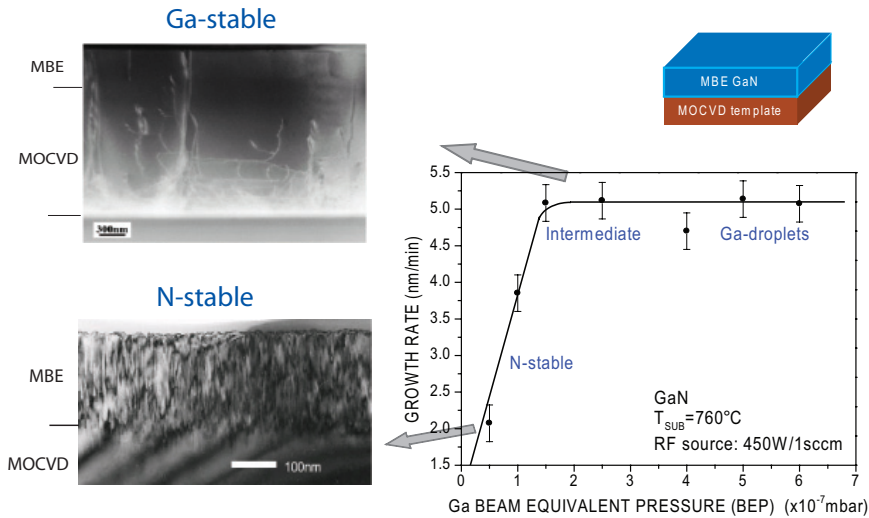


Figure 3.1: Transmission electron micrographs (TEM) of GaN epilayers grown at different conditions, showing a remarkable decrease in dislocation density when going from the N-rich to the intermediate, slightly Ga-rich regime. The III/V flux ratio is controlled by the Ga-beam equivalent pressure (BEP) at constant N-plasma conditions, taken from [33].

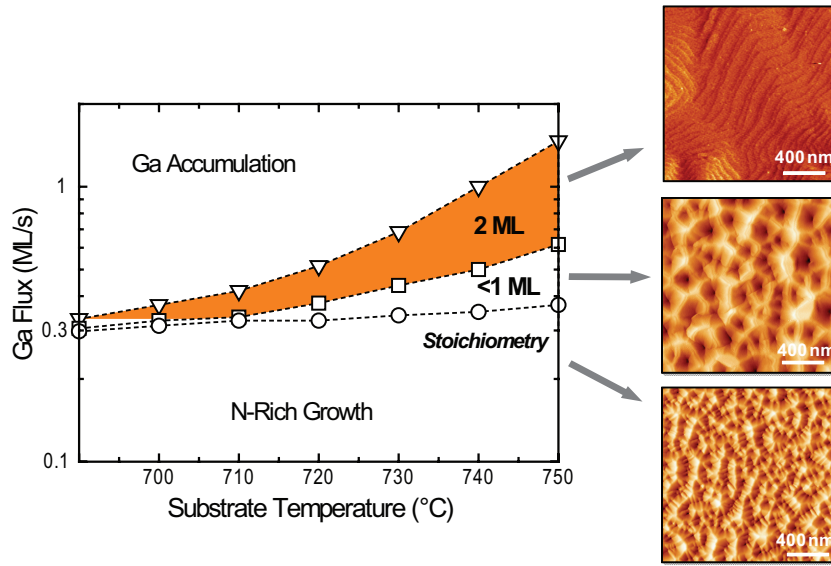


Figure 3.2: Atomic force micrographs (AFM) indicating an improvement in the resulting surface morphology when the Ga- surface coverage during growth amounts to two monolayers (2ML), taken from [33].

Only samples grown directly either on semi-insulating 6H-SiC(0001) or GaN:C/Al₂O₃ have been considered for electrical transport characterization, so that multi-layer and interface contributions to the conductivity [96] can be avoided. Two 6H-SiC substrate batches have been used in the present work, acquired from the company Sterling (SiC-ST) and Dow Corning (SiC-DowC). Their resistivities differ by a few orders of magnitude, being the batch from Dow Corning the most insulating. The GaN:C/Al₂O₃ substrates were provided by the Fraunhofer Institute (IAF), and showed unmeasurable resistances below 300 K. Recall that for avoiding parallel channel conductivity, not the resistivity, but the resistance R of the substrate has to be much higher than the one from the epilayer. Fig. 3.3 shows the resistances of all the substrates used in this work, compared to a GaN epilayer grown on SiC, which clearly shows that the measured resistance in a typical GaN/SiC sample has to come from the epilayer.

The temperature dependence of the resistivity and the Hall-Effect of unintentionally doped GaN layers have been measured between 5 K and 300 K. In order to have an insight of the carrier transport mechanisms which may occur, it is often instructive to plot the resistivity against the inverse temperature ($1/T$). In the introductory part (see Fig. 1.6), the semiconductor germanium with a donor concentration of $\approx 10^{15} \text{ cm}^{-3}$ was exemplified, since it exhibits the main four conduction ranges at experimentally accessible temperatures. In the case of unintentionally doped GaN, depicted in Fig. 3.4, the crossover from hopping to single-activated transport is observed. A hopping activation energy of 0.51 meV could be fitted between 4.5 and 10 K. It should be remembered that hopping conductivity with a constant activation energy resembles the case of nearest-neighbor-hopping (NNH). At low temperatures, it can

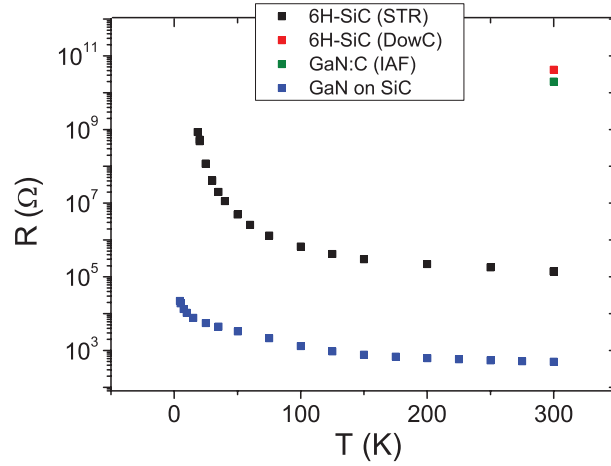


Figure 3.3: Temperature dependence of the resistance of GaN grown on 6H-SiC(0001), which is around three orders of magnitude lower than the 6H-SiC(ST) substrate. The 6H-SiC (DowC) and GaN:C/Al₂O₃ (IAF) substrate batches were not measurable below 300 K.

be thus concluded that the electronic transport in GaN occurs by hopping between neighboring (donor) defect states. The occurrence of hopping conduction within a donor impurity band has been also observed by Look *et al.*, both in unintentionally doped MOCVD-GaN [34] and in N-rich grown MBE-GaN samples [97].

At higher temperatures, it can be observed that the resistivity shows another linear dependence, characteristic of the thermal activation of electrons from the donor states to the conduction band, as shown in Fig. 3.4. In fact, the activation energy can be better quantified by measuring the temperature dependence of the carrier concentration $n(T)$ by means of the Hall-Effect. Fig. 3.5 shows the results of the $\ln(|n|)$ vs T^{-1} fit, yielding an activation energy of $\Delta E = E_c - E_d = (20.3 \pm 0.6)$ meV. For better accuracy, the data has been fitted in the temperature range which lies outside the crossover-regime, so that the hopping contribution to the conductivity can be neglected. Note that, for clarity, the y-scale in Figs. 3.4 and 3.5 is shown as $\log(\rho)$ and $\log(|n|)$, respectively. The sign of $|n|$ is negative, confirming electrons as majority carriers.

The activation energy was fitted according to the charge neutrality equation (1.8), assuming a negligible concentration of compensating acceptors. In order to evaluate the validity of this assumption, we recall the defect formation scenario depicted in Figs. 1.2 and 1.4. First, the existence of the „freeze-out“ range at 300 K implies that not all the donors have been ionized, i.e., that the Fermi energy lies between the donor state and the conduction band. Second, the free carrier concentration at 300 K amounts to $n = 5.8 \times 10^{17} \text{ cm}^{-3}$, suggesting a donor concentration $N_D \geq n$, since the saturation range has not been reached yet. Both arguments rule out the native vacancy V_N as the dominant donor, because the position of the Fermi-energy near the conduction band reduces the probability that V_N defects appear in

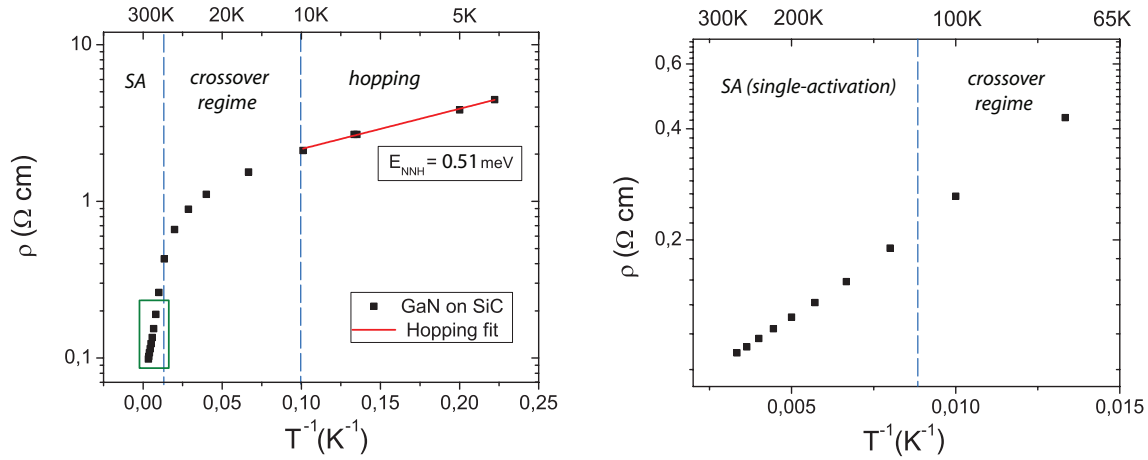


Figure 3.4: Logarithm of the resistivity against the inverse temperature T^{-1} , giving an overview of the present carrier transport mechanisms in as-grown GaN on 6H-SiC (left). At low temperatures, nearest-neighbor-hopping between donors is observed, and as the temperature is increased, the conduction changes from hopping to thermal activation to the conduction band, inferred from the linear relationship at high temperatures (right).

appreciable concentrations. Concerning the formation energies of residual impurities, the incorporation of either O_N or Si_{Ga} would be consistent with the observed shallow activation energy. Taking the acceptors into account, the formation energies of V_{Ga} and $V_{Ga}-O_N$ defects are the lowest at n-type conditions, so that they are expected to be the main compensation centers (the concentration of C_N impurities is expected to be negligible). The presence of single vacancies (V_{Ga}) and vacancy complexes ($V_{Ga}-O_N$) in n-type samples grown by MBE, MOCVD and HVPE have been confirmed by positron annihilation spectroscopy (PAS) studies [40, 41, 42, 98]. Oila *et al.* [98] investigated the effect of Si- and O-doping on the formation of V_{Ga} , and found that the incorporation of Si_{Ga} suppressed the formation of gallium vacancies ($[V_{Ga}] \leq 10^{16} \text{cm}^{-3}$) within a doping level range of $[Si] = 10^{17} - 5 \times 10^{18} \text{cm}^{-3}$, whereas for unintentionally doped as well as for oxygen-doped samples the vacancy concentration was detectable and ranged between $10^{17} \text{cm}^{-3} - 10^{18} \text{cm}^{-3}$. In collaboration with the Aalto University in Finland (the same research group who has extensively studied vacancy defects in GaN cited in the references above), positron annihilation spectroscopy measurements have been performed in our unintentionally doped samples ¹, yielding a vacancy concentration in the mid 10^{16}cm^{-3} range. The detectable concentration of vacancies suggests that not Si_{Ga} , but rather substitutional oxygen impurities (O_N) are the dominant donors in our as-grown samples. Furthermore, since the MBE growth technique does not make use of carrier gases or metal-organic compounds, a possible Si contamination of the sample might rather occur if the Ga-source is not very pure.

¹in fact, the purpose of the study was to investigate the correlation between V_{Ga} formation and Gd-doping in GaGdN, for which reference GaN samples had to be measured.

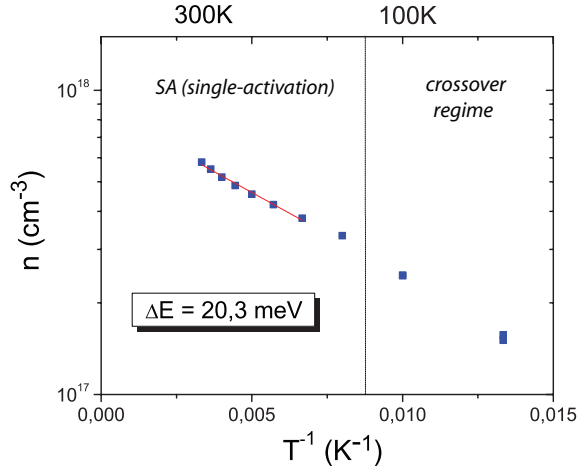


Figure 3.5: Temperature dependence of the carrier concentration n (Arrhenius-Plot). The slope yields an activation energy of $\Delta E = (20.3 \pm 0.6) \text{ meV}$, assuming the existence of a single dominant donor and a negligible acceptor concentration. The data from the crossover regime has been not considered.

According to the specified purity (6N) of the Ga-ingots which are evaporated from the MBE-effusion cells, the concentration of residual impurities is estimated to be less than $4 \times 10^{16} \text{ cm}^{-3}$, so that Si_{Ga} impurities are unlikely to be responsible for the n-type conductivity in our samples. Regarding possible compensation effects of the charged acceptors, V_{Ga} defects should trap three electrons from each donor, whereas $V_{\text{Ga}}\text{-O}_\text{N}$ complexes just two. The concentration of Ga-vacancies measured by PAS ($\approx 10^{16} \text{ cm}^{-3}$) is rather low for a donor concentration of $N_d \geq 6 \times 10^{17} \text{ cm}^{-3}$, since the n-type conditions should promote the Ga-vacancy formation. A quantitative analysis of the PAS-measurements [99] showed that instead of single V_{Ga} point defects, rather vacancy clusters containing 3-4 V_{Ga} and a comparable number of nitrogen vacancies (V_N) were present in unintentionally doped GaN layers grown both on 6H-SiC and MOCVD-GaN. These open-volume defects ($V_{\text{Ga}}\text{-}V_\text{N}$) are supposed to be electrically inactive, hence having a negligible compensation effect. However, they might represent an additional source of electron scattering and would explain the rather low mobilities ($\approx 100 \text{ cm}^2 \text{ V}^{-1} \text{ s}^{-1}$) which are observed in these samples.

Following these considerations, it can be concluded that (i) O_N is the dominant donor in our MBE-grown GaN samples, with a concentration of $N_D \geq 5.8 \times 10^{17} \text{ cm}^{-3}$ estimated from the room-temperature free carrier concentration n measured by Hall-Effect, (ii) the concentration of a second potential donor, Si, is estimated to be less than $4 \times 10^{16} \text{ cm}^{-3}$, and (iii) the main compensating acceptors are supposed to be the Ga-vacancies or $V_{\text{Ga}}\text{-O}_\text{N}$ complexes, whose concentration are in the mid 10^{16} cm^{-3} , but it has been inferred from PAS-measurements that these V_{Ga} defects exist in form of clusters (with comparable concentration of V_N), being electrically inactive. As a consequence, the fitting of the carrier concentration in a single-donor model with

negligible compensation is a good approximation. The activation energy which corresponds to O_N yields (20.3 ± 0.6) meV. However, it is known that the energy difference between two bands may differ, depending if it is inferred from thermal activation or optical probing [100]. For thermally activated transport, screening effects lead to the obtention of a lower donor activation energy than the actual donor binding energy E_{D0} . The donor concentration plays thereby an important role and is considered in the following relation [34]:

$$E_D = E_{D0} - \beta N_D^{1/3} \quad (3.1)$$

where $\beta = 2.1 \times 10^{-5}$ meV cm [101]. Setting tentative values of $N_D = 6 \times 10^{17} \text{ cm}^{-3}$ ($\approx n$) and $N_D = 2 \times 10^{18} \text{ cm}^{-3}$, we obtain donor binding energies E_{D0} of 38 meV and 47 meV, respectively. These screening considerations suggest that the concentration of O_N should be in the order of the free carrier concentration, since the second value deviates from the donor energy ascribed to O_N (33-40 meV) [37, 100, 102].

Although the total donor concentration cannot be quantitatively determined, the estimated concentration range serves as a reference to interpret the effect of extrinsic doping on the electronic properties of GaN. Furthermore, the identification of oxygen as a dominant donor, as well as the detection of $(V_{Ga}-V_N)$ clusters, should be considered as a ground defect landscape when considering the realization of GaN-based magnetic semiconductors. In particular, if the magnetic doping is in the highly-diluted regime (10^{16} cm^{-3} - 10^{18} cm^{-3}), as in the case of GaGdN, defects and/or Gd-defect complexes have been predicted to play a role in mediating ferromagnetic interactions [103, 104, 105, 106, 107]. The inferred defect parameters in undoped GaN should therefore help to judge the feasibility of the aforementioned theories, which will be discussed in Sec.(3.3.4) in great detail.

3.2 Mn-doped GaN

In the last decade, since Dietl *et al.* predicted high temperature ferromagnetism in Mn-doped GaN [5], there have been plenty of experimental reports claiming the existence of room-temperature ferromagnetic coupling in diluted GaMnN. Most of them relied simply on the observation of a ferromagnetic-like hysteresis loop when measuring the integral magnetic properties by superconducting quantum interference magnetometry (SQUID). The interesting point was that ferromagnetism was found using diverse growth methods and at different growth conditions, and the samples were not sharing the same properties (e.g. in terms of conductivity, some of them were n-type, others p-type and others even semi-insulating). These experimental observations made it very difficult to understand the underlying physics. In many cases, it turned out that the ferromagnetic signal was either due to magnetic impurities in the substrate or due to the formation of nanoclusters or magnetic precipitates in the sample [108]. Moreover, there are still some ongoing discussions which support the role of point defects in mediating ferromagnetic interactions in Mn-doped GaN [109, 110].

An approach to solve this empirical puzzle relies on the question, which coupling mechanism should be considered for a given diluted magnetic semiconductor. This depends strongly on the separation of the magnetic ions (\propto coupling strength) and the electronic properties of the doped semiconductor; more precisely, on the energetic position of the electronic states of the magnetic dopant with respect to the band edges of the semiconductor. For a substitutional incorporation of Mn in the GaN-matrix (Mn^{3+}), it is expected that Mn induces *deep* energy states in the GaN-bandgap. If the Mn-concentration exceeds the unintentional doping concentration of GaN, the Fermi-energy will lie within the Mn-impurity band, where a strong localization of the carriers is expected. According to this scenario, a p-d exchange coupling or a carrier-mediated coupling mechanism (e.g. RKKY) can be ruled out. In turn, the most suitable mechanism to explain ferromagnetic coupling in Mn-doped GaN, is the so-called *double-exchange* interaction, which is strong but short-ranged [111, 112]. In this sense, two important aspects need to be investigated: (i) how the electronic localization of Mn-states develops with increasing Mn-concentration, and (ii) in how far the solubility limit can be extended to achieve a shorter Mn-Mn average distance without the formation of precipitates or secondary phases. To answer these questions, the structural, magnetic, optical and electrical transport properties of Mn-doped GaN will be presented and discussed in the following sections considering a wide range of Mn-concentrations. While a high Mn content is desirable to study a possible onset of ferromagnetic coupling between Mn-atoms, a rather low impurity concentration is required to characterize the electronic properties of a *single* Mn-impurity via optical and electrical transport measurements.

3.2.1 Growth conditions and structural properties

The optimal growth conditions for undoped GaN, already discussed in section 3.1, have been taken as a reference for the GaMnN growth, in order to maintain the crystal quality of the layers. However, it turned out to be very difficult to incorporate Mn at such conditions. Even at the GaN-stoichiometry, the Mn-incorporation is not so efficient due to the lower diffusion barrier of the Ga-atoms, which are preferably incorporated. Therefore, the growth conditions have to be shifted towards the nitrogen-rich regime to reach a higher Mn incorporation. On the other hand, in the nitrogen-rich regime, the crystal quality of the layers decreases; a higher dislocation density and a rough surface is expected [113]. In order to achieve a relatively efficient Mn-incorporation without losing the crystal quality, three growth regimes have been investigated, as summarized in Fig. 3.6. Series A and B have been grown with high Mn-supply with the aim of achieving ferromagnetic ordering at short Mn-Mn distances; Series C with low Mn-supply in order to understand the properties of single, non-interacting Mn-atoms incorporated in the GaN-matrix.

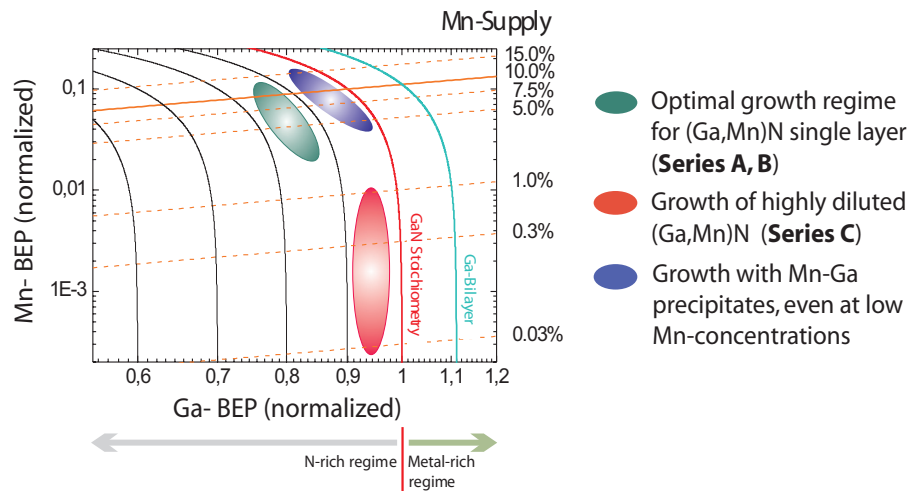


Figure 3.6: Growth regimes of the Mn-doped GaN samples studied in the present work, taken from [95].

Starting with high Mn-concentrations, an important issue is the determination of the solubility limit, in other words, the critical concentration at which precipitates or secondary phases start to form. The Mn-concentration has been measured by energy-dispersive X-ray spectroscopy (EDX) and the identification of crystalline phases has been performed by X-ray diffraction (XRD). θ - 2θ scans performed on samples grown on semi-insulating 6H-SiC (series B), show the onset of Mn-Ga precipitates already at 5%² Mn. The secondary phases observed in this series correspond to the Mn_3GaN

²in the following, in terms of Mn-concentration, the notation „%“ should be understood as „at%“, which is the atomic percent of Mn with respect to Ga

phase (BaTiO_3 perovskite structure) with the $[111]$ direction parallel to the c -axis of GaN, as shown in Fig. 3.7. It is worth to mention that nearly the same critical concentration was found for samples grown homoepitaxially on GaN-templates (5%), which means that the substrate choice does not have a strong influence on the formation of precipitates. Assuming that the Mn_3GaN phase takes the form of spherical clusters, the cluster size can be estimated from the full width at half maximum (FWHM) of the θ - 2θ reflection according to the Scherrer-formula [114]

$$d = \frac{0.9\lambda}{\text{FWHM} \cos\theta} \quad (3.2)$$

where d denotes the cluster diameter, λ the incident wavelength ($\text{Cu K}\alpha = 1.5405\text{\AA}$), and θ the reflection angle, respectively. The FWHM is extracted from a Gaussian fit, as shown in Fig. 3.7, and has to be converted to radians to be consistent with the units in Eq. (3.2). This analysis has been done with the highest doped samples of series B (8% Mn), yielding a cluster diameter of 26-27 nm. Note that if the cluster dimensions are not isotropic, the Scherrer-formula delivers the dimension d which is perpendicular to the diffraction planes, in our case along the direction $[0001]_{\text{GaN}}$ ($[111]_{\text{Mn}_3\text{GaN}}$).

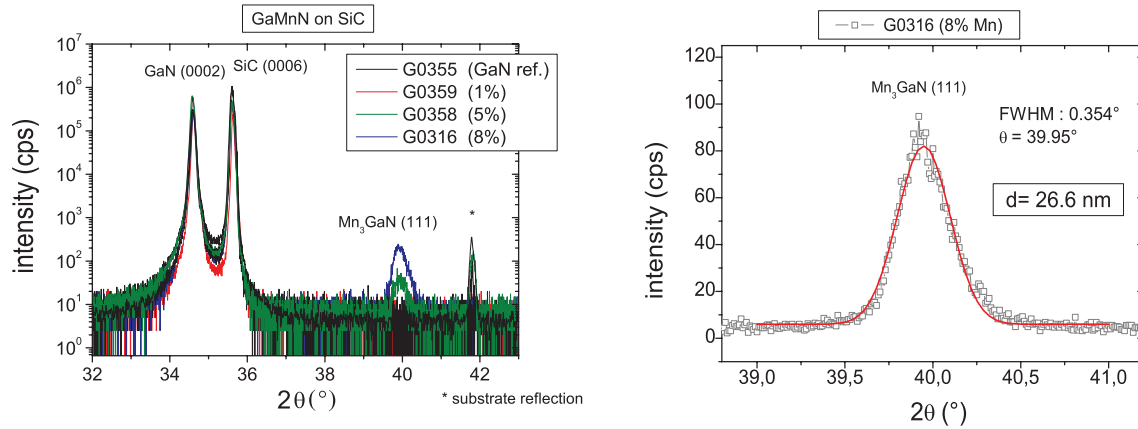


Figure 3.7: θ - 2θ scans of GaMnN epitaxial layers grown on 6H-SiC(0001) substrates, showing the presence of the Mn_3GaN phase for $[\text{Mn}] \geq 5\%$ (left). A Gaussian fit is used to extract the FWHM of the Mn_3GaN (111) reflection and estimate the cluster diameter (right).

The X-ray diffraction technique is also very sensitive to determine the lattice parameters and to quantify strain. Thus the influence of Mn-doping on the lattice parameters and the crystalline quality of the layers can be well investigated, especially at Mn-concentrations of a few percent. However, for the samples grown on GaN-templates (series A and C), this evaluation has its limitations. It is a difficult task to separate the superimposed reflections of the GaN-template and the GaMnN layer, especially because Mn has a very similar size and ionic radius as Ga, so that the small effect on strain due to the substitutional incorporation of Mn in GaMnN epilayers will

be masked by the strong reflection coming from the $2.5\mu\text{m}$ thick GaN-template, as depicted in Fig. 3.8. Therefore, we will concentrate on the sample series B, grown directly on SiC (0001), where the reflections of substrate and the MBE-grown layer are clearly at different positions, both for the symmetric (0002) and asymmetric $(10\bar{1}2)$, $(11\bar{2}2)$ reflections.

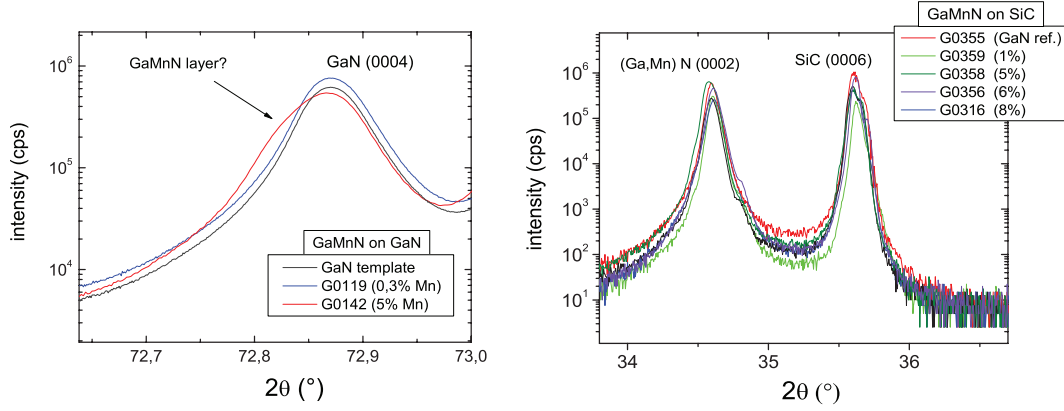


Figure 3.8: θ - 2θ scans of GaMnN layers grown on different substrates. The influence of Mn-doping can be better investigated on the sample series B (right), since the high-intensity reflections of substrate (6H-SiC) and grown layer (GaMnN) are at different positions.

A four-circle diffractometer with the χ (tilt) and ϕ (rotation) degrees of freedom allows to search for the Bragg-condition at any lattice plane. This equipment was used to find the $(10\bar{1}2)$ and $(11\bar{2}2)$ reflections of GaMnN, so that the c and a lattice parameters can be obtained from the respective peak positions. The dependence of these parameters on the Mn-concentration is presented in Fig. 3.9. The lattice parameter c shows a monotonic decrease with increasing Mn-concentration, fact which has been attributed to the substitutional incorporation of Mn in the GaN matrix [115, 116]. Thaler *et al.* [116] observed an increase of the c lattice parameter for samples with $[\text{Mn}] \geq 3\%$, and attributed this finding to the formation of Mn-interstitials. In this sense, the evolution of the c lattice parameter seems to be a good indicator for the substitutional incorporation of Mn in GaN. However, less attention has been paid to the concentration dependence of the in-plane lattice constant a . Before doing such an analysis, it is important to recall the effects which might change the lattice parameters in undoped GaN, like the lattice mismatch at the interface or post-growth thermal effects when cooling the sample from growth- to room-temperature. The difference between in-plane lattice parameters of 6H-SiC ($a_{\text{SiC}}=3.081 \text{ \AA}$) [117] and fully relaxed homoepitaxial GaN ($a_{\text{GaN}}=3.1877 \text{ \AA}$) [20] is high enough to account for a relief of the compressive strain during growth. On the other hand, the difference in thermal expansion coefficients ($\alpha_{\text{GaN}}=5.6 \times 10^{-6}/\text{K}$, $\alpha_{\text{SiC}}=3.2 \times 10^{-6}/\text{K}$) [118] will induce a tensile strain in the GaN layer when cooling the sample from $T_s=770^\circ\text{C}$ to room-temperature. The in-plane lattice parameter in our undoped reference sample

amounts to $a=3.1888$ Å, which indicates a residual tensile component due to post-growth cooling. The fact that the growth of GaN on SiC(0001) (series B) without any buffer layer results in biaxial tensile strain, is a common feature also observed by other groups [117, 119, 120].

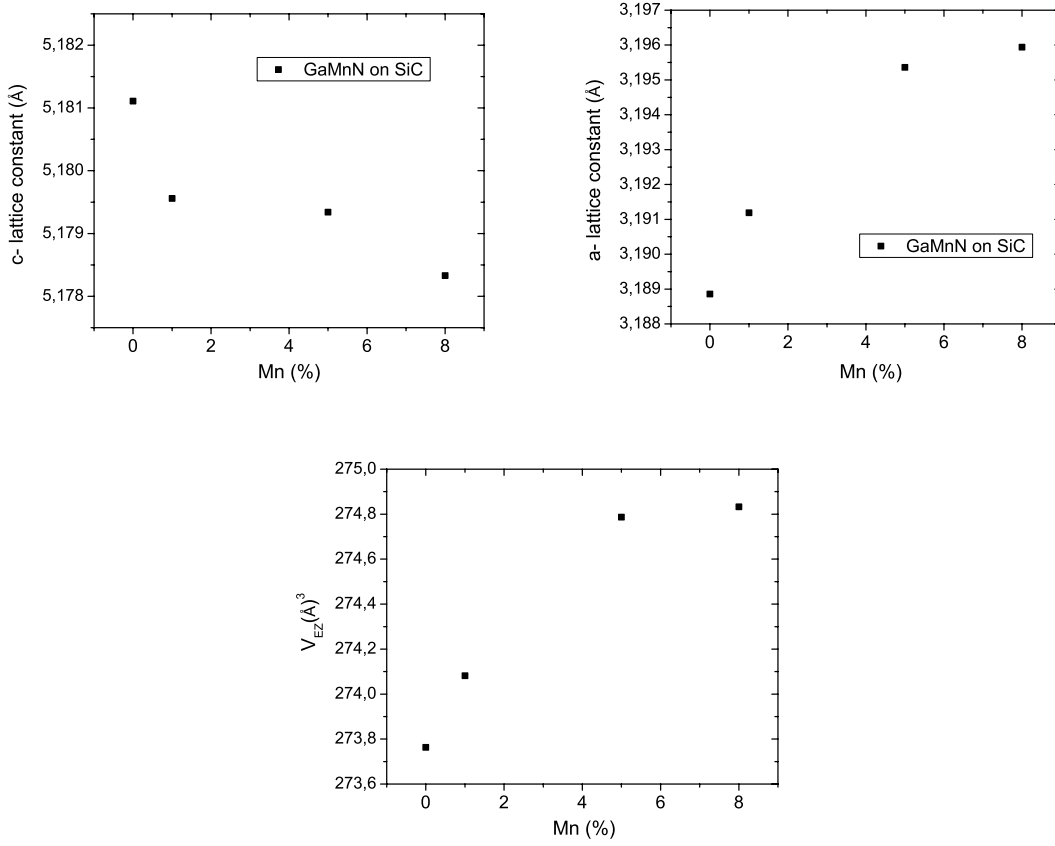


Figure 3.9: Influence of the Mn-doping on the GaN in- and out-of-plane lattice parameters. The volume of the unit cell has been also calculated, suggesting the presence of an hydrostatic strain component.

Coming back to the Mn-doping dependence, Fig 3.9 shows a monotonic increase of the in-plane lattice constant a with Mn-concentration. Since the samples on 6H-SiC(0001) have been grown under the same conditions, it is expected that the residual tensile strain is constant over the whole series, suggesting that the change in the a lattice parameter is exclusively a result of Mn-doping. Interestingly, the lattice parameters c and a show opposite trends upon doping with Mn. In order to evaluate if the strain is only of biaxial nature, the average volume of the unit cell was also calculated. An overall increase of the average cell volume is observed with increasing Mn-concentration, an indication of a hydrostatic strain component. The existence of hydrostatic strain in undoped GaN epilayers has been attributed to point defects

or impurities [117, 121], and in our case, it might be related to the substitutional Mn-incorporation. The saturation of the hydrostatic strain ($\propto V$) component at Mn-concentrations where Mn_3GaN precipitates start to form (decrease in the substitutional incorporation rate), might support this hypothesis. Below the clustering threshold, atom localization by channeling enhanced microanalysis (ALCHEMI) experiments of our samples grown on GaN-template confirm that ($96 \pm 6\%$) of the Mn atoms are located on the substitutional Ga-site [122]. Since a similar result is expected for the series grown on SiC (0001), we suggest that the hydrostatic strain is a better indicator for the substitutional Mn-incorporation, rather than just the decrease in the c lattice constant.

Regarding the crystalline quality of the samples, ω scans, better known as *rocking curves*, have been measured around the (0002), (10 $\bar{1}$ 2) and (11 $\bar{2}$ 2) reflections. For the series grown homoepitaxially on GaN-templates (A and C), the full width at half maximum (FWHM) values of the GaN-buffer and the GaMnN epitaxial layer are expected to be very similar and therefore difficult to distinguish. The ω scans of the samples grown on 6H-SiC(0001) have been fitted by a Gauss or Voigt- function and the FWHM has been extracted. The FWHM value describes the mosaicity (tilt) among the crystal planes and is therefore an indicator of the crystal quality. The scans are shown in Fig 3.10, and the FWHM values for different Mn-concentrations are summarized in Table 3.1.

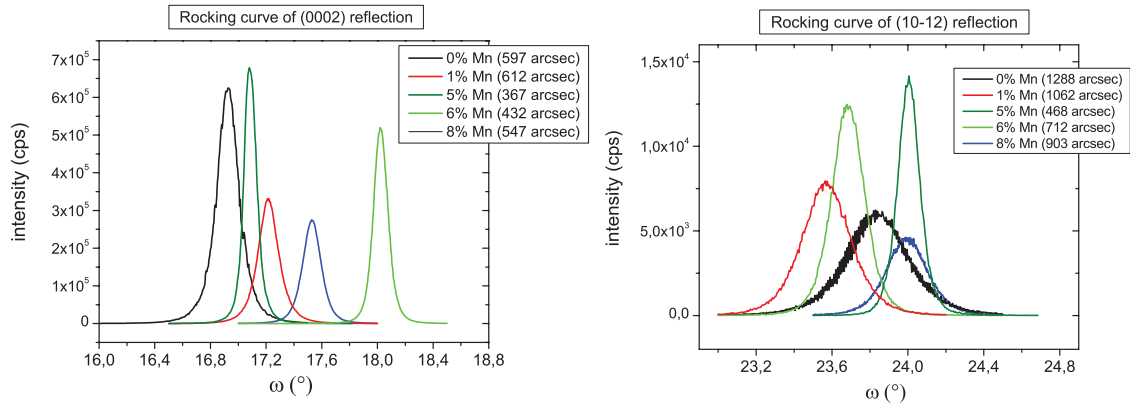


Figure 3.10: Rocking curves of the (0002) and (10 $\bar{1}$ 2) reflections of GaMnN layers and GaN reference samples grown on 6H-SiC (series B).

The FWHM values of the GaMnN layers grown on SiC are comparable with the ones reported in literature [115], ranging from 350 to 600 arcsec for the (0002) reflection and from 450 to 1000 arcsec for the asymmetric reflections. Although there is no clear correlation of the rocking widths with Mn-composition, it is worth to mention that the undoped samples have a clearly higher mosaicity, especially for the asymmetric reflections. One possible reason could be that the growth conditions for the whole

Sample	$\Delta\omega$ (0002) [arcsec]	$\Delta\omega$ (10 $\bar{1}2$) [arcsec]	$\Delta\omega$ (11 $\bar{2}2$) [arcsec]
G0316 (8%)	547	903	950
G0356 (6%)	432	712	799
G0358 (5%)	367	468	975
G0359 (1%)	612	1062	892
G0355 (GaN on 6H-SiC)	597	1288	1378
GaN on MOCVD-template	434	403	409

Table 3.1: Full Width at Half Maximum ($\Delta\omega$) values of GaMnN layers grown on SiC (0001). An undoped GaN epilayer grown on GaN-template (at the bilayer point) is shown for comparison.

samples series were fixed at 80% of the Ga-flux that corresponds to the bilayer point (see Fig. 3.6- green region), such that the Mn-atoms are able to be incorporated in the GaN-matrix, as discussed at the beginning of the section. In the absence of Mn, this may lead to the formation of extended defects and/or dislocations which affect the crystalline quality of the undoped samples (see sample G0355, Table 3.1). Another important point is that the asymmetric reflections of the whole series are substantially higher than the ones from samples grown on GaN-template, which is not the case for the symmetric (0002) reflections. Heying *et al.* [123] studied the role of threading dislocation structure on the rocking curve widths in epitaxial GaN, concluding that the (0002) rocking scans are sensitive just to screw dislocations; while pure edge dislocations with Burgers vectors parallel to the film/substrate interface have a strong impact on the asymmetric (10 $\bar{1}2$) rocking widths. In our case, the higher FWHM values of the asymmetric reflections are thus another evidence of the strain relief in form of edge dislocations -due to the GaN/SiC lattice mismatch in the basal plane- which is experienced during growth; consistent with the fact that homoepitaxial growth does not have much influence on the symmetric, but on the asymmetric rocking widths.

3.2.2 Magnetic properties

Magnetic measurements by SQUID-magnetometry integrate the signals of all the phases present in the volume which is subjected to the measurement. It is therefore imperative to subtract the signal coming from the substrate ($\geq 99\%$ of the sample volume), to ascertain that the detected magnetic phases belong to the epilayer. In addition, when *doping* is used to tune the magnetic properties, undoped reference samples have to be characterized as well. The reference samples grown on MOVPE-GaN/Al₂O₃ templates (Series A and C) show a very large diamagnetic signal with a small paramagnetic contribution [95]. Since GaN, Al₂O₃ and SiC (the substrate materials used in this work) are known diamagnets, the paramagnetic contribution

is expected to arise mainly from isolated impurities present in the large substrate volume.

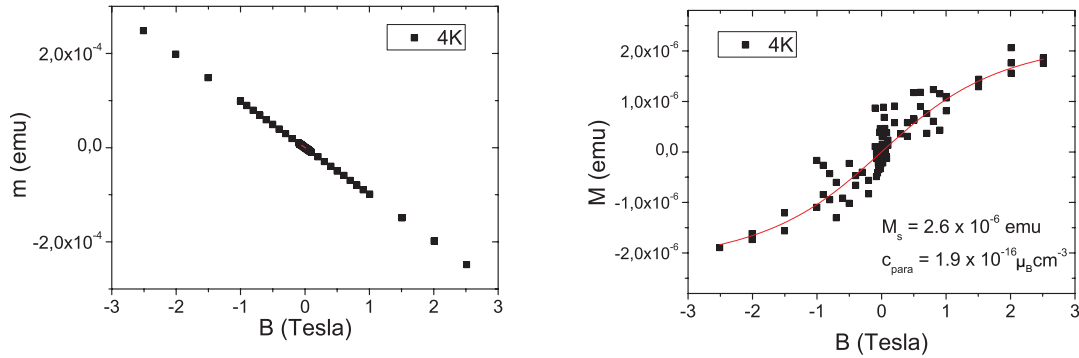


Figure 3.11: Dia- and paramagnetic signal of the 6H-SiC substrate batch used in this work.

The present magnetic characterization study will concentrate on GaMnN epilayers grown on semi-insulating 6H-SiC substrates (Series B), so that electrical transport measurements can be carried out in the same samples for an optimal correlation of magnetic and electrical properties. Concerning the GaN reference samples grown on the 6H-SiC substrate batch used in this study, the saturation magnetization M_S of the residual paramagnetic moment amounts to 2.6×10^6 emu, as inferred from the field-dependent magnetization at 4 K after subtracting the dominating diamagnetic contribution³. The results are shown in Fig. 3.11. The magnetic impurity „contamination“ of the substrate batch can be quantified as $1.95 \times 10^{16} \mu_B/\text{cm}^3$. For the integral magnetization measurements of the GaMnN epilayers, however, the paramagnetic M_s of 2.6×10^{-6} emu stemming from the substrate is the quantity which should be taken into account. Following these considerations, any additional magnetic signals in the GaMnN epitaxial layers have to come from Mn- and related phases.

Field-dependent magnetization measurements have been performed on samples with Mn-concentrations $c_{Mn} \geq 1\%$ in order to search for any ferromagnetic signature. Fig. 3.12 shows the results for GaMnN epilayers with 8% and 1% Mn, after subtracting the diamagnetic contribution⁴, which is expected to be temperature-independent. A remarkable feature in the highest doped sample (8% Mn) is the existence of an open hysteresis loop with a coercive field $H_c = 60$ Oe and a remanent magnetization of $3.3 \text{ emu}/\text{cm}^3$ at $T = 4$ K (inset of Fig. 3.12). Going towards higher temperatures, these features disappear and the field dependence adopt a paramagnetic-like behavior. Regarding the sample with $c_{Mn} = 1\%$, the observed paramagnetic response and

³extracted from the $M(H)$ at 300 K

⁴an iterative method to determine the diamagnetic contribution with accuracy is described in Appendix A

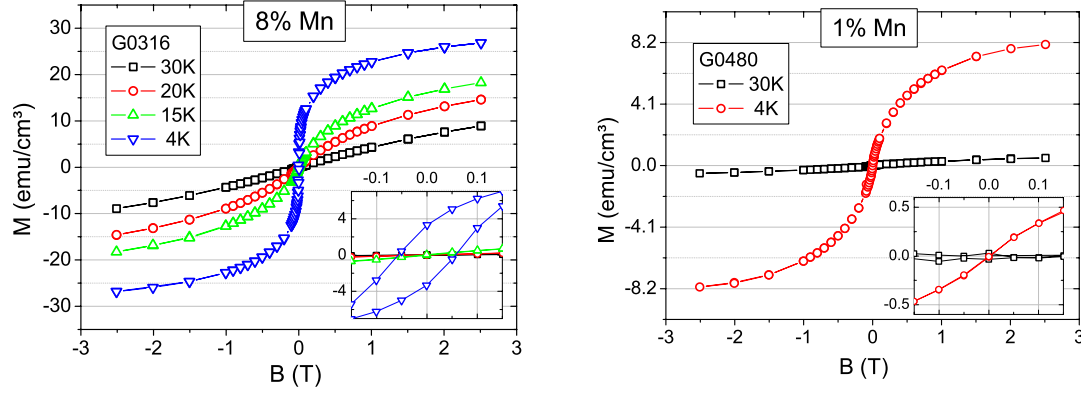


Figure 3.12: Field-dependent magnetization of GaMnN samples with different Mn-content, after subtracting the diamagnetic contribution. Even at $c_{Mn} = 1\%$, the saturation magnetization coming from the Mn-atoms is two orders of magnitude higher than the residual substrate contamination.

the absence of a coercive field is not surprising, since the Mn^{3+} ions incorporated at Ga-sites in the GaN-matrix are expected not to interact with each other at such concentrations. The paramagnetic contribution can be described as follows

$$M_{para} = M_s \cdot B_J(B, T) \quad (3.3)$$

where M_s is the paramagnetic saturation magnetization of the non-interacting Mn-atoms and $B_J(B, T)$ is the Brillouin-function defined as

$$B_J(B, T) = \frac{2J+1}{2J} \coth \left(\frac{2J+1}{2J} \frac{g\mu_B JB}{kT} \right) - \frac{1}{2J} \coth \frac{1}{2J} \frac{g\mu_B JB}{kT} \quad (3.4)$$

where J is the total angular momentum and g_j the Landé g-factor. The quantity J is the quantum number which considers both spin (S) and orbit (L) momentum for a determined electronic configuration. Following Hund's rule, the electronic configuration of Mn^{3+} ($[\text{Ar}]3d^4$), having the d -orbital less than half filled, implies a negative coupling between spin and orbit momentum, as $J = |L - S|$. Assuming a total quenching of the orbital moment of the Mn^{3+} ions in the GaN-matrix, J will be equal to $S=2$ for the Mn^{3+} electronic structure. With the determination of J , the calculation of the paramagnetic contribution to the magnetization can be performed, since all the other quantities present in the Brillouin-function and its argument are well defined. However, if the orbital moment is not fully quenched, the situation turns complicated. First, the coupling of the spin and orbital moments might be parallel or anti-parallel, not only depending on the fact if the d -orbitals of Mn are more than half filled as in the free ion case; moreover, the L - S coupling will be drastically affected by the ion environment in the crystal. Therefore, the J value could be either $J = |L - S|$ or $J = |L + S|$. Second, the value of the quantum number L is uncertain. In the case of Mn^{3+} in wurtzite GaN, the tetrahedral crystal field, the Jahn-Teller effect and a

trigonal distortion along the c-axis due to hexagonal lattice, added to the spin-orbit interaction, play an important role in modifying the spin and orbital momentum. Third, both the alignment of the orbital and spin moment and the value of L changes the Landé g-factor, which also appears in the argument of the Brillouin-Function. Table 3.2 lists some possible combinations of quantum numbers and Landé g-factors. The resulting values of J and g_J are taken for the Brillouin-Function in order to fit the experimental data of the paramagnetic sample with $c_{Mn}=1\%$, as shown in Fig. 3.13. It can be easily observed that none of the parameter sets is able to describe the field-dependent magnetization of the sample. Unlike in the free ion case, the effective orbital moment of Mn^{3+} in GaN does not seem to be an integer (L is in the crystal environment not a good quantum number), so that the Brillouin function fails to describe the magnetic behavior of Mn^{3+} -ions.

Table 3.2: Parameter sets for possible electronic configurations of Mn-ions in the GaN host crystal, and the resulting paramagnetic saturation magnetization gained from the Brillouin-Fits.

Config.	L	S	$J = L - S $	$J = L + S $	g_J	M_S (μemu)
Mn_{3+}	2	2	-	4	1.5	307
Mn_{3+}	1	2	-	3	1.66	335
Mn_{3+}	0	2	2	2	2	351
Mn_{3+}	1	2	1	-	2.5	397
Mn_{2+}	0	5/2	5/2	5/2	2	317

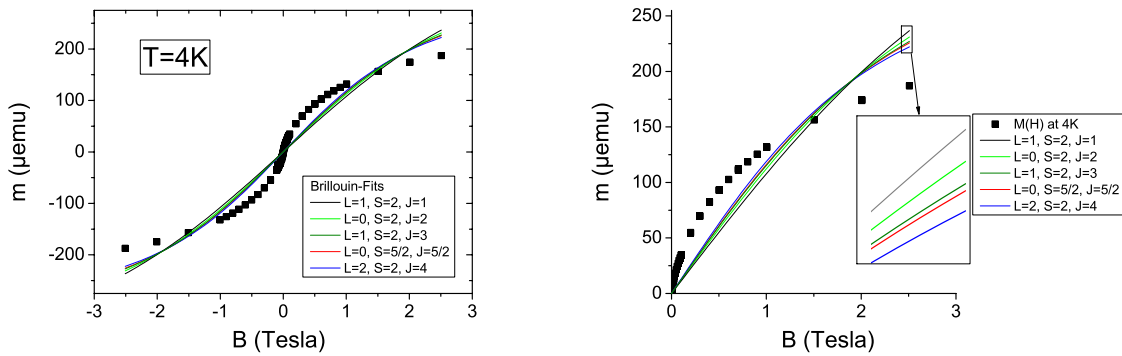


Figure 3.13: Brillouin-Fits with possible combinations of integer quantum numbers J , L and S of a Mn-ion in the GaN-matrix, showing bad agreement with the experimental magnetization data.

However, if the charge state of the Mn-atoms is rather $2+$, the half filled $3d^5$ configuration results a quenching of the orbital moment, due to the spherical symmetry of the electronic wave functions. The well-defined parameter set for a Mn^{2+} configuration is also listed in Table 3.2, and did not provide a good description of the

experimental data with reasonable Brillouin-fits either, which is an indication that we are not dealing with Mn^{2+} ions in our samples. Interestingly, Gosk *et al.* [124], performing the same data analysis, could indeed describe the paramagnetic behavior of n-type GaMnN samples ($c_{\text{Mn}} \leq 1\%$) with a Brillouin function using the parameters for a Mn^{2+} configuration ($L=0$, $J=S=5/2$, $g=2$). Unlike the $3d^4$ case, the effect of orbital quenching in the $3d^5$ configuration might be so strong, that the crystal environment do not have a major influence. The existence of the Mn^{2+} state was consistent with the fact that the samples in [124] exhibited n-type conductivity with a large electron concentration, implying that the 3d states of Mn are completely filled ($S=5/2$). The insulating character of our paramagnetic samples and the failure of the Brillouin model for a $3d^5$ configuration is therefore consistent. This is a good example of how the magnetic and electrical transport properties are closely related to each other. A detailed study of the electrical transport properties, and its implications on the magnetic nature of GaMnN, will be discussed in the next section.

Coming back to the description of the Mn^{3+} centers incorporated in the wurtzite GaN-matrix, there is one model developed by Vallin *et al.* [125] in the early 70s, which has been recalled later to successfully describe the magnetic properties of Cr^{2+} ($3d^4$) in II-V semiconductors [126]. The Hamiltonian to properly describe the $3d^4$ wave function in a host crystal can be written in the general form

$$H = H_{CF} + H_{JT} + H_{SO} + H_B \quad (3.5)$$

where the contributions of the tetragonal crystal field (CF), Jahn-Teller distortion (JT), spin-orbit coupling (SO) and magnetic field (B) are explicitly included. Gosk *et al.* [124] used the same approach to describe the energy structure of Mn^{3+} centers in GaN, adding a term H_{TR} to Eq. (3.5) arising from the hexagonal crystal field, simulated by a trigonal distortion along the c-axis; and found a very good agreement. Since the calculations of the eigenfunctions, eigenvalues and derived observables are very demanding⁵, this analysis has not been performed in this work. Nevertheless, a qualitative comparison can be still made: both our in-plane magnetization data (perpendicular to the c-axis) and the ones in Refs. [12, 124] show a more pronounced S-shape than in the case of Brillouin-paramagnets, suggesting that the crystal field model of Mn^{3+} centers in wurtzite lattices might be applicable to our case. The pronounced S-shape of the field-dependent magnetization is ascribed to the effect of the trigonal distortion of the c-axis and non-equivalent Jahn-Teller centers [12, 124] in wurtzite lattices.

The temperature dependence of the magnetization and in particular, of the magnetic susceptibility χ , has been investigated to gain additional information about the magnetic nature of the Mn^{3+} centers. A typical paramagnet will follow the *Curie-Weiss* law

⁵numerical diagonalisation of a full 25x25 Hamiltonian matrix

$$\chi = \frac{n\mu_0\mu_{eff}^2}{3k_B} \frac{1}{T} \quad (3.6)$$

where μ_0 and k_B are the permittivity of free space and the Boltzmann constant, respectively, n represents the concentration of paramagnetic species, and μ_{eff} is the effective magnetic moment of the ion, defined as [127]

$$\mu_{eff} = gJ\mu_B\sqrt{J(J+1)} \quad (3.7)$$

Fig. 3.14 shows the temperature dependence of the zero-field cooled (zfc) and field-cooled (fc) magnetization, measured at $H_{ext}=100$ Oe. Consistent with the high-resolution X-ray diffraction results, there is no sign of secondary phases or nanosized Mn-clusters which typically give rise to a blocked superparamagnetic contribution, whose characteristic feature is a splitting between the zfc and fc magnetization, and a maximum in the zfc curve which denotes the *Blocking-Temperature* (T_B). By cooling the sample under T_B in the absence of magnetic field (zfc), the superparamagnetic particles freeze in their random state. Upon heating in a small magnetic field, an energy of the order k_BT_B would be necessary to overcome the anisotropy energy and release the frozen moments. Above T_B , the moments will follow the magnetic field and thus behave paramagnetic. As observed in Fig. 3.14, the zfc and fc magnetization curves follow the same line down to low temperatures, suggesting the absence of Mn-clusters in the 1% Mn doped sample. Furthermore, the analysis of the mag-

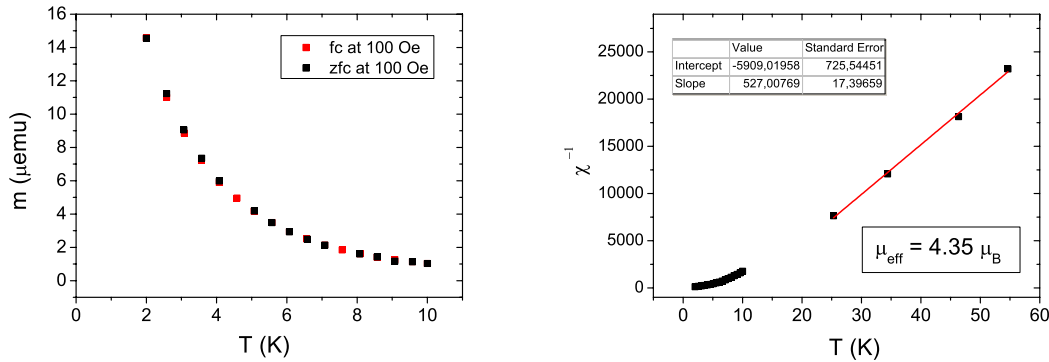


Figure 3.14: Temperature dependence of the magnetization and the magnetic susceptibility for the sample with $c_{Mn}=1\%$.

netic susceptibility points towards a Curie-Weiss behavior typical for non-interacting paramagnetic moments. The low-field approximation

$$\chi = \frac{dM}{dH_{ext}} \approx \frac{m/V}{H_{ext}} \quad (3.8)$$

has been used to calculate the susceptibility, and a linear regression of χ^{-1} against T yields the effective magnetic moment μ_{eff} according to Eq. (3.6), provided that

the magnetic impurity concentration n is known. The χ^{-1} over T relation could be well fitted between 25 and 60 K (Fig. 3.14), yielding an effective moment of $\mu_{eff}=(4.35\pm0.07)\mu_B/\text{Mn}$. Although the values of J and g_J cannot be determined this way either, this is another indication that the orbital moment of the Mn^{3+} is not fully quenched, since an effective moment of $4.9\mu_B/\text{Mn}$ is expected when $L=0$ and $J=S$, according to Eq. (3.7).

So far, the magnetic properties of GaN doped with $c_{Mn}=1\%$ have been discussed. In this concentration range, more than 90% of the Mn-atoms do not have nearest Mn-neighbors. By increasing the concentration, exchange interactions between Mn moments become important. At the same time, the probability that Mn-atoms form clusters or segregate in secondary phases turns higher. One important finding of the X-ray-diffraction characterization was the detection of the cubic Mn_3GaN phase for Mn-concentrations $\geq 5\%$. In terms of magnetic behavior, first studies of Mn_3GaN reported an antiferromagnetic coupling between the Mn-atoms with a Neel temperature (T_N) of 298 K by means of neutron diffraction [128, 129], while recent ones found a spin-glass behavior with a freezing temperature around 133 K [130]. It should be noted that these properties have been measured on polycrystalline bulk samples synthesized by solid-solid reaction methods. Yoon *et al.* [131] studied the magnetic properties of a $\text{Ga}_{1-x}\text{Mn}_x\text{N}$ layer ($x=0.12$) grown on sapphire containing Mn_3GaN precipitates, and found a broad cusp in zero-field-cooled (zfc) temperature dependent magnetization. The authors in [131] discussed the results in terms of blocked superparamagnetic nanoclusters with size distribution -which leads to a broad cusp in the zfc curve- rather than a spin-glass state. The inferred blocking temperature (T_B) was around 200 K. Regarding our GaMnN layers with $c_{Mn} \geq 5\%$, the temperature dependent magnetization (Fig. 3.15) shows a splitting of the zfc and fc curves at low temperatures, with a cusp in the zfc magnetization, characteristic feature of a blocked superparamagnetic ensemble or a spin-glass state. Depending on the Mn-concentration, there is a shift in the maximum of the zfc-magnetization, which suggests the presence of nanosized superparamagnetic particles with a different blocking temperature T_B , due to differences in size and/or concentration. A spin-glass state arising from Mn-Mn interactions seems rather unlikely, since an overall antiferromagnetic coupling with magnetic moment frustrations usually occurs at higher concentrations ($\approx 10\%$ Mn), as reported by Dhar *et al.* [115]. In any case, the behavior of the field-dependent magnetization might tell more about the existence of superparamagnetic clusters in the sample.

Assuming that the superparamagnetic precipitates have a large effective magnetic moment ($\mu_{eff} \propto J \gg 1$), their magnetic behavior can be described in terms of the *Langevin*-function, which is an approximation of the *Brillouin*-function for the limit $J \gg 1$:

$$L(B, T) = \coth\left(\frac{\mu_{eff}B}{k_B T}\right) - \left(\frac{\mu_{eff}B}{k_B T}\right)^{-1} \quad (3.9)$$

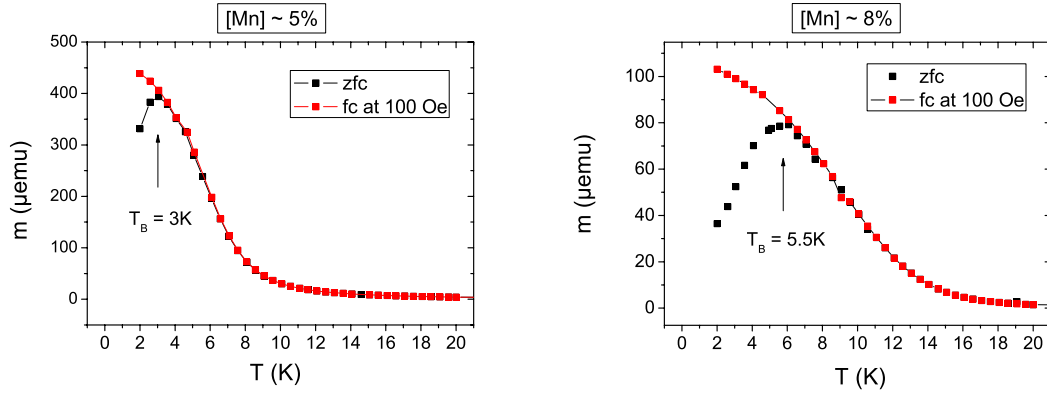


Figure 3.15: Temperature dependence of the magnetization of the samples with higher Mn-concentrations. Note that the absolute magnetic moment m is higher for the sample with 5% Mn due to the larger sample volume.

where $\mu_{eff} = g_J \mu_B J$. The field-dependent magnetization can be better analyzed at temperatures above T_B , where the thermal energy is high enough to overcome the anisotropy energy of the superparamagnetic clusters, such that they follow the magnetic field behaving as paramagnets. The coexistence of superparamagnetic clusters with substitutional paramagnetic Mn-atoms will result in a total magnetization

$$M_{total}(B, T) = M_s^{pm} \cdot L^{pm}(B, T) + M_s^{spm} \cdot L^{spm}(B, T) + M_{dia} \quad (3.10)$$

It is worth to mention that the paramagnetic term is just an approximation, since the isolated Mn^{3+} centers in GaN require a more careful treatment in terms of orbital moment quenching, as discussed before. However, taking the effective magnetic moment $\mu_{eff}^{pm} = 4.1 \mu_B$ derived from the magnetic susceptibility measurements, should yield a good estimate for the paramagnetic contribution, so that the superparamagnetic contribution can be separated. The optimal parameter sets are listed in Table 3.3, and the Langevin-Fits are shown in Fig. 3.16. As expected, the sample with lower Mn-content has a lower concentration of superparamagnetic nano-clusters, derived from the M_s^{spm} value; and a lower μ_{eff}^{spm} indicating a smaller cluster size. The first finding is consistent with the intensity of the XRD-reflections at $2\theta = 39.9^\circ$ (Fig. 3.7), which is a strong indication that the superparamagnetic behavior arises from the Mn_3GaN phase. The second result of the Langevin analysis is consistent with the shift in the blocking temperature T_B observed in the zfc magnetization. The size of the cluster changes the anisotropy energy contribution and therefore scales as $\propto T_B$.

The total Mn-concentration should be at least as high as the concentration of paramagnetic species, condition which is not fulfilled in the sample G0358 ($c_{Mn}^{pm} \approx 5.6\%$), suggesting either a slight underestimation of the Mn-concentration determined by energy dispersive X-ray spectroscopy ($c_{Mn} \approx 5\%$), or a slightly lower μ_{eff}^{pm} per Mn-center. Since the cluster concentration in this sample is three orders of magnitude smaller

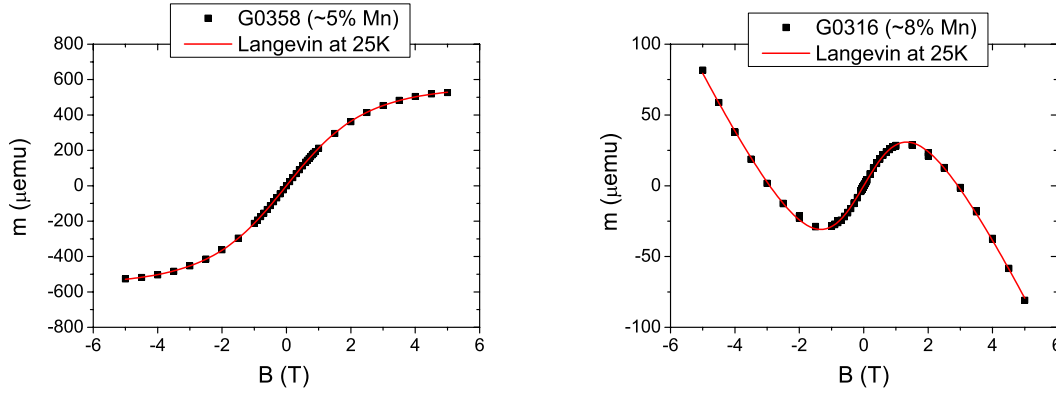


Figure 3.16: Langevin-Fits of the field-dependent magnetization taking into account the three contributions (spm + pm + dia) described in Eq. (3.9), showing a good agreement with the experimental data. The sample with 5% (left) and 8% Mn (right) content have been analyzed. Note that the absolute magnetic moment m is higher for the sample with 5% Mn due to the larger sample volume.

than c_{Mn}^{pm} , and the substrate background signal of $m_s = 2.6 \times 10^{-6}$ emu is negligible compared to the paramagnetic contribution of the Mn-atoms, upward corrections in the concentration should be small. On the other hand, sample G0316, the highest doped in this series, shows a lower paramagnetic concentration (6.2%) than the total Mn-concentration inferred from EDX-measurements (8%). In order to find out if this difference can be explained by the Mn-atoms which participate in the cluster formation, the average Mn-atoms per cluster has to be estimated. Each Mn_3GaN has an effective magnetic moment of $54.7\mu_B$, however, it is *a priori* not clear if the coupling of the Mn-atoms inside the cluster is ferro- or ferrimagnetic. Miao *et al.* [132] studied by first-principles calculations the electronic structure of Mn_3GaN , coming to the conclusion that both the magnetic state and the magnetic moment per Mn-atom in the antiperovskite Mn_3GaN structure is sensitive to the lattice strain. While it is expected to be ferromagnetic at equilibrium volume, the Mn-spins in one sublattice point antiparallel to the other under volume expansion, resulting in a ferrimagnetic ensemble. From X-ray diffraction characterization, it should be recalled that the average volume of the elementary cell of the GaMnN epilayers showed a saturation

Sample	μ_{eff}^{spm} [μ_B]	μ_{eff}^{pm} [μ_B]	m_s^{spm} [emu]	m_s^{pm} [emu]	$c_{clusters}^{spm}$ [cm ⁻³]	c_{Mn}^{pm} [cm ⁻³]
G0316 (8%)	54.7	4.35	1.69×10^{-4}	1.13×10^{-3}	32.5×10^{18}	2.73×10^{21} (6.2%)
G0358 (5%)	36.9	4.35	6.9×10^{-5}	2.91×10^{-3}	6.9×10^{18}	2.46×10^{21} (5.6%)

Table 3.3: Best-Fit parameters using the Langevin model, and the inferred concentrations of superparamagnetic and magnetic species. The Mn-concentrations of 8% and 5% have been obtained via energy dispersive X-ray spectroscopy (EDX).

trend at Mn-concentrations where Mn_3GaN inclusions start to form (Fig. 3.9). That means, the Mn_3GaN formation affects the GaMnN strain state, and viceversa. Given the low concentration of Mn_3GaN inclusions in the GaMnN matrix, it is not possible to determine the lattice constants of Mn_3GaN . From the (111) reflection (Fig. 3.7), the only parameter which can be inferred from the peak position is the d-spacing d_{111} , insufficient to determine if the Mn_3GaN nano-sized crystals are under lattice expansion or not. Consequently, the magnetic interactions between the Mn-atoms in Mn_3GaN and hence the determination of the total Mn atoms per cluster cannot be performed quantitatively. Nevertheless, a lower bound for the concentration can be set if a ferromagnetic coupling within Mn_3GaN clusters is assumed. Considering the value of $\approx 1\mu_B$ per Mn as calculated in [132] for the ferromagnetic configuration, we derive the number of Mn-atoms per cluster as

$$n_{Mn}^{cluster} = \frac{\mu_{eff}^{spm}}{1\mu_B} = 54.7 \quad (3.11)$$

so that the Mn concentration in the superparamagnetic phase can be obtained according to

$$c_{Mn}^{spm} = n_{Mn}^{cluster} c_{clusters}^{spm} \quad (3.12)$$

This results in a total Mn-concentration ($c_{Mn}^{spm} + c_{Mn}^{pm}$) of $4.5 \times 10^{21} \text{ cm}^{-3}$ ($\approx 10.2\%$) for the sample G0316 and $2.88 \times 10^{21} \text{ cm}^{-3}$ ($\approx 6.1\%$) for sample G0358, respectively. Note that the major uncertainty in this estimation comes from the magnetic moment of $1\mu_B$ per Mn taken by [132] assuming equilibrium conditions. In particular, the derived concentration of $\approx 10.2\%$ for sample G0316 would mean that all the Mn-atoms which were supplied during growth ($\approx 10\%$) have been incorporated, scenario which have been found to be unlikely during the GaMnN growth process [95]. Nevertheless, what is evident from the Langevin-analysis is that the sample G0316 has an appreciable concentration of Mn-atoms which participate in the formation of the Mn_3GaN phase. Concerning the paramagnetic Mn-atoms, an important finding is that their concentration still increases slightly with further Mn-doping, despite the formation of Mn_3GaN clusters. This suggests that the substitutional incorporation rate is indeed suppressed, but not completely „shut down“. In this sense, we estimate the clustering onset in our GaMnN samples grown on 6H-SiC(0001) to be around 5%, whereas the saturation of homogeneous Mn-incorporation might be reached at 6.5%. Mn can be incorporated either in the substitutional or in the interstitial site. Previous studies of atom localization by channeling enhance microanalysis (ALCHEMI) done in our group demonstrated an substitutional to interstitial ratio of $(95 \pm 6)\%$ [122], but at a Mn-concentration of (1.4%). Regarding higher Mn-concentrations, a parameter which has been used to indicate the formation of Mn-interstitials is the increase of lattice constant c [116]. This behavior is not observed in our samples (see Fig. 3.9), suggesting that the Mn-atoms which do not participate in the cluster formation should be mainly on the substitutional site.

Another interesting feature of the temperature dependent magnetization in the highest doped samples is the behavior of the field-cooled scan at low temperatures. Unlike typical paramagnetic systems with superparamagnetic inclusions, where a monotonic increase of the slope is observed [133], the FC-magnetization curve of our highest-doped samples exhibit a point of inflection. A minimum in the first derivative of the temperature dependent magnetization has been already used to identify ferromagnetic transitions [10], where the point of inflection defines the Curie-temperature T_c . The study by Sarigiannidou *et al.* [10] inferred a Curie-temperature of $T_C=8$ K in a GaMnN epilayer with 6.3% Mn-concentration. The absence of ZFC-magnetization data in [10] is not helpful to interpret the observed hysteretic $M(H)$ loops as an exclusive result of ferromagnetic interactions at low temperatures. In our case, the existence of a coercive field and remanent magnetization at low temperatures (Fig. 3.12) can be primarily attributed to the nanosized superparamagnetic particles with anisotropy barrier blocking. However, the shape of the field-cooled magnetization in the highest doped samples, leads to the suspicion whether a weak ferromagnetic contribution could be present at low temperatures. In order to clarify this issue, a sample exhibiting clusters at a substantially lower Mn-concentration -due to unoptimized growth conditions- is taken for comparison. Fig. 3.17 shows that the shape of the FC-magnetization is substantially different in both samples, despite a very similar ZFC-magnetization behavior. In the lowest doped sample, the concentration of substitutionally incorporated Mn-atoms lies between 0.5 and 0.8%, so that the Mn^{3+} centers do not interact with each other, and is consistent with the paramagnetic-like increase of the FC-magnetization. This is not the case for the sample having almost ten times higher concentration of paramagnetic species (G0358), where there is indeed the possibility of a weak interaction between Mn-atoms due to the shorter Mn-Mn distance, which would result in a ferromagnetic coupling with a low Curie-temperature. The inferred T_c in our samples with $c_{Mn} \geq 5\%$ fall in the same range as the one derived in the study of Sarigiannidou *et al.* [10], which determined a Curie-Temperature of 8 K in a GaMnN epilayer with 6.3% Mn-concentration from the maximum of the first derivative. Using the same approach, we obtain for sample G0358 a $T_c=(5\pm0.5)$ K and for sample G0316 a $T_c=(10.5\pm1.5)$ K. The increase of the Curie-Temperature with increasing concentration of paramagnetic atoms, is another indication that the formation of superparamagnetic Mn_3GaN precipitates in the samples doped with $c_{Mn} \geq 5\%$ does not necessarily „shut down“ the substitutional incorporation of Mn. The average Mn-Mn distance decreases with increasing Mn-concentration as $d_{Mn-Mn}=(c_{Mn}^{pm})^{-1/3}$. The results are summarized in Table 3.4. Interestingly, the inferred average Mn-Mn distance falls in the range where the magnetic exchange coupling constant J_{ij} in Mn-doped GaN is very small, as calculated by several first-principle studies [134, 135, 136], which would be consistent with the low Curie-temperature observed in our GaMnN samples.

In order to separate the superparamagnetic and ferromagnetic phase at low temperatures, the effect of thermal cycles on the hysteretic behavior has been analyzed.

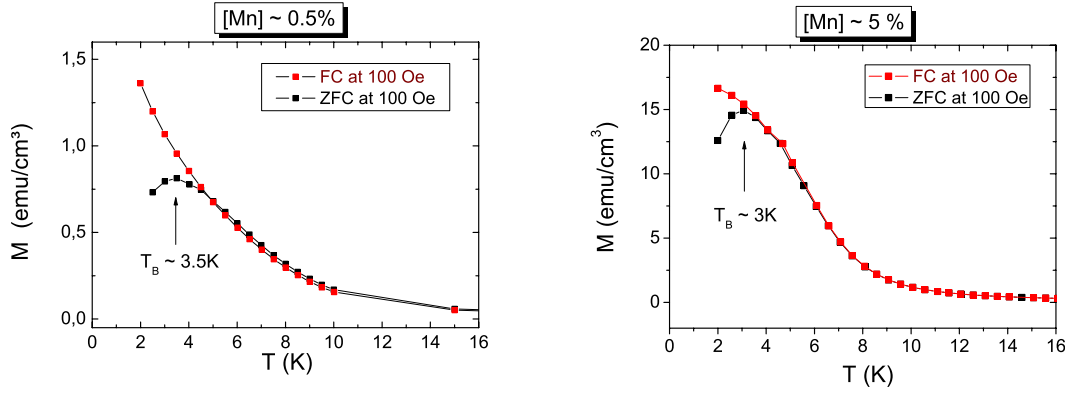


Figure 3.17: Comparison of the temperature dependent magnetization between a sample containing around 0.5% paramagnetic Mn-species and Mn₃GaN precipitates, and another containing the same precipitates but ten times larger concentration of paramagnetic Mn (G0358). The latter shows a point of inflection in the FC-magnetization indicative of a ferro-to paramagnetic transition.

Sample	$c_{clusters}^{spm}$ [cm ⁻³]	$c_{Mn}^{fm/pm}$ [cm ⁻³]	d_{Mn-Mn} [Å]	T_c [K]
G0316 (8%)	32.5×10^{18}	2.73×10^{21} (6.2%)	7.1	(10.5 ± 1.5)
G0358 (5%)	6.9×10^{18}	2.46×10^{21} (5.6%)	7.4	(5 ± 0.5)

Table 3.4: Dependence of the Curie-temperature T_c on the concentration of paramagnetic species derived from the Langevin-Fits.

A thermoremanent state was prepared by removing the magnetic field at the lowest temperature (2 K), then, the remanent magnetization M_R is measured by cooling and re-heating the sample in thermal cycles of different ΔT 's in the absence of external magnetic field. While a ferromagnet should almost fully recover its spontaneous magnetization, the superparamagnetic particles, once heated, will not be able to recover their magnetization state by re-cooling [137]. Fig. 3.18 shows a comparison between the thermoremanent magnetization of FeN nano-particles with an anisotropy barrier of 0.1 eV taken from [137], and of a GaMnN epitaxial layer (G0316) containing both superparamagnetic clusters and diluted Mn-atoms in the GaN-matrix. The thermal behavior looks very similar at the first glance, however, a partial recovery of the magnetization can be observed in the GaMnN epilayer by undergoing every thermal cycle, suggesting the existence of a ferromagnetic contribution. In particular, in the last cycle, where the temperature is increased up to 15 K, the remanent magnetization decreases to a value as low as 6.5×10^{-3} emu/cm³ which corresponds to an absolute value of $m = 1 \times 10^{-7}$ emu. This value lies closer to the detection limit of the SQUID-magnetometer and can be therefore regarded as the state of zero-remanence. By cooling the sample towards 2 K, the remanent magnetization is recovered reaching

a value of 0.43 emu/cm^3 ($\approx 7 \times 10^{-6} \text{ emu}$), which can be interpreted as the *ferromagnetic* remanent magnetization. Note that the thermoremanent magnetization is exempted from any measurement correction, since additional dia- and paramagnetic contributions in the sample volume do not have any effect at zero-field.

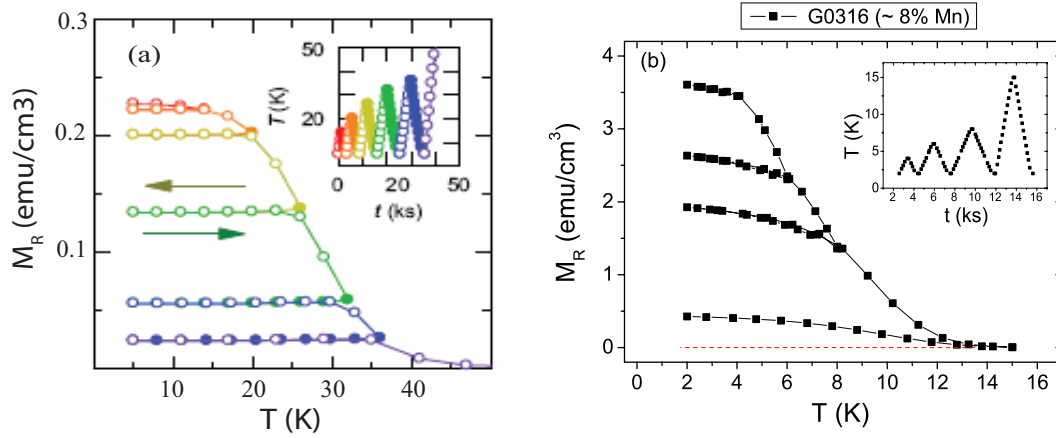


Figure 3.18: (a) Temperature dependence of the thermoremanent magnetization for typical nano-sized FeN superparamagnetic particles, taken from [137]. (b) The same experiment done at our highest doped sample ($\approx 8\%$ Mn), showing a partial recover of the remanent magnetization.

Fig. 3.19 recalls the field-dependent magnetization of sample G0316 recorded at 4 K. The inferred values of the *total* remanent magnetization in the field scans ($M_R(4\text{K})=3.3 \text{ emu/cm}^3$) are consistent with the values obtained by thermoremanence measurements. Furthermore, by extrapolating the value of M_R^{ferro} at 4 K, the ferromagnetic contribution can be visualized. The sketch of the field dependent ferromagnetic contribution (Fig. 3.19-right) should be taken just to compare the orders of magnitude of the contributions, since it is not possible to extract the real field dependence within the present measurement sets.

Despite the formation of nanosized superparamagnetic clusters for $c_{\text{Mn}} \geq 5\%$, which give rise to a field-dependent magnetization with considerable remanence and coercive fields at low temperatures, there are indications of ferromagnetic coupling between the diluted Mn-magnetic moments, suggested by the existence of a point of inflection in the FC-magnetization and further investigated via thermoremanent measurements at low temperatures. The separation of paramagnetic, diluted Mn^{3+} moments and superparamagnetic ensembles by means of Langevin-Fits at higher temperatures ($T > T_B, T_C$) suggest that still an appreciable amount of Mn-atoms are incorporated in the GaN-matrix, in turn, there is indeed a possibility that the diluted Mn-atoms induce a ferromagnetic coupling. These observations can be explained in the framework of a double-exchange mechanism proposed for magnetic impurities with localized

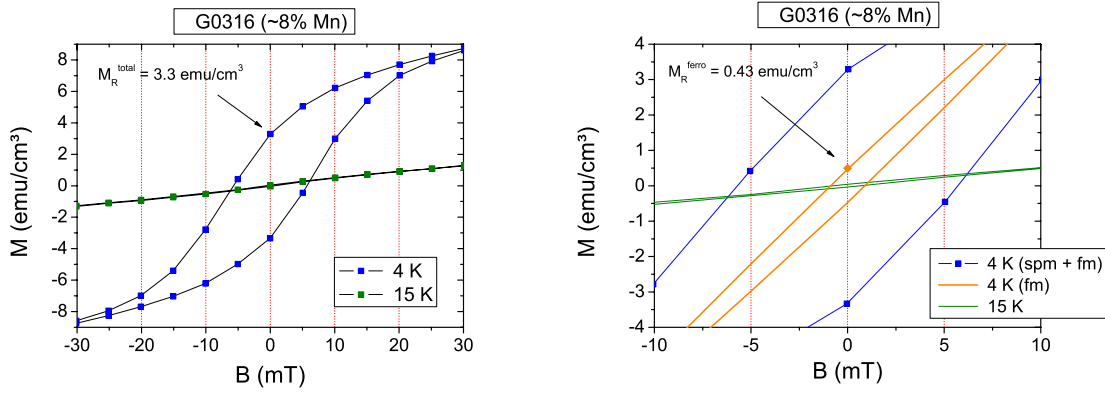


Figure 3.19: Magnetization of the sample with $c_{Mn} = 8\%$ at low fields, highlighting the negligible remanence at 15 K (left). By extrapolating the ferromagnetic remanence value M_R^{ferro} obtained by thermoremanence measurements, the ferromagnetic contribution is simulated and shown as guide for the eye (right).

electronic states [112, 138], as is the case of GaMnN. Furthermore, the Mn-Mn average distance seems to be short enough to activate a weak ferromagnetic coupling persistent up to a few kelvin, in agreement with theoretical studies which predict low Curie-temperatures taking into account experimentally realistic Mn-concentrations ($\leq 10\%$) [111, 134].

3.2.3 Optical properties: Photo-Luminescence

Optical measurements are a useful tool for probing the electronic and defect structure of - either unintentionally or intentionally- doped semiconductors. Concerning Mn-doped GaN, a few studies addressed the observation of Mn-related transitions in absorption and cathodoluminescence experiments [139, 140]: an intra-atomic transition of the Mn^{3+} ion at 1.42 eV and a broad feature above 1.8 eV related to a transition from the valence band. If the Mn-atoms occupy Ga-sites, they will experience the action of the crystal field which causes an energy splitting of the Mn-states. The last filled 3d-states split in the sublevels e and t_2 , which are 1.4 eV apart. The observation of the internal transition (${}^5T_2 \rightarrow {}^5E$) at 1.42eV in photoluminescence (PL) is thus a fingerprint of substitutional occupation of Mn in the GaN-matrix. Unfortunately, this transition is quenched as the Mn-concentration is increased, and does not allow to probe for substitutional incorporation in samples where Mn already starts to segregate [141]. Therefore, highly diluted GaMnN samples ($\leq 1\%$) (series A) were grown to observe the internal transition [142]. The results were reproduced on GaMnN samples grown on highly-resistive GaN:C substrates (series C), as shown in Fig. 3.20. The concentration of this sample series was determined by secondary ion mass spectroscopy (SIMS) and ranges from 10^{17} cm^{-3} to 10^{20} cm^{-3} . The sensitivity of our PL-setup by probing the presence of substitutional Mn amounts to

10^{18} cm^{-3} , where the intensity of the luminescence peak at 1.414 eV vanishes. The evidence of substitutional inclusion of Mn probed by photoluminescence in highly-diluted samples, is consistent with the magnetic characterization (paramagnetism of isolated Mn^{3+} -ions) and will be important for the discussion of the electrical transport properties presented in the next section.

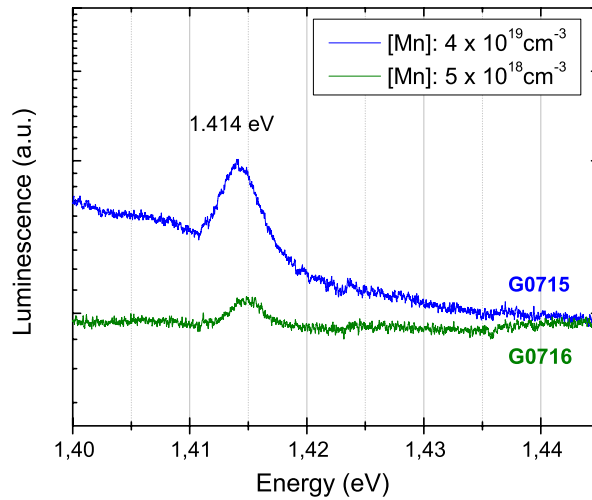


Figure 3.20: Photoluminescence spectra of GaMnN epitaxial layers at $T=4\text{K}$.

3.2.4 Electrical transport properties

The electrical transport properties, mainly through the temperature dependence of the resistivity, have been investigated in a wide range of Mn-concentrations (10^{16} cm^{-3} - 10^{21} cm^{-3}). As discussed in previous sections, nominally undoped GaN possess an electronic structure which is defined by native donors ($N_D \geq 6 \times 10^{17} \text{ cm}^{-3}$). Mn-doping in the highly-dilute concentration limit (10^{16} cm^{-3} - 10^{19} cm^{-3}) is thus interesting to study the effect of compensation. At the same time, the evolution of the electronic properties with increasing Mn-concentration can be followed in a systematic way. Motivated by the observation of ferromagnetic signatures at higher Mn-concentrations (10^{21} cm^{-3}), the electrical transport properties are investigated in this regime with the aim of recognizing any feature which might be connected to the presence of magnetic interactions.

Starting with Mn-doping in the highly-diluted regime, the substitutional incorporation of Mn-atoms will progressively compensate the native donors by inducing deep states in the GaN bandgap. The compensation ratio depends both on the amount of Mn-states which are available ($\propto N_{Mn}$) and on the occupation of the last filled states (location of the Fermi-Energy). From the results of the optical and magnetic

measurements, we suggest that the charge state is Mn^{3+} , which has the electronic configuration $[\text{Ar}]3d^4$ corresponding to one unoccupied state in the last filled d-band. As a consequence, every Mn-atom will catch one electron residing in a shallow donor level, so that at $N_{\text{Mn}} \approx N_D$ the shallow donor states are fully depleted. At the same time, the Fermi energy shifts towards the energetic position of the Mn-states, as the Mn-concentration is further increased. If the Mn-concentration is lower than the electron concentration in the shallow donor states, than we expect still an n-type conductive material but with lower free carrier density due to compensation. A sample with Mn-concentration⁶ around 10^{17}cm^{-3} (G0731) should be therefore suitable to investigate the partial compensation of the residual donors by the Mn-impurities. The electron concentration of the Mn-doped sample was measured at 300 K via Hall-Effect, and is found to be reduced from $5 \times 10^{17}\text{cm}^{-3}$ (reference sample) to $1.3 \times 10^{17}\text{cm}^{-3}$, attributed to the electron trapping effect of the deep Mn-states. A reliable fit of the carrier concentration $\ln(n)$ vs T^{-1} to determine the activation energy could not be performed due to the influence of hopping conductivity (*crossover regime*) up to high temperatures, as depicted in Fig. 3.21.

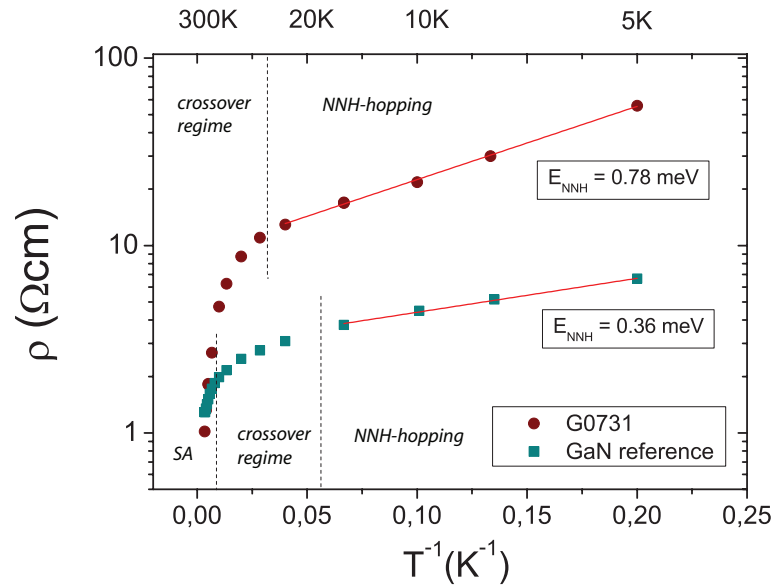


Figure 3.21: Temperature dependence of a GaMnN sample with $N_{\text{Mn}} \approx 10^{17}\text{cm}^{-3}$ compared to a reference undoped GaN sample. Note that the activation energies are inferred from the fit $\ln\rho$ against T^{-1} . The conduction regimes are shown in either case, for clarity.

The resistivity is plotted against $1/T$ (Fig. 3.21), and a linear dependence on the semi-logarithmic scale could be observed at low temperatures, indicative of nearest-neighbor hopping transport. The activation energy $E_{\text{nnh}}=0.78$ meV is found to be

⁶the concentration was under the measurement limit of secondary ion mass spectroscopy (SIMS), and was estimated by extrapolation

higher than the one from the reference sample grown in this series ($E_{nnh}=0.36$ meV). Note that in the nearest-neighbor hopping regime, the hopping conductivity is determined by the mean impurity separation r_{ij} ($\propto N^{-1/3}$) rather than by the energy barrier between states. To elucidate that, we recall Eqs.(1.17),(1.51) to formulate the resistivity in the NNH-regime

$$\rho_{nnh}(T) = \rho_0 \exp\left(\frac{c}{N_D^{1/3} a}\right) \exp\left(\frac{E_{nnh}}{k_B T}\right) = \rho_3 \exp\left(\frac{E_{nnh}}{k_B T}\right) \quad (3.13)$$

where the parameter $c=1.73\pm0.03$ is known from the solution of the „sphere problem“ in percolation theory. It should be remarked that the resulting dependence of the resistivity on the donor concentration N_D is only applicable for hydrogenic wave functions. In our case, the description should apply since the electrons are supposed to be weakly bound to the oxygen donors. The temperature independent part of Eq. (3.13) corresponds to the y-axis intercept of the fit in Fig. 3.21, and is inversely proportional to the donor concentration, as $\rho_3 \propto \exp(N_D^{-1/3})$. The higher value of the y-axis intercept in the Mn-doped sample ($N_{Mn} \leq N_D$) would suggest that the incorporated Mn-atoms not only act as a compensating centers but also may suppress the formation of the dominant donors (O_N) during growth. However, the donor concentration cannot be quantified since the constant ρ_0 is unknown, precluding a quantitative analysis of the influence of Mn-doping on the donor formation. Note that the occurrence of hopping conduction within a shallow donor impurity band has been also observed by Look *et al.*, both in unintentionally doped MOCVD-GaN [34] and in N-rich grown MBE-GaN samples⁷ [97]. These observations demonstrate that „shallow“ states do have an energy dispersion, which is revealed by the occurrence of hopping transport at low temperatures. The very low activation energies obtained in this scenario are consistent with the general accepted picture of a „single energy level“ (impurity band width $\rightarrow 0$) for shallow impurities.

As the Mn-concentration is further increased, there is a enormous shift in the temperature dependent resistivity: after a critical concentration is reached, the resistivity increases sharply by many orders of magnitude, as shown in Fig. 3.22. In this regime, the carrier concentration could not be determined via Hall-effect. Furthermore, by analysing the scaling behavior of the temperature, a $T^{-1/4}$ dependence is found as a common feature for the samples containing $N_{Mn} \geq 10^{18} \text{ cm}^{-3}$, as shown in Fig. 3.23, which is characteristic of Mott-variable-range hopping transport in an impurity band of localized states. This observation supports the localized character of Mn-3d states, and, at the same time, implies that the totality of the electrons which are weakly bound to the shallow donors have been trapped by the *deep* Mn states. As a consequence, the Fermi-energy will shift towards the 3d-energy levels of Mn and lie within

⁷In [97], a transition from shallow to deep impurity-band hopping conduction is observed as a function of N-supply during growth, demonstrating that the III/V ratio is a crucial parameter which re-defines the formation energy landscape of the defects.

the partially filled Mn-impurity band ($3d^4$), more precisely, in the upper t_2 band resulting from the crystal field splitting. Analogously, for the residual donor impurities (O_N), the occurrence of variable-range hopping transport between the Mn-states at $N_{Mn} \geq 10^{18} \text{ cm}^{-3}$ sets an upper bound for the donor concentration ($N_D \leq 10^{18} \text{ cm}^{-3}$), since the donor states have to be fully compensated.

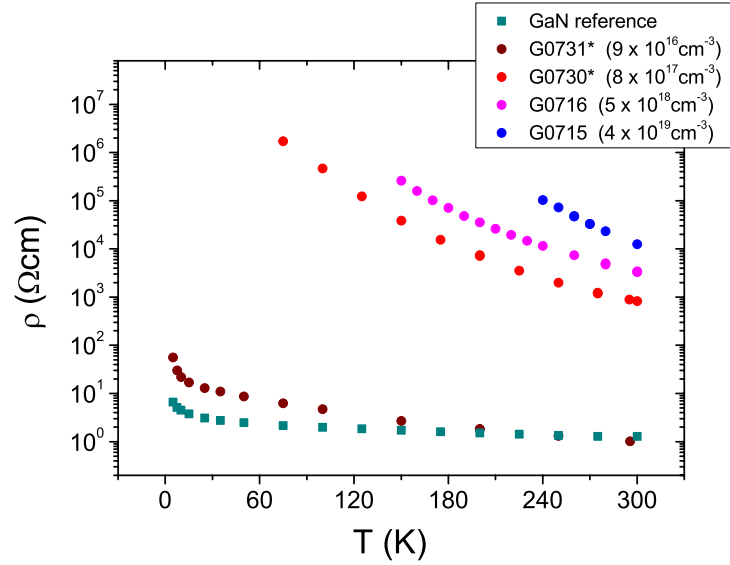


Figure 3.22: Temperature dependent resistivity of GaMnN epilayers with different Mn-concentrations. Note the jump over many orders of magnitude by surpassing a critical Mn-concentration. The two lowest concentration could not be measured by SIMS and were determined by extrapolation.

For a quantitative description of the scenario, as discussed in Chapter 1, the quantities which can be derived in the Mott variable-range hopping regime are the localization length ξ and the density of states at the Fermi-level $N(E_F)$. The characteristic temperature $T_0^{(Mott)}$ is extracted from the fit $\ln(\rho)$ vs. $T^{-1/4}$, since the Mott-VRH hopping obeys the law

$$\rho(T) = \rho_0 \exp \left(\frac{T_0^{(Mott)}}{T} \right)^{1/4} \quad (3.14)$$

where

$$T_0^{(Mott)} = \frac{\beta}{k_B N(E_F) \xi^3} \quad (3.15)$$

which means that the slope is inversely proportional to the product $N(E_F) \xi^3$. Note that the density of states at the Fermi-energy depends on the bandwidth (integrated in energy will correspond to the total density of states) and the band filling, i.e. the position of E_F . In a simple tight-binding model, it is known that the bandwidth will

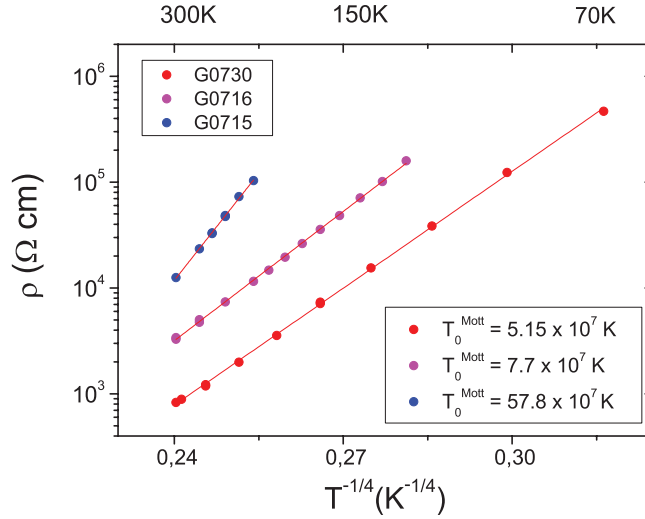


Figure 3.23: Linear behavior of $\log \rho$ with $T^{-1/4}$, indicating Mott-VRH transport at $N_{Mn} \geq 10^{18} \text{ cm}^{-3}$. The value of characteristic temperature T_0^{Mott} is derived from the slope of $\ln \rho$ vs $T^{-1/4}$.

scale with impurity concentration ($\propto \sqrt{c}$) [134], and thus we expect a rather narrow band at concentrations far below the percent range. Concerning the band filling, each Mn atom in the (3^+) state will contribute with 4 electrons in the d^5 shell, which means that 2 of 3 states will be occupied in the t_2 band. The 2/3 band filling ratio would determine the position of the Fermi-energy within the Mn-impurity band if there were not additional impurities in the crystal, which is not the case. The presence of shallow donor electrons does affect the band filling if their concentration is in the same order of magnitude than the Mn-atoms. To clarify the evolution of $N(E_F)$ with Mn-concentration, we assume a fixed concentration of donor electrons N_d and start at the limit $N_{Mn} \approx N_d$, where the Mn-impurity band is almost fully occupied with the Fermi-energy lying in the upper band tail. As the Mn-concentration is further increased, more states will be available for the donor electrons, shifting E_F towards the middle of the band. As a consequence of compensation, $N(E_F)$ increases with Mn-concentration. On the other hand, increasing the Mn-concentration leads to impurity band broadening, which attenuates the increase of $N(E_F)$. The localization length, on the other hand, is expected to be independent of Mn-concentration, as far as the impurity distance is great enough to avoid an overlap of the electronic wave functions. This condition is satisfied in highly-diluted GaMnN. Nevertheless, the localization length is affected when N_{Mn} and N_D are in the same order of magnitude, since the presence of ionized residual donors in the vicinity of the Mn-impurities influences the structure of the localized impurity wave function. Furthermore, a reduction in the Mn-Mn average distance (still far from the overlap), gives rise to an enhancement of the activation energy ($\propto T_0^{Mott}$) due to the increasing random Coulomb-potential of charged Mn-impurities [83].

These facts make the quantitative analysis of both $N(E_F)$ and ξ , and in particular, their product, rather complicated in the highly-diluted regime. In this sense, the increase of $T_{(Mott)}$ with Mn-concentration, which correspond to a decrease of the product $N(E_F) \xi^3$, is the only clear trend which can be inferred from our experimental data. An interesting study which would help to simplify the analysis would be to investigate the effect of the degree of compensation on both $N(E_F)$ and ξ at fixed impurity band characteristics, by the controlled addition of donors at a fixed Mn-concentration (e.g. by Si-codoping of GaMnN).

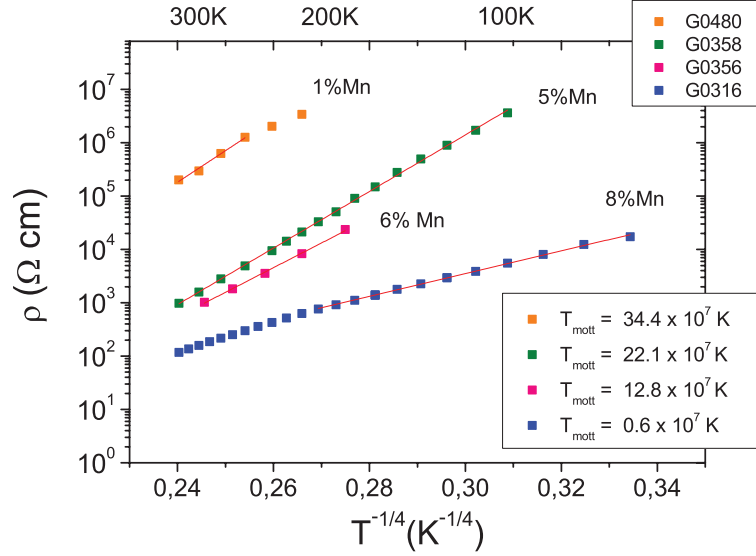


Figure 3.24: Linear behavior of $\log \rho$ with $T^{-1/4}$, indicating Mott-VRH transport. In the highest doped sample, the Mott-scaling behavior is not fulfilled at high temperatures. Note that the characteristic temperature $T_0^{(Mott)}$ is derived from the slope of $\ln \rho$ vs $T^{-1/4}$.

Regarding Mn-concentrations of a few percent, the temperature dependence of the resistivity also shows a $T^{-1/4}$ scaling behavior, as depicted in Fig. 3.24. Only in the highest doped sample, a deviation from the Mott-scaling behavior was observed, indicative of a crossover to nearest-neighbor hopping (NNH). However, the occurrence of NNH-hopping transport could not be confirmed, due to the lack of a constant activation energy ($\log \rho \propto T^{-1}$) within the measured temperature range ($T < 300$ K). Interestingly, both absolute resistivity and characteristic temperature $T_0^{(Mott)}$ decrease with increasing Mn-concentration, just the opposite trend than in the highly-diluted samples. In this series, the electronic properties are completely dominated by the Mn-impurities ($N_{Mn} \gg N_D$), so that compensation effects can be neglected. This implication has important consequences. First, the impurity band filling of the t_2 -band will hold the constant ratio of 2/3. Second, the localization length will not be affected by the degree of compensation, and hence is expected to be constant below the concentration where the localized wave functions start to overlap. The bandwidth still scales with Mn-concentration as $\propto \sqrt{c}$. Taking into account these points,

the density of states $N(E_F)$ is expected to show an overall increase with increasing Mn-concentration: the total density of states $N(E)$ behaves proportional to the concentration, increasing the value of $N(E_F)$, while band broadening effects weaken the proportionality. The localization length, on the other hand, might increase with Mn-concentration just in the case when the mean impurity distance d_{Mn-Mn} is short enough to account for a wave function overlap. Considering the exponential fits of the Mott-VRH law in Fig. 3.24, we observe a monotonic decrease of $T_0^{(Mott)}$ as the Mn-concentration is increased, which means that the product $N(E_F)\xi^3$ becomes larger, according to Eq. (3.15). Since the value of $N(E_F)$ has a rather weak proportionality to impurity concentration, small changes in ξ will dictate the behavior of $T_0^{(Mott)}$. Fig. 3.25 shows the evolution of $T_0^{(Mott)}$ with Mn-concentration. The sudden decrease of $T_0^{(Mott)}$ indicates the concentration range where the localization length is enhanced due to overlap effects.

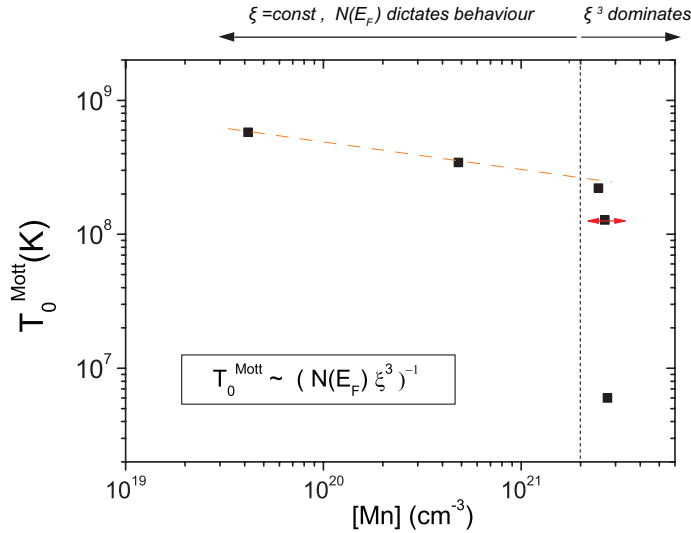


Figure 3.25: Evolution of the characteristic temperature T_0^{Mott} with Mn-concentration. Note that the concentration of substitutionally incorporated Mn^{3+} , inferred from the magnetic characterization, has been considered for the analysis. The red error bar is due to the uncertainty of determining substitutional Mn-concentration in sample G0356 (no magnetic data). The sharp decrease of T_0^{Mott} at high Mn-concentrations indicates an increase in the localization length ξ due to overlap effects.

In the studied concentration range (1 - 8% Mn), the mean impurity distance varies from 13.1 to 6.5 Å, respectively. In order to account for an impurity wave function overlap, the mean impurity distance should not be greater than two times the localization radius ($d_{Mn-Mn} \leq 2\xi$). It is worth to mention, however, that the average impurity distances inferred above are valid provided that the totality of the Mn-atoms incorporates in the GaN matrix. The X-ray diffraction characterization revealed the onset of secondary phase formation at $c_{Mn} \geq 5\%$ ($d_{Mn-Mn} \approx 8\text{Å}$). By separating

the paramagnetic (isolated Mn) and superparamagnetic (Mn_3GaN clusters) contributions to the magnetization, the concentration of substitutional Mn^{3+} centers has been estimated. Furthermore, the magnetic characterization suggested the existence of a low-temperature ferromagnetic phase in the highest doped samples. Considering the scenario of localized magnetic moments, the onset of ferromagnetic coupling defines the impurity concentration where the localized wave functions start to overlap. Fig. 3.26 shows the dependence of the characteristic temperature T_0^{Mott} on the average Mn-Mn distance estimated from the corrected Mn-concentration obtained from magnetometry. Although it contains the same information as Fig. 3.25, which is the sharp decrease of T_0^{Mott} due to the enhancement of the localization radius, it should serve as guide for the eye to interpret the correlation between carrier localization and magnetic interactions. The increase of localization radius happens at Mn-Mn average distances below 8 Å, in the same range where magnetic interactions between Mn-atoms in GaMnN become important. Below 8 Å, the calculated magnetic coupling constants $J_{ij}(d)$ for the GaMnN system start to deviate from zero [134, 143, 135, 144, 136], suggesting the onset of ferromagnetic coupling via *double-exchange*.

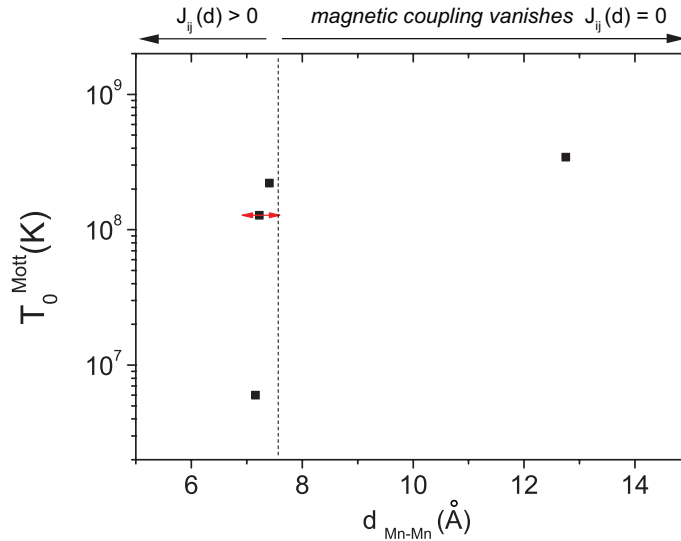


Figure 3.26: Evolution of the characteristic temperature T_{Mott} with the Mn-Mn average distance. The red error bar is due to the uncertainty of determining substitutional Mn-concentration in sample G0356. The sharp decrease of T_{Mott} at distances around 7 Å indicates an increase in the localization length ξ due to overlap effects, which, at the same time, coincides with non-zero magnetic coupling constants J_{ij} calculated from first-principles [134, 143, 135, 144, 136].

The effective mean impurity distance in highest doped sample ($T_c \approx 11$ K) lies around 7 Å, which should correspond to a localization radius on the order of 3-4 Å to fulfill the weak overlap condition ($d_{\text{Mn-Mn}} \approx 2\xi$). The accurate knowledge of T_0^{Mott} for each concentration is not sufficient to quantify the localization radius, since the

density of states at E_F is unknown (see Eq. 3.15). Fortunately, impurity concentrations in the percent range will have an additional advantage: they are accessible for ab-initio density-functional theory (DFT) calculations. The numerous theoretical studies of GaMnN electronic structure agree about the location of the Mn (e and t_2) spin-up impurity bands in the midgap region of GaN, still detached from conduction and valence band for concentrations below 20% [111, 144, 145]. It is worth to mention, however, that the absolute energy difference between the e and t_2 spin-up impurity bands to the CBM/VBM cannot be determined with accuracy because of the underestimation of the experimental bandgap. Nevertheless, a quantity which can be well described is the spin-resolved partial density of states (PDOS) of the Mn d-states. In connection with our experiment, it would be interesting to extract the density of states at the Fermi-energy from the calculations, and, in turn, combine them with the experimental $T_0^{(Mott)}$ via Eq. (3.15) in order to get estimated values of the localization radius ξ . Table 3.5 lists the density of states at E_F extracted from several theoretical studies and the inferred values of ξ . As common for theoretical studies, the input Mn-concentration for the calculation of $N(E_F)$ has discrete values due to the size of the supercell, and thus we have combined the experimental $T_0^{(Mott)}$ of the samples which contains a similar concentration of incorporated Mn. The $N(E_F)$ values from $c_{Mn}(\text{supercell})=6.25\%$ are therefore connected with samples G0316 ($c_{Mn}(\text{fm/pm})=6.2\%$) and G0358 ($c_{Mn}(\text{fm/pm})=5.6\%$). Localization radii around 3 and 1 Å are respectively inferred taking into account the scattered values of $N(E_F)$ from different authors.

Reference	$c_{Mn}^{(exp)}$ [%]	$c_{Mn}^{(spc)}$ [%]	$N(E_F)$ [eV ⁻¹ cm ⁻³]	T_{Mott} [K]	ξ [Å]	$R_{hop}^{(100K)}$ [Å]	$R_{hop}^{(5K)}$ [Å]
Titov <i>et al.</i> [145]	6.2	6.25	6.6×10^{20}	5.8×10^6	3.8	22.1	46.4
Antonov <i>et al.</i> [146]	6.2	6.25	1.3×10^{21}	5.8×10^6	3.0	17.5	36.7
Sandratskii <i>et al.</i> [147]	6.2	6.25	2.4×10^{21}	5.8×10^6	2.5	14.6	30.7
Sanyal <i>et al.</i> [144]	6.2	6.25	3.2×10^{21}	5.8×10^6	2.3	13.4	28.1
Titov <i>et al.</i> [145]	5.6	6.25	6.6×10^{20}	2.2×10^8	1.2	17.4	36.5
Antonov <i>et al.</i> [146]	5.6	6.25	1.3×10^{21}	2.2×10^8	0.9	13.1	27.5
Sandratskii <i>et al.</i> [147]	5.6	6.25	2.4×10^{21}	2.2×10^8	0.8	11.6	24.3
Sanyal <i>et al.</i> [144]	5.6	6.25	3.2×10^{21}	2.2×10^8	0.7	10.2	21.4

Table 3.5: Localization radii ξ estimated from the experimental T_0^{Mott} and several values of $N(E_F)$ extracted from theoretical studies. The T_0^{Mott} of samples G0316 and G0358 have been considered, which had the closest Mn-concentration $c_{Mn}^{(exp)}$ (fm/pm) to the input $c_{Mn}^{(spc)}$ taken for the calculations. The theoretical value of $N(E_F)$ has not been scaled for the sample with $c_{Mn}^{(exp)}$ (fm/pm)=5.6%. The average hopping distances R_{hop} have been also calculated at two different temperatures.

The localization radius derived for the highest doped sample (G0316- $c_{Mn}^{(exp)}=6.2\%$)

seems to fulfill the weak overlap condition ($d_{Mn-Mn} \approx 2\xi$) within the accuracy of determining $N(E_F)$ from ab-initio calculations. This is consistent with the sharp decrease of $T_0^{(Mott)}$ and the onset of ferromagnetic interactions observed by magnetometry. The weak overlap of the localized wave functions at such Mn-Mn distances, is also in well agreement with the observation of a low Curie-temperature ($T_c \approx 11$ K). Regarding the sample with ($c_{Mn}^{exp} = 5.6\%$), which also showed indications of ferromagnetic coupling⁸ at very low temperatures, the localization radius appear too short to account for a direct wave function overlap. However, since the transport is governed by variable-range hopping, the electrons are able to hop over larger distances than nearest-neighbors. The average hopping distance can be derived from the localization length as

$$R_{hop}(T) = \frac{3}{8} \xi \left(\frac{T_0^{(Mott)}}{T} \right)^{1/4} \quad (3.16)$$

Table 3.5 lists the average hopping distances inferred at two different temperatures. Already at 100 K, the electrons are able to hop over distances larger than 10\AA . The values of R_{hop} at 5 K are valid only assuming that Mott-VRH transport still holds in this temperature range. Recall that an eventual crossover to the Efros-Shklovskii VRH-regime could not be evaluated due to the unmeasurable resistances below 100 K. Regarding sample G0358 (lower half of Table 3.5), the large average hopping distances suggest that if the electron spin is conserved during the hopping process (*coherent hopping*), magnetic interactions can be mediated, in spite of a short localization radius. Although this approach has been put forward to explain ferromagnetic interactions in oxide DMS [44], we estimate that the magnetic coupling between Mn-states cannot arise *exclusively* due to spin-coherent hopping, especially at such large distances. However, it may enhance the magnetic coupling strength when the localization radii are not far from the overlap ($d_{Mn-Mn} \approx 2\xi$). The spin coherence length in a hopping process is the unknown parameter which precludes a further analysis of the scenario. Independently on the conclusions which can be drawn from the hopping parameters, i.e., the evolution of T_0^{Mott} and ξ , several *ab-initio* studies found out that the ferromagnetic exchange interaction is negligible for average Mn-Mn distances higher than 8\AA [135, 134, 136]. This situation is in well agreement with our experimental observations of a very small localization radius ($\xi \leq 1\text{\AA}$) and the absence of ferromagnetic signatures at such concentrations ($c_{Mn} \leq 5\%$). The prospects of high- T_c ferromagnetism in GaMnN are not so encouraging. The window for the achievement of a strong overlap between Mn-states is enormously narrowed by the formation of secondary phases at high Mn-concentrations. On the other hand, it has been demonstrated that by surpassing a critical average distance d_{Mn-Mn} , the strong localization of the states will soften (increase in ξ), enabling a

⁸based on the point of inflection of the FC-magnetization

more effective playground for magnetic interactions to take place. The limitation thereby is that this critical distance ($d_{Mn-Mn} \approx 2\xi$) cannot be tuned, because the localization radius is an *intrinsic* property of an impurity state in a given host matrix. As a consequence, given the localized nature of substitutional Mn in GaN ($3d^4$ centers), the only hope to boost T_c in GaMnN is to face the hard job of extending the solubility limit, as it is being done in GaMnAs. At this stage, although the weak ferromagnetic coupling and the derived Curie-Temperature in GaMnN do not allow room for applications, it represents a good example to show the interplay between electronic localization and the magnetic coupling in dilute magnetic semiconductors.

3.3 Gd-doped GaN

Among the variety of potential DMS systems which have been studied in the last decade, Gd-doped GaN represents one of the most intriguing cases. Doping of GaN with very low Gd concentrations ($N_D \leq 10^{17} \text{cm}^{-3}$) has been reported to give a colossal room-temperature magnetic moment of around $1000\mu_B$ per magnetic impurity [19, 14]. The authors attempted to explain the magnetic moment exceeding the $8\mu_B$ per Gd atom by an empirical model in which an extended polarization of the GaN-matrix is assumed. However, x-ray magnetic circular dichroism (XMCD) experiments at the Ga K-edge ruled out a significant polarization of the matrix [148]. The generation of intrinsic defects in GaN layers by implantation of Gd^{3+} ions and the evolution of the saturation magnetization after annealing, suggest the formation of local magnetic moments on Ga and/or N interstitials [15]. On the other hand, other experimental reports attempt to explain that long-ranged ferromagnetic interactions in GaGdN are carrier-induced, supported by the observed magnetization enhancement by Si-codoping [16, 149]. Also the calculations by Dalpian and Wei [150] support an electron stabilized ferromagnetism in GaGdN. Recent theoretical studies, however, came to the conclusion that Ga-vacancies are crucial in inducing the ferromagnetic coupling in GaGdN [103, 105]. Moreover, the possibility that localized defect states without any magnetic ions may form local moments and exhibit collective magnetism has been investigated. Cation vacancies in wide-bandgap nitrides might promote the formation of local magnetic moments, and the magnetic coupling between these defect-induced moments is supposed to be long-ranged due to extended tails of the defect wave function [104]. Last but not least, the most recent theoretical study by Mitra *et al.* [106] suggests that the presence of interstitial nitrogen and oxygen in octahedral sites is a more likely source of defect-induced ferromagnetism, based on the formation energy of native defects in GaN.

As evident from the scattered results reported so far, there is still ongoing discussion about this unexpected magnetic behavior in Gd-doped GaN. The aim of the present work is to perform a comprehensive study about the electrical transport properties of the ferromagnetic GaGdN epilayers, in order to have an insight of the electronic properties and defect landscape in this intriguing material. This might also help to clarify which picture is suitable to interpret the still controversial origin of the observed room-temperature ferromagnetic coupling. Special attention will be paid on identifying the defects which could be induced by Gd-doping; for this purpose, additional spectroscopy studies have been performed. The structural and magnetic properties have been also investigated, in particular their Gd-concentration dependence.

3.3.1 Growth conditions and structural properties

Unlike the case of Mn-doped GaN, the epitaxial growth of Gd-doped GaN was carried out with the same optimized parameters for the growth of undoped GaN, near the

stoichiometric point in the slightly metal-rich regime at a substrate temperature of 760 °C. The samples were grown both on GaN(0001)/Al₂O₃ templates (series A) and semi-insulating 6H-SiC(0001) substrates for electrical characterization (series B), with a thickness of about 500nm. The range of Gd-concentration varied from 10¹⁶cm⁻³ to 10²⁰cm⁻³, measured by time-of-flight secondary ion mass spectroscopy (TOF-SIMS). The Gd concentration is calculated from the ¹⁶⁰Gd peak because no mass interferences are expected there.

Under optimized growth conditions, the structural characterization by X-ray diffraction showed the absence of secondary phases or Gd-related precipitates, except for the highest doped sample ($N_{Gd} = 1.6 \times 10^{20} \text{cm}^{-3}$). The θ -2 θ -scan revealed an additional reflection at $2\theta = 31.1^\circ$, which corresponds to the GdN (111) reflection characteristic of GdN in the rocksalt structure. The cluster diameter inferred from the Scherrer-formula (Eq. 3.2) amounts to $d = 27.8 \text{ nm}$. A close-up of the θ -2 θ -scan with the Gaussian-fit is shown in Fig. 3.27. It is worth to mention, that samples grown directly on Al₂O₃(0001) show a tendency to form GdN clusters even at lower Gd-concentrations. For comparison, a sample with these characteristics is also shown in Fig. 3.27. For this sample, the intensity of the GdN (111) reflection is ten times stronger, although the Gd-concentration is one order of magnitude lower ($\approx 10^{19} \text{cm}^{-3}$). These observations suggest that a significant lattice mismatch by the choice of the substrate -leading to a degradation of crystalline quality- and strain effects catalyze the formation of GdN clusters.

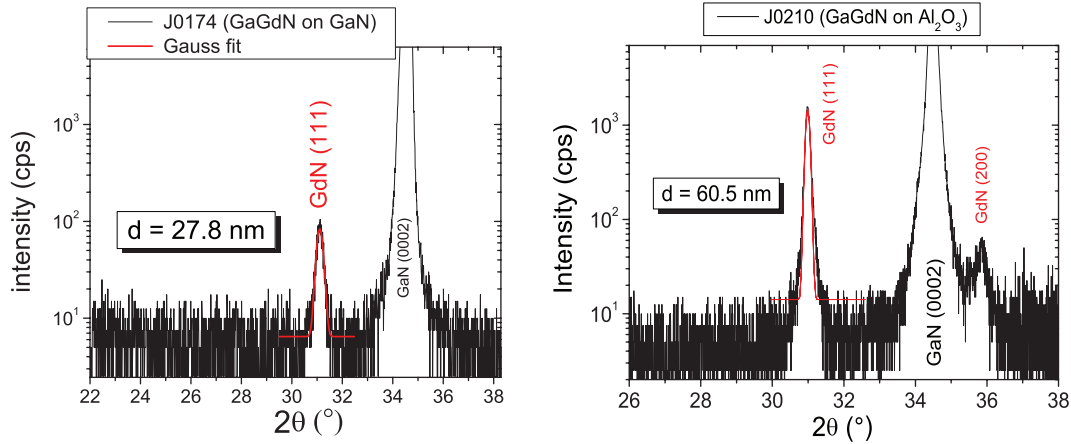


Figure 3.27: θ -2 θ -scan indicating the presence of GdN clusters at $[\text{Gd}] \approx 10^{20} \text{cm}^{-3}$ (left). The formation of the GdN phase is favored when growing GaGdN directly on Al₂O₃ substrates (right).

Since the detection of secondary phases by XRD has its limitations going towards low Gd-concentrations, the set of samples with $[\text{Gd}] \leq 10^{19} \text{cm}^{-3}$ have been studied by means of X-ray fluorescence (XRF) and X-ray absorption near edge structure

(XANES) experiments at the microprobe ID22 of the European Synchrotron Radiation Facility [151]. The composition homogeneity was examined by X-ray fluorescence. By setting regions of interest around the fluorescence lines, in particular the one from Gd, uniform patterns with no intensity changes (≤ 0.02) were observed, suggesting no tendency for agglomeration at those low Gd concentrations. Furthermore, the XANES spectra at the Gd L_3 edge show a fingerprint of the Gd^{+3} state, indicating the incorporation of Gd on Ga-sites. The shape of the X-ray linear dichroism (XLD) of the XANES at the Ga K and Gd L_3 edges confirmed the homogeneous substitutional inclusion of Gd in the GaN-matrix [151]. The experimental study is in well agreement with total energy calculations which reveal Ga substitution as the most favorable site for rare earths in GaN [152].

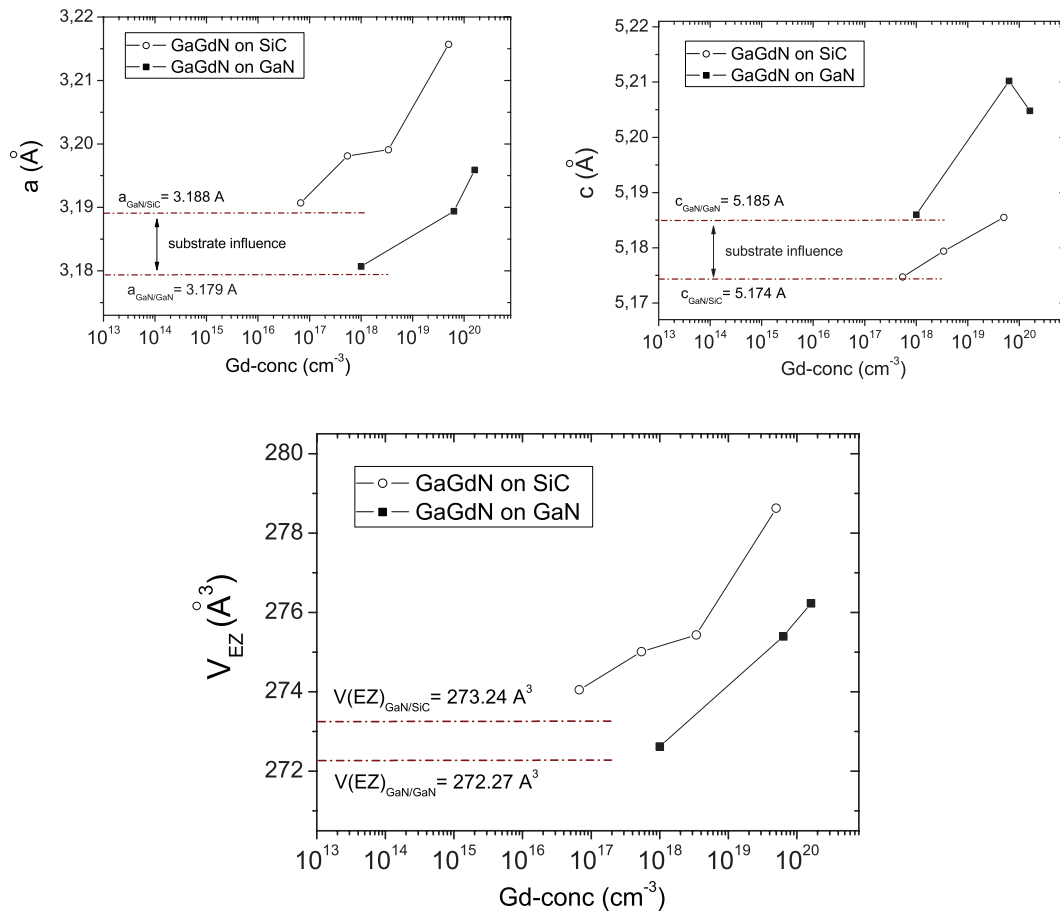


Figure 3.28: Influence of the Gd-doping on the GaN in- and out-of-plane lattice parameters and on the volume of the elementary cell. The dashed lines represent the lattice constant value of undoped GaN for each substrate.

Since the atomic size of Gd-atoms is much larger than the one of Ga, it is expected that substitutional inclusion of Gd causes strain effects in the lattice. At a Gd-concentration of $1 \times 10^{18} cm^{-3}$, the extended x-ray absorption fine structure (EXAFS)

at the Ga K edge did not show any change of the local structure [151], inferring negligible shifts in the lattice parameters. However, for higher Gd-concentrations, high resolution X-ray diffraction could give an information about lattice constant changes. Like in the case of Mn-doped GaN, the samples grown on 6H-SiC (0001) (series B) are much more suitable for the analysis of the lattice constants, since there is no overlap between the reflections of the epilayer and the substrate. The results, plotted in Fig. 3.28, show that the first significant deviations from the lattice parameters of undoped GaN evolve already at concentrations of 10^{18}cm^{-3} for series B and at 10^{19}cm^{-3} for series A. It is worth to mention, that the given reference lattice parameters of undoped GaN in Fig. 3.28 are our experimental values. As discussed in the previous section, high temperature growth of GaN epitaxial layers on SiC results in a residual tensile strain component due to the difference in thermal expansion coefficients. The in-plane biaxial tensile strain (compressive in the out-of-plane direction) has been quantified, and it is shown in Fig. 3.28 as the difference between the reference lattice constants (dashed lines). As expected, the lattice parameters converge to this value when decreasing the Gd-concentration. The increase of both a and c parameters with Gd-concentration, leading to an overall expansion of the unit cell, suggests that there is an hydrostatic strain component which might be related to the incorporation of Gd. Note that the highest doped sample in series A ($N_{\text{Gd}} = 1.6 \times 10^{20}\text{cm}^{-3}$), where GdN clusters were detected, shows a slight decrease in the lattice constant c leading to a weaker hydrostatic strain dependence on Gd-concentration. The relatively high magnitude of the hydrostatic strain component already at concentrations below the percent range, suggest that the GaGdN lattice experiences a distortion which can be relieved in form of dislocations, or by forming other crystallographic phases. This could explain the very low solubility limit in Gd-doped GaN.

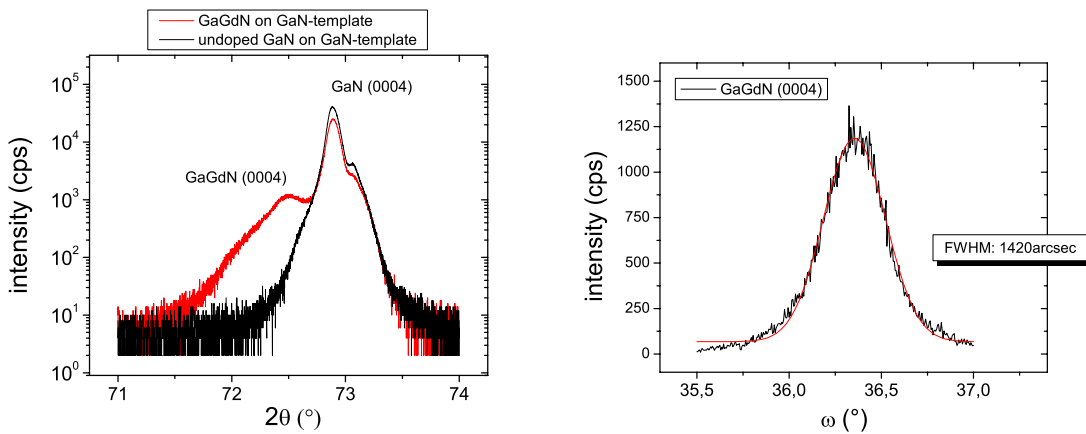


Figure 3.29: θ - 2θ -scan near the (0004) reflection of the highest doped sample (left). The reflections from the GaGdN epilayer and GaN-MOVPE-template can be clearly distinguished. *Rocking curve* scan of the GaGdN (0004) reflection with the Gaussian fit (right).

Regarding the crystalline quality of the samples, symmetric and asymmetric *rocking curve* scans have been performed on both sample series. Like in the case of Mn-doped GaN, the homoepitaxial growth on MOCVD-templates yields the best results in terms of crystal quality, as the FWHMs values range between 400 and 470 arcsec for the (0002) and between 400 and 630 arcsec for the $(10\bar{1}2)$ and $(11\bar{2}2)$ reflections, respectively. Interestingly, the highest doped sample -containing GdN inclusions- has much higher FWHMs values, reaching 1420 arcsec for the symmetric and 1584 arcsec for the asymmetric reflection. Fig. 3.29 depicts the identification of the (0004) reflection of GaGdN grown on GaN-template and the *rocking curve* on this reflection. The GdN clusters embedded in the GaGdN matrix have a detrimental impact of the crystalline quality of the epilayers, fact which is revealed in the increase of the symmetric rocking widths by a factor of 3. Concerning the series grown directly on 6H-SiC(0001), the symmetric rocking FWHM widths lie between 500 and 750 arcsec, while the asymmetric widths lie between 1300 and 1800 arcsec, the latter being much higher than the series grown on MOCVD-templates. As discussed in the previous section, the lattice mismatch between GaN and SiC in the basal plane creates edge dislocations with Burgers vectors parallel to the film/substrate interface, which have an strong impact on the tilt of the asymmetric planes. High FWHM values corresponding to a broad angular distribution of the crystal planes will be thus a good indicator of the dislocation density. In order to visualize the crystal quality and the role of dislocations in our samples grown on 6H-SiC, we have performed high-resolution transmission electron microscopy (HRTEM). As observed in the cross-sectional images (Fig. 3.30), there are some threading dislocations which extend from the interface to the surface of the GaGdN layer. The \vec{g} vector, which denotes the direction of the electron beam, is perpendicular to the growth direction [0001]. According to the $\vec{g} \cdot \vec{b}$ criterion, the defects with Burgers vector perpendicular to the growth direction (edge and mixed type) will be visualized in this configuration [153].

From a set of low-magnification cross sectional images, the average distance between dislocations has been extracted in one dimension. Since the dislocations tend to coalesce with increasing crystal thickness, the distinction between interface and surface dislocation density has been established. The average distance between dislocations amounts to 43 nm at the interface and 0.2 μm at the surface. Extrapolating the values to 2 dimensions, we estimate the edge dislocation density to be $5 \times 10^{10}\text{cm}^{-2}$ and $2 \times 10^9\text{cm}^{-2}$ for the interface and surface, respectively. These values are comparable with other TEM-studies of GaN grown directly on 6H-SiC (0001) [153, 154]. Recent studies have shown that the dislocation density in GaN/SiC heteroepitaxy can be greatly reduced by the growth of self-assembled GaN-nanoislands [155] or by forming a thin SiN layer through nitridation [156] in the early stage of growth. This methods were not applied in the present work since interfacial layers might create parallel conductive channels and are therefore not desirable for electrical characterization. Given the importance of the interface, high-resolution TEM images have been acquired to confirm the epitaxial growth of GaGdN layers on SiC from the early stage, where no

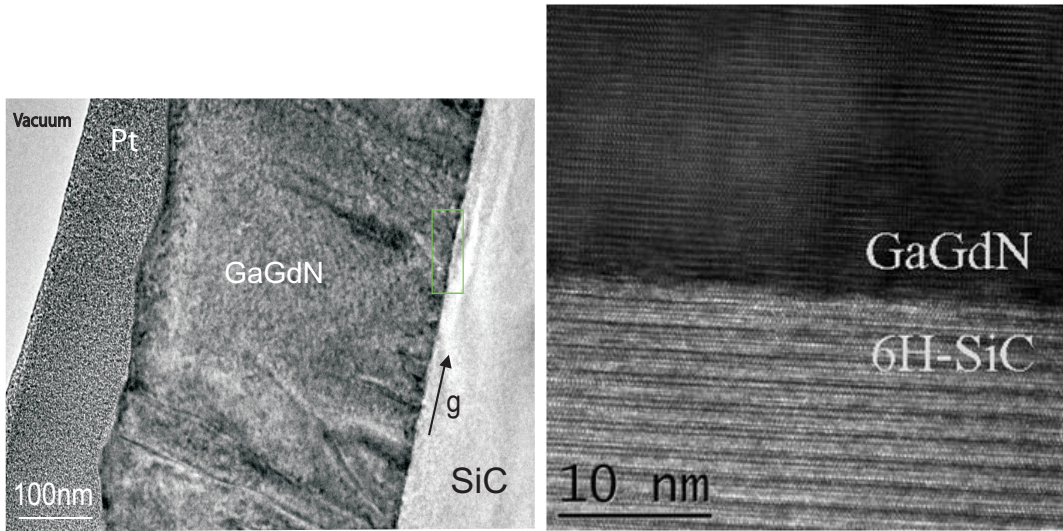


Figure 3.30: Transmission electron micrographs of a GaGdN epilayer grown on 6H-SiC. An overview cross-section image of the whole layer thickness (left) and a high resolution image of the interface (right) are presented.

amorphous or highly defective layer is observed at the interface. Although there are some stacking faults/edge dislocations which can be clearly visualized, we conclude that the overall crystalline quality and interface properties are comparable to the homoepitaxial GaGdN layers.

3.3.2 Magnetic properties

The magnetic properties of Gd-doped GaN epitaxial layers have been investigated in a wide range of Gd-concentrations. The magnetization results reported by Dhar *et al.* [19] pointed towards a colossal magnetic moment per Gd-atom at very low Gd-concentrations, fact which was taken with scepticism. Before searching which atoms or defects are supposed to carry the rest of the moments (Gd alone might carry a maximum of $8\mu_B$), it is more natural to think that a certain amount of ferromagnetic contamination present either in the substrate or in the Gd-cell might be responsible for the observed magnetic signals. In this sense, a very careful analysis of the possible origin of the magnetic signals has been done. As in the case of Mn-doped GaN, ferromagnetic-like contributions stemming from the substrate have been ruled out. Following these findings, the last spurious effect could be the purity of the Gd ingot in the effusion cell. For the range of concentrations investigated in this work, the Gd-cell temperature T_{cell} was held between 675 °C and 1400 °C. To probe for transition metal contaminations from the source, a sample with a high Gd concentration (10^{20} cm^{-3}), corresponding to the highest cell temperature (1400 °C) was analyzed by secondary ion mass spectroscopy (SIMS). To increase the sensitivity of the measurement an oxygen background pressure of 10^{-6} mbar was applied. Note that the detection limit

is 10^{16}cm^{-3} for rare earth elements and 10^{17}cm^{-3} for transition metal elements as determined with ion implanted Gd and Mn reference samples. Figure 3.31 shows an integrated mass spectrum of the highest doped GaGdN sample. No transition metal signals can be observed, whereas the Gd isotopes are clearly visible. We conclude that the transition metal contamination is smaller than the Gd concentration by a factor of at least 10^{-3} , suggesting that even when the source is heated at the highest temperature, the transition metal contamination is under the detection limit of SIMS. In turn, all the ferromagnetic-like signals measured by SQUID have to be related to the Gd-incorporation.

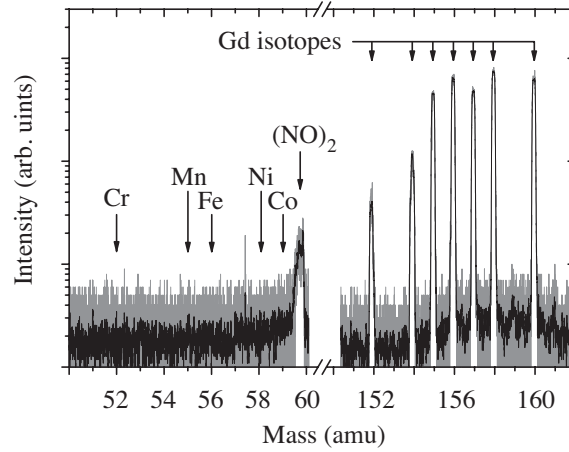


Figure 3.31: Integrated TOF-SIMS spectrum of a 500 nm thick GaGdN layer with a Gd concentration of 10^{20}cm^{-3} . The gray curve shows the raw data. Between 50 and 60 amu no traces of transition metal elements are found. Between 152 and 160 amu the Gd isotopes are clearly visible. The black curve shows a 10-point adjacent average smoothing of the raw data to reveal any hidden signals in the background.

Concerning the magnetic properties of the Gd-doped GaN epilayers, the first series grown both on MOVPE-GaN and 6H-SiC has been found to be ferromagnetic at room temperature in Gd-concentrations ranging from 10^{14}cm^{-3} to 10^{18}cm^{-3} . A field-dependent magnetization scan of a sample with $N_{\text{Gd}} = 1 \times 10^{18}\text{cm}^{-3}$ is presented in Fig. 3.32. The magnetization typically saturates at 10 kOe, and the coercive field is rather small, yielding values between 40 and 100 Oe. Interestingly, the saturation magnetization does not show a strong dependence on Gd-concentration in the investigated range, behavior which has been previously reported by Dhar *et al.* [19, 14]. In terms of the effective spin polarization created by Gd, we could observe nearly the same trend as in Refs. [19, 14], where the average magnetic moment per Gd-atom decreases with increasing concentration and finally saturates near its atomic moment. For clarity, both datasets are superimposed in Fig. 3.33. The black squares and the solid line represent the data and the fit taken from Ref.[19], and the red squares correspond to our experimental values. The filled squares denote that the Gd-concentration has been measured by SIMS, while the open square means that the concentration has

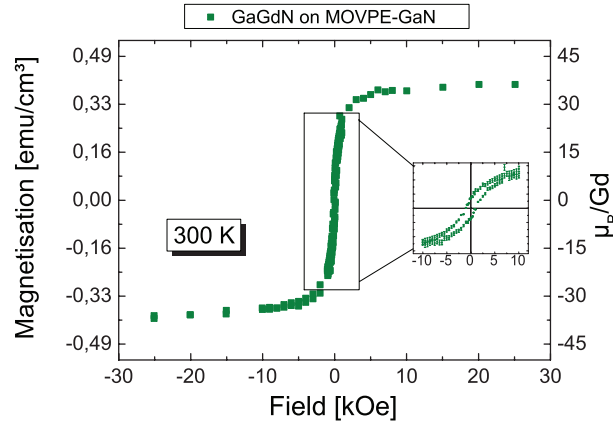


Figure 3.32: Typical field-dependent magnetization of a GaGdN epitaxial layer exhibiting ferromagnetic ordering at room-temperature. The inset shows the small magnitude of coercive field and remanent magnetization.

been extrapolated. Therefore, the inferred value of $p_{eff} \approx 30000\mu_B/\text{Gd}$ has to be taken with caution. Moreover, it is important to mention that the sample J0188 has been grown on 6H-SiC, while all others have been grown homoepitaxially on MOVPE-GaN. This indicates that the choice of the substrate does not have a major influence on the magnetic properties of the samples; it supports an effect related to the Gd incorporation rather than to substrate impurities.

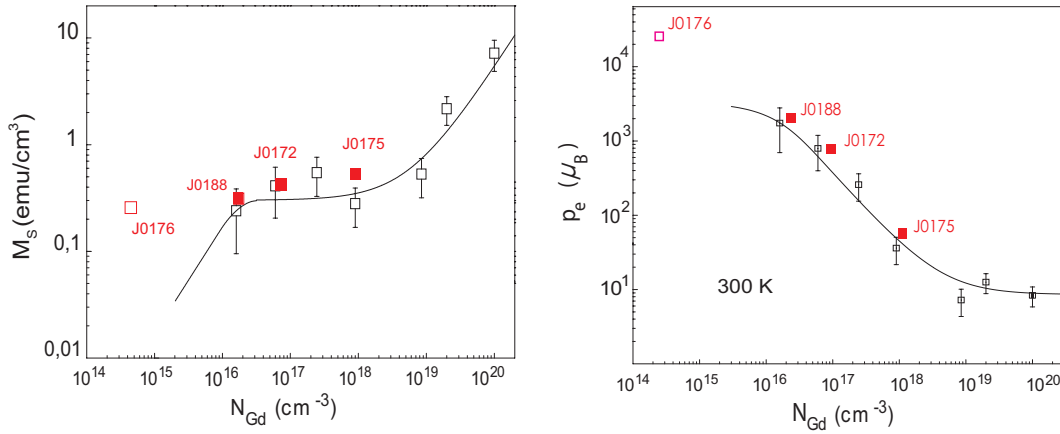


Figure 3.33: Trends of saturation magnetization M_s (left) and effective magnetic moment per Gd-atom p_{eff} (right) with respect to the Gd-concentration. The red squares correspond to our experimental data, the black squares and the solid fit line are taken from Ref.[19].

At a Gd-concentration of 10^{20}cm^{-3} , a ferromagnetic transition could be detected at around 70 K by measuring the temperature dependent magnetization in zero-field cooled (zfc) and field-cooled (fc) mode, as shown in Fig. 3.34. At high temperatures, there is still a difference of 0.02 emu/cm^3 between zfc and fc magnetization which

persists up to 250 K. The magnetic behavior of the highest doped GaGdN epilayer can be interpreted as follows: the transition at around 70 K is in well agreement with the reported Curie-Temperature T_c of the GdN rocksalt structure [157], and can be attributed to the GdN-clusters detected by X-ray diffraction. They will act as a blocked superparamagnetic ensemble up to T_c when they loose the ferromagnetic coupling within the cluster. At high temperatures, they will behave as isolated paramagnetic moments and will not account for the difference between zfc and fc curves (Fig. 3.34-right). This suggests that a part of the Gd atoms, which do not contribute to the GdN phase and have been substitutionally incorporated in the matrix, induce ferromagnetic ordering like in the case of lower Gd-concentrations. The magnetic classification of the GdN phase in the highest doped sample has important implications for the cases with lower Gd-concentrations: even if GdN clusters are present in the samples with $N_{Gd} \leq 10^{20} \text{cm}^{-3}$ -under the detection limit of XRD-, they cannot account for room-temperature ferromagnetism.

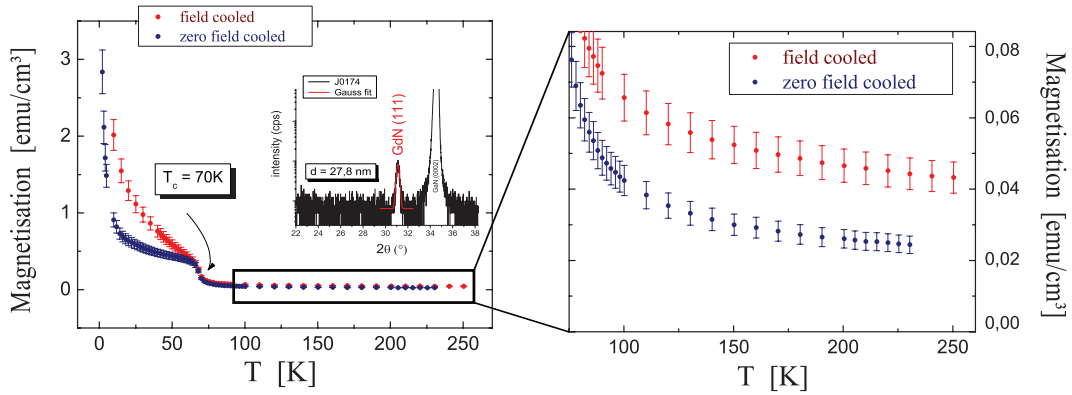


Figure 3.34: Temperature dependent magnetization of the highest doped GaGdN sample. Right: The transition at $T \approx 70$ K is attributed to the GdN clusters detected by XRD (inset). Left: A small difference between zfc and fc measurements persist up to 250K, suggesting a ferromagnetic contribution.

The magnetic properties of highly diluted GaGdN epitaxial layers grown on different substrates has been described so far. However, there are two issues which need to be discussed due to their unprecedented nature: (i) the origin of the long-ranged ferromagnetic ordering, especially at very low Gd-concentrations ($d_{Gd-Gd} \approx 40$ nm), and (ii) the magnitude of the colossal magnetic moments. As mentioned before, element specific X-ray magnetic circular dichroism (XMCD) measurements on the Gd L_3 and the Ga K edge of the samples extensively characterized in Refs.[19, 14], showed a very small polarization of Ga and paramagnetic behavior of Gd [148]. In turn, the empirical model suggesting polarization of the GaN-matrix in form of spheres of influence, which fitted well even with our experimental data (solid line in Fig. 3.33) and was somehow a reasonable approach, could be definitely ruled out. Since then, many theoretical efforts have been made to understand the intriguing phenomena.

The approaches which have been considered to hopefully explain the observations (i) and (ii), rely on the role of point defects on the magnetic properties of GaGdN. In this sense, many theoretical studies included Ga-vacancies [104, 105], Gd- V_{Ga} , Gd- V_{Ga} -O complexes [103], Gd- N_I , Gd- O_I complexes [106] in the supercell to perform *ab-initio* calculations. The results were disencouraging: all calculations found ferromagnetic interactions taking into account the defect of their preference, fact which makes the topic even more controversial. On the other hand, experimental hints towards defect-induced magnetism were rather very feeble: the decrease in magnetization upon annealing [15] or the highly-resistive character of the epilayers [19, 14]. At this point, it is important to mention that our second series of GaGdN epitaxial layers (sample ID J02xx), which aimed to reproduce the first series (sample ID J01xx) to perform further characterization methods, did not share the same properties: the ferromagnetic features disappeared. The results were surprising, since the samples have been grown in the same MBE-chamber and under apparent equal conditions. This points towards the presence of one important change in the growth conditions which cannot be controlled at the first sight. Nevertheless, the existence of both ferromagnetic and non-ferromagnetic GaGdN epitaxial layers grown on both MOCVD-GaN and 6H-SiC substrates, opens up the possibility to find any difference in the electronic properties which might be connected to the presence or absence of ferromagnetic coupling. A detailed knowledge of the electrical transport properties of ferromagnetic and non-ferromagnetic samples is therefore of great interest and will be discussed in the next section.

3.3.3 Electrical transport properties

From the first series, one sample grown on highly-resistive 6H-SiC(0001) which exhibited not only ferromagnetic features at room-temperature but also colossal magnetic moments per Gd-atom, fulfills all the requisites to investigate the correlation between magnetic and electrical transport properties. The temperature dependence of the resistivity, even at moderate doping with Gd concentrations of $N_{Gd}=2\times 10^{16} \text{ cm}^{-3}$ shows an increase of nearly five orders of magnitude when cooling the sample from room temperature to 5 K, as depicted in Fig 3.35. A reference sample of unintentionally doped GaN grown on semi-insulating SiC, which is *n*-type with an activation energy of 20.6 meV and a background carrier concentration of $5.8\times 10^{17} \text{ cm}^{-3}$, is shown for comparison. Under the assumption that the residual *n*-type doping is not significantly altered neither by the incorporation of Gd nor by growth kinetics, the highly-resistive character of GaGdN suggests that Gd-induced deep states fully compensate these native donors.

The temperature dependence of the resistivity does not follow the Arrhenius behavior ($\propto T^{-1}$, but scales with a power law $T^{-1/2}$ at lower temperatures ($T < 25$ K) and with $T^{-1/4}$ in the intermediate temperature range, as depicted in Fig. 3.36. This behavior is characteristic of Efros-Shklovskii variable-range-hopping (ES-VRH) and

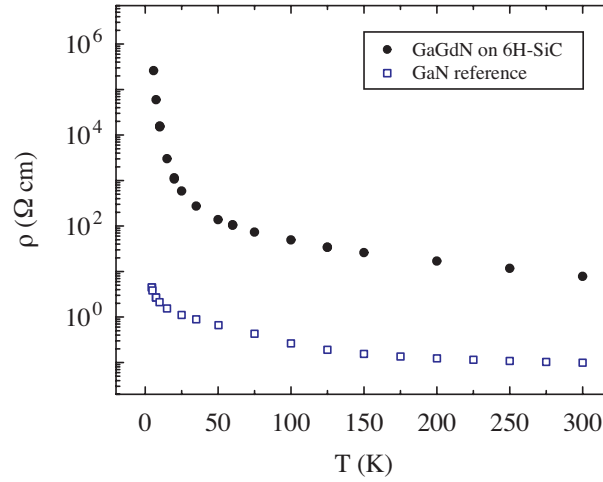


Figure 3.35: Temperature dependence of the resistivity of a GaN reference and a GaGdN epitaxial layer. The Gd-concentration amounts to $2 \times 10^{16} \text{ cm}^{-3}$.

Mott variable-range -hopping (Mott-VRH) in an impurity band of localized states. Above 120 K, the conductances of the GaGdN layer and the bulk substrate fall in the same order of magnitude, neglecting the possibility of further analysis.

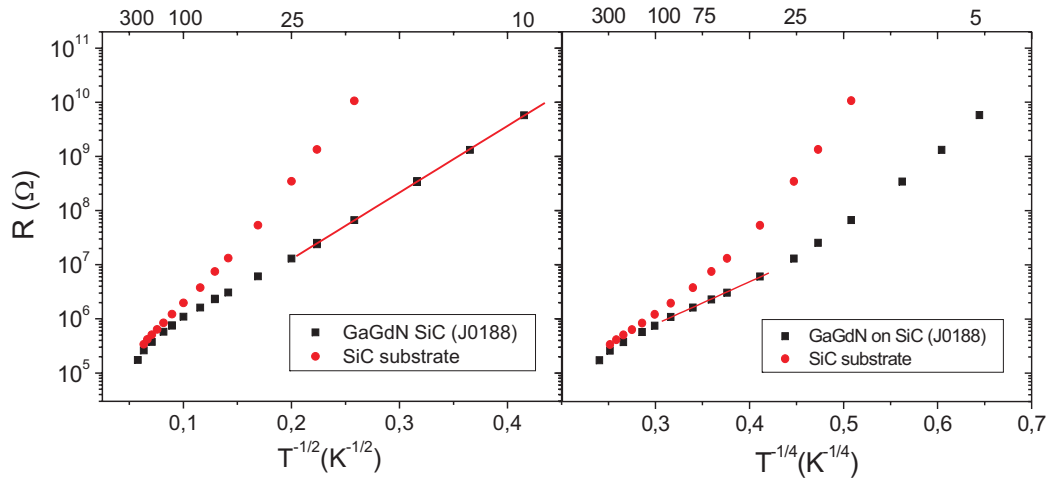


Figure 3.36: Efros-Shklovskii-VRH (left) and Mott-VRH (right) behavior, in the respective temperature ranges. At temperatures above 120 K, the measurement is affected by the parallel substrate conductivity.

A linear regression of the relationship described in Fig. 3.36 yields the characteristic temperature T_0 in each regime. The degree of localization of the electronic states in the impurity band is described in terms of the localization radius ξ which can be estimated from the characteristic temperature T_0 . In the ES-VRH regime, the localization radius scales inversely proportional with $T_0^{(ES)}$

$$\xi = \frac{\beta_{ES}e^2}{k_B T_0^{(ES)} \epsilon} \quad (3.17)$$

where ϵ is the static dielectric constant and $\beta_{ES}=2.8$ is a coefficient obtained by the percolation treatment of hopping conductivity with coulomb interactions [158], e and k_B are the elementary charge and the Boltzmann-constant, respectively. The static dielectric constant is composed of the normal host lattice and an additional contribution due to many-electron interactions [158, 159], following the relation (in cgs units)

$$\epsilon = \epsilon_{host} + 4\pi e^2 N(E_F) \xi^2 \quad (3.18)$$

where $N(E_F)$ is the unperturbed DOS at the Fermi-energy. In the Mott-VRH regime, $N(E_F)$ can be estimated from the Mott characteristic temperature $T_0^{(Mott)}$ and the localization radius ξ , as

$$N(E_F) = \frac{\beta_{Mott}}{k_B T_0^{(Mott)} \xi^3} \quad (3.19)$$

where the coefficient β_{Mott} (obtained from percolation treatment) is 21.2 as calculated by Skal and Shklovskii [66], and $\beta_{Mott}=18.1$ as revised by Castner [77] (the latter has been taken for further analysis). In order to calculate the hopping parameters without knowing $N(E_F)$, one has to be able to observe both the ES-VRH and the Mott-VRH regime in the same sample. The transition occurs when, by increasing the temperature, the average carrier hopping energy ΔE_{hop} becomes larger than the coulomb gap Δ_{CG} , such that electron-electron interactions become comparably small, resulting in a nearly constant density of states at E_F . This transition has been measured in some other material systems like indium oxide [160] or boron-doped diamond [80]. Just few experimental studies of VRH transport in DMS layers are found in the literature [161, 162]. Concerning GaN-based DMS materials, Wu *et al.* observed Mott-VRH in Cr-doped GaN [162]. In their analysis, however, the value of $N(E_F)$ had to be taken from theoretical calculations, due to the lack of data from the ES-VRH regime, as we did in the preceding section for the case of Mn-doped GaN. For GaGdN, all the relevant parameters can be determined from the experiment. The analysis of the temperature dependent resistivity has been done according to the method suggested by Zabrodskii [163], which by starting from the general temperature dependent hopping law

$$\rho(T) = BT^n \exp(T_0/T)^m \quad (3.20)$$

provides a precise way to estimate the hopping exponent m and thus distinguish between hopping regimes by evaluating the quantity $w(T)$, which corresponds to temperature dependent exponential part of the hopping probability ($\cong \Delta E/k_B T$)

$$w(T) = \Delta E/kT = -\frac{\partial \ln \rho}{\partial \ln T} = n + m(T_0/T)^m \quad (3.21)$$

where ΔE is the temperature dependent activation energy. For an exponential hopping dependence of ρ where the second term of $w(T)$ is much larger than the first term ($n \ll (T_0/T)^m$), it follows $\log w(T) \cong \log(mT_0^m) - m \log(T)$. This last expression has the form of a linear equation $y=a-bx$, where $y=\log w(T)$ and $x=\log T$. The hopping exponent is thus obtained directly from the slope, and the characteristic temperature T_0 from the y-axis intercept by plotting $w(T)$ on a log-log scale. For calculational purposes, the quantity $w(T)$ is obtained using the equivalent expression

$$-\frac{\partial \ln \rho}{\partial \ln T} \cong -\bar{T} \frac{\Delta \ln \rho}{\Delta T} \quad (3.22)$$

where ΔT is the temperature difference between two adjacent data points and \bar{T} denotes their average temperature. The result of the analysis of the GaGdN layer grown on SiC is shown in Fig. 3.37. The data in the ES-VRH regime (up to 25 K) can be well fitted, yielding a value of $x = -m_1 = (0.52 \pm 0.02)$ for the hopping exponent. In the Mott-VRH regime, the data are masked by the conductivity of the substrate for temperatures above 120 K, so that the temperature dependence of the resistivity is fitted with an exponent of $x = -m_2 = (0.26 \pm 0.09)$ in the intermediate temperature range below 120 K.

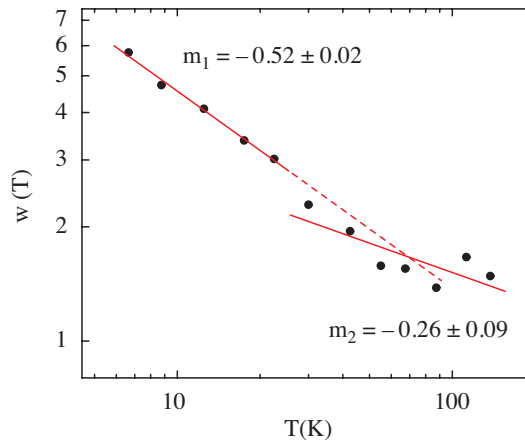


Figure 3.37: Transition from ES-VRH to Mott-VRH as determined by the method suggested by Zabrodskii [163].

The characteristic temperature in the different regimes is calculated using the relation

$$T_0 = \left(-\frac{10^A}{m} \right)^{(-1/m)} \quad (3.23)$$

where A is the intercept of the linear regression with the y -axis and m denotes the slope of the fit. Using error propagation for the covariant variables A and m , one obtains values of $T_0^{(ES)} = (657 \pm 186)$ K and $T_0^{(Mott)} = (1.0 \pm 3.7) \times 10^5$ K for

the characteristic temperatures. The large error, especially in the determination of $T_0^{(Mott)}$ precludes a fully quantitative analysis. Still, some important conclusions can be drawn from the evaluation of the hopping parameters. These parameters, which are the localization length ξ , the static dielectric constant ϵ and the unperturbed density of states at the Fermi-level $N(E_F)$ in the impurity band, are fingerprints of the present defects and can be determined in terms of $T_0^{(ES)}$ and $T_0^{(Mott)}$ according to Eqs. (3.17–3.19). The obtained localization length is $\xi = (3.7 \pm 16)$ nm, and the static dielectric constant ϵ has a value of (19 ± 85) . This is an indication that GaGdN with $N_{Gd} = 2 \times 10^{16} \text{ cm}^{-3}$ is not in the critical regime close to the metal-insulator transition (MIT), where the anomalous contribution of ϵ becomes huge due to the divergence of the localization length. The critical behavior of ϵ when approaching the MIT is known as polarization catastrophe [78]. The obtained unperturbed density of states at the Fermi-level amounts to $N(E_F) = (4.3 \pm 73) \times 10^{19} \text{ eV}^{-1} \text{ cm}^{-3}$. Another intrinsic property of the system is the coulomb gap energy Δ_{CG} , determined from the relation

$$\Delta_{CG} = \frac{e^3 N(E_F)^{1/2}}{\epsilon^{3/2}} \quad (3.24)$$

and yielding a value of (4.2 ± 8.0) meV. In order to evaluate the consistency of the derived hopping parameters, temperature dependent quantities as the average hopping energy

$$\Delta E_{hop}^{(ES)} = \frac{1}{2} k_B T (T_0^{(ES)}/T)^{1/2} \quad (3.25)$$

or the average hopping distance

$$R_{hop}^{(ES)} = \frac{1}{4} \xi (T_0^{(ES)}/T)^{1/2} \quad (3.26)$$

have been calculated in the Efros-Shlikovskii regime, where the substrate contribution is negligible throughout the whole temperature range. At 25 K, the average hopping energy in the ES-VRH regime is $\Delta E_{hop}^{(ES)} = (5.9 \pm 0.9)$ meV and is of the same order of magnitude as the coulomb gap energy Δ_{CG} , an indication of the onset of the transition to the Mott-VRH regime. This is in agreement with the crossover data presented in Fig. 3.37. Furthermore, for consistency, the average hopping distance R_{hop} has to be larger than the localization radius ξ and larger than the mean impurity distance. At the high-temperature boundary, where the smallest hopping distance is expected, we obtain $R_{hop}^{(ES)}(25 \text{ K}) = (5.0 \pm 21)$ nm. Therefore, it is reasonable to assume that the first condition is fulfilled. However, assuming Gd as the impurity responsible for the VRH-transport, the mean distance between two centers estimated from the experimental Gd-concentration would be $d_{Gd-Gd} = 36.8$ nm, which is larger than the inferred mean hopping distance, even considering the uncertainty in determining R_{hop} . In this case, the second condition would not be fulfilled. Moreover, at concentrations of $N_{Gd} = 2 \times 10^{16} \text{ cm}^{-3}$ it would not be possible to fully compensate the residual donors

in unintentionally doped GaN. Both arguments suggest that other defects, which are present in a larger concentration than the Gd atoms, are the effective source for the electronic localization and VRH-transport in GaGdN. These defects have to be either deep donors or acceptors, in order to account for the observed compensation.

The coexistence of ferromagnetism and variable-range-hopping was studied by Sheu *et al.* for lightly doped GaMnAs [161]. In this material system, an impurity band of substitutional Mn acceptors is formed, and its compensation ratio can be changed by the controlled addition of As antisites which act as double donors. It has been shown that the mixed valences of the Mn-acceptor will account for ferromagnetic behavior via a double-exchange mechanism [161, 164]. In the GaGdN system, the situation is slightly different. A sizable concentration of acceptors (or deep donors) is introduced even at very low Gd-doping, forming an impurity band in which the donor electrons are trapped. However, in both cases, the result is a partially filled impurity band where VRH transport occurs. Therefore, the scenario of double-exchange between defect states with local and energetic disorder may be also applicable to GaGdN, given that the number and extension of defect states is enough to account for hybridization.

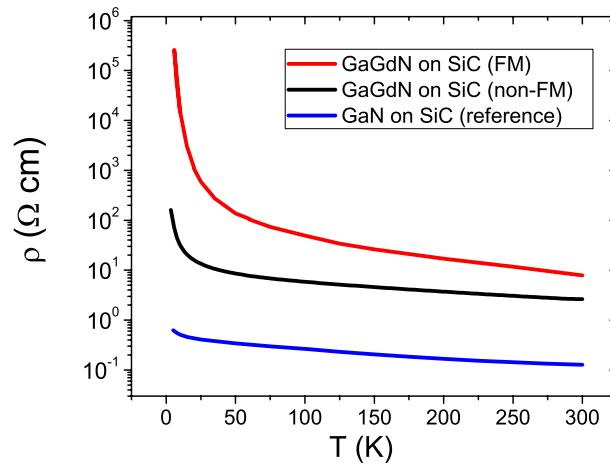


Figure 3.38: Temperature dependence of the resistivity of a ferromagnetic (FM) and non-ferromagnetic GaGdN epilayer, compared to an undoped GaN reference sample.

So far, the electrical transport characteristics of highly-diluted, ferromagnetic GaGdN have been investigated and discussed. For comparison, a sample from the second series, which failed to reproduce the room-temperature ferromagnetic properties of the first series, was analyzed in the same way. The epilayer was grown on semi-insulating 6H-SiC (0001) and under the same growth conditions, with a concentration of $N_{Gd} = 5.4 \times 10^{17} \text{ cm}^{-3}$, as measured by SIMS. The temperature dependence of the resistivity is shown in Fig. 3.38, in comparison to the ferromagnetic GaGdN sample with $N_{Gd} = 2 \times 10^{16} \text{ cm}^{-3}$ and an undoped GaN reference. The absolute resistivity is higher than the reference undoped sample by two orders of magnitude, but lower than the ferromagnetic sample throughout the whole temperature range.

On the other hand, the temperature dependence of the resistivity is not as strong as in the ferromagnetic sample, yielding an increase of at most two orders of magnitude by cooling down the sample from 300 K to 4 K. The measurement of the Hall-resistivity in order to determine the carrier type and activation energy, did not give reasonable values, an indication of electronic transport by hopping within an impurity band of localized states. Following the same systematic procedure, the temperature dependent resistivity was plotted against $T^{-1/2}$ and $T^{-1/4}$ to evaluate if the transport is dominated by variable-range-hopping. As shown in Fig. 3.39, both ES- and Mott-VRH regimes could be identified at different temperature ranges, revealing the same qualitative features which were already observed in the ferromagnetic GaGdN sample. Furthermore, the residual donor states are fully compensated in both cases. Then, the interesting question is whether both ferromagnetic and non-ferromagnetic GaGdN layers share the impurity band characteristics, in other words, if the same defect is responsible for the electronic localization.

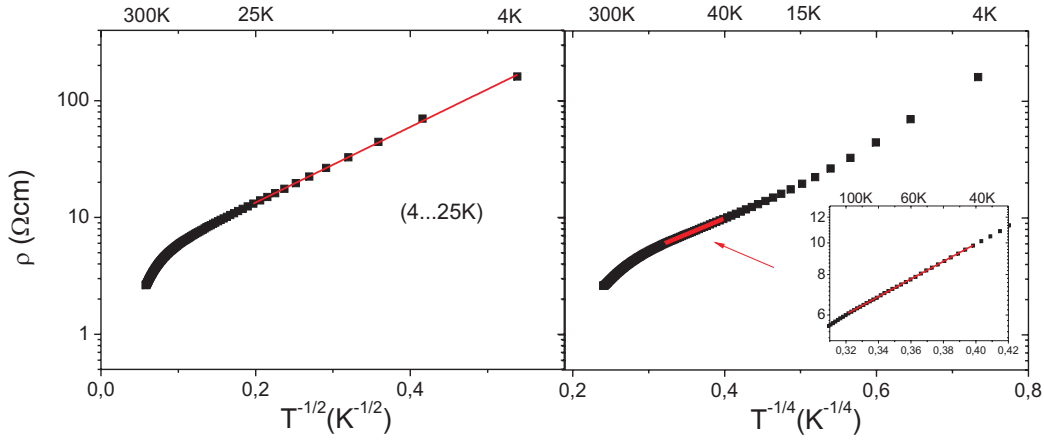


Figure 3.39: Efros-Shklovskii and Mott-VRH behavior in a non-ferromagnetic GaGdN epilayer grown on 6H-SiC. The Gd-concentration amounts to $5.4 \times 10^{17} \text{ cm}^{-3}$

For that purpose, the hopping parameters are calculated using the method of Zabrodskii [163], in analogy to the ferromagnetic sample. The transition is found to occur at around 30K, and the linear regressions for each regime are plotted in Fig. 3.40. The values for the slope m are similar to the ones inferred from the ferromagnetic sample, but the y-axis intercepts differ clearly. Consequently, the characteristic temperatures in the Efros- and Mott-regime will be drastically different, yielding values of $T_0^{(ES)} = (36 \pm 6) \text{ K}$ and $T_0^{(Mott)} = (3.3 \pm 2.1) \times 10^3 \text{ K}$. The parameters ξ , $N(E_F)$, ϵ and Δ_{CG} have been derived using Eqs.(3.17-3.19) and are summarized in Table 3.6, together with the obtained parameters of the ferromagnetic sample.

By direct comparison, the hopping parameters are very different, especially the localization radius ξ and the static dielectric constant ϵ . However, it is not easy to determine at a first glance whether the same defect is responsible for the observed

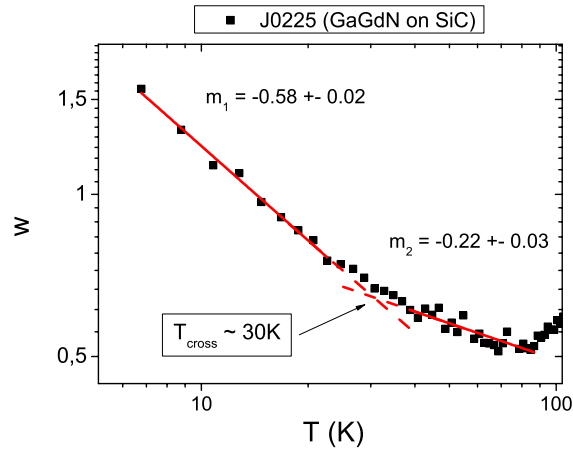


Figure 3.40: Transition from ES-VRH to Mott-VRH as determined by the method of Zabrodskii and Zinovewa. The slope and the y-axis intercept determine the characteristic temperature T_0 .

Sample	N_{Gd} [cm^{-3}]	$T_0^{(ES)}$ [K]	$T_0^{(Mott)}$ [K]	$N(E_F)$ [$eV^{-1}cm^{-3}$]	ϵ	ξ [nm]	Δ_{CG} [meV]
J0188 (FM)	2×10^{16}	768	100000	4×10^{19}	19	3.7	4.2
J0225 (non-FM)	5.4×10^{17}	36	3306	1.2×10^{19}	74.4	17.4	0.3

Table 3.6: Hopping parameters of a ferromagnetic and non ferromagnetic GaGdN epilayer grown on 6H-SiC.

electronic localization, since the Gd-concentration differs by more than an order of magnitude. In particular, the Gd-concentration of the non-FM GaGdN layer could be sufficient to compensate the residual donors, assuming Gd itself (Gd^{3+} centers) as the compensating impurity. Still, there are two arguments which speak against this idea. First, the Gd-4f spin-split states, due to its large exchange splitting, are expected to be resonant with the valence and conduction band, thus not inducing deep states in the GaN bandgap. Second, the rather large localization length would not be consistent with the localized nature of Gd-4f states. Therefore, Gd-states can be ruled out as the source for electronic localization in both ferromagnetic and non ferromagnetic GaGdN. The inferred impurity band characteristics could be then explained in terms of (i) two different dominating defects or (ii) the same type of defect but present at different concentrations. The latter possibility seems rather unlikely, since the localization radius, a fingerprint of the impurity potential, differ too much for such similar values of $N(E_F)$. So it is more natural to think that the impurity band of the non-ferromagnetic sample, hosting more delocalized states and with a narrow Coulomb-gap width, is caused by another type of defect.

The role of defects in mediating magnetic interactions in dilute magnetic semiconductors is currently being investigated with great effort. Many experimental results suggesting room-temperature ferromagnetic coupling in novel material systems are

very sensitive to the growth conditions and thus difficult to reproduce. GaGdN is not the exception; from our results it is evident that there is an uncontrolled formation of defects during growth, which lead to electronic localization and VRH-transport. In order to explain the coexistence of VRH transport and defect-induced ferromagnetism, especially at very low magnetic impurity concentrations (e.g. sample J0188, $N_{Gd}=2\times 10^{16}\text{cm}^{-3}$), it is necessary that the defects possess a non-zero magnetic moment, and that their wave functions show an appreciable overlap despite their localized nature. This overlap ($d \approx 2\xi$) will occur at a characteristic defect distance, defined by the localization length ξ , as we have seen in GaMnN. In this sense, the obtained localization radius of the ferromagnetic sample which extends over many GaGdN unit cells enable more room for a sizable overlap of the localized wave-functions. Additionally, in order to explain the observed colossal magnetic moments, the defects should be present in a great number per Gd impurity, and preferably couple ferromagnetically to the Gd^{3+} ions incorporated in the matrix. The existence of a defect (or defect complex) which fulfills *all* the above considerations seems indeed very difficult. Surprisingly, several *ab-initio* total-energy calculations proved the suitability of several defects and complexes (with or without Gd) in mediating a ferromagnetic coupling in GaGdN [103, 104, 105, 106, 107].

The most commonly discussed defect in connection to the ferromagnetism of GaGdN is the Ga vacancy [103, 104, 105, 107] which is a triple acceptor. Recall that according to thermodynamic considerations, the Ga-vacancies have a low formation energy at n-type conditions and are therefore likely to be incorporated during the GaGdN growth. Dev *et al.* investigated the formation of local magnetic moments for Ga vacancies in GaN *without* inclusion of any magnetic impurities by first-principles calculations [104]. Neutral Ga vacancies are found to have an antiferromagnetic arrangement whereas charged states do couple ferromagnetically. In a recent report, the same authors [107] extended the study to evaluate the magnetic properties of $V_{Ga}\text{-O}_N$ in GaN, finding a ferromagnetic ground state for charged $V_{Ga}\text{-O}_N$ complexes. The addition of oxygen in the study was an attempt to approach more realistic growth conditions, where O_N are the dominant residual impurities, and are supposed to decorate the Ga-vacancies [42]. Besides, the formation of decorated V_{Ga} with oxygen substitutionals has been found to be energetically favored towards the single vacancy. In similar fashion as Ga-vacancies, $V_{Ga}\text{-O}_N$ complexes induce deep energy states in the bandgap. The calculated spin-resolved density of states is shown in Fig. 3.41.

Both cases would fit well with our observation of ferromagnetism in compensated GaGdN, since the partial filling of the defect impurity band will account for charged acceptor states. The authors in [104, 107] also highlight that Ga vacancy states are indeed localized but do possess extended defect wave function tails which are supposed to mediate the ferromagnetic interactions. This fact is in qualitative agreement with our experimental observations of VRH transport with a localization length which turns out to be much larger than expected for 5d- or strongly localized 4f-Gd states (and ten times larger than the 3d-states of Mn in GaN). In any case, to account

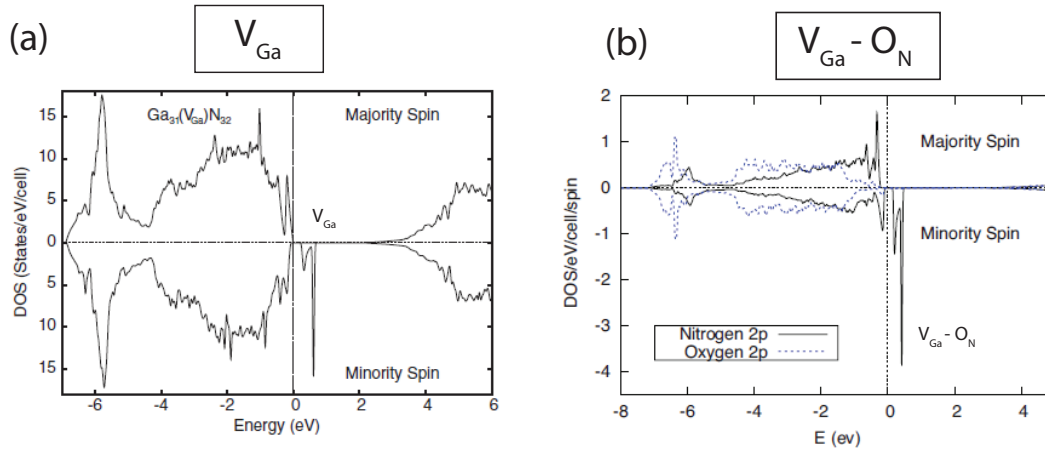


Figure 3.41: Spin-resolved density of states for V_{Ga} (a) and for $V_{Ga}-O_N$ (b) defects, calculated in a 64-atom GaN supercell, taken from [104, 107]. The spin-polarized defect band lies within the bandgap of GaN.

for compensation of the residual donor states, the concentration of V_{Ga} or $V_{Ga}-O_N$ complexes should be around 10^{18}cm^{-3} . Interestingly, the presence of magnetic impurities is not a requirement for the magnetic coupling in this scenario. However, it is likely that the supply of Gd during growth promotes the formation (or suppression) of certain point defects in GaN, having an indirect effect which promotes the scenario of Ga-vacancy mediated ferromagnetism.

Another theoretical study by Gohda *et al.* included both Ga-vacancies and Gd impurities in the supercell [105]. It is found that the local moments of the Gd atoms and the Ga vacancies order ferromagnetically, as well as the moments of the Ga-vacancies among themselves. The authors suggest that the colossal magnetic moments observed in GaGdN arise mainly due to a high number of Ga vacancies per Gd atom. According to our experimental observations, magnetization values exceeding $1000 \mu_B$ per Gd would require a ratio of $N_{V_{Ga}}/N_{Gd} \approx 300$ vacancies per Gd atom. For a Gd concentration of $2 \times 10^{16} \text{cm}^{-3}$ this would result in a Ga vacancy concentration of about $6 \times 10^{18} \text{cm}^{-3}$, which would be high enough to fully compensate the residual donors. A further study involving V_{Ga} and Gd was done by Liu *et al.* [103]. They found a strong $p-d$ exchange interaction between $5d$ -Gd states and valence band p -like states of GaN in the presence of V_{Ga} . This scenario implies the existence of free holes, since the p -states will be pushed above the Fermi-energy in one spin channel to account for spin polarization of the valence band. The authors in [103] explained the high resistivity of GaGdN samples by the scattering of the free holes on a high density of intrinsic defects. However, the existence of free holes (though with very low mobility due to scattering) is not consistent the observation of variable range hopping transport.

Based on formation energy arguments, Mitra and Lambrecht [106] suggested oxygen and nitrogen interstitials (O_I , N_I) as a more plausible source of ferromagnetism in GaGdN. The authors in [106] calculated a ferromagnetic ground state both for a

Gd- N_I and Gd- O_I complex state, and, in addition, showed that both interstitial defects preferably migrate towards Gd at typical growth conditions. It was found that while N_I is attracted toward the Gd_{Ga} by a high binding energy keeping the bond stable, the resulting bond in the case of the Gd_{Ga} - O_I complex was not particularly strong. However, the oxygen migration towards Gd was motivated by an energetically favorable reaction between a remote oxygen substitutional O_N with a Gd_{Ga} to form a Gd_{Ga} - O_I pair, provided that N replaces the substitutional site left behind by oxygen ($O_N \rightarrow O_I$). This is not unlikely since there is sufficient N-supply during growth. In addition, both complex states are found to induce localized states in the midgap region of GaN, as depicted in Fig. 3.42, fact which make them also feasible candidates to explain our observation of variable-range hopping transport in ferromagnetic GaGdN.

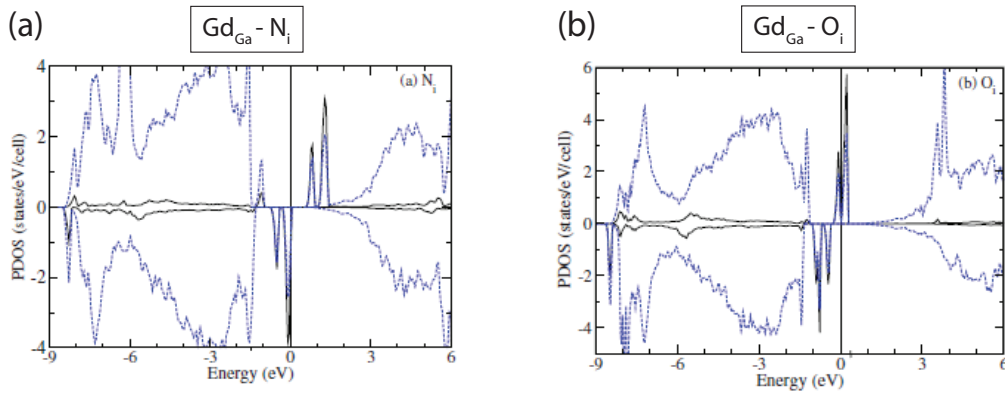


Figure 3.42: Spin-resolved density of states for the Gd_{Ga} - N_I (a) and Gd_{Ga} - O_I (b) complex, calculated in a 64-atom GaN supercell, taken from [106]. The partial density of states on the interstitial site is highlighted in black. In both cases, the spin-polarized defect band lies within the bandgap of GaN.

Independently on the theoretical studies presented above, we conclude from electrical transport measurements that there are three types of defects which are involved in the process of compensation, whereas only one has been identified: in unintentionally doped GaN, it has been argued that the O_N is the dominant donor. Upon doping with Gd, depending on the availability of the residual impurities and the affinity of certain defects to form complexes with Gd, two alternative defects dominate the electrical transport properties. Defect A, which forms an impurity band sufficiently deep in the bandgap of GaN, with a density of states at E_F of around $10^{19} \text{ cm}^{-3} \text{ eV}^{-1}$ and a localization radius of $\xi=3.7 \text{ nm}$, is the one which accounts for ferromagnetism. Defect B, which is expected to form a broad impurity band owing to an appreciable delocalization of states ($\xi \approx 17 \text{ nm}$), and with a high concentration which is presumably near the Mott-transition, is the one which does not yield ferromagnetic properties. Against the mere intuition, delocalization of states does not seem to favor ferromagnetic interactions where point defects are involved. At this point, the presented theoretical studies agree with the notion that the *localized nature* of the defect states gives rise to

the formation of magnetic moments, whereas the extended tails of the wave function mediates the coupling.

Although the various proposals for defect-induced ferromagnetism in GaGdN seem to be plausible, it is somehow difficult to believe that so many defect configurations -either alone or complexed with Gd- give rise to sizable magnetic effects which are able to explain a high Curie-temperature T_c . In this sense, an experimental analysis of the defect distribution and an unambiguous identification of the acceptor (or deep donor) states would be the next step to verify which of the aforementioned defects and/or complexes are responsible for the observed coexistence of VRH-transport and ferromagnetism in GaGdN.

3.3.4 Defect identification: Spectroscopy studies

The theoretical studies about defect-induced ferromagnetism in GaGdN have been taken as a starting point to evaluate the role of point defects. While a specific investigation on the vacancies can be performed by positron annihilation spectroscopy (PAS), deep level transient spectroscopy (DLTS) should give an general overview of the existing deep trap states which can account for electronic localization in ferromagnetic and paramagnetic GaGdN. An attempt to parse the relevant and irrelevant defects concerning both magnetic and transport phenomena is applied by the suggested methods.

Positron annihilation spectroscopy (PAS)

Positron annihilation spectroscopy (PAS) is the method of choice for studying vacancy type defects in semiconductors [41] and has been extensively applied to GaN [40, 42, 38]. Positrons can get trapped and annihilate at neutral and negatively charged open volume defects. The reduced electron density at vacant lattice sites increases the positron lifetime and narrows the momentum distribution of the emitted annihilation radiation, which can be used as a fingerprint for their experimental detection. By combining positron experiments with ab-initio density functional theory calculations it is possible to determine the chemical species of positron trapping centers ⁹. In this sense, V_{Ga} and $V_{Ga}-O_N$ [42] defects have been identified in unintentionally doped n-type GaN, consistent with the formation energy trends discussed in section 3.1.

In collaboration with the Aalto University in Finland, a set of ferromagnetic and non-ferromagnetic GaGdN samples was investigated, in order to find out if the magnetic properties of our MBE-grown epilayers are correlated to the presence of V_{Ga} and/or $V_{Ga}-O_N$ defects, as suggested by the calculations of Dev *et al.* [104, 107]. Depth dependent Doppler broadening spectra have been recorded at room temperature and the measured characteristic S and W parameters of the Gd-doped GaN layers are displayed in Figure 3.43. All points have been normalized to the determined values

⁹more details about the positron annihilation method is found in Appendix B

for a suitable reference sample where positrons annihilate solely in the delocalized state of the GaN lattice („vacancy free“ GaN). Additionally, the characteristic (S,W) values for the GaN lattice, the isolated (V_{Ga}) and oxygen decorated (V_{Ga-O_N}) gallium vacancies [165] are shown for orientation.

The position of a measured point in a SW plot is given as a linear combination of the characteristic values of the present positron trapping states, each weighted with the fraction of positrons trapped in the respective state. In other words, all the (S,W) values which lie on a same line correspond to a specific trapping state, and a weaker proportionality of the (S,W) values (slope) indicates a greater vacancy volume for positron trapping. The absolute values of the (S,W) parameters scale with the vacancy concentration. The roadmap for understanding these relationships is plotted in Fig. 3.43(b).

From Fig. 3.43(a) it can be observed that the measured (S,W) values for all GaGdN samples -with one exception-, independently on their magnetic nature, roughly fall on a line (in red color) which is located outside the region formed by the characteristic points for „vacancy free“ GaN, V_{Ga} and V_{Ga-O_N} . The positron trapping volume has been identified to contain around 2-3 V_{Ga} and a comparable number of V_N . The existence of these „vacancy clusters“ seems to be a general feature of our MBE-grown GaGdN epitaxial layers. Even the reference sample (as-grown GaN) deviates from the slope defined by the decorated vacancies (V_{Ga-O_N}). Note that the characteristic (S,W) points for single (and decorated) vacancy defects, marked with a cross (+), correspond already to a vacancy concentration of 10^{19} cm^{-3} , which is the upper concentration limit for the PAS-method. The fact that neither *single* vacancies nor decorated V_{Ga-O_N} can be detected in appreciable concentrations¹⁰ in our GaGdN samples, does not support the theories of long-ranged ferromagnetic ordering due to Ga-vacancy states [104, 107]. At the same time, they can be ruled out as the effective source for the colossal magnetic moments per Gd-atom measured by magnetometry, as previously suggested by Gohda *et al.* [105]. Moreover, the strong p-d exchange coupling of 5d-Gd states with the GaN valence band with participation of V_{Ga} states, proposed by Liu *et al.* [103], can be also ruled out since a similar amount of V_{Ga} and Gd is required for the p-d exchange coupling to be effective. Even if the aforementioned theories would work taking into account Ga-vacancy clusters as the source of localized magnetic moments and long-ranged coupling, the scenario would not be supported by the PAS-measurements. From the seven samples which have been measured, three of them show ferromagnetic properties (described in section 3.3.2) while the four others failed to reproduce them. From Fig. 3.43 it is evident that there is no correlation between V_{Ga} cluster concentration and magnetic properties. At this point, we exclude all the vacancy-related defects to be responsible for the ferromagnetic coupling in GaGdN.

However, although not directly related to the ferromagnetism, there seems to be a

¹⁰lower detection limit for single vacancies in PAS: 10^{16} cm^{-3}

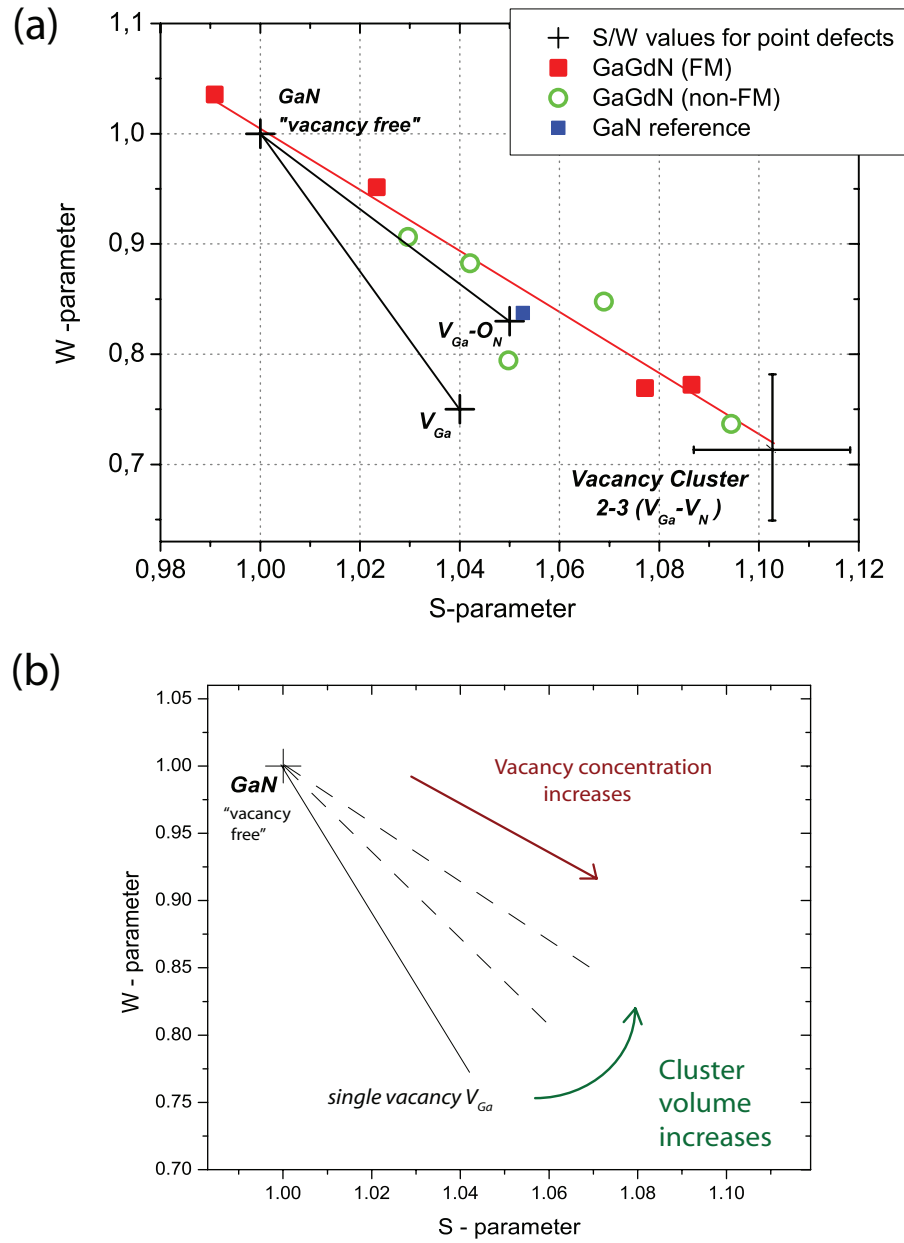


Figure 3.43: (a) Characteristic S and W parameters for a set of ferromagnetic and non-ferromagnetic GaGdN layers, recorded at room-temperature and at a depth of 150 nm. Characteristic values for the „vacancy free“ GaN lattice, V_{Ga} and $V_{Ga}-O_N$ are marked in black. The large black cross indicates the area for vacancy clusters. (b) Roadmap of the most important correlations in SW plots.

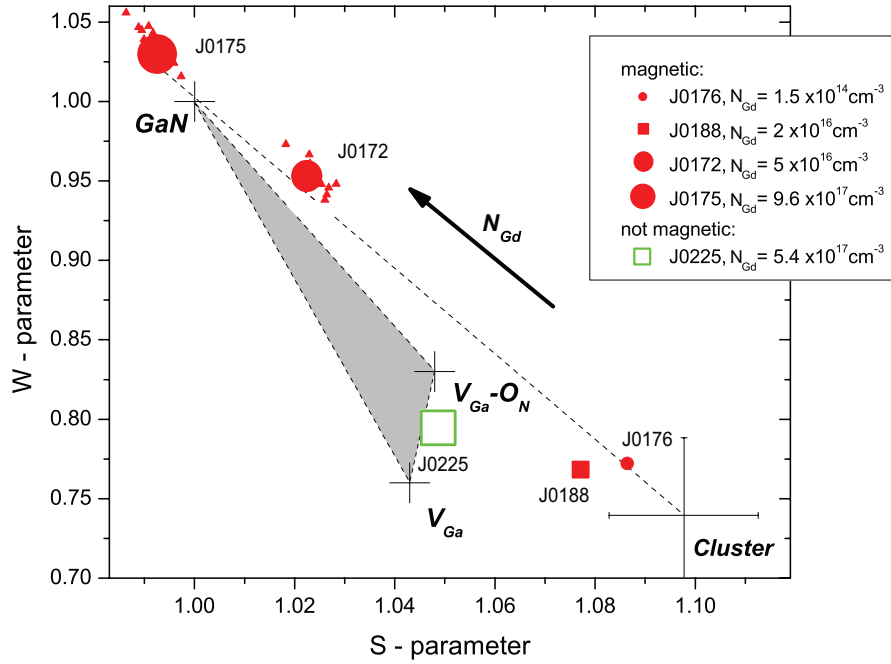


Figure 3.44: (a) Characteristic room-temperature S and W parameters for a set of ferromagnetic GaGdN layers, showing the dependence of V_{Ga} -cluster formation on Gd-concentration. The characteristic values for the „vacancy free“ GaN lattice, V_{Ga} and $V_{Ga}-O_N$ are marked in black. The point size scales with Gd-concentration, whereas the symbol shape denotes the substrate used for growth (circles for GaN-template, squares for SiC). Note that the sample which lies near the characteristic points of V_{Ga} and $V_{Ga}-O_N$ is not ferromagnetic. The small triangles around some points correspond to measured (S,W) values at higher temperatures (up to 500 K)

correlation between Gd-concentration and vacancy cluster concentration in the ferromagnetic samples. Fig. 3.44 shows the S-W plot of the ferromagnetic samples grown on MOCVD-GaN template (circles) and 6H-SiC (squares). Sample J0225, the only one of the series showing (S,W) values between the characteristic points of V_{Ga} and $V_{Ga}-O_N$, has been also included. The highest cluster concentrations are observed in the sample with the lowest Gd-concentration¹¹ ($N_{Gd} \approx 10^{14} \text{ cm}^{-3}$) and then the cluster signal decreases with increasing Gd doping towards the characteristic „vacancy free“ (S,W) value of GaN.

Interestingly, in the magnetic sample with the highest Gd concentration (J0175- $N_{Gd}=9.6 \times 10^{17} \text{ cm}^{-3}$), no positron trapping to clusters nor single gallium vacancy related defects is observed. The characteristic S (W) value is located even below (above) the GaN reference and the apparent diffusion length which can be deduced from the energy dependent spectra is significantly reduced compared to the GaN reference. In order to guarantee that the depicted room temperature (RT) points are not influenced by positron detrapping from vacancies to negative ions, temperature dependent measurements from 300-550 K for selected samples (see small triangles in

¹¹under the detection limit of SIMS, estimated by extrapolation

Figure 3.44) have been performed. At low temperatures positrons can be additionally trapped at Rydberg states around negatively charged non-open volume defects (e.g. negative ions) [166], which possess annihilation characteristics that are very similar to the lattice. This process competes with the trapping to vacancies and could therefore lead to lower apparent vacancy concentrations. In the measured samples, the small change of the S and W parameters with increasing temperature proves that no significant competition between vacancies and negative ions is taking place. This is a consistency check to affirm that characteristic values at room-temperature are representative for the vacancy concentration in the ferromagnetic samples. Thus we conclude that, at least for the ferromagnetic samples, the formation of vacancy clusters is suppressed the more Gd is incorporated in the GaN-matrix. The limit is reached in sample J0175 ($N_{Gd}=9.6 \times 10^{17}\text{cm}^{-3}$), where the concentration of all vacancy-type defects is under the detection limit of PAS ($\leq 10^{16}\text{ cm}^{-3}$), so that the GaGdN lattice can be regarded as „vacancy free“.

On the other hand, sample J0225, having a similar Gd-concentration as the „vacancy free“ sample J0175, does not show an appreciable concentration of vacancy clusters either; it rather contains a large number of single vacancies (see Fig. 3.44). The total concentration of single (plus oxygen-decorated) vacancies is estimated to lie between 10^{18} cm^{-3} and 10^{19} cm^{-3} . Note that this sample shows paramagnetic behavior. Despite the similar Gd-concentration between J0175 and J0225, the formation of single vacancies is suppressed only in the ferromagnetic sample. According to formation energy arguments (section 1.1), the formation of Ga-vacancies is suppressed when the Fermi-energy is shifted towards the midgap region of GaN. In this region, however, the formation of O_N donors is favored, which leads to a shift in the Fermi-energy towards the conduction band minimum, where the formation of V_{Ga} is promoted again¹². The interplay between V_{Ga} and O_N formation leads to following implication: in order to have negligible concentrations of V_{Ga} , a new defect, which suppresses the formation of *both* V_{Ga} and O_N , has to be formed during growth. This might be the sought defect which accounts for ferromagnetism in GaGdN.

So far, the results from positron annihilation spectroscopy have been discussed in connection to the magnetic behavior of the GaGdN epitaxial layers. However, the type and concentration of vacancy defects strongly affects the electronic structure of (Gd-doped) GaN, and consequently, might also determine the electrical transport properties. In this sense, the correlation between vacancy distribution and electrical transport can be investigated on the samples grown on semi-insulating 6H-SiC, which are J0225 (paramagnetic) and J0188(ferromagnetic). Recall from the previous section that both samples exhibit variable-range-hopping transport, but with different impurity band characteristics. This was attributed to the existence of two different dominant *deep* defect states, the more localized corresponding to the ferromagnetic

¹²This scenario is typical for as-grown GaN samples which are n-type due to O_N and with V_{Ga} as the main compensating centers

and the more extended to the paramagnetic sample, respectively. In the paramagnetic sample (J0225), the detection of a high concentration of single vacancies (see Fig. 3.44) suggests that the electronic structure of GaGdN is dominated by *deep* V_{Ga} states, which are expected to lie around 0.3 eV above the valence band[27]. This would be consistent with the occurrence of VRH-transport in an impurity band with relatively delocalized states (due to the high V_{Ga} concentration and large localization radius ξ presumably close to the Mott-transition). Thus, what we denoted as Defect B (see section 3.3.3) is assigned to the single Ga-vacancy V_{Ga} , consistent with variable-range-hopping and the lack of ferromagnetic behavior. The fact that the electronic structure is dominated by V_{Ga} states implies that the formation of O_N has been also suppressed in sample J0225 (otherwise we would expect n-type conductivity). One possibility is that a significant amount of the O_N have formed complexes with the V_{Ga} ($V_{Ga}-O_N$), leaving less amount of single O_N donors which may account as background compensation. The second possibility is that, in this series, less residual oxygen was available during growth.

For the sample J0188, the identification of Defect A, which accounts for VRH-transport and presumably for the magnetic behavior, is not an straightforward issue considering the available PAS-data. The low concentration of Gd in this sample ($N_{Gd}=2 \times 10^{16} \text{cm}^{-3}$) is apparently not sufficient to suppress the formation of vacancy clusters (see J0188, Fig. 3.44). However, the vacancy clusters are supposed to be electrically inactive ($V_{Ga}-V_N$). This is confirmed by the fact that the reference GaN samples, which also contain these open-volume defects, show n-type conductivity with a small compensation effect. In turn, it is unlikely that the vacancy clusters dominate the electronic transport in the ferromagnetic sample (J0188). The defect state which accounts for VRH-transport (Defect A) remains thus unidentified. Nevertheless, according to the PAS-signatures, and consistent with the identification of Defect B, the single V_{Ga} and decorated $V_{Ga}-O_N$ vacancies can be ruled out to be Defect A. The absence of n-type conductivity and the missing fingerprints for sizable concentrations of V_{Ga} and/or $V_{Ga}-O_N$, suggests that the formation of Defect A suppresses *both* O_N and V_{Ga} during growth, being itself the one which dominates the electronic structure in ferromagnetic GaGdN. Further efforts for the identification of this defect are presented in the next section.

Deep-level-transient spectroscopy (DLTS)

Preliminary studies on deep level transient spectroscopy characterization (DLTS), in collaboration with the University of Bologna, Italy, were done on GaGdN samples grown on 6H-SiC(0001), in order to correlate the electrical transport behavior with the presence of deep electron traps. To gain further insight on the role of defects in mediating ferromagnetic interactions, two samples with different magnetic behavior have been analyzed. Sample J0188, thoroughly characterized by magnetometry, electrical transport and positron annihilation spectroscopy, has been investigated with

the aim to find the unidentified Defect A, which is the source of electronic localization and VRH-transport at low Gd-concentrations ($N_{Gd}=2 \times 10^{16} \text{cm}^{-3}$). By comparison, a sample with similar Gd-concentration from the second series, which failed to reproduce the magnetic behavior, has been measured as well.

In DLTS, a common method to identify deep traps in semiconductors, one electrode consist in a Schottky contact to induce a depletion layer (space charge region) at the interface, where a constant reverse external bias defines the steady-state. A voltage pulse is applied to reduce the space charge region, thus allowing carriers to recharge defect states *transiently*. When the voltage returns to its steady-state value, the defects start to emit trapped carriers due to thermal emission. Thus, the temperature at which the emission is observed, is a fingerprint of the energetic position of the trap in the semiconductor bandgap. More details about this technique can be found in Ref.[167].

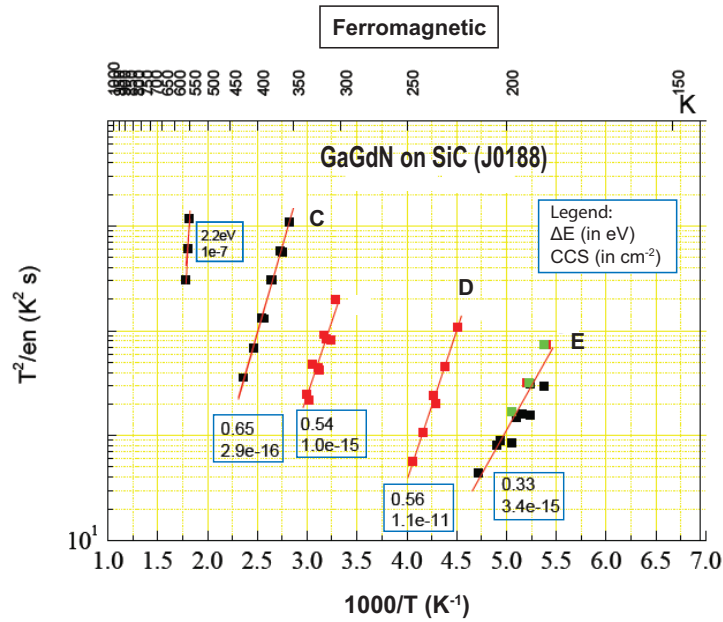


Figure 3.45: Arrhenius plots showing the activation energy and the capture cross-section of several traps found in sample J0188 ($N_{Gd}=2 \times 10^{16} \text{cm}^{-3}$). The defects which have not been labeled exhibit unusual capture cross section values

Fig. 3.45 summarizes all the traps which have been observed in the ferromagnetic sample J0188. The activation energy (in eV - first row) and the capture cross section are shown for each trap. According to [168], capture cross section values above 10^{-12}cm^{-2} are unusual and scarcely reliable, and might come from measurement artifacts. Therefore, we restrict to the evaluation of 3 different traps with activation energies of 0.65 eV, 0.56 eV and 0.33 eV, which we denote as C, D and E, respectively. Note that if the sample is n-type, the thermal activation of traps will occur to the conduction band, while for p-type samples, the measured activation energy is related to the valence band. However, this question is difficult to address for sample J0188, since it exhibits variable-range-hopping transport in an impurity band of unknown

energetic location relative to the band edges. Although the presence of different deep traps could be confirmed in the ferromagnetic sample J0188, their identification cannot be achieved with these preliminary results. In particular, the aforementioned Defect A, responsible for the suppression of single V_{Ga} and O_N formation during growth and variable-range hopping transport, cannot be preferentially addressed to any of the observed traps. All observed traps (C,D,E) could account for localization and VRH-transport due to their deep character. However, finding out which trap is present in higher concentration could help to identify Defect A, since the dominant defect states will determine the position of the Fermi-energy in the bulk¹³ and thus account for VRH-transport. The required data analysis is currently being performed by our collaborators.

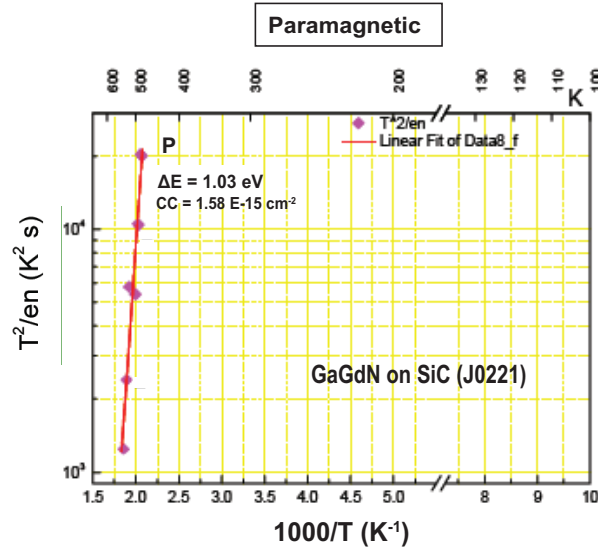


Figure 3.46: Arrhenius plots showing the activation energy and the capture cross-section of a single trap found in sample J0221 ($N_{Gd} \leq 10^{16} \text{ cm}^{-3}$).

Regarding the paramagnetic sample (J0221) with similar Gd-concentration, the deep trap distribution is very different. A single trap state (denoted as P) with an activation energy of 1.03 eV could be identified, as shown in Fig. 3.46. Note that this sample does not show variable-range hopping transport, and is found to be n-type with similar characteristics as the reference undoped GaN sample. We therefore conclude that (i) the concentration of the single trap (P) is not sufficient to compensate the dominant donors, and (ii) Defect A, responsible for O_N and V_{Ga} suppression, and presumably connected to the ferromagnetic behavior, is not the dominant one in this sample, neither corresponds to trap (P). Unlike sample J0188, the Gd incorporation in this series does not seem to have a sizable effect in compensating the residual O_N donors, consistent with the n-type conductivity and the lack of other deep traps (e.g. C,D,E in Fig. 3.45). The DLTS results suggest that ferromagnetic samples might

¹³in DLTS, the bulk region is defined as the region which is far away from the depletion layer

have in general a different defect landscape than paramagnetic ones, at least at low Gd-concentrations ($\approx 10^{16} \text{cm}^{-3}$), which was already anticipated from electrical transport characterization. Still, Defect A could not be unambiguously assigned to any of the traps (C,D,E) observed in the ferromagnetic sample.

GaGdN: Defect-induced ferromagnetism?

The theories of defect-induced ferromagnetism in GaGdN have been put forward in the last two years aiming to explain following controversial experimental results: (i) the observation of colossal magnetic moments per Gd-impurity [19], (ii) a high Curie-Temperature at very low Gd-concentrations [14], (iii) the high resistivity of the samples [14], ruling out any coupling with the valence (p-d) or conduction (s-f) band as well as any carrier-mediated coupling, and (iv) the X-ray magnetic dichroism (XMCD) results ruling out a significant polarization of the GaN-matrix [148]. In this study, the ferromagnetic features related to points (i) and (ii) have been achieved in a first series (J01xx), but in a second sample series (J02xx) they failed to be reproduced. In this sense, the attempt to unravel the role of defects on the magnetic properties has been performed using diverse characterization techniques: electrical transport, PAS and DLTS. The results of the defect distribution for representative samples has been summarized in Table 3.7.

Sample	Substrate	SQUID	el.Transport	PAS	Dominant defect
J0175	MOCVD-GaN	FM	-	„vacancy free“	Defect A?
J0188	6H-SiC	FM	VRH	$V_{Ga}-V_N$ clusters	Defect A
J0225	6H-SiC	PM	VRH	$V_{Ga}, V_{Ga}-O_N$	$V_{Ga}, V_{Ga}-O_N$
J0221	6H-SiC	PM	n-type	-	O_N
GaNref	6H-SiC	PM	n-type	$V_{Ga}-V_N$ clusters	O_N

Table 3.7: Overview of the GaGdN samples characterized in this work. The different defect landscapes for each case suggest that there is a sensitive parameter which strongly influence the growth kinetics, which cannot be controlled.

According to PAS-measurements, there is no correlation between Ga-vacancies (and related defects) and ferromagnetic properties, so that our experimental results do not support the theory of vacancy-mediated ferromagnetism in GaN [104, 105, 103, 107]. Electrical transport measurements showed the occurrence of variable-range-hopping, which means that the dominant defect has to induce states which are energetically *deep* in the GaN bandgap. As discussed at the end of section (3.3.3), the only theory of defect-induced ferromagnetism in GaGdN which is not related to vacancies (consistent with PAS) and where the defects induce deep states in the gap (consistent with VRH-transport), is the one of Gd- N_i and Gd- O_i complexes suggested by Mitra and Lambrecht [106]. The authors in [106] based on formation energy arguments and calculated that these complex states are likely to be formed during growth. Combining

the results of the characterization methods, we suggested that a certain defect (Defect A) which suppresses the formation of both residual donors O_N and native acceptors V_{Ga} during growth, might be connected to the ferromagnetic behavior in GaGdN. The formation of the complex Gd- O_i during growth seems to fulfill these conditions: the residual oxygen donors, instead of going to the usual nitrogen substitutional site, prefer to form a complex with Gd. Thus, the concentration of O_N donors is greatly reduced, and the n-type conductivity vanishes. At the same time, the preferable formation of the Gd- O_i complex during growth, will shift the Fermi-energy towards the midgap region, so that the formation energy of V_{Ga} (V_{Ga} - O_N) defects becomes higher. As a consequence, a negligible concentration of V_{Ga} (V_{Ga} - O_N) is expected, and the incorporation of oxygen is „redirected“ from the usual substitutional O_N site to the interstitial site Gd- O_i due to the affinity to migrate towards Gd, as calculated by [106]. The Gd- N_i complex, on the other hand, while it suppresses the formation of vacancies in similar fashion as Gd- O_i , might not have the same influence on the oxygen donors. Due to the deep energy states induced by Gd- N_i , the Fermi-energy during growth is also shifted towards midgap, where the residual donors O_N have the lowest formation energy. Being not bonded with Gd, all the available oxygen atoms occupy the substitutional site. Thus, in this scenario we would expect an n-type conductive material for $N_D \geq N_{Gd}$ and otherwise variable-range-hopping among the deep Gd- N_i states. The observation of VRH-transport in sample J0188, with a concentration of $N_{Gd} = 2 \times 10^{16} \text{cm}^{-3}$, suggests that the compensation is more likely to be reached by the formation of Gd- O_i during growth, since this process involves not only a simple compensation: at the same time, effectively reduces the formation of O_N donors. Although there is no direct evidence of the presence of Gd- O_i in our samples, we suggest that this complex should be the dominant one in the ferromagnetic samples, since their preferable formation is in well agreement with the electrical transport (VRH) and positron annihilation spectroscopy (no single vacancies) results. From x-ray absorption near edge structure (XANES) characterization, the substitutional incorporation of Gd at low concentrations has been already confirmed [151]; while atom channeling experiments should give the last word for confirming the oxygen atoms at interstitial site. Fig. 3.47 depicts a tentative scenario of ferromagnetic coupling via Gd- O_i .

In Table 3.7, we have addressed a different defect landscape for samples which are not ferromagnetic (J0221, J0225). Since they have a similar Gd-concentration as their ferromagnetic counterparts, there must be a change in the growth environment (or in the growth kinetics) to account for a different defect distribution. If we assume that Gd- O_i complexes are the source for the ferromagnetic behavior, we have to seek for a scenario which supports an unfavorable environment for the Gd- O_i formation, and, at the same time, are able to explain the observed electrical transport characteristics. Starting with the sample with a low Gd-concentration (J0221), the occurrence of n-type conductivity points towards a still high concentration of oxygen donors. That means, either Gd has not formed complexes with O at all, or there is not enough Gd

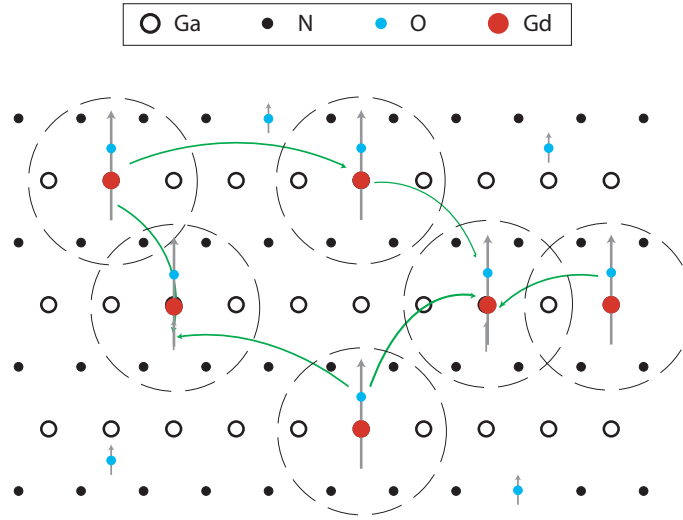


Figure 3.47: Scenario of magnetic coupling in GaGdN through localized Gd-O_i defects which fulfill the weak overlap condition ($d=2\xi$). The dashed circles represent the spatial extension of the electron wave function (localization radius ξ). Note that this scenario does not account for colossal magnetic moments.

such that the amount of „uncomplexed“ O_N exceeds the Gd-O_i concentration. The compensating vacancies, if existent, should be also present in less concentration than O_N. There is no positron annihilation data for that sample (J0221), so that the effect of the vacancies on the complex formation is unknown. On the other hand, sample J0225, with a higher Gd-concentration, presents a remarkably high concentration of single- and oxygen decorated vacancies, which dominate the electrical transport. That means, there was neither sufficient Gd-O_i nor O_N formation during growth. A possible reason is an overall lower oxygen availability in the growth chamber, so that the low content of residual oxygen atoms preferably form Gd-O_i complexes, letting a certain number of Gd-atoms unpaired. For the realization of this hypothesis, the oxygen donor concentration should be $N_D \leq N_{Gd} = 5.4 \times 10^{17} \text{ cm}^{-3}$ in sample J0225, fact which does not seem unrealistic. While for sample J0221 the very low concentration of Gd seems to be the limiting factor, for sample J0225 is the (relatively) low concentration of oxygen. So we conclude that for the formation of Gd-O_i complexes which dominate the electrical transport, both Gd and O_i should be supplied in sufficient number during growth. To confirm this hypothesis, a quantitative determination of the oxygen concentration via secondary ion mass spectroscopy (SIMS), is highly desirable for all the samples listed in Table.3.7.

Even if the preferable formation of Gd-O_i complexes in the ferromagnetic GaGdN samples seems plausible, the feasibility of a long-ranged magnetic coupling via Gd-O_i defects, as well as the colossal magnetic moments at low Gd-concentrations, is not automatically given. The possibility of magnetic coupling via double-exchange, as in the case of GaMnN, is very unlikely due to the very large Gd-Gd average distance, if we assume that only the Gd-O_i defects among themselves are able to couple ferromagnetically. However, due to the localization radius of $\xi \approx 4 \text{ nm}$ found in ferromagnetic

GaGdN, which is ten times larger than the one from GaMnN, enlarges the window for ferromagnetic coupling towards lower concentrations. Considering the weak overlap condition ($d_{\text{Gd-Gd}} \approx 2\xi$), an average Gd-Gd distance of 8 nm would be required to account for a *weak* ferromagnetic coupling. This distance corresponds to a concentration of $N_{\text{Gd}} = 2 \times 10^{18} \text{ cm}^{-3}$. In turn, a magnetic coupling via double exchange might apply for modest up to high Gd (and oxygen) concentrations. The order of magnitude of the localization radius inferred from our electrical transport measurements seems to be in agreement with the extended tails of the wave functions which are localized at the Gd-O_i defects [106]. In this sense, neither the high Curie-temperature nor the colossal magnetic moments in GaGdN can be explained by a double-exchange interaction between Gd-O_i defects for concentrations $N_{\text{Gd}} \leq 10^{18} \text{ cm}^{-3}$. Further possibilities to explain the scenario at low Gd-concentrations are: (i) enhancement of the long-ranged coupling via spin coherent variable-range-hopping between Gd-O_i states, or (ii) the existence of a second defect in the GaGdN lattice which takes part in mediating the coupling. For scenario (i) an average hopping length of $R_{\text{hop}}(100\text{K}) = 3/8 \xi(T_0^{(\text{Mott})}/T)^{1/4} \approx 8 \text{ nm}$ is obtained at $N_{\text{Gd}} = 2 \times 10^{16} \text{ cm}^{-3}$, which is still too short to account for a long-ranged coupling, even at 100 K. Scenario (ii) needs the presence of another point defect which is not bonded with Gd, and which is also present in significant number. The only defect state which has been suggested to mediate long-ranged magnetic interactions independently on the Gd presence, is the single (V_{Ga}) and decorated ($V_{\text{Ga-O}_N}$) Ga-vacancy [104, 107]. Since a significant concentration of vacancy defects has been ruled out by PAS measurements, the „mediator“ between magnetic Gd-O_i localized centers would remain unidentified. At this time, there is no indication of another defect in the GaN lattice which exhibit spontaneous magnetic moments, so that the magnetic coupling at low Gd-concentrations remains a controversial issue. A tentative scenario for the low-doped regime is depicted in Fig. 3.48.

The identification of the relevant defects, which are supposed to play a role in the ferromagnetism and in the electrical transport properties of GaGdN, could be partially achieved. Vacancy-related defects have been ruled out to be the mediators of ferromagnetic interactions, but they might play a role in carrier localization and electrical transport. The presence of another defect (Defect A) with *deep* energy states, which suppresses the formation of both V_{Ga} and O_N , supports the coexistence of variable-range-hopping transport and ferromagnetism. Based on formation energy arguments, this defect has been suggested to be Gd-O_i , and its characteristics are consistent with the characterization results presented in this section. While a Gd-O_i -induced ferromagnetism seems plausible for modest Gd-concentrations, the scenario fails to describe the magnetic coupling and the origin of colossal magnetic moments at low concentrations. It is worth to mention that, while the formation of Gd-O_i is favorable under growth conditions, the stability of these defects has been predicted to be feeble under normal conditions [106]. A very recent finding within our group, indicates an aging effect of the magnetic properties in the first sample series (J01xx), which could be related to the instability of the Gd-O_i complexes, as suggested by [106].

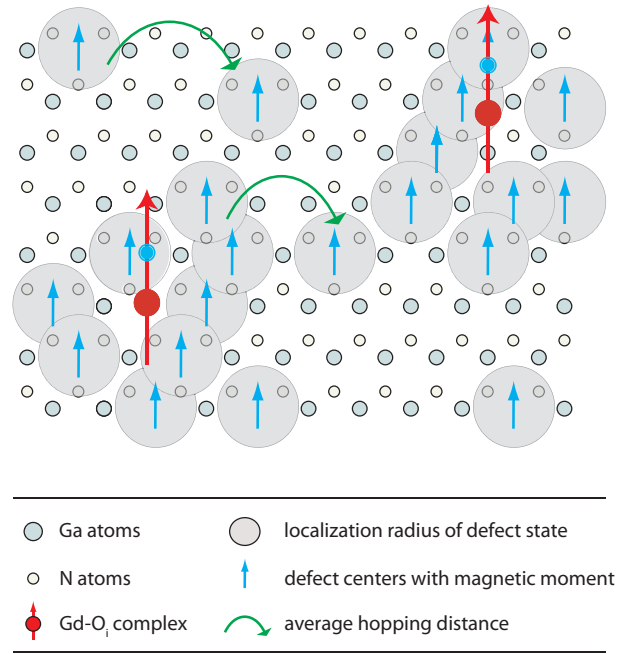


Figure 3.48: Scenario of magnetic coupling in GaGdN at low Gd-concentrations ($N_{Gd} \leq 10^{18} \text{cm}^{-3}$). The presence of a second defect, which is spin polarized and couple ferromagnetically with the Gd-O_i moments, is strictly required. The concentration of these unknown defects has to be much higher than the Gd-O_i complexes.

In this sense, further efforts to unambiguously confirm the presence of Gd-O_i in the ferromagnetic samples are currently being done. Even if the unambiguous identification of the relevant defects would be successful, the challenge would still be to achieve a controlled defect formation during growth, which, as evident from Table 3.7, is a difficult task. In this sense, the prospects for the (very) dilute magnetic semiconductor GaGdN towards applications, are very challenging. The solubility limit is thereby not the limiting factor, as in Mn-doped GaN, but the sample reproducibility and the basic understanding within the young theory of defect-induced ferromagnetism in dilute magnetic semiconductors.

3.4 MnGa/GaN hybrid structures

Given the limited suitability of the realization of room-temperature ferromagnetism in dilute magnetic semiconductors, an alternative approach to combine the magnetic properties of ferromagnetic materials with the already well-established optical and electrical functionality of semiconductor devices, consists in the preparation of hybrid structures to inject spin-polarized currents from the ferromagnetic layer into the semiconductor. Thereby, the existence of a high spin polarization at the Fermi edge and/or a good interface for coherent tunneling is required. Two magnetic phases of the alloy MnGa have recently gained attention for their potential in spintronic applications: the heusler-type ferrimagnetic Mn_3Ga [169, 170, 171] which is supposed to have 88 % spin polarization at the Fermi-edge [172], and the ferromagnetic δ -MnGa phase with $\text{AuCu}(\text{L}1_0)$ structure which is predicted to have a magnetic moment as high as $2.5\mu_B$ per Mn-atom [173]. While the growth and characterization of the δ -MnGa phase has been intensively studied on GaAs [174, 175, 176], eventually achieving spin-injection at low temperatures [177], there has been just one report devoted to the growth of δ -MnGa on the wide-gap semiconductor GaN [178]. A detailed knowledge of the electrical and magneto-transport properties, as well as a smooth interface of metal/semiconductor heterostructure are required to aim for spin-injection.

3.4.1 Experimental details

In the present work, a set of $\text{Mn}_x\text{Ga}_{1-x}$ epitaxial layers has been grown by plasma-assisted molecular-beam epitaxy (MBE) onto $\text{Al}_2\text{O}_3/\text{MOCVD-GaN}$ (0001) substrates, with the Mn-concentration varying from $x = 0.39 \dots 0.67$. High purity Mn and Ga were evaporated from conventional effusion cells in an ultra high vacuum chamber with a base pressure of $p \leq 7 \times 10^{-11}$ mbar. The stoichiometry of the films was carefully adjusted by the Mn/(Mn+Ga) ratio and confirmed by Rutherford backscattering spectrometry (RBS). The growth and surface reconstructions of the layers were monitored in-situ by reflection high energy electron diffraction (RHEED). Crystal structures, epitaxial relationships, in- and out-of-plane lattice parameters were determined by x-ray-diffraction (XRD) using Cu $K\alpha$ radiation (Bruker D8). High-resolution transmission electron microscopy (HRTEM) has been used to visualize the structure of the MnGa/GaN interface, supported by selected area diffraction (SAD) patterns. Integral magnetic measurements were performed with a superconducting quantum interference device (SQUID) with magnetic fields up to 6 T. The electrical and magneto-transport characterization were carried out in a physical property measurement setup (PPMS) within a temperature range from 2 to 400K and magnetic fields up to 7 T.

3.4.2 Growth and structural properties

Prior to MnGa growth, a 50nm GaN layer was grown onto the MOCVD-GaN template at a temperature of 800 °C to improve the surface characteristics, which resulted in a streaky (2 x 2) RHEED pattern. The substrate temperature was then set to $T_s = 250^\circ\text{C}$ to initiate the MnGa growth. A (1 x 1) surface reconstruction related to $\text{Mn}_x\text{Ga}_{1-x}$ appeared almost immediately after opening the Mn and Ga shutters, suggesting the existence of a smooth and abrupt interface. This (1 x 1) pattern remains streaky until the final thickness of $d = 150\text{ nm}$ is reached. The evolution of the RHEED patterns along the [1120] and [1100] directions corresponds to a 30° rotation of the $\text{Mn}_x\text{Ga}_{1-x}$ lattice with respect to the GaN (0001) substrate, in agreement with previous studies [178]. High-resolution transmission electron micrographs have been acquired in cross-sectional geometry to visualize the interface properties of the layers. Fig. 3.49 shows the presence of a sharp and high-quality interface, in contrast to TEM-images of MnGa/GaAs structures, where an amorphous interfacial layer of 1nm exists [177]. Furthermore, the 30° rotation of the $\text{Mn}_x\text{Ga}_{1-x}$ lattice is confirmed by selected area diffraction (SAD). Fig. 3.49 shows an excellent agreement between the SAD-pattern and the calculated diffraction patterns for the 30° rotated MnGa(111) on the GaN(0001) surface.

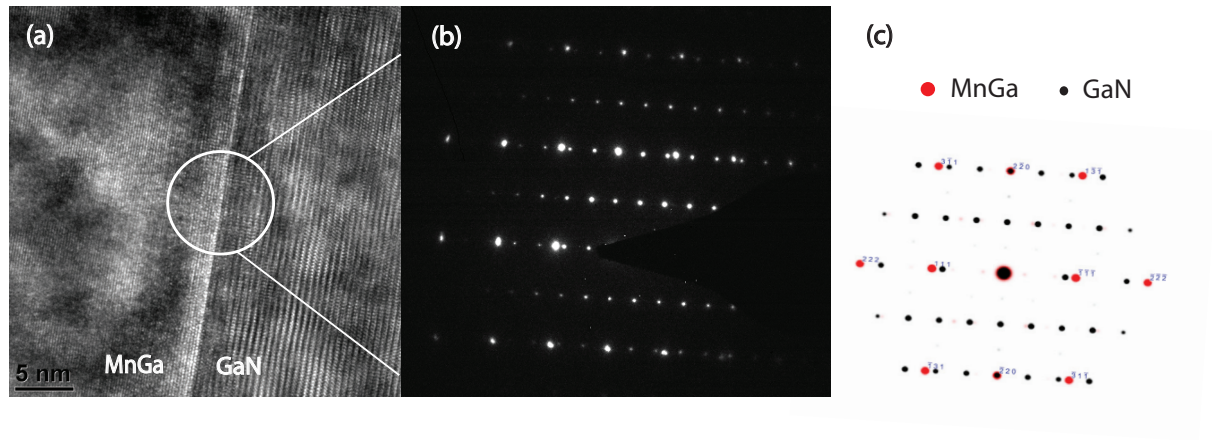


Figure 3.49: (a) Cross-sectional TEM image of the MnGa/GaN interface. (b) Selected area diffraction pattern at the interfacial region. (c) Superposition of the calculated diffraction patterns of GaN (black) and the 30° rotated MnGa (red) crystal plane, showing an excellent agreement with the SAD-pattern.

The epitaxial relationship of the $\text{Mn}_x\text{Ga}_{1-x}$ layers is confirmed by XRD, where $\text{Mn}_x\text{Ga}_{1-x}[111]//\text{GaN}[0001]$. In addition, a 30° shift in the radial ϕ -scans of the GaN(11 $\bar{2}$ 2) plane with respect to the $\text{Mn}_x\text{Ga}_{1-x}$ (002) plane, is used to ascertain the in-plane rotation between substrate and layer in the whole composition range. The θ -2 θ -scan of the $\text{Mn}_x\text{Ga}_{1-x}$ layers (Fig. 3.50), clearly shows the evolution of the $\text{Mn}_x\text{Ga}_{1-x}$ (111) reflection with increasing Mn-content. The d-spacing of the (111) plane shows a nearly linear relationship with x , as shown in the inset of Fig. 3.50.

After determining the a and c lattice parameters of the tetragonal AuCu-L1_0 structure of $\text{Mn}_x\text{Ga}_{1-x}$, it is found that the out-of-plane d -spacing is mainly influenced by the c lattice constant which is dependent of the Mn-concentration, while the a lattice constant remains unchanged. Table 3.8 summarizes the composition dependence of the lattice parameters and the full width at half maximum (FWHM) values of the (111),(200) and (002) main reflections in the θ - 2θ and ω 2θ (*rocking curve*) scan mode. There is a clear increasing trend of all FWHM values towards higher Mn-concentrations. From the width of both the 2θ and ω reflections, we infer that the structural coherence length and the crystal quality decreases as the Mn/Ga ratio deviates from stoichiometry. With the exception of the layer with $x=0.39$ which corresponds to the χ - Mn_2Ga_5 phase, the $\text{Mn}_x\text{Ga}_{1-x}$ epitaxial layers retain the AuCu-L1_0 -type structure over the range $x = 0.49...0.67$. These observations suggest that the crystal is able to host a remarkable amount of Mn_{Ga} antisites, without undergoing a structural phase transition. This property is a key issue for the tunability of the magnetic and electrical transport properties in this material system.

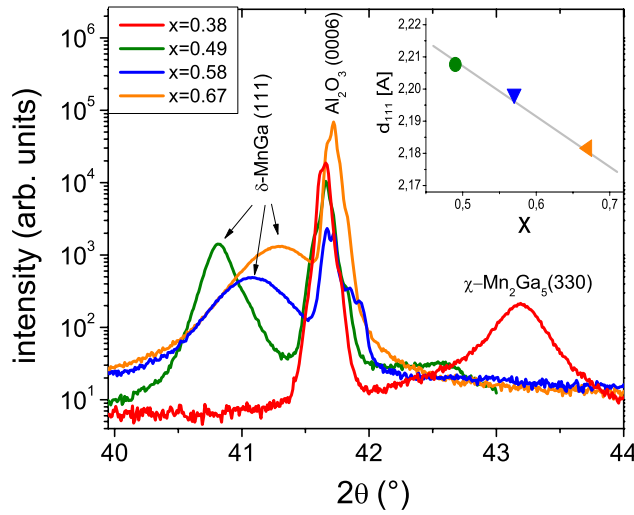


Figure 3.50: θ - 2θ scan of $\text{Mn}_x\text{Ga}_{1-x}$ layers, confirming the (111) growth direction for $x=0.49...0.67$ and the structural phase transition at $x=0.39$. The inset shows the composition dependence of d_{111} .

Table 3.8: Lattice parameters and FWHM values of the δ - $\text{Mn}_x\text{Ga}_{1-x}$ epitaxial layers.

x	d_{111} (Å)	c (Å)	a (Å)	$\Delta 2\theta_{111}$ (°)	$\Delta 2\theta_{200}$ (°)	$\Delta 2\theta_{002}$ (°)	$\Delta \omega_{111}$ (°)	$\Delta \omega_{200}$ (°)	$\Delta \omega_{002}$ (°)
0.49	2.208	3.742	3.883	0.21	0.31	0.45	0.48	1.08	0.58
0.58	2.198	3.699	3.886	0.34	0.61	1.08	0.89	1.92	-
0.67	2.186	3.659	3.886	0.47	0.64	1.45	0.87	2.19	2.21

3.4.3 Magnetic properties

The magnetic properties of the AuCu(L1₀)-type δ -Mn_xGa_{1-x} grown on GaN show two important features in the studied composition range: while the saturation magnetization M_s is found to decrease with increasing Mn-content, the coercive field show the opposite trend, as shown in Fig. 3.51. These observations are in agreement with previous reports of δ -Mn_xGa_{1-x} in bulk [179] and thin films on GaAs [174, 175, 176]. Lu *et al.* [178], however, measured maximal M_s values at $x=0.55$ and not at $x=0.5$. A theoretical study by Sakuma *et al.* [173] started by 50% Mn and predicted that the excess Mn-atoms will have an antiparallel alignment to the rest. In addition, another theoretical work by Yang *et al.* [180] calculated that the magnetic moment is also sensitive to strain, in particular, it is found that reducing the c lattice parameter leads to a smaller magnetic moment. In this sense, the maximum magnetization is expected where Mn:Ga ratio is close to 1:1, and where the c lattice parameter is the highest. In our samples, the partial replacement of Ga by Mn-atoms for $x \geq 0.5$ in the AuCu-L1₀ structure not only leads to the formation of local antiparallel moments, but also changes the c lattice parameter towards smaller values, facts which are consistent with a monotonical decrease of the saturation magnetization with increasing Mn-concentration.

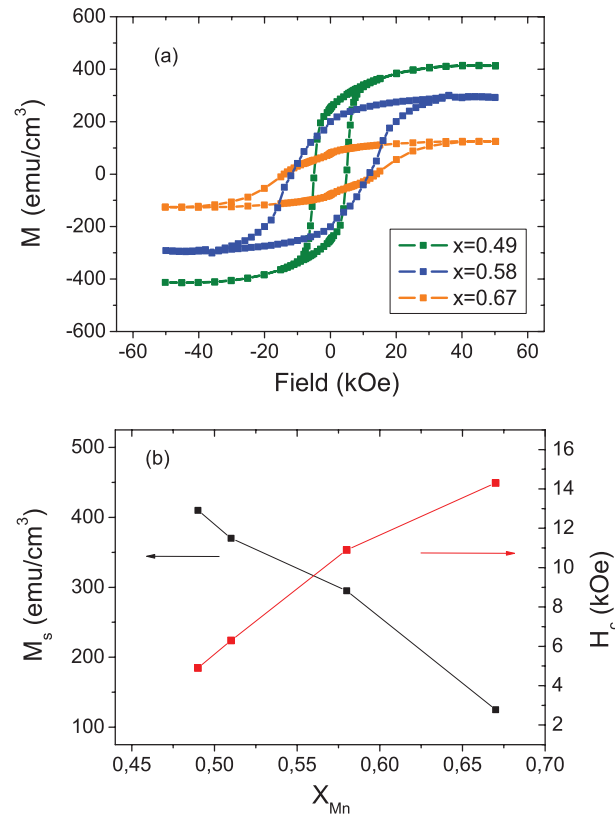


Figure 3.51: (a) Field-dependent magnetization of δ -Mn_xGa_(1-x) layers, at 300K. (b) Composition dependence of saturation magnetization and coercive field.

3.4.4 Electrical transport

Temperature dependence of the resistivity

The temperature dependence of the resistivity $\rho(T)$ of a ferromagnetic metal is, in general, sensitive to three main effects: (i) scattering with defects or impurities, described by the magnitude of the residual resistivity ρ_0 , (ii) scattering due to electron-phonon interactions (ρ_L) and (iii) electron-spin wave scattering (ρ_m). According to Matthiesen's rule these contributions will sum up, as

$$\rho = \rho_0 + \rho_L + \rho_m \quad (3.27)$$

It should be noted that in $3d$ metals and alloys, as is the case of $\delta\text{-Mn}_x\text{Ga}_{(1-x)}$, both s and d states are present at the Fermi-level. Consequently, for both lattice (L) and magnetic (m) scattering, the conduction electrons might undergo intraband (s - s) as well as interband (s - d) transitions. The contribution due to electron-phonon scattering can be generally described as

$$\rho_L = C \left(\frac{T}{\theta_D} \right)^n \int_0^{\theta_D/T} \frac{x^n}{(e^x - 1)(1 - e^{-x})} \quad (3.28)$$

where C is a numerical constant and θ_D is the Debye-temperature. The exponent in the temperature dependence in (3.28) is equal to $n=5$ when considering just intraband $s-s$ electron-phonon scattering (Bloch-Grueneisen) [181], and equal to $n=3$ for metals with high density of d -states at the Fermi-level where the conduction is determined by s - d scattering (Bloch-Wilson)[182]. Above the Debye-temperature θ_D both cases converge to a linear dependence $\rho \propto T$, while for low temperatures ($T \ll \theta_D$) the temperature dependence can be well described by a T^5 or T^3 behavior. The magnetic contribution to the resistivity (ρ_m) has to be subjected to an analogous treatment. It is worth to mention, that both s - s and s - d electron-magnon scattering arise due to the exchange interaction between conduction electrons (s) and magnetic electrons ($3d$), where the spin-wave excitations happen. At low temperatures, the magnetic part of the resistivity is dominated by intraband s - s scattering, since interband s - d transitions require spin waves with larger momentum. The single-band approximation which is valid at low temperatures has been studied by Kasuya and Mannari [183, 184] and results in a quadratic dependence

$$\rho_m^{s-s} = BT^2 \quad (3.29)$$

where the parameter B includes the strength of the $s-d$ interaction. On the other hand, at temperatures where interband scattering becomes important (usually $T \leq 30$ K), the temperature dependence of ρ_m turns complicated [185]. In order to parse the s - s and s - d scattering contribution of the lattice (ρ_L) and magnetic (ρ_m) temperature dependence of the resistivity, several temperature ranges have been separately considered, where some specific terms are expected to be dominant. In general,

the s - s scattering will dominate upon the s - d scattering at low temperatures, since the scattering process does not need an additional momentum Δq_{s-d} (provided by the phonon or magnon) which is required when an s -electron is scattered into the d band. However, for a high d density of states at the Fermi-energy, s - d scattering might become dominant at high temperatures.

The temperature dependence of the δ - $\text{Mn}_x\text{Ga}_{1-x}$ series is shown in Fig. 3.52 as a function of Mn-composition. The residual resistivity ratio (RR)= $\rho_{300\text{K}}/\rho_{2\text{K}}$ is a quantity which is used to analyze if the resistance is dominated rather by lattice (+ magnetic) or impurity scattering, thus being an indicator of the purity/quality of the samples. The highest value was found in the sample with $x=0.49$. The value of RR=1.95 is slightly higher to the one reported for the heusler-type Mn_3Ga grown on $\text{MgO}(111)$ substrates (RR=1.7) [186].

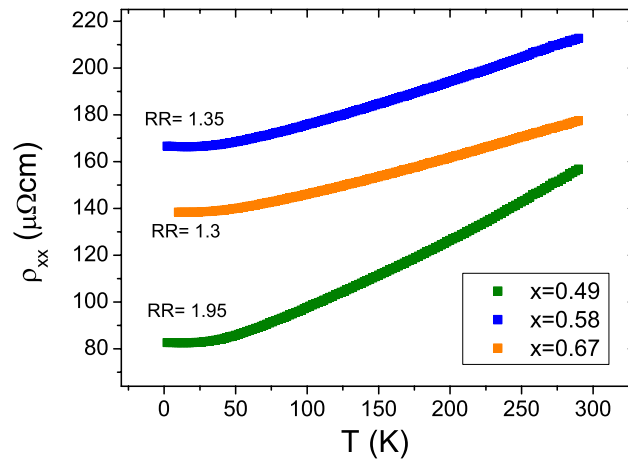


Figure 3.52: Temperature dependence of the resistivity in δ - $\text{Mn}_x\text{Ga}_{1-x}$ epitaxial layers as a function of Mn-composition. The resistivity ratios are shown in each case.

For the quantitative analysis of the temperature dependent resistivity, three temperature ranges are considered. In the intermediate temperature range ($30\text{ K} \leq T \leq 150\text{ K}$), an excellent fit was obtained considering the Bloch-Wilson expression (Eq. 3.28 with power $n=3$), characteristic for phonon s - d scattering. This indicates the existence of a high d density of states in the $\text{Mn}_x\text{Ga}_{1-x}$ layers near the Fermi-energy, so that the mobile s electrons are able to undergo interband transitions. At the same time, a high d density of states implies that the magnon s - d scattering contribution to the resistivity has to be taken into account. Fig. 3.53 shows that the Bloch-Wilson fit (ρ_L^{s-d}) to the temperature dependent resistivity does not hold for high temperatures ($T \geq 150\text{ K}$). This deviation is attributed to the magnon-assisted interband scattering contribution, which has a complicated temperature dependence [185]. The Bloch-Wilson fit at intermediate temperatures, where the phonon s - d scattering dominates, is used to derive the Debye-Temperature Θ_D .

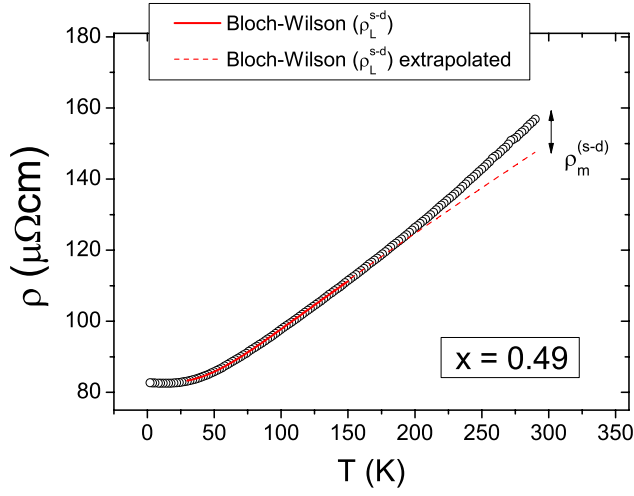


Figure 3.53: Temperature dependent resistivity of $\delta\text{-Mn}_x\text{Ga}_{1-x}$ with $x=0.49$. In the intermediate temperature range, the resistivity can be well fitted considering the lattice (Bloch-Wilson) contribution due to s - d interband scattering. The deviation at higher temperatures is ascribed to the magnetic s - d scattering contribution.

In the low temperature range ($T \leq 30$ K), where the intraband s - s scattering events dominate, the temperature dependence of the resistivity can be fitted using the Bloch-Grueneisen expression for the lattice contribution (ρ_L^{s-s}) plus the magnetic contribution ($\rho_m^{s-s} \propto BT^2$). Fig. 3.54 shows the results for the $\text{Mn}_x\text{Ga}_{1-x}$ layer with $x=0.49$. The fit loses accuracy below 20 K, due to the upturn of the resistivity at very low temperatures ($T \leq 10$ K). This „Kondo-like“ increase of the resistivity at low temperatures has been investigated in $\text{Mn}_5\text{Si}_3\text{C}_x$ metallic thin films as a function of thickness [187], and was attributed to structural disorder and scattering at grain boundaries. Indeed, for the $\text{Mn}_x\text{Ga}_{1-x}$ layers, this increase becomes stronger with higher Mn-concentration and correlates with the structural quality determined by X-ray diffraction (see. Table 3.8). Nevertheless, the fit gives reasonable results by using the same Debye-Temperature (Θ_D) inferred from the Bloch-Wilson fit at intermediate temperatures. The various parameters obtained from the analysis of the temperature dependent resistivity in the different temperature ranges are summarized in Table 3.9. The Debye-temperature changes slightly with Mn-composition, while the coefficient $B_m^{(s-s)}$ involving magnon scattering at low temperatures is found to be much shorter in

x	ρ_0 ($\mu\Omega$ cm)	RR	Θ_D (K)	$B_m^{(s-s)}$ (Ω cm K $^{-2}$)	$C_L^{(s-s)}$ (Ω cm)	$C_L^{(s-d)}$ (Ω cm)
0.49	82.5	1.95	346 ± 2	$(2.3 \pm 0.5) \times 10^{-10}$	$(7.8 \pm 0.6) \times 10^{-4}$	1.7×10^{-4}
0.58	166.3	1.35	362 ± 3	$(2.4 \pm 0.7) \times 10^{-10}$	$(5.2 \pm 0.8) \times 10^{-4}$	1.1×10^{-4}
0.67	138.4	1.3	375 ± 3	$(4.2 \pm 0.9) \times 10^{-12}$	$(4.4 \pm 0.5) \times 10^{-4}$	1×10^{-4}

Table 3.9: Quantities derived from the temperature dependent resistivity, taking into account both phonon and magnon scattering and intra- and interband electron transitions.

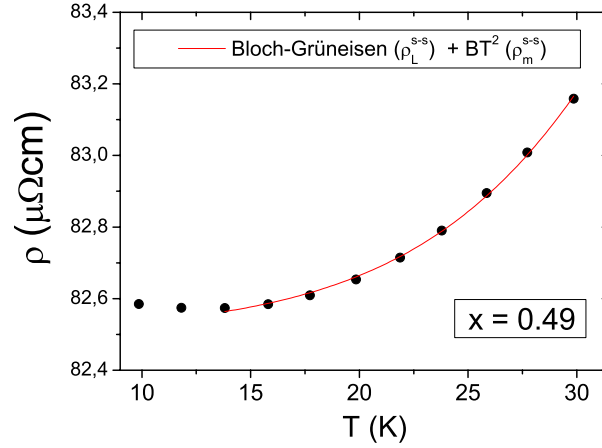


Figure 3.54: Temperature dependent resistivity of $\delta\text{-Mn}_x\text{Ga}_{1-x}$ with $x=0.49$. In the low temperature range, the resistivity can be fitted considering the lattice (Bloch-Grüneisen) and magnetic contributions ($\propto BT^2$), assuming intraband s - s scattering as the dominant process in this temperature range.

the sample with the highest Mn-concentration. However, a clear correlation between the magnon contribution to the resistivity and the magnetization of the samples cannot be observed. The constants involving s - s and s - d phonon scattering are in the same order of magnitude. The error in the coefficient $C_L^{(s-d)}$ is negligible due to the excellent accuracy of the Bloch-Wilson fit at intermediate temperatures (see Fig. 3.53). Although a quantitative interpretation of these constants appears difficult within the scattering theory in metals, they should be taken as a reference to be compared with literature values of different metals and alloys.

Anomalous Hall-Effect

Field-dependent resistivity measurements in ferromagnetic metals lead to the observation of the anomalous hall effect (AHE), commonly used to describe the spin-dependent scattering. As expected from the relation

$$\rho_{xy} = \rho_{OHE} + \rho_{AHE} = R_0 H + R_s \mu_0 M \quad (3.30)$$

the anomalous part of the transverse or hall-resistivity ρ_{xy} is proportional to the magnetization of the sample. By subtracting the ordinary part of ρ_{xy} , we observed the same trends in terms of coercive field of the $\rho_{AHE}(H)$ and $M(H)$ hysteresis loops, as the Mn-concentration is increased. Furthermore, the temperature dependence of the AHE has been measured from 2K up to room-temperature, as depicted in Fig 3.55. The magnetization has been found to be independent in the relevant temperature interval, according to $M(T)$ scans performed by SQUID, so that the temperature dependence of the AHE is governed by the coefficient R_s .

The scaling behavior between ρ_{AHE} and the longitudinal resistivity ρ_{xx} has been used

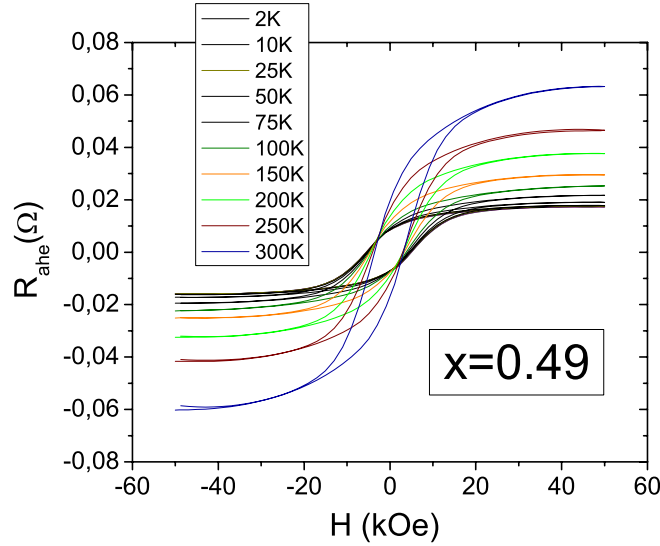


Figure 3.55: Temperature dependence of the anomalous hall resistivity, after subtracting the linear (ordinary) term.

to identify the scattering mechanisms in ferromagnetic metals. From the empirical point of view, a linear dependence $\rho_{AHE} \propto \rho_{xx}$ is attributed to the skew scattering, while a quadratic one $\rho_{AHE} \propto \rho_{xx}^2$ is attributed to the side-jump mechanism. The former is an asymmetric scattering due to the effective spin-orbit coupling at impurity sites and is found to be dependent on the impurity concentration; the latter originates through the deflection of the electron velocity in opposite directions by the opposite electric fields experienced upon approaching and leaving an impurity [188], and is found to be independent on the impurity concentration. A third mechanism, called intrinsic contribution, is only dependent on the band structure of the crystal and is discussed in terms of geometric concepts of Berry phase and curvature in momentum space [188]. We first concentrate on the scaling behavior of ρ_{AHE} and ρ_{xx} . Within this analysis, it is just possible to separate the skew scattering contribution from the other two (intrinsic and side-jump). A log-log plot of ρ_{AHE} against ρ_{xx} yields the exponent of the scaling behavior, as shown in Fig. 3.56 for different Mn-concentrations.

At $x=0.49$, the exponent is found to be $n=1.82$, which means that scattering mechanism behind the AHE could be the intrinsic and/or side-jump contribution. A recent review by Nagaosa *et al.* [188] surveyed a large number of experimental studies of the scaling behavior of the AHE and classified them in three different regimes: (i) a high conductivity regime ($\rho_{xx} \leq 10^{-6} \Omega\text{cm}$), in which the skew-scattering mechanism dominates; an intrinsic or scattering-independent regime ($10^{-4} \Omega\text{cm} \geq \rho_{xx} \geq 10^{-6} \Omega\text{cm}$), where $\rho_{AHE} \propto \rho_{xx}^2$; and a bad metal regime ($\rho_{xx} \leq 10^{-6} \Omega\text{cm}$) in which ρ_{AHE} increases with ρ_{xx} at a rate faster than linear ($n=1..2$). According to this classification, the resistivity of the $\delta\text{-Mn}_x\text{Ga}_{1-x}$ series (80 to 200 $\mu\Omega\text{cm}$) lie at the boundary between

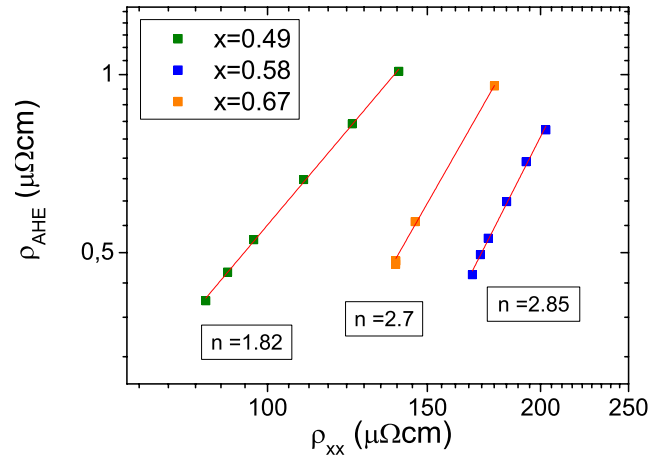


Figure 3.56: Scaling behavior of the anomalous hall resistivity.

the intrinsic and the bad metal regime, so that a scaling exponent around $n=2$ is expected. This is the case for the sample with $x=0.49$. As the Mn-concentration is increased, the exponent turns to be greater than 2, which is actually not expected taking into account the classical models. Xiong *et al.* [189], reported exponents as high as $n=3.7$ in granular Co-Ag systems and attributed the large deviation from the maximum expected scaling behavior ($n=2$) to scattering at grain boundaries. In our set of $\delta\text{-Mn}_x\text{Ga}_{1-x}$ samples with $x \geq 0.5$, the scaling exponent lies between 2.7 and 2.85, as inferred from Fig. 3.56. From the structural point of view, there is a correlation between the width of the $\delta\text{-Mn}_x\text{Ga}_{1-x}$ Bragg-reflections and the Mn-concentration (Fig. 3.50 and Table.3.8), which means that the structural coherence length decreases with increasing Mn-concentration, hence favoring scattering at grain boundaries. Since the influence of scattering at interfaces and grain boundaries has not been included yet in the AHE-theory, it is very difficult to perform further interpretation of the data.

In summary, the composition dependence of the structural, magnetic, electrical and magneto-transport properties of $\delta\text{-Mn}_x\text{Ga}_{1-x}$ epitaxial layers grown on GaN (0001) has been investigated. The epitaxial growth with an in-plane rotation of 30° is so favorable, that the AuCu($L1_0$)-crystallographic phase can be grown over a wide range of Mn-compositions ($x=0.49\ldots 0.67$). In turn, the magnetic and magnetotransport properties can be tuned by changing the amount of Mn-antisites (Mn_{Ga}) without undergoing a structural phase transition. However, this is done at expense of losing structural coherence length, as observed by the increase of the full width at half maximum (FWHM) values of the θ - 2θ and ω - 2θ X-ray diffraction scans with increasing Mn-concentration. This is consistent with the upturn of the resistivity at low temperatures and the unusual scaling behavior of the anomalous Hall-Effect. In the latter, the scaling exponent between ρ_{xx} and ρ_{xy} exceeds the value of 2 corresponding to side-jump scattering, experimentally observed in materials where grain boundaries

affect the behavior of the anomalous Hall-Effect. In view of potential applications, the existence of a smooth and abrupt interface enables the possibility to achieve an efficient spin-injection into the wide-gap semiconductor GaN. By changing the stoichiometry in the range ($x = 0.49...0.67$), both the room-temperature saturation magnetization and the coercive field can be scaled by a factor of 4. The ability of tuning these parameters without undergoing a structural phase transition, combined with the well-matched epitaxy onto GaN, makes this ferromagnetic alloy a versatile material to be integrated in wide-gap semiconductor spintronics.

4. Summary and Outlook

In this work, three material systems have been investigated with the aim of achieving spin polarization in the wide-gap semiconductor GaN. While the feasibility of synthesizing *intrinsic* dilute magnetic semiconductors has been studied for the cases of (Ga,Mn)N and (Ga,Gd)N, the characterization of MnGa ferromagnetic layers grown on GaN has been investigated in view of spin injection.

In (Ga,Mn)N, low concentrations of Mn (≤ 1 at%) have been studied with the aim of characterizing the properties of a single substitutional Mn^{3+} atom. It is found that Mn induces deep states in the bandgap of GaN, which account for a total compensation of residual donors at a concentration of ($N_{Mn} \geq 10^{18} \text{cm}^{-3}$). Above this concentration, the electrical transport behavior changes from activated band transport to Mott-variable range hopping between localized states within the t_2 Mn-impurity band. A wave-function localization radius of ($\xi \leq 0.1 \text{ nm}$) could be estimated in this regime, which is much shorter than the average impurity distance, so that the Mn electron spins behave as non-interacting paramagnetic centers, confirmed by SQUID-magnetometry. As the Mn-concentration is increased, X-ray diffraction characterization revealed the formation of a secondary phase, Mn_3GaN , at concentrations of about 5 at%. However, despite the onset of cluster formation, the substitutional incorporation is not „shut down“ as suggested by the evolution of the lattice parameters up to concentrations of 6.2 at%. The magnetic characterization in this concentration regime confirmed the coexistence of two magnetic phases: one superparamagnetic phase with anisotropy barrier blocking, arising from nano-sized Mn_3GaN clusters; and one paramagnetic phase arising from diluted Mn-atoms incorporated in the GaN-matrix. A signature of a para- to ferromagnetic transition could be observed by analyzing the shape of the temperature dependent field-cooled magnetization in the highest doped samples (5.6 and 6.2 at%). From the point of inflection of the FC-magnetization curve, Curie-temperatures of around 5 and 11 K are inferred, respectively. The Curie-temperatures fall in the same range as the blocking temperature (T_B) from the superparamagnetic phase, so that the field hysteresis observed at low temperatures cannot be unambiguously ascribed to a ferromagnetic coupling between the Mn-Mn spins. In this sense, the separation of superparamagnetic and ferromagnetic contributions at low temperatures was done by thermoremanence measurements. The recovery of the remanent magnetization after the application of thermal cycles confirmed the existence of a ferromagnetic phase. The weak ferromagnetic coupling is explained by a double-exchange interaction between localized Mn-states. In this concentration regime, the Mn-Mn average impurity distance of

($\approx 7\text{\AA}$) is consistent with very small magnetic coupling constants J_{ij} obtained from theoretical studies. Interestingly, the onset of ferromagnetic coupling coincides with an increase of the localization radius of the Mn-states, derived by the sharp decrease of the characteristic temperature $T_0^{(Mott)}$ determined by the analysis of the temperature dependence of the resistivity. Thereby, the observed signatures constitute a nice example to elucidate the correlation between magnetic coupling and carrier localization: the inferred localization radii account for a weak overlap of the Mn wave functions, which gives rise to a weak ferromagnetic interaction between the Mn-spins. However, for achieving high Curie-temperatures in (Ga,Mn)N in the framework of the double exchange mechanism, a strong overlap of the wave functions is required, which can be only fulfilled by incorporating much higher concentrations of Mn atoms on the substitutional Ga-site. Structural, magnetic and electrical transport characterization reveal that the localized nature of the Mn-states and the onset of phase segregation at concentrations above 5 at%, make Mn-doped GaN an unsuitable material system for spintronic applications; nevertheless, it represents an interesting example to show the interplay between electron localization and spin ordering in dilute magnetic semiconductors.

Gd-doping in GaN, on the other hand, accounts for unexpected ferromagnetic signatures at very low doping concentrations ($N_{Gd} \ll 0.01$ at%), showing colossal magnetic moments ($\approx 1000\mu_B$) per Gd-impurity and a high Curie-Temperature revealed by field-dependent magnetization measurements at 300 K. However, these properties have been found to be difficult to reproduce. The origin of the Curie-temperature above 300 K, has been ruled out to arise from substrate contamination and from GdN inclusions, since samples containing the latter phase present a ferro- to paramagnetic transition of around 70 K, characteristic of GdN in the rocksalt structure. In this sense, the onset of GdN cluster formation occurs at $N_{Gd} \approx 0.2$ at% $\approx 10^{20}\text{cm}^{-3}$, as determined by high resolution X-ray diffraction. Upon doping with Gd, the lattice constants of GaN are subjected to hydrostatic strain which becomes significant already at concentrations about $N_{Gd} \geq 10^{18}\text{cm}^{-3}$, and accounts for a volume expansion ($\Delta V/V_{GaN}$) of 1.8% at Gd-concentrations below 0.1 at%. This is attributed to the large atomic size and ionic radius of Gd compared to Ga and seems to be the explanation why secondary phases -which might relieve the strain- are formed at very low Gd-concentrations. Below the clustering threshold, the substitutional incorporation and the charge state (Gd^{3+}) of Gd have been confirmed by X-ray absorption near edge structure (XANES), so that the resulting Gd electronic structure is determined by the last filled ($4f^7$) states. Due its large exchange spin-splitting, these states are expected to be resonant with the conduction and valence band, respectively, so that Gd-doping should not affect the electronic structure of GaN, which has been found to be dominated by shallow oxygen donors with an activation energy of 20.6 meV, inferred by temperature dependent Hall-Effect measurements. Electrical transport characterization of the GaGdN epitaxial layers grown on 6H-SiC, reveal different types of electronic transport, correlated with the non-reproducibility of the magnetic

properties. The coexistence of variable-range hopping transport and ferromagnetism at very low Gd-concentrations suggests that Gd induces deep states which account for electronic localization, contrary to the expected effect of substitutional Gd^{3+} on the electronic structure of GaN. This is a key finding which points to the presence of certain defects formed during growth, which compensate and/or suppress the formation of shallow oxygen donors, and account for the formation of an impurity band deep in the GaN bandgap. Interestingly, such an electrical transport behavior has not been found for samples which are not ferromagnetic, suggesting that these defects might also play a role in the magnetic behavior of GaGdN. An attempt to parse the relevant and irrelevant defects for the observed electrical transport and magnetic characteristics, has been done by means of positron annihilation spectroscopy (PAS) and deep-level transient spectroscopy (DLTS). Ga-vacancies, the most commonly discussed defect for mediating ferromagnetic interactions in both undoped GaN and Gd-doped GaN, could be ruled out to be responsible for the magnetic behavior in the studied GaGdN epitaxial layers. Furthermore, the defect accounting for VRH-transport and presumably for the ferromagnetic interactions in GaGdN, has been found to suppress both the oxygen donor and the Ga-vacancy formation. Combining formation energy arguments and the available spectroscopy data, the favorable formation of the complex Gd-O_i during growth is consistent with the suppression of the dominant donors (O_N) and acceptors (V_{Ga}) and with the occurrence of variable-range hopping transport in an impurity band of localized states. Although there is no direct evidence of the existence of this complex in the ferromagnetic samples, aging effects of the ferromagnetic properties, possibly due to the Gd-O_i instability, and trends of magnetization enhancement with increasing oxygen partial pressure during growth, support this hypothesis. However, even taking into account the relatively large localization radius of the defect wave functions inferred by electrical transport characterization, the model of Gd-O_i fails to explain ferromagnetic coupling and colossal magnetic moments per Gd-impurity in the highly-diluted regime ($N_{\text{Gd}} \leq 10^{18} \text{cm}^{-3}$). In order to explain this unprecedented results at very low Gd-concentrations, the existence of a second defect which act as a „mediator“ is strictly necessary. Further efforts on the defect identification and special attention on the new developments of the theory of defect-induced ferromagnetism should be taken into consideration to address this question. Although some hints towards defect-induced ferromagnetism in GaGdN could be gained from this work, the control and stability of the involved defects are the biggest drawbacks to establish GaGdN as a room-temperature dilute magnetic semiconductor.

In view of the physical hurdles to achieve GaN-based ferromagnetic semiconductors suitable for spintronic applications, an alternative approach to induce spin polarization in GaN has been investigated. The high-quality epitaxial growth of ferromagnetic MnGa metal layers on GaN substrates opens up the possibility of extrinsic spin-injection into the semiconductor. In this sense, $\text{Mn}_x\text{Ga}_{1-x}$ epitaxial layers have been thoroughly characterized, putting special emphasis in the composition dependence of the structural, magnetic and electrical transport properties. A stoichiometrical

composition ratio ($x \approx 0.5$) of $\text{Mn}_x\text{Ga}_{1-x}$ has been found to exhibit excellent interface properties as visualized by transmission electron microscopy. The correlation of structural and magnetotransport properties suggests an increase of grain boundaries with increasing Mn-concentration which could be detrimental for the injection of spin-polarized currents. The characterization and eventual tunability of Schottky-barriers at the interface, as well as the spin detection in GaN via non-local geometry, would be the next steps to be carried out in this new metal-semiconductor hybrid system.

Appendix

A. Diamagnetic background correction: An iterative method

Magnetic measurements by SQUID-magnetometry integrate the signals of all the phases present in the volume which is subjected to the measurement. It is therefore imperative to subtract the signal coming from the substrate ($\geq 99\%$ of the sample volume), to ascertain that the detected magnetic phases belong to the epilayer. The dominant background signal of the GaMnN and GaGdN layers grown on MOCVD-GaN/Al₂O₃ and 6H-SiC substrates is expected to be diamagnetic, since GaN, Al₂O₃ and SiC are all diamagnetic materials.

The most common method to subtract the diamagnetic background signal is to evaluate the as-obtained field-dependent magnetization $M(B)$ of the sample volume recorded at room-temperature. Usually, the as-obtained $M(B)$ curve at 300 K of thin epilayers on a large diamagnetic substrate is a straight line with a negative slope, as depicted in Fig. A.1(a).

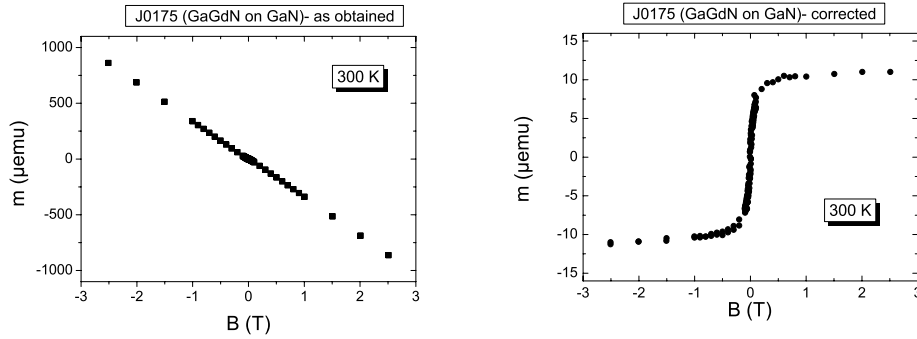


Figure A.1: Field dependent magnetization of a GaGdN ferromagnetic sample at 300 K: As-obtained data (left) and after performing the diamagnetic subtraction from the as-obtained slope at high fields (right).

If the epilayer shows ferromagnetic properties at 300 K (as in the case of GaGdN), the magnetization from the ferromagnetic phase is expected to saturate at relatively low fields (≈ 1 T). Therefore, the diamagnetic background contribution is inferred from the slope of the $M(B)$ dependence at high magnetic fields, where the ferromagnetic contribution is supposed to be constant. This approach usually gives a very reasonable quantification of the diamagnetic contribution, so that its subtraction from the as-obtained $M(B)$ curve allows to investigate the ferromagnetic phase belonging to the

epilayer, as depicted in Fig.A.1(right). Since the diamagnetic contribution is expected to be temperature independent, the inferred diamagnetic slope at 300 K can be used to subtract the as-obtained $M(B)$ dependences at any temperature.

On the other hand, if the epilayer contains a paramagnetic phase whose magnetization saturates at much larger fields, the slope of the as-obtained $M(B)$ curves at high fields is not an exclusively result of the diamagnetic contribution. However, it is usually taken for granted that the paramagnetic magnetization at 300 K, due to its sharp decay towards high temperatures ($\propto 1/T$) is negligible compared to the temperature-independent diamagnetic background contribution. Concerning the (Ga,Mn)N epitaxial layers studied in this work, an accurate determination of the paramagnetic Mn-atoms is of crucial importance to estimate the average Mn-Mn distance, quantity which has been taken as the starting point to argue about a ferromagnetic coupling between Mn-atoms that fulfill the weak overlap condition ($d_{Mn-Mn} \approx 2\xi$), one of the main findings of this work. Therefore, the best approach to perform the diamagnetic subtraction is not to neglect the paramagnetic contribution even at high temperatures. The equation which has been used to fit the field-dependent magnetization of the (Ga,Mn)N layers containing three magnetic phases (spm + pm + dia) for temperatures $T > 20$ K is given by

$$M_{total}(B, T) = M_s^{pm} \cdot L^{pm}(B, T) + M_s^{spm} \cdot L^{spm}(B, T) + M_{dia}(B, 300K) \quad (A.1)$$

where the fitting parameters are M_s^{pm} , M_s^{spm} and μ_{eff}^{spm} , the latter included in the Langevin-function

$$L(B, T) = \coth\left(\frac{\mu_{eff} B}{k_B T}\right) - \left(\frac{\mu_{eff} B}{k_B T}\right)^{-1} \quad (A.2)$$

For the (Ga,Mn)N epitaxial layers, the effective magnetic moment of the paramagnetic contribution (μ_{eff}^{pm}) has been obtained from the temperature dependence of the magnetic susceptibility, in order to reduce the number of fit parameters. Note that the term $M_{dia}(B, 300K) = -m_{dia}B$ in Eq. A.1 is the one which is usually replaced by $M_{dia}(B, 300K) \approx -m_{asobt}B$, where m_{asobt} denotes the slope of the as-obtained $M(B)$ dependence at 300 K. However, the rigorous definition of the diamagnetic background contribution at 300 K is given by

$$M_{dia}(B, 300K) = M_{asobt}(B, 300K) - M_{pm}(B, 300K) - M_{spm}(B, 300K) \quad (A.3)$$

$$M_{dia}(B, 300K) = M_{asobt}(B, 300K) - M_s^{pm} \cdot L^{pm}(B, 300K) - M_s^{spm} \cdot L^{spm}(B, 300K) \quad (A.4)$$

The second and third term in Eq. A.4 depend on the Langevin-functions $L(B)$ at 300 K. By substituting $M_{dia}(B, 300K)$ (Eq. A.4) in $M_{total}(B, T_i)$ (Eq. A.1), we note that the appearance of two different temperatures (T_i and 300 K) within the same fitting

equation does not enable to solve the problem in a single step. T_i is the temperature of interest, i.e., where the field dependence of superparamagnetic and paramagnetic contributions are clearly visible, so that the total magnetization can be separated according to Eq. A.1. In the analysis of the (Ga,Mn)N epilayers, T_i amounts to 25 K, as shown in Fig. 3.16 (replotted as Fig. A.2). In view of these limitations, the diamagnetic contribution $M_{dia}(B, 300K)$ has been obtained using the following procedure:

- 1) Start with the approach $M_{dia}(B, 300K) \approx -m_{asobt}B$ to set an initial value for M_{dia} in Eq. A.1. The initial value is defined as M_{dia}^0 .
- 2) Proceed with the Langevin-Fit of the $M(B, T=T_i)$ dependence (Eq. A.1) and get the fitting parameters M_s^{pm} , M_s^{spm} and μ_{eff}^{spm} .
- 3) Calculate the values for $M_s^{pm} \cdot L^{pm}(B_a, 300K)$ and $M_s^{spm} \cdot L^{spm}(B_a, 300K)$ and replace them in Eq. A.4 in order to get the first „corrected“ value of $M_{dia}(B=B_a, 300K)$ and define it as M_{dia}^1 (B_a can be any magnetic field value corresponding to a measured data point, with $B_a \neq 0$).
- 4) If $M_{dia}^1 \neq M_{dia}^0$ than set M_{dia}^1 as initial value in step 1)
- 5) Iterate steps 1)- 4) until $M_{dia}^{n+1} = M_{dia}^n$. The correction of the diamagnetic contribution has converged. The slope m_{dia} can be inferred using the simple relation $M_{dia}^n = -m_{dia}B_a$.

As a result, one obtains the set of best-fit parameters (M_s^{pm} , M_s^{spm} and μ_{eff}^{spm}) for the desired $M(B)$ dependence at the temperature of interest, which, at the same time, defines the true value of M_{dia} by starting with the initial value of M_{asobt} (Eq. A.4) and correcting it iteratively.

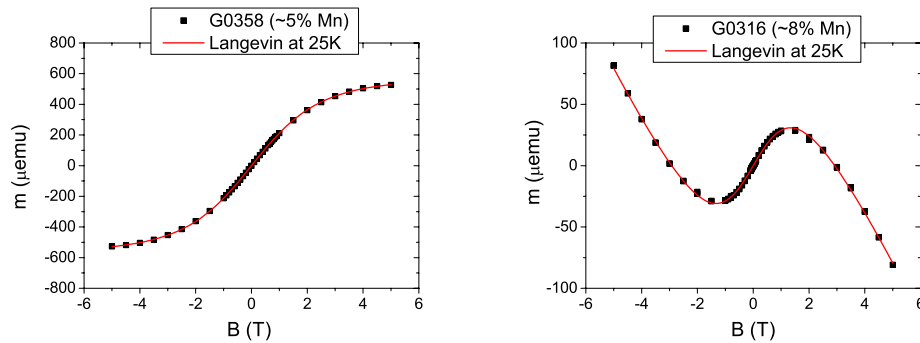


Figure A.2: Langevin-Fits of the field-dependent magnetization taking into account the three contributions (spm + pm + dia), where the diamagnetic background contribution has been determined using the iterative approach described in this appendix.

In order to visualize the influence of the iterative approach on the inferred concentrations of paramagnetic and superparamagnetic species in the studied (Ga,Mn)N epitaxial layers, the uncorrected (using $m_{dia} \approx m_{asobt}$) and corrected best-fit parameters are summarized in Table.A.1. The concentration of superparamagnetic species remains nearly equal before and after the iterative correction, while the paramagnetic contribution is drastically affected. The values of M_s^{pm} and hence the concentration c_{Mn}^{pm} for the highest doped (Ga,Mn)N epilayers are underestimated by about 35% when the approximation $m_{dia}(300K) \approx m_{asobt}(300K)$ is taken to calculate the fit parameters in the framework of the Langevin-model.

Therefore, it is strongly recommended to consider any paramagnetic/superparamagnetic contribution in order to perform the diamagnetic background correction at 300 K, even when the dimensions of diamagnetic substrates appear to be large enough to justify the neglect of all other phases which are not diamagnetic.

Sample	m_{dia} [emu/T]	M_s^{spm} [emu]	M_s^{pm} [emu]	$c_{clusters}^{spm}$ [cm ⁻³]	c_{Mn}^{pm} [cm ⁻³]
G0316 (uc)	7.69×10^{-5}	1.72×10^{-4}	8.22×10^{-4}	33.1×10^{18}	1.99×10^{21} (4.5%)
G0316 (c)	8.83×10^{-5}	1.69×10^{-4}	1.13×10^{-3}	32.5×10^{18}	2.73×10^{21} (6.2%)
G0358 (uc)	8.49×10^{-5}	7.02×10^{-5}	2.07×10^{-3}	7.01×10^{18}	1.75×10^{21} (3.9%)
G0358 (c)	1.15×10^{-4}	6.9×10^{-5}	2.91×10^{-3}	6.87×10^{18}	2.46×10^{21} (5.6%)

Table A.1: Best-Fit parameters obtained using the uncorrected (uc) and corrected (c) diamagnetic background contribution. The concentration of the paramagnetic species are underestimated by about 35% when using the uncorrected m_{dia} values, while the superparamagnetic contribution remains nearly unaffected.

B. Positron Annihilation Spectroscopy: Experimental details

Positron annihilation spectroscopy is a characterization technique where neutral and negatively charged open volume defects can be identified by measuring the Doppler broadening of the γ -radiation emitted during the annihilation process. The lineshape of the emitted radiation depends on the electron potential where the annihilation occurs, thus being a fingerprint of a determined (neutral or negatively charged) open volume defect.

The Doppler broadening of the positron annihilation radiation has been measured by two germanium detectors with a resolution of 1.3 keV at 511 keV, using a mono-energetic slow positron beam. A spectrum of $n > 5 \times 10^5$ counts was accumulated for each point. The lineshape of the doppler broadened annihilation γ -radiation is analyzed using the conventional lineshape parameters S ($|E_\gamma - 511 \text{ keV}| < 0.75 \text{ keV}$) and W ($2.86 \text{ keV} < |E_\gamma - 511 \text{ keV}| < 7.33 \text{ keV}$). Thereby, the measured S parameter is a weighted linear superposition of annihilations in different positron annihilation states

$$S = \eta_{GaN} S_{GaN} + \sum_{i=1}^N \eta_i S_i \quad (\text{B.1})$$

where S_{GaN} is the characteristic value for the annihilation of a delocalized positron in the GaN lattice, and S_i stands for the characteristic S value of one of the N present positron trapping centers. The fractions of positrons trapped in the respective states, η_{GaN} and η_i , are proportional to the defect concentrations. A similar equation is valid for the W parameter.

Fig. B.1 shows the dependence of the S and W parameters on the energy of the incident positron beam for a ferromagnetic (J0175) and non-ferromagnetic (J0225) GaGdN sample. In this way, the annihilation characteristics of the dominant vacancy defects can be probed along the depth of the sample. The S and W values which are taken for the construction of the S/W plots described in section (3.3.4), consist in the average value between 4 and 10 keV which corresponds to the depth region which is not affected by surface and interface effects.

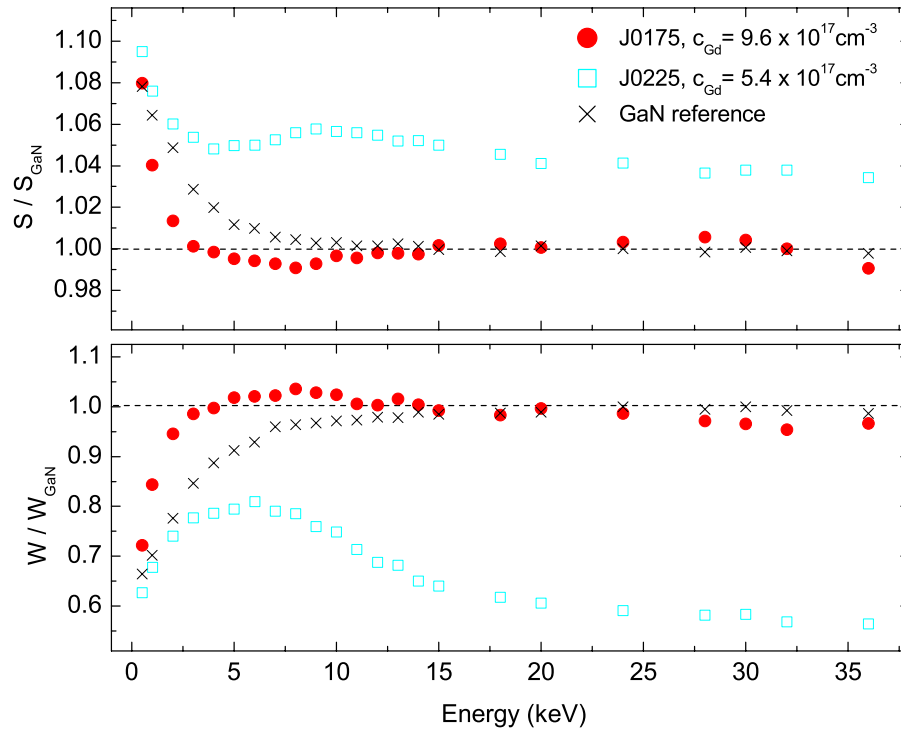


Figure B.1: S and W parameters as a function of the positron implantation energy, which is proportional to the sample depth. All spectra have been divided by the GaN reference value.

Bibliography

- [1] M. N. Baibich, J. M. Broto, A. Fert, F. Nguyen van Dau, and F. Petroff. Giant magnetoresistance of (001)Fe/(001)Cr magnetic superlattices. *Physical Review Letters*, 61:2472, 1988.
- [2] G. Binasch, P. Grünberg, F. Saurenbach, and W. Zinn. Enhanced magnetoresistance in layered magnetic structures with antiferromagnetic interlayer exchange. *Physical Review B*, 39:4828, 1989.
- [3] J. M. Kikkawa, I. P. Smorchkova, N. Samarth, and D. D. Awschalom. Room-temperature spin memory in two-dimensional electron gases. *Science*, 277:1284, 1997.
- [4] T. Jungwirth *et al.* Prospects for high temperature ferromagnetism in (Ga,Mn)As semiconductors. *Physical Review B*, 72:165204, 2005.
- [5] T. Dietl, H. Ohno, F. M. J. Cibert, and D. Ferrand. Zener Model Description of Ferromagnetism in Zinc-Blende Magnetic Semiconductors. *Science*, 287:1019, 2000.
- [6] M. Overberg, C. Abernathy, S. Pearton, N. Theodoropoulou, K. McCarthy, and A. Hebard. Indication of ferromagnetism in molecular-beam epitaxy-derived n-type GaMnN. *Applied Physics Letters*, 79:327, 2001.
- [7] M. L. Reed, N. A. El-Masry, H. Stadelmeier, M. K. Ritums, M. J. Reed, C. A. Parker, J. C. Roberts, and S. M. Bedair. Room temperature ferromagnetic properties of (Ga,Mn)N. *Applied Physics Letters*, 79:3473, 2001.
- [8] S. Sasaki, S. Sonoda, Y. Yamamoto, K. Suga, S. Shimizu, K. Kindo, and H. Hori. Magnetic and transport characteristics on high Curie temperature ferromagnet of Mn-doped GaN. *Journal of Applied Physics*, 91:7911, 2002.
- [9] S. Dhar, O. Brandt, A. Trampert, L. Däweritz, A. J. Friedland, K. H. Ploog, J. Keller, B. Beschoten, and G. Güntherodt. Origin of high-temperature ferromagnetism in (Ga,Mn)N layers grown on 4H-SiC(0001) by reactive molecular-beam epitaxy. *Applied Physics Letters*, 82:2077, 2003.

- [10] E. Sarigiannidou, F. Wilhelm, E. Monroy, R. M. Galera, E. Bellet-Amalric, A. Rogalev, J. Goulon, J. Cibert, and H. Mariette. Intrinsic ferromagnetism in wurtzite (Ga,Mn)N semiconductor. *Physical Review B*, 74:041306(R), 2006.
- [11] N. Nepal, M. Oliver Luen, J. M. Zavada, S. M. Bedair, P. Frajtag, and N. A. El-Masry. Electrical field control of room temperature ferromagnetism in III-N dilute magnetic semiconductor films. *Applied Physics Letters*, 94:132505, 2009.
- [12] V. Stefanowicz *et al.* Structural and paramagnetic properties of $\text{Ga}_{1-x}\text{Mn}_x\text{N}$. *Physical Review B*, 73:235210, 2010.
- [13] N. Teraguchi, A. Suzuki, Y. Nanishi, Y. Zhou, M. Hasimoto, and H. Asahi. Room-temperature observation of ferromagnetism in diluted magnetic semiconductor GaGdN grown by RF-molecular beam epitaxy. *Solid State Communications*, 122:651, 2002.
- [14] S. Dhar, L. Perez, O. Brandt, A. Trampert, K. H. Ploog, J. Keller, and B. Beschoten. Gd-doped GaN: A very dilute ferromagnetic semiconductor with a Curie Temperature above 300K. *Physical Review B*, 72:245203, 2005.
- [15] M. Khaderbad, S. Dhar, L. Perez, K. H. Ploog, A. Melnikov, and A. D. Wieck. Effect of annealing on the magnetic properties of Gd focused ion beam implanted GaN. *Applied Physics Letters*, 91:072514, 2007.
- [16] J. K. Hite, R. M. Frazier, R. P. Davies, G. T. Thaler, C. R. Abernathy, S. J. Pearton, J. M. Zavada, E. Brown, and U. Hoemmerich. Effect of Si co-doping on Ferromagnetic Properties of GaGdN. *Journal of Electronic Materials*, 36 (4):391, 2006.
- [17] F. Y. Lo, A. Melnikov, D. Reuter, Y. Cordier, and A. D. Wieck. Magnetotransport in Gd-implanted wurtzite GaN/ $\text{Al}_x\text{Ga}_{1-x}\text{N}$ high electron mobility transistor structures. *Applied Physics Letters*, 92:112111, 2008.
- [18] R. P. Davies, B. P. Gila, C. R. Abernathy, S. J. Pearton, and C. J. Stanton. Defect-enhanced ferromagnetism in Gd- and Si-coimplanted GaN. *Applied Physics Letters*, 96:212502, 2010.
- [19] S. Dhar, O. Brandt, M. Ramsteiner, V. F. Sapega, and K. H. Ploog. Colossal magnetic moment in Gd-doped GaN. *Physical Review Letters*, 94:037205, 2005.
- [20] V. Darakchieva, B. Monemar, and A. Usui. On the lattice parameters of GaN. *Applied Physics Letters*, 91:031911, 2007.

- [21] I. Grzegory, S. Krukowski, M. Leszczynski, P. Perlin, T. Suski, and S. Porowski. The application of high pressure in physics and technology of III-V nitrides. *Acta Physica Polonica A*, 100:57, 2001.
- [22] R. Dwilinski, R. Doradzinski, J. Garczynski, L. P. Sierzputowski, A. Puchalski, Y. Kanbara, K. Yagi, H. Minakguchi, and H. Hayashi. Bulk ammonothermal GaN. *Journal of Crystal Growth*, 311:3015, 2009.
- [23] H. P. Maruska and J. J. Tietjen. Preparation and properties of vapor-deposited single-crystalline GaN. *Applied Physics Letters*, 15:327, 1969.
- [24] T. L. Tansley and R. J. Egan. Point defect energies in the III-Nitrides of Aluminium, Gallium and Indium. *Physical Review B*, 45:10942, 1992.
- [25] P. Perlin, T. Suski, H. Teisseyre, M. Leszczynski, I. Grzegory, J. Jun, S. Porowski, P. Bogulawski, J. Bernholc, J. C. Chervin, A. Polian, and T. D. Moustakas. Towards the identification of the dominant donor in GaN. *Physical Review Letters*, 75:296, 1995.
- [26] D. W. Jenkins, J. D. Dow, and M. H. Tsai. Impurity conduction in transmutation-doped *p*-type germanium. *Journal of Applied Physics*, 72:4130, 1992.
- [27] P. Boguslawski, E. L. Briggs, and J. Bernholc. Native defects in gallium nitride. *Physical Review B (R)*, 51:17255, 1995.
- [28] J. Neugebauer and C. Van de Walle. Atomic geometry and electronic structure of native defects in GaN. *Physical Review B (R)*, 50:8067, 1994.
- [29] C. Van de Walle and J. Neugebauer. First-principles calculations for defects and impurities: Applications to III-Nitrides. *Journal of Applied Physics*, 95:3851, 2004.
- [30] S. Limpijumnong and C. Van de Walle. Diffusivity of native defects in GaN. *Physical Review B*, 69:035207, 2004.
- [31] M. Kocan, A. Rizzi, H. Lueth, S. Keller, and U. K. Mishra. Surface potential at as-Grown GaN(0001) MBE layers. *Physica Status Solidi B*, 234:773, 2002.
- [32] T. Zywietz, J. Neugebauer, and M. Scheffler. Adatom diffusion at GaN (0001) and (000-1) surfaces. *Applied Physics Letters*, 73:487, 1998.
- [33] M. Kocan. MBE-Praktikum. *Universitaet Göttingen*, 2005.

- [34] D. C. Look. Electrical transport properties of III-nitrides. *Material Science and Engineering B*, 50:50, 1997.
- [35] J. Neugebauer and C. Van de Walle. Gallium vacancies and the yellow luminescence in GaN. *Applied Physics Letters*, 69:503, 1996.
- [36] C. Van de Walle. Interactions of hydrogen with native defects in GaN. *Physical Review B*, 56:R10020, 1997.
- [37] A. F. Wright. Substitutional and interstitial oxygen in wurtzite GaN. *Journal of Applied Physics*, 98:103531, 2005.
- [38] F. Tuomisto, J. M. Mki, and M. Zajac. Vacancy defects in bulk ammonothermal GaN crystals. *Journal of Crystal Growth*, 312:2620, 2010.
- [39] D. Bliss, B. Wang, M. Suscavage, R. Lancto, S. Swider, W. Eikenberry, and Lynch. C. Ammonothermal GaN: Morphology and properties. *Journal of Crystal Growth*, 312:1069, 2010.
- [40] K. Saarinen *et al.* Observation of Native Ga Vacancies in GaN by Positron Annihilation. *Physical Review Letters*, 79:3030, 1997.
- [41] K. Saarinen, P. Seppl, J. Oila, P. Hautojrvi, C. Corbel, O. Briot, and R. L. Aulombard. Gallium vacancies and the growth stoichiometry of GaN studied by positron annihilation spectroscopy. *Applied Physics Letters*, 73:3253, 1998.
- [42] S. Hautakangas, I. Makkonen, V. Ranki, M. J. Puska, K. Saarinen, X. Xu, and D. C. Look. Direct evidence of impurity decoration of Ga vacancies in GaN from positron annihilation spectroscopy. *Physical Review B*, 73:193301, 2006.
- [43] A. Van Esch, L. Van Bockstal, J. De Boeck, G. Verbanck, A. S. Steenbergen, P. J. Wellmann, B. Grietens, R. Bogaerts, F. Herlach, and G. Borghs. Interplay between the magnetic and transport properties in the III-V diluted magnetic semiconductor $\text{Ga}_{1-x}\text{Mn}_x\text{As}$. *Physical Review B*, 56:13103, 1997.
- [44] H. Chou, C. P. Lin, J. C. A. Huang, and H. S. Hsu. Magnetic coupling and electric conduction in oxide dilute magnetic semiconductors. *Physical Review B*, 77:245210, 2008.
- [45] T. Dietl. Interplay between Carrier Localization and Magnetism in Dilute Magnetic and Ferromagnetic Semiconductors. *Journal of the Physical Society of Japan*, 77:031005, 2008.

- [46] J. K. Lang, Y. Baer, and P. A. Cox. Study of the 4f and valence band density of states in rare-earth metals: II. Experiments and results. *Journal of Physics F: Metal Physics*, 11:121, 1981.
- [47] H. Ibach and H. Lüth. Festkörperphysik. *Springer*, page 396, 1999.
- [48] B. Sapoal and C. Herrmann. *Physics of Semiconductors*. Springer, 1995.
- [49] C. Yamanouchi. Hall-coefficient and resistivity in the intermediate impurity conduction of *n*-type germanium. *Journal of the Physical Society of Japan*, 20:1029, 1965.
- [50] E. I. Gershenzon, G. N. Goltsmann, and Melnikov. Binding energy of a carrier on a neutral impurity atom in germanium and in silicon. *JETP-Letters*, 14:185, 1971.
- [51] H. Fritzsche and M. Cuevas. Impurity conduction in transmutation-doped *p*-type germanium. *Physical Review*, 119:1238, 1960.
- [52] L. Essaleh, S. Wasim, and J. Galibert. Effect of impurity conduction on the electrical characteristics of *n*-type CuInSe₂. *Journal of Applied Physics*, 90:3993, 2001.
- [53] A. Miller and E. Abrahams. Impurity conduction at low concentrations. *Physical Review*, 120:745, 1960.
- [54] L. D. Landau and E. M. Lifshitz. *Quantum Mechanics*. Pergamon, London, 1965.
- [55] V. Ambegaokar and B. I. Halperlin. Hopping conductivity in disordered systems. *Physical Review B*, 4:2612, 1971.
- [56] M. Pollak. A percolation treatment of dc hopping conduction. *Journal of Non-Crystalline Solids*, 11:1, 1972.
- [57] B. I. Shklovskii and A. L. Efros. Impurity band and conductivity of compensated semiconductors. *JETP-Letters*, 33:468, 1971.
- [58] S. Kirkpatrick. An introduction to percolation theory. *Advances in Physics*, 20:325, 1973.
- [59] J. Kurkijarvi. Conductivity in random systems. II. Finite-size-system percolation. *Physical Review B*, 9:770, 1974.

- [60] G. E. Pike and C. H. Seager. Percolation and conductivity: A computer study. *Physical Review B*, 10:1421, 1974.
- [61] N. W. Dalton and C. Domb. Dependence of critical concentration of dilute ferromagnet on the range of interaction. *Proceedings of the Physical Society (London)*, 83:496, 1954.
- [62] A. S. Skal, B. I. Shklovskii, and A. L. Efros. Activation energy of hopping conduction. *Sov.Phys.-Solid State*, 17:316, 1975.
- [63] K. J. Hayden and P. N. Butcher. Analysis of hopping conduction in impurity bands. *Philosophical Magazine*, B38:603, 1978.
- [64] V. L. Nguyen, B. I. Shklovskii, and A. L. Efros. Activation energy of hopping conduction in lightly doped semiconductors. *Sov.Phys.-Semicond.*, 13:1281, 1979.
- [65] N. F. Mott. Conduction in glasses containing transition metal ions. *Journal of Non-Crystalline Solids*, 1:1, 1968.
- [66] A. S. Skal and B. I. Shklovskii. Mott equation for low temperature edge conductivity. *Sov.Phys.-Solid State*, 67:1820, 1971.
- [67] A. L. Efros, B. I. Shklovskii, and I. Y. Yanchev. Impurity conductivity in low compensated semiconductors. *Physical Review B*, 50:45, 1972.
- [68] M. L. Knotek and M. Pollak. Correlation effects in hopping conduction: A treatment in terms of multielectron interactions. *Physical Review B*, 9:644, 1974.
- [69] S. D. Baranowski, A. L. Efros, and B. L. Gel'mont. Coulomb gap in disordered systems. Computer simulation. *Solid State Communications*, 27:1, 1978.
- [70] A. L. Efros, V. L. Nguyen, and B. I. Shklovskii. Impurity band structure in lightly doped semiconductors. *Journal of Physics C*, 12:1869, 1979.
- [71] A. L. Efros and B. I. Shklovskii. Coulomb-gap and low-temperature conductivity of disordered systems. *Journal of Physics C*, 8:L49, 1971.
- [72] A. L. Efros and B. I. Shklovskii. Coulomb-gap in disordered systems. *Journal of Physics C*, 9:2021, 1976.
- [73] S. D. Baranovski, B. I. Shklovskii, and A. L. Efros. Elementary excitations in disordered systems with localized electrons. *JETP-Letters*, 51:199, 1980.

- [74] N. F. Mott. The effect of electron interaction on variable-range hopping. *Philosophical Magazine*, 34:643, 1976.
- [75] J. H. Davies. The density of states in the coulomb gap. *Philosophical Magazine*, 52:511, 1985.
- [76] R. Chicon, M. Ortuno, and M. Pollak. Hardening of the Coulomb gap by electronic polarons. *Physical Review B*, 37:10520, 1988.
- [77] T. Castner. *Hopping transport in solids*. North-Holland (Amsterdam), 1991.
- [78] T. Castner, N. K. Lee, G. S. Cieloszyk, and G. L. Salinger. Dielectric Anomaly and the Metal-Insulator transition in n-type Silicon. *Physical Review Letters*, 34:1627, 1975.
- [79] H. Hess, K. DeConde, T. F. Rosenbaum, and G. A. Thomas. Giant dielectric constants at the approach to the insulator-metal transition. *Physical Review B*, 25:5578, 1982.
- [80] T. Sato, K. Ohashi, H. Sugai, T. Sumi, K. Haruna, N. Maeta, N. Matsumoto, and H. Otsuka. Transport of heavily boron-doped synthetic semiconductor diamond in the hopping regime. *Physical Review B*, 61:12970, 2000.
- [81] I. Terry, T. Penney, S. von Molnar, and P. Becla. Low-temperature transport properties of $\text{Cd}_{0.91}\text{Mn}_{0.09}\text{Te}:\text{In}$ and evidence for a magnetic hard gap in the density of states. *Physical Review Letters*, 69:1800, 1992.
- [82] P. Dai, Y. Zhang, and M. P. Sarachik. Low-temperature transport in the hopping regime: Evidence for correlations Due to Exchange. *Physical Review Letters*, 69:1804, 1992.
- [83] B. I. Shklovskii and A. L. Efros. *Electronic properties of doped semiconductors*. Springer, 1984.
- [84] H. Böttger and V. V. Bryskin. Theory of Hall-Effect in hopping region in disordered systems: 2. Random resistor network and Hall-Effect. *Physica Status Solidi B*, 81:1, 1977.
- [85] L. Friedman and M. Pollak. The Hall effect in the variable-range-hopping regime. *Philosophical Magazine B*, 44:487, 1981.
- [86] M. Grünewald, H. Mueller, P. Thomas, and D. Wuertz. The Hopping Hall Mobility- A percolation approach. *Solid State Communications*, 38:1011, 1981.

- [87] T. Holstein. Hall Effect in Impurity Conduction. *Physical Review*, 124:1329, 1961.
- [88] M. Amitay and M. Pollak. An experimental investigation of Hall effect in hopping region. *Journal of the Physical Society of Japan*, S21:549, 1966.
- [89] R. Klein. Investigation of the Hall Effect in impurity-hopping conduction. *Physical Review B*, 31:2014, 1985.
- [90] D. Emin. The sign of the Hall effect in hopping conduction. *Philosophical Magazine B*, 35:1189, 1977.
- [91] E. Dona. MBE growth of AlGa_N/Ga_N Heterostructures for Resonant Tunneling Diode Applications. *Diploma Thesis, Universita Degli Studi Di Modena/FZJ Jülich*, pages 45–46, 2002.
- [92] Z. Fan, N. Mohammad, W. Kim, O. Aktas, A. Botchkarev, and H. Morkoc. Very low resistance multilayer Ohmic contact to Ga_N. *Applied Physics Letters*, 68:1672, 1996.
- [93] L. J. van der Pauw. A method of measuring specific resistivity and Hall effect of discs of arbitrary shape. *Philips Research Reports*, 13:1, 1958.
- [94] M. Roever. GaMnN- MBE on Si(111). *Diploma Thesis, Universität Göttingen*, 2005.
- [95] D. D. Mai. Ferromagnetismus bei Raumtemperatur in mehrphasigen (Ga,Mn)N Schichten und Heterostrukturen. *Dissertation, Universität Göttingen*, 2009.
- [96] D. C. Look and R. J. Molnar. Degenerate layer at Ga_N/sapphire interface: Influence on Hall-Effect measurements. *Applied Physics Letters*, 70:3377, 1997.
- [97] D. C. Look, D. C. Reynolds, W. Kim, O. Aktas, A. Botchkarev, A. Salvador, and H. Morkoc. Deep-center hopping conduction in Ga_N. *Journal of Applied Physics*, 80:2960, 1996.
- [98] J. Oila, V. Ranki, K. Saarinen, P. Hautojrv, J. Likone, J. M. Baranowski, K. Pakula, T. Suski, M. Leszczynski, and I. Grzegory. Influence of dopants and substrate material on the formation of Ga vacancies in epitaxial Ga_N layers. *Physical Review B*, 63:045205, 2001.
- [99] C. Rauch and F. Tuomisto. *Private Communication*, 2010.

- [100] W. J. Moore, J. A. Freitas, G. C. B. Braga, R. J. Molnar, S. Lee, K. Lee, and I. Song. Identification of Si and O donors in hydride-vapor-phase epitaxial GaN. *Applied Physics Letters*, 79:2570, 2001.
- [101] B. K. Meyer, D. Volm, A. Graber, H. C. Alt, T. Detchprohm, A. Amano, and I. Akasaki. Shallow donors in GaN- The binding energy and the electron effective mass. *Solid State Communications*, 95:597, 1995.
- [102] W. Götz, N. M. Johnson, C. Chen, H. Liu, C. Kuo, and W. Imler. Activation energies of Si donors in GaN. *Applied Physics Letters*, 68:3144, 1996.
- [103] L. Liu, P. Yu, Z. Ma, and S. Mao. Ferromagnetism in GaN:Gd: A Density Functional Theory Study. *Physical Review Letters*, 100:127203, 2008.
- [104] P. Dev and P. Zhang. Defect-Induced Intrinsic Magnetism in Wide-Gap III-Nitrides. *Physical Review Letters*, 100:117204, 2008.
- [105] Y. Gohda and A. Oshiyama. Intrinsic ferromagnetism due to cation vacancies in Gd-doped GaN: First-principles calculations. *Physical Review B*, 78:161201(R), 2008.
- [106] C. Mitra and W. R. L. Lambrecht. Interstitial-nitrogen- and oxygen-induced magnetism in Gd-doped GaN. *Physical Review B*, 80:081202(R), 2009.
- [107] P. Dev and P. Zhang. Unconventional magnetism in semiconductors: Role of localized acceptor states. *Physical Review B*, 81:085207, 2010.
- [108] A. Bonanni and T. Dietl. A story of high-temperature ferromagnetism in semiconductors. *Chemical Society Reviews*, 39:528, 2010.
- [109] D. J. Keavney, S. H. Cheung, S. T. King, M. Weinert, and L. Li. Role of Defect Sites and Ga Polarization in the Magnetism of Mn-doped GaN. *Physical Review Letters*, 95:257201, 2005.
- [110] J. Hong. Local magnetic moment induced by Ga vacancy defect in GaN. *Journal of Applied Physics*, 103:063907, 2008.
- [111] K Sato, P. H. Dederichs, H. Katayama-Yoshida, and J. Kudrnovsky. Exchange interactions in dilute magnetic semiconductors. *Journal of Physics: Condensed Matter*, 16:S5491, 2004.
- [112] P. H. Dederichs. *Diluted Magnetic Semiconductors*. Magnetism Goes Nano, 36th Spring School, Forschungszentrum Jülich, 2005.

- [113] M. Kocan, J. Malindretos, M. Roever, J. Zenneck, T. Niermann, D. D. Mai, M. Bertelli, M. Seibt, and A. Rizzi. Mn-incorporation in GaN thin layers grown by molecular-beam epitaxy. *Semiconductor Science and Technology*, 21:1348, 2006.
- [114] A. L. Patterson. The Scherrer Formula for X-ray particle size determination. *Physical Review*, 56:978, 1939.
- [115] S. Dhar, O. Brandt, A. Trampert, A. J. Friedland, Sun K. Y., and K. H. Ploog. Observation of spin-glass behavior in homogeneous (Ga,Mn)N layers grown by reactive molecular-beam epitaxy. *Physical Review B*, 67:165205, 2003.
- [116] G. Thaler, R. Frazier, J. Gila, B. Stapleton, M. Davidson, C. R. Abernathy, S. J. Pearton, and C. Segre. Effect of Mn concentration on the structural, optical and magnetic properties of GaMnN. *Applied Physics Letters*, 84:1314, 2004.
- [117] P. Waltereit, O. Brandt, A. Trampert, M. Ramsteiner, M. Reiche, M. Qi, and K. H. Ploog. Influence of AlN nucleation layers on growth mode and strain relief of GaN grown on 6H-SiC(0001). *Applied Physics Letters*, 74:3660, 1999.
- [118] T. Perry, T. Zheleva, M. D. Bremser, R. F. Davis, W. Shan, and J. J. and Song. Correlation of Biaxial Strains, Bound Exciton Energies, and Defect Microstructures in GaN Films Grown on AlN/6H-SiC(0001) Substrates. *Journal of Electron Materials*, 26:224, 1997.
- [119] K. Jeganathan, M. Shimizu, and H. Okumura. Influence of the AlGaIn buffer layer on the biaxial strain of GaN epilayers grown on 6H-SiC(0001) by molecular-beam epitaxy. *Journal of Applied Physics*, 97:013524, 2005.
- [120] W. Li and W. Ni. Residual strain in GaN epilayers grown on sapphire and (6H)SiC substrates. *Applied Physics Letters*, 68 (19):2705, 1996.
- [121] V. S. Harutyunyan, A. P. Aivazyan, E. R. Weber, Y. Kim, Y. Park, and S. G. Subramanya. High-resolution x-ray diffraction strain-stress analysis of GaN/Sapphire heterostructures. *Journal of Physics D: Applied Physics*, 34:A35–A39, 2001.
- [122] T. Niermann, D. Mai, M. Roever, M. Kocan, J. Zenneck, J. Malindretos, A. Rizzi, and M. Seibt. Substitutional to interstitial ratio of Mn in nanostructured GaN by electron channeling enhanced microanalysis. *Applied Physics Letters*, 103:073520, 2008.

- [123] B. Heying, X. H. Wu, S. Keller, Y. Li, D. Kapolnek, B. P. Keller, S. P. DenBaars, and J. S. Speck. Role of threading dislocation structure on the x-ray diffraction peak widths in epitaxial GaN films. *Applied Physics Letters*, 68(5):643, 1996.
- [124] J. Gosk, M. Zajac, A. Wolos, M. Kaminska, A. Twardowski, I. Grzegory, M. Bockowski, and S. Porowski. Magnetic anisotropy of bulk GaN:Mn single crystals codoped with Mg acceptors. *Physical Review B*, 71:094432, 2005.
- [125] J. T. Vallin, G. A. Slack, S. Roberts, and A. E. Hughes. Infrared absorption in some II-VI compounds doped with Cr. *Physical Review B*, 2:4313, 1970.
- [126] W. Mac, A. Twardowski, P. Eggenkamp, H. Swagten, Y. Shapira, and M. Demianiuk. Magnetic properties of Cr-based diluted magnetic semiconductors. *Physical Review B*, 50:14144, 1994.
- [127] S. Blundell. Magnetism in Condensed Matter. *Oxford, University Press*, page 29, 2001.
- [128] J. P. Bouchaud. Magnetic and structural properties of manganese carbonitrides and perowskites Mn_3GaC and Mn_3GaN . *Ann. Chim.*, 3:81, 1968.
- [129] E. F. Bertaut, D. Fruchart, J.P. Bouchaud, and R. Fruchart. Diffraction Neutronique de Mn_3GaN . *Solid State Communications*, 6:251, 1968.
- [130] B. Song, J. Jian, H. Bao, M. Lei, H. Li, G. Wang, Y. Xu, and X. Chen. Observation of spin-glass behavior in antiperovskite Mn_3GaN . *Applied Physics Letters*, 92:192511, 2008.
- [131] I. T. Yoon, T. W. Kang, and D. J. Kim. Magnetic behavior of Mn_3GaN precipitates in ferromagnetic $\text{Ga}_{1-x}\text{Mn}_x\text{N}$ layers. *Material Science and Engineering B*, 134:49–53, 2006.
- [132] M. S. Miao, A. Herwadkar, and W. R. L. Lambrecht. Electronic structure and magnetic properties of Mn_3GaN precipitates in $\text{Ga}_{1-x}\text{Mn}_x\text{N}$. *Physical Review B*, 72:033204, 2005.
- [133] M. Opel, K. W. Nielsen, S. Bauer, S. T. B. Goennenwein, J. C. Cezar, D. Schmeisser, J. Simon, W. Mader, and R. Gross. Nanosized superparamagnetic precipitates in cobalt-doped ZnO. *European Physical Journal B*, 63:437, 2008.
- [134] K. Sato, W. Schweika, P. H. Dederichs, and H. Katayama-Yoshida. Low-temperature ferromagnetism in (Ga,Mn)N: Ab-initio calculations. *Physical Review B*, 70:201202(R), 2004.

- [135] P. Boguslawski and J. Bernholc. Fermi-level effects on the electronic structure and magnetic couplings in (Ga,Mn)N. *Physical Review B*, 72:115208, 2005.
- [136] J. Kang, J. K. Chang, and H. Katayama-Yoshida. First-principles study of ferromagnetism in Mn-doped GaN. *Journal of Superconductivity and Novel Magnetism*, 18:55, 2005.
- [137] H. Mamiya, S. Nimori, M. Ohnuma, I. Nakatani, M. Demura, and T. Furubayashi. Comparison of field-cooled, zero-field-cooled and thermoremanent magnetization in nanomagnet, random magnet and bulk ferromagnet. *Journal of Magnetism and Magnetic Materials*, 316:e535, 2007.
- [138] B. Belhadji, L. Berqvist, R. Zeller, P. H. Dederichs, K. Sato, and H. Katayama-Yoshida. Trends of exchange interactions in dilute magnetic semiconductors. *Journal of Physics: Condensed Matter*, 19:436227, 2007.
- [139] T. Graf, M. S. Gjukic, M. abd Brandt, M. Stutzmann, and O. Ambacher. The $\text{Mn}^{3+/2+}$ acceptor level in group III nitrides. *Applied Physics Letters*, 81(27):5159, 2002.
- [140] S. Marcet, D. Ferrand, D. Halley, S. Kuroda, H. Mariette, E. Gheeraert, F. J. Teran, M. L. Sadowski, R. M. Galera, and J. Cibert. Magneto-Optical spectroscopy of (Ga,Mn)N epilayers. *Physical Review B*, 74:125201, 2006.
- [141] J. Zenneck. Optische Eigenschaften von verdnnnten magnetischen Halbleitern auf GaN-Basis. *Dissertation, Universität Göttingen*, 2007.
- [142] J. Zenneck, T. Niermann, D. Mai, Roever M., M. Kocan, J. Malindretos, M. Seibt, A. Rizzi, N. Kaluza, and H. Hardtdegen. Intra-atomic photoluminescence at 1.41eV of substitutional Mn in GaMnN of high optical quality. *Journal of Applied Physics*, 101:063504, 2007.
- [143] O. Eriksson, L. Bergqvist, B. Sanyal, J. Kudrnovsky, V. Drchal, P. Korzhavyi, and I. Turek. Electronic structure and magnetism of diluted magnetic semiconductors. *Journal of Physics: Condensed Matter*, 16:S5481, 2004.
- [144] B. Sanyal, O. Bengone, and S. Mirbt. Electronic structure and magnetism of Mn-doped GaN. *Physical Review B*, 68:205210, 2003.
- [145] A. Titov, X. Biquard, D. halley, S. Kuroda, E. Bellet-Amalric, H. Mariette, J. Cibert, A. E. Merad, G. Merad, M. B. Kanoun, E. Kulatov, and Y. A. Uspenskii. X-ray absorption near-edge structure and valence state of Mn in (Ga,Mn)N. *Physical Review B*, 72:115209, 2005.

- [146] V. N. Antonov, A. N. Yaresko, and O. Jepsen. X-ray magnetic dichroism in III-V diluted magnetic semiconductors: First-principles calculations. *Physical Review B*, 81:075209, 2010.
- [147] L. M. Sandratskii, P. Bruno, and J. Kudrnovsky. On-site Coulomb interaction and the magnetism of (GaMn)N and (GaMn)As. *Physical Review B*, 69:195203, 2004.
- [148] A. Ney, T. Kammermeier, V. Ney, s. Ye, K. Ollefs, E. Manuel, S. Dhar, K. H. Ploog, E. Arenholz, F. Wilhelm, and A. Rogalev. Element specific magnetic properties of Gd-doped GaN: Very small polarization of Ga and paramagnetism of Gd. *Physical Review B*, 77:233308, 2008.
- [149] Y. K. Zhou, S. W. Choi, S. Emura, S. Hasegawa, and H. Asahi. Large magnetization in high Gd concentration GaGdN and Si-doped GaGdN grown at low temperatures. *Applied Physics Letters*, 92:062505, 2008.
- [150] G. M. Dalpian and S. H. Wei. Electron-induced stabilization of ferromagnetism in GaGdN. *Physical Review B*, 72:115201, 2005.
- [151] G. Martinez-Criado, O. Sancho-Juan, N. Garro, J. A. Sans, A. Cantarero, J. Susini, M. Roever, D. D. Mai, A. Bedoya-Pinto, J. Malindretos, and A. Rizzi. X-ray absorption in GaGdN: A study of local structure. *Applied Physics Letters*, 93:021916, 2008.
- [152] A. Svane, N. E. Christensen, L. Petit, Z. Szotek, and W. M. Temmermann. Electronic structure of rare-earth impurities in GaAs and GaN. *Physical Review B*, 74:165204, 2006.
- [153] P. Waltereit, S. H. Lim, M. McLaurin, and J. S. Speck. Heteroepitaxial growth of GaN on 6H-SiC(0001) by Plasma-Assisted Molecular Beam Epitaxy. *Physica Status Solidi (a)*, 194 (2):524–527, 2002.
- [154] C. D. Lee, V. Ramachandran, A. Sagar, R. M. Feenstra, D. W. Greve, W. L. Sarney, L. Salamanca-Riba, D. C. Look, S. Bai, W. J. Choyke, and R. P. Devaty. Properties of GaN Epitaxial layers Grown on 6H-SiC(0001) by Plasma-Assisted Molecular Beam Epitaxy. *Journal of Electronic Materials*, 30(3):162, 2001.
- [155] K. Jeganathan, M. Shimizu, and H. Okumura. Reduction of dislocations in GaN epilayers using templated three-dimensional coherent nanoislands. *Applied Physics Letters*, 86:191908, 2005.

- [156] T. H. Kim, S. Choi, M. Morse, P. Wu, C. Yi, A. Brown, M. Losurdo, M. Gianregorio, and G. Bruno. Impact of unintentional and intentional nitridation of the 6H-SiC(0001) substrate on GaN epitaxy. *Journal of Vacuum Science and Technology*, 23(3):1181, 2005.
- [157] F. Leuenberger, A. Parge, W. Felsch, K. Fauth, and M. Hessler. GdN thin films: Bulk and local electronic and magnetic properties. *Physical Review B*, 73:214430, 2006.
- [158] A. L. Efros and B. Shklovskii. *Electronic Properties of Doped Semiconductors*, p.235. Springer, New York, 1984.
- [159] T. Castner. *Hopping Transport in Solids*, p.10. North-Holland, Amsterdam, 1991.
- [160] R. Rosenbaum. Crossover from Mott to Efros-Shklovskii variable-range-hopping conductivity in In_xO_y films. *Physical Review B*, 44:3599, 1991.
- [161] B. L. Sheu, R. C. Myers, J. M. Tang, N. Samarth, D. D. Awschalom, P. Schiffer, and M. E. Flatte. Onset of Ferromagnetism in Low-Doped $\text{Ga}_{1-x}\text{Mn}_x\text{As}$. *Physical Review Letters*, 99:227205, 2007.
- [162] S. Wu and N. Newman. Electrical transport properties of ferromagnetic $\text{Ga}_x\text{Cr}_{1-x}\text{N}$ thin films. *Applied Physics Letters*, 89:142105, 2006.
- [163] A. G. Zabrodskii. Coulomb gap, its critical behavior, and the metal-insulator transition in doped semiconductors. *Czechoslovak Journal of Physics*, 46 S5:2455, 1996.
- [164] S. C. Erwin and A. G. Pethukov. Self-compensation in manganese doped ferromagnetic semiconductors. *Physical Review Letters*, 89:227201, 2002.
- [165] F. Tuomisto, V. Ranki, D. C. Look, and G. C. Farlow. Introduction and recovery of Ga and N sublattice defects in electron irradiated GaN. *Physical Review B*, 76:165207, 2007.
- [166] M. J. Puska, C. Corbel, and R. M. Nieminen. Positron trapping in semiconductors. *Physical Review B*, 41:9980, 1990.
- [167] D. V. Lang. Deep level transient spectroscopy: a new method to characterize traps in semiconductors. *Journal of Applied Physics*, 45:3023, 1974.
- [168] A. Cavallini. *Private Communication*, September 2010.

- [169] H. Niida, T. Hori, H. Onodera, Y. Yamaguchi, and Y. Nakagawa. Magnetization and coercivity of $\text{Mn}_{3-\delta}\text{Ga}$ alloys with a D0_{22} -type structure. *Journal of Applied Physics*, 79:5946, 1996.
- [170] J. Winterlik, B. Balke, H. Fecher, C. Felser, M. C. Alves, f. Bernardi, and J. Morais. Structural, electronic, and magnetic properties of tetragonal Mn_{3-x}Ga : Experiments and first-principles calculations. *Physical Review B*, 77:054406, 2008.
- [171] F. Wu, S. Mizukami, D. Watanabe, H. Naganuma, M. Oogane, Y. Ando, and T. Miyazaki. Epitaxial $\text{Mn}_{2.5}\text{Ga}$ thin film with giant perpendicular magnetic anisotropy for spintronic devices. *Applied Physics Letters*, 94:122503, 2009.
- [172] B. Balke, G. Fecher, J. Winterlik, and C. Felser. Mn_3Ga , a compensated ferri-magnet with high Curie temperature and low magnetic moment for spin torque transfer applications . *Applied Physics Letters*, 90:152504, 2007.
- [173] A. Sakuma. Electronic structures and magnetism of CuAu-type MnNi and MnGa. *Journal of Magnetism and Magnetic Materials*, 187:105, 1998.
- [174] K. Krishnan. Ferromagnetic $\delta\text{-Mn}_{1-x}\text{Ga}_x$ thin films with perpendicular anisotropy. *Applied Physics Letters*, 61:2365, 1992.
- [175] M. Tanaka, J. P. Harbison, J. DeBoeck, T. Sands, B. Phillips, T. L. Cheeks, and V. G. Keramidas. Epitaxial growth of ferromagnetic ultrathin MnGa films with perpendicular magnetization on GaAs. *Applied Physics Letters*, 62:1565, 1993.
- [176] W. Van Roy, H. Akinaga, and S. Miyanishi. Interlayer coupling and magnetoresistance of MnGa-based trilayers with semiconducting, antiferromagnetic, and ferrimagnetic space layers. *Physical Review B*, 63:184417, 2001.
- [177] C. Adelman, J. L. Hilton, B. D. Schultz, S. McKernan, C. J. Palmstrom, X. Lou, H. Chiang, and P. A. Crowell. Spin injection from perpendicular magnetized ferromagnetic $\delta\text{-MnGa}$ in to (Al,Ga)As heterostructures. *Applied Physics Letters*, 89:112511, 2006.
- [178] E. Lu, D. Ingram, A. Smith, J. W. Knepper, and F. Y. Yang. Reconstruction Control of Magnetic Properties during Epitaxial Growth of Ferromagnetic $\text{Mn}_{3-\delta}\text{Ga}$ on Wurtzite GaN (0001). *Physical Review Letters*, 97:146101, 2006.
- [179] T. Bither and W. Cloud. Magnetic Tetragonal δ Phase in the Mn-Ga Binary. *Journal of Applied Physics*, 36:1501, 1965.

- [180] Z. Yang, J. Li, D. Wang, K. Zhang, and X. Xie. Electronic structure and magnetic properties of δ -MnGa. *Journal of Magnetism and Magnetic Materials*, 182:369, 1998.
- [181] J. M. Ziman. *Electrons and Phonons*. Clarendon, Oxford, page 364, 1960.
- [182] A. H. Wilson. The electrical conductivity of the transition metals. *Proceedings of the Royal Society of London, Serie A*, 167:580, 1938.
- [183] T. Kasuya. Electrical resistance of ferromagnetic metals. *Progress of Theoretical Physics*, 16:58, 1956.
- [184] I. Mannari. Electrical resistance of ferromagnetic metals. *Progress of Theoretical Physics*, 22:335, 1959.
- [185] D. Goodings. Electrical Resistivity of Ferromagnetic Metals at Low Temperatures. *Physical Review*, 132:542, 1963.
- [186] F. Wu, E. P. Sajitha, S. Mizukami, D. Watanabe, Miyazaki. T., H. Naganuma, M. Oogane, and Y. Ando. Electrical transport properties of perpendicular magnetized Mn-Ga epitaxial films. *Applied Physics Letters*, 96:042505, 2010.
- [187] B. Gopalakrishnan, C. Suergers, R. Montbrun, A. Singh, M. Uhlarz, and H. v. Loehneysen. Electronic transport in magnetically ordered $\text{Mn}_5\text{Si}_3\text{C}_x$ films. *Physical Review B*, 77:104414, 2008.
- [188] N. Nagaosa, J. Sinova, A. H. MacDonald, and N. P. Ong. Anomalous Hall Effect. *Reviews of Modern Physics*, 82:1539, 2010.
- [189] P. Xiong, G. Xiao, J. Q. Wang, J. Xiao, J. Jiang, and C. L. Chien. Extraordinary Hall Effect and Giant Magnetoresistance in the Granular Co-Ag System. *Physical Review Letters*, 69:3220, 1992.

Acknowledgments

This Ph.D thesis is an effort which lasted a little bit more than four years, where i was (fortunately) able to confirm my deep interest for physics. After my diploma thesis, i dared to keep „fighting“ in the controversial field of dilute magnetic semiconductors. This journey through many physical labyrinths helped me to judge where are the dead-end streets and to see the light at the end of the tunnels. This would have been impossible without the advice, support or just presence of some people whom i would like to thank gratefully:

- *Prof. Dr. Angela Rizzi*, for giving me the opportunity to start the Ph.D thesis in a competent research group, and for the constant support and excellent guidance during these years; as well as for the friendly atmosphere in the group, which helped me to almost instantaneously after my arrival in Göttingen. Grazie mille!
- *Prof. Dr. Thomas Schäpers*, for the problemless commitment to be the second corrector of this thesis, as well as for the friendly and uncomplicated way to adjust his agenda in order to find a suitable defense date.
- *Dr. Jörg Malindretos*, who was an excellent supervisor, in my opinion, the Post-Doc every Ph.D student dream of to work with. Always friendly and helpful, and with an enormous patience to answer even the most basic questions. My sincere thanks for his unconditional time disposition, either to discuss about the DMS theory or to solve any technical problem in the lab; and for being the most critical corrector of this thesis. I learned a lot from his expertise. Efharisto poli, Jörgus!
- *Prof. Dr. Rainer G. Ulbrich, Prof. Dr. Michael Seibt and Dr. Martin Wenderoth*, for their critical comments and wise suggestions every time i gave a talk in front of the audience of the IV. Physikalisches Institut.
- *Martin Röver, Dr. Dong-Du Mai and Dr. Jan Zenneck*, the fellows with whom i shared the journey through the DMS road, which was everything else than a highway. Many thanks for growing the samples which i was able to play with, for the interesting discussions and the many activities we did together outside the institute (e.g. the legendary dinner sessions with *Wan-tan soup*, *Frühlingsrolle* and *Causa*).

- *Dr. Marco Bertelli*, for his unconditional helpfulness in- and outside the institute, his moral support and for just being a real „compagno“. Our escapades to the *Zentralmensa* and to the *Lumiere*, as well as the good old *Pasta della mamma* will be always remembered.
- *Daniel Broxtermann, Murat Sivis and Christian Zube*, the fellows with whom i shared the office and the Hall-Lab, for being not the ones which just talk about physics. The room B.04.112 was just the right working atmosphere.
- *Christian Denker and Arne Urban*, for the friendly acceptance to correct some sections of this thesis, which helped me a lot when the final countdown was approaching. Thanks Arne for the nice TEM-images which made this characterization study a little bit more colorful.
- *Boris Landgraf, Till Benter, Friedrich Limbach, Michael Carsten, Clemens Trinks, Florian Werner, Janna Emkes, Dominik Ruttke, Sönke Hüls* and all the actual and former members of *La Famiglia*, as well as all the other colleagues from the IV. Physikalisches Institut, for the friendly atmosphere in- and outside the institute, and for the great time during the *Institutsausflüge*.
- *Thomas Lehmann*, for the technical support, especially in the first months where i had to revive the old e-gun evaporation facility to make the first ohmic contacts.
- *Daniel Jürgens* from the II. Physikalisches Institut, for the uncomplicated way to manage the XRD-beam time, which gave me the opportunity to measure almost all the samples i had to characterize.
- *Dr. Kun Zhang*, also from the II. Physikalisches Institut, for his incredible efficiency in measuring the concentration of the MnGa layers by means of Rutherford Backscattering.
- An our collaborators *Prof. Dr. Anna Cavallini, Dr. Filip Tuomisto, Christian Rauch, and Dr. Gema Martinez-Criado* for the valuable characterization data which helped us to keep the track in the DMS business.
- *Dr. Karl Moesgen*, for being an excellent teacher and mentor in the early years. He was able to transmit his passion for physics in such a way that, without his motivation, i would have never been immersed in the interesting field of physics.

Last but not least, I want to dedicate this thesis once again to my parents, who invested a lot of efforts for my education, giving me the possibility to go abroad to search for better opportunities. In spite of the long distance which divides us, their constant moral support and encouragement was always a motivation to complete the goal i started on my own, nine years ago. „No hay palabras para agradecer lo que han hecho por mi, todo lo que soy es gracias a ustedes. Terminar mi doctorado y seguir creciendo como cientifico es lo menos que puedo hacer para retribuir vuestros esfuerzos. Los amo.“

Lebenslauf

Persönliche Daten

Name: Amilcar Bedoya Pinto
Geburtsdatum: 02. Juli 1980
Geburtsort: Lima, Peru
Adresse: Gosslerstrasse 51, 37075 Göttingen
Staatsangehörigkeit: peruanisch
Familienstand: ledig

Schulbildung

1987 - 1991 Grundschole „La Salle“, Lima, Peru
Apr.'91- Dez.'99 Gymnasium an der Deutschen Schule „Alexander von Humboldt“ in Lima, Peru -Abschluß Abitur

Hochschulausbildung

Okt.'00 - Mar.'06 Studium der Physik an der Technischen Universität München – Abschluß Diplom
Titel der Arbeit: „Novel ferromagnetic semiconductors: Preparation and characterization of bulk samples and thin films of Cu-doped ZnO“
bei Prof. Dr. R.Gross

Seit Jun.'06 Promotion an der Georg-August Universität Göttingen – am IV.Physikalisches Institut - Halbleiterphysik
Titel der Arbeit: „Structural, magnetic and electrical transport properties of GaN-based magnetic semiconductors and hybrid structures“
bei Prof. Dr. A. Rizzi